Spectroscopic approaches for the localization and dynamics of β_1- and β_2-adrenergic receptors in cardiomyocytes

–

Spektroskopieansätze zur Bestimmung der Lokalisation und Dynamiken von β_1- und β_2-Adrenozeptoren in Kardiomyozyten

Doctoral thesis for a doctoral degree
at the Graduate School of Life Sciences,
Julius-Maximilians-Universität Würzburg,
Section Biomedicine
submitted by

Marc Bathe-Peters

from

Berlin

Würzburg **2021**

Submitted on: ....

Office stamp

Members of the *Promotionskomitee*:

Chairperson: Prof. Dr. Manfred Gessler

Primary Supervisor: Prof. Dr. Martin J. Lohse

Supervisor (Second): Prof. Dr. Markus Sauer

Supervisor (Third): Prof. Dr. Christoph Maack

Supervisor (Fourth): Prof. Dr. Katrin Heinze

Supervisor (Fifth): Dr. Paolo Annibale

Date of Public Defence: ....

Date of Receipt of Certificates: ....

Affidavit

I hereby confirm that my thesis entitled ‘Spectroscopic approaches for the localization and dynamics of β_1- and β_2- adrenergic receptors in cardiomyocytes’ is the result of my own work. I did not receive any help or support from commercial consultants. All sources and / or materials applied are listed and specified in the thesis.

Furthermore, I confirm that this thesis has not yet been submitted as part of another examination process neither in identical nor in similar form.

Place, Date Signature

Eidesstattliche Erklärung

Hiermit erkläre ich an Eides statt, die Dissertation „Spektroskopieansätze zur Bestimmung der Lokalisation und Dynamiken von β_1- and β_2-Adrenozeptoren in Kardiomyozyten“ eigenständig, d.h. insbesondere selbstständig und ohne Hilfe eines kommerziellen Promotionsberaters, angefertigt und keine anderen als die von mir angegebenen Quellen und Hilfsmittel verwendet zu haben.

Ich erkläre außerdem, dass die Dissertation weder in gleicher noch in ähnlicher Form bereits in einem anderen Prüfungsverfahren vorgelegen hat.

Ort, Datum Unterschrift

Abstract

In the heart the β_1-adrenergic receptor (AR) and the β_2-AR, two prototypical G protein-coupled receptors (GPCRs), are both activated by the same hormones, namely adrenaline and noradrenaline. Both receptors couple to stimulatory G_s proteins, mediate an increase in cyclic adenosine monophosphate (cAMP) and influence the contractility and frequency of the heart upon stimulation. However, activation of the β_1-AR, not the β_2-AR, lead to other additional effects, such as changes in gene transcription resulting in cardiac hypertrophy, leading to speculations on how distinct effects can arise from receptors coupled to the same downstream signaling pathway.

In this thesis the question of whether this distinct behavior may originate from a differential localization of these two receptors in adult cardiomyocytes is addressed. Therefore, fluorescence spectroscopy tools are developed and implemented in order to elucidate the presence and dynamics of these endogenous receptors at the outer plasma membrane as well as on the T-tubular network of intact adult cardiomyocytes. This allows the visualization of confined localization and diffusion of the β_2-AR to the T-tubular network at endogenous expression. In contrast, the β_1-AR is found diffusing at both the outer plasma membrane and the T-tubules. Upon overexpression of the β_2-AR in adult transgenic cardiomyocytes, the receptors experience a loss of this compartmentalization and are also found at the cell surface. These data suggest that distinct signaling and functional effects can be controlled by specific cell surface targeting of the receptor subtypes.

The tools at the basis of this thesis work are a fluorescent adrenergic antagonist in combination of fluorescence fluctuation spectroscopy to monitor the localization and dynamics of the lowly expressed adrenergic receptors. Along the way to optimizing these approaches, I worked on combining widefield and confocal imaging in one setup, as well as implementing a stable autofocus mechanism using electrically tunable lenses.

Zusammenfassung

Im Herzen werden der β_1-adrenerge Rezeptor (AR) und der β_2-AR, zwei prototypische GPCR, durch die Hormone Adrenalin und Noradrenalin aktiviert. Dabei interagieren beide Rezeptoren mit dem stimulatorischen G_s Protein, bewirken eine Erhöhung des cyclischen Adenosinmonophosphates (cAMP) und beeinflussen die Kontraktionskraft und Frequenz des Herzens nach einem Stimulus. Jedoch hat die Aktivierung des β_1-ARs, nicht des β_2-ARs, auch weitere Effekte, wie z.B. Veränderungen in der Transkription von Genen. Dies wiederum führt zu Spekulationen, wie solch unterschiedliche Effekte von Rezeptoren hervorgerufen werden können, die gleiche Signalwege bedienen.

In dieser Arbeit wird untersucht, ob dieses unterschiedliche Verhalten durch eine ungleiche Verteilung dieser beiden Rezeptoren in adulten Kardiomyozyten hervorgerufen werden könnte. Dazu wird die Lokalisation und die Dynamik dieser endogenen Rezeptoren in der Plasmamembran sowie im T-tubulären Netzwerk von intakten adulten Kardiomyozyten, unter Entwicklung und Verwendung hochsensitiver Fluoreszenzspektroskopiemethoden, bestimmt. Dies ermöglicht die örtliche und dynamische Eingrenzung des β_2-adrenergen Rezeptors unter endogener Expression ausschließlich auf das T-tubuläre Netzwerk. Dementgegen stellt sich heraus, dass sich der β_1-adrenerge Rezeptor ubiquitär auf der äußeren Membran und den T-Tubuli befindet und diffundiert. In β_2-AR überexprimierenden transgenen Kardiomyozyten hingegen werden diese Kompartments nicht beibehalten und es findet eine Umverteilung der Rezeptoren, auch unter Einbezug der Zelloberfläche, statt. Diese Daten können stärker darauf hindeuten, dass einige Rezeptorsubtypen sich gezielt und spezifisch bestimmte Zelloberflächen aussuchen, um somit ihre verschiedenen Signale und funktionären Effekte erzeugen zu können.

Zu den Techniken, die in dieser Arbeit die Bestimmung der Lokalisation und der Dynamiken der niedrig exprimierten adrenergen Rezeptoren zulassen, gehört die Anwendung von Fluoreszenzspektroskopiemethoden in Kombination mit einem fluoreszierenden β-adrenergen Antagonisten. Weitere Techniken, die im Rahmen dieser Arbeit entwickelt wurden und in weiterführenden Studien aufschlussreiche Erkenntnisse liefern könnten, umfassen die Entwicklung eines Setups aus einer Kombination aus Weitfeld- und Konfokalmikroskopie und die Implementierung eines stabilen Autofokus mit Hilfe einer elektrisch veränderbaren Linse.

Contents

Acronyms

$\boldsymbol{\omega_0}$	lateral beam waist
$\boldsymbol{\beta_1/\beta_2}$**-AR-k.o.**	β_1/β_2-AR knock-out
$\boldsymbol{\beta_1}$**-AR-TG4**	transgenic mouse line overexpressing the β_1-AR
$\boldsymbol{\beta_2}$**-AR-TG32**	transgenic mouse line overexpressing the β_2-AR
$\boldsymbol{\tau_D}$	diffusion time
1D	1 dimension
2D	2 dimensions
3D	3 dimensions
A431	human epidermoid carcinoma cell line, derived from an 85-year-old female
AAV	adeno-associated viruses
AC	autocorrelation curve
AR	adrenergic receptor
BCS	bovine calf serum
BSA	bovine serum albumin
cAMP	cyclic adenosine monophosphate
cDNA	complementary DNA
CFP	cyan fluorescent protein
cGMP	cyclic guanosine monophosphate
CGP 20712	1-[2-((3-Carbamoyl-4-hydroxy)phenoxy)ethylamino]-3-[4-(1-methyl-4-trifluoromethyl-2-imidazolyl)phenoxy]-2-propanol
CM	cardiomyocyte
D	dimenional
DAQ	data acquisition
DMEM	Dulbecco's modified Eagle's medium
ECL	extracellular loop
EDTA	(ethylenedinitrilo)tetraacetic acid
EGFP	enhanced green fluorescent protein

ETL	electrically tunable lens
FBS	fetal bovine serum
FCS	fluorescence correlation spectroscopy
FFT	fast Fourier transform
FITC	fluorescein isothiocyanate
FRET	fluorescence resonance energy transfer
GDP	guanosine diphosphate
GEF	guanine-nucleotide exchange factor
GIRK	G protein-activated inwardly rectifying potassium channel
GPCR	G protein-coupled receptor
GRK	G protein-coupled receptor kinase
GTP	guanosine triphosphate
H9c2	rat cardiomyoblast cell line
HEK	human embryonic kidney
Hepes	4-(2-hydroxyethyl)-1-piperazineethanesulfonic acid
HF	heart failure
hiPSC	human induced pluripotent stem cell
HyD	hybrid detectors
IC_{50}	half maximal inhibitory concentration
ICI 118,551	(2R,3R)-rel-3-isopropylamino-1-(7-methylindan-4-yloxy)-butan-2-ol
ICL	intracellular loop
IR	infrared
JE1319	novel β_1- and β_2- adrenergic receptor specific fluorescent antagonist
K_d	dissociation constant
K_i	inhibitory constant
ko	knock-out
MC	myocyte
mCherry	monomeric red fluorescent protein
MDC	Max Delbrück Center for Molecular Medicine

MEM	minimum essential medium
mRNA	messenger ribonucleic acid
MSD	mean square displacement
NA	numerical aperture
NAM	negative allosteric modulator
NHERF	Na^+/H^+ exchange regulatory factor
NSF	N-ethylmaleimide-sensitive factor
PALM	photoactivated localization microscopy
PAM	positive allosteric modulator
PBS	phosphate buffered saline
PDZ	PSD-95/Discs-large/ZO-1
PID	proportional-integral-derivative
PKA	protein kinase A
PKC	protein kinase C
PM	plasma membrane
PSF	point spread function
QPD	quadrant photodiode
ROI	region of interest
RPMI	Roswell Park Memorial Institute
RT	room temperature
SD	standard deviation
SEM	standard error of the mean
STICS	spatio-temporal image correlation spectroscopy
STORM	stochastic optical reconstruction microscopy
TG	transgene
TIR	total internal reflection
TIRF	total internal reflection fluorescence
TM	transmembrane
TT	T-tubule
wt	wild-type
Y_2R	neuropeptide Y receptor type 2

List of Figures

List of Tables

1 Introduction

In industrialized countries ischemic heart diseases or coronary heart diseases are the leading causes of death. Each year 15 million people worldwide die from or as a consequence of these heart complications [1]. In cardiovascular diseases a variety of disorders affect the myocardium and the vasculature with potential risks of cardiomyocyte loss, an increase of cardiac work and afterload. In order to stimulate cardiac function the sympathetic nervous system releases the catecholamines adrenaline and noradrenaline into the heart via the bloodstream. These catecholamines, like many other hormones and neurotransmitters bind to and activate G protein-coupled receptors (GPCRs), which represent the largest group of cell surface receptors regulating virtually all physiological functions. As a family which comprises several hundred members, GPCRs transmit signals into the cell by coupling to G proteins and by provoking second messenger responses to generate diverse physiological responses to control metabolic, humoral, neural and developmental functions, such as vision, taste, olfaction, immune response, neurotransmission and cardiac function [1–4].

The catecholamines find their interaction partners in the adrenergic receptors (ARs) in cardiomyocytes (CMs). Under physiological conditions and in order to maintain cardiac output and function in particular, β-ARs regulate a multitude of functions involving the regulation of inotropic, lusitropic, chronotropic and dromotropic activity [1, 2]. Out of the three β-AR subtypes, the β_1- and the β_2-ARs are predominantly expressed in the heart. Both receptors couple to G_s proteins and stimulate the production of the second messenger cyclic adenosine monophosphate (cAMP) [5]. Although both receptors stimulate contractility, in addition they also lead to distinct physiological and pathophysiological responses. It is the β_1-AR, not the β_2-AR, that alters gene expression to induce hyperthrophy [6, 7], stimulates protein kinase A (PKA) mediated phosphorylation of phospholamban and cardiac contractile proteins [8], and promotes CM apoptosis [9, 10]. Prolonged stimulation of β_1-ARs, less of the β_2-ARs, leads to cardiac remodeling and results ultimately in the development of heart failure. The ability of the β_2-ARs to couple to inhibitory G_i proteins may account in part for some of these distinct effects [11, 12].

Also spatial differences in signaling may be involved in specific downstream effects. An interesting discovery has been made by demonstrating that the β_2-AR generated second messenger cAMP signals only upon a stimulus directly to the T-tubules (TTs) of the CMs, while stimulated β_1-ARs elicited cAMP signals over the entire cell surface, also including TTs [13], thus suggesting that different cardiac effects of the two receptors could be based on their differential locations. Direct evidence of this suggested differential localization has yet not been attained, mainly due to lack of visualization tools and the challenging environment adult CMs present; fairly high autofluorescence [14], the difficulty of isolating them and their short lifespan. Despite the enormous advancement of high-resolution microscopy and the steady improvement of biosensors, visualization of endogenous proteins in cells remains challenging. Here, in order to overcome this hurdle a fluorescence correlation spectroscopy (FCS) approach, a technique sensitive to very low concentrations [15, 16], is applied in combination with a fluorescent ligand, specific for the β_1-AR and β_2-AR, to determine the localization and dynamics of these two receptors.

1.1 G protein-coupled receptors

G protein-coupled receptors (GPCRs) represent the largest class of membrane proteins in the human genome. Located on the cell membrane they transduce extracellular signals into physiological effects to control metabolic, humoral, neural, and developmental functions by endogenous ligands including amongst others odors, hormones, neurotransmiters, chemokines in form of photons, amines, carbohydrates, lipids, peptides and proteins [4, 17]. As cell surface receptors they are not only substantially involved in physiological functions, but also in pathophysiological functions and play a role in diseases, such as e.g. diabetes, obesity, Alzheimer or cancer and in disorders of the central nervous or cardiovascular system [2, 18, 19]. This has made them and GPCR-mediated signaling pathways, among other receptor types such as ion channels, nuclear hormone receptors etc., targets of an estimate of 30-50% of all drugs currently on the market [18, 20, 21]. Also known as the seven transmembrane (TM) receptor, they comprise approximately 800 members of which about half have sensory functions mediating olfaction, taste, light perception and pheromone signalling [22]. Two main requirements classify a protein as a GPCR. The first one relates to the seven hypdrophobic α-helices (TM domains) that span the plasma membrane (PM) in a counter-clockwise manner to form a recognition and connection unit, a receptor, that enables the cell to exert a specific effect upon extracellular stimulation. The single polypeptide forms an among GPCRs common architecture consisting of an extracellular N-terminus, the seven hydrophobic transmembrane domains (TM1-TM7) connected by three intracellular loops (ICL1-ICL3) and three extracellular loops (ECL1-ECL3) to end intracellularly with the C-terminus (fig. 1.1). The second requirement is the capability of the receptor to interact with a G-protein [23, 24].

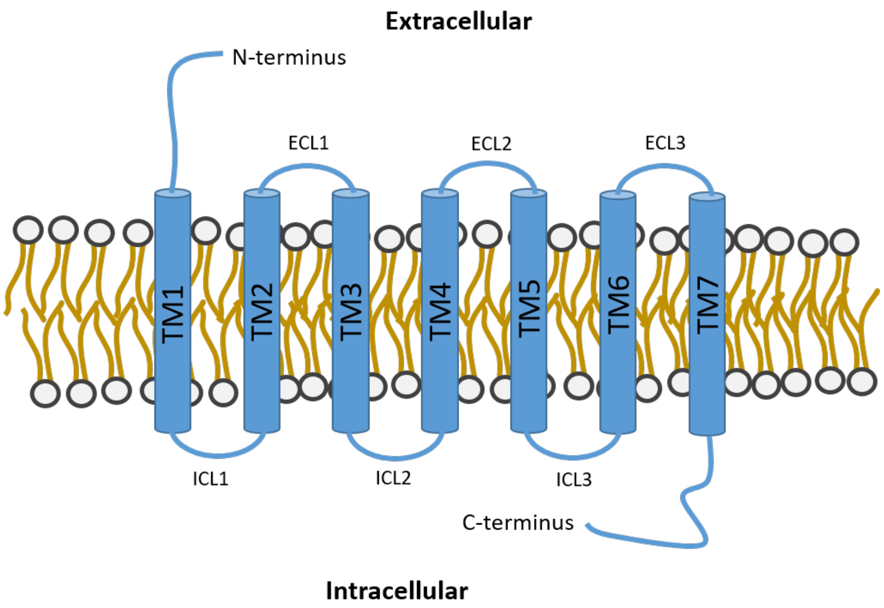

Figure 1.1: Two dimensional schematic structure of a GPCR. The in the plasma membrane of living cells embedded GPCRs consist of an extracellular N-terminus, seven hydrophobic TM domains (TM1-TM7), the intracellular loops (ICL1-ICL3), the extracellular loops (ECL1-ECL3) and the intracellular C-terminus.

1.1.1 GPCR classification

Several classification systems of GPCR have been proposed. The most commonly used system covers all GPCRs in vertebrates and invertebrates and groups them into six classes based on structural similarities to prototypical receptors (table 1.1). Therefore some of the families, such as classes D and E, do not exist in humans and are not found in vertebrates [23, 25].

Class	Family name
A	rhodopsin-like
B	secretin
C	metabotropic glutamate
D	fungal mating pheromone
E	cyclic AMP
F	frizzled/smoothened

Table 1.1: GPCR classification based on structural similarities.

A second classification, termed as the GRAFS system, contains most of the functional GPCRs in vertebrates and therefore in the human genome and consists of five main families as shown in table 1.2 [23].

These classes contain many GPCRs which still lack reliable assignment of interacting ligands and are therefore referred to as orphan receptors [19].

Class	Family name
G	glutamate
R	rhodopsin
A	adhesion
F	frizzled/taste2
S	secretin

Table 1.2: GPCR classification based on phylogenetic relationships.

Based on the division on structural similarities (table 1.1), the adrenergic receptors belong to the rhodopsin family or class A receptors which with its 700 members contains the largest number of receptors among the groups [17, 23, 24, 26].

1.1.2 GPCR activation and signaling

GPCRs regulate highly diverse physiology although they share a common signaling mechanism. This signaling mechanism is initiated by an extracellular stimulus, exemplified by an extracellular ligand, inducing a conformational change of the receptor which enables the activation of heterotrimeric G proteins and other intracellular effectors initiating the starting point of an intracellular signaling cascade.

There are different ways of how a cell response is provoked and how cellular function is fine-tuned to regulate receptor signaling. The vast majority of 7TM receptors are coupled to G proteins, which in turn transduce the external signal to effectors. This serves as the classical example of how GPCRs signal. The G proteins are heterotrimers consisting of an α, β and γ subunit. In mamalian cells G protein subunits are known to be encoded by families or related genes. To date there are 16 α, 5 β and 12 γ subunits [2, 3, 27–29].

G proteins are generally referred to by their α subunits and the 16 G_α subunits are divided into four major families, namely the G_{α_s}, the G_{α_i}, the G_{α_q} and the $G_{\alpha_{12/13}}$ (fig. 1.2). The activation of the receptor by a ligand (e.g. agonist) induces a conformational change which causes the 'activated receptor' to interact with the heterotrimeric G protein serving as a guanine-nucleotide exchange factor (GEF) to promote guanosine diphosphate (GDP) dissociation and guanosine triphosphate (GTP) binding in the G_α subunit. As a consequence of this guanine nucleotide exchange the dissociation of the heterotrimer from the carboxyl terminus of the receptor as well as the detachment of the G_α from the $G_{\beta\gamma}$ subunit is induced. The subunits possess the capacity to regulate separate effectors and to initiate signaling pathways independently. After the termination of the activation cycle and signaling, hydrolysis of GTP to GDP leads to reassociation of the heterotrimer, as depicted in fig. 1.2, allowing for the reactivation of the receptor and reinitiation of the process [2, 3, 30–32].

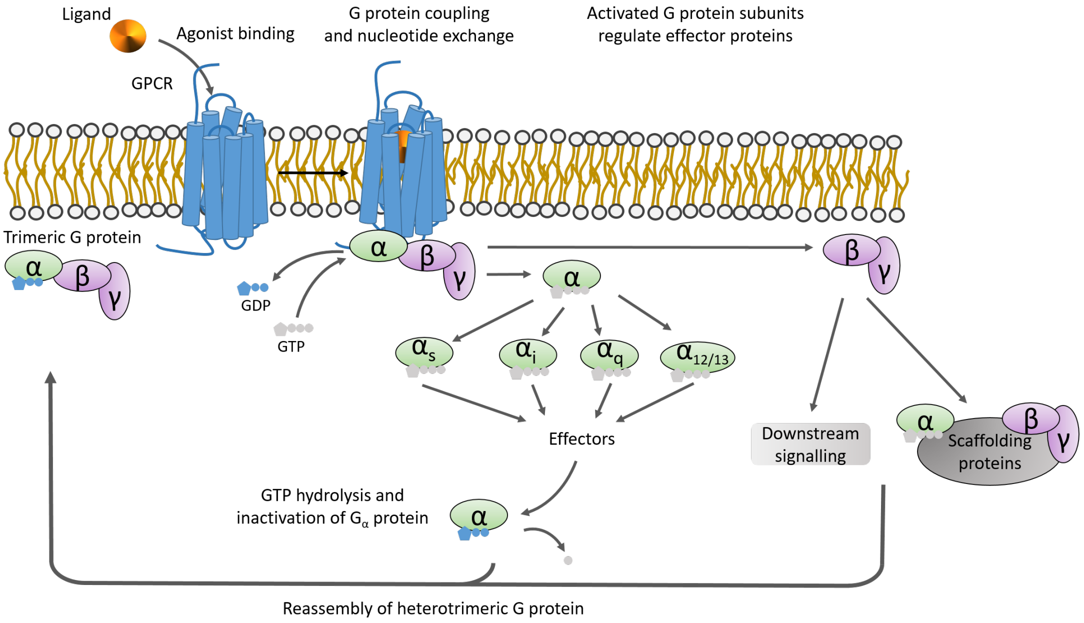

Figure 1.2: Activation by ligand binding promotes the interaction of the GPCR with the GDP-bound heterotrimeric G protein, leading to an exchange of GDP for GTP and the dissociation of the G_α from the $G_{\beta\gamma}$ subunit. Four major classes of G_α proteins regulate their respective effector proteins. The signaling is terminated with the hydrolysis of GTP to GDP in the α subunit and the reassembly of the G_α and the $G_{\beta\gamma}$ subunit.

1.1.2.1 GPCR ligand classification

Binding of GPCR ligands to their receptors is able to modulate receptor-mediated signaling. Classically receptor-ligand interactions are characterized by saturation and competition binding experiments often applying radiolabeled ligands or fluorescence assays. Both experiments require a labeled compound which is either measured at increasing concentrations (saturation experiment) or at a fixed concentration upon displacement by an increasing concentration of unlabeled ligand (competition experiment) [33–38]. One way to classify ligands is based on the targeted receptor binding site. This way ligands which bind to the same binding site as the endogenous ligand are called orthosteric ligands. Allosteric modulators can alter receptor signaling, but bind to sites that are topographically distinct from the orthosteric binding site [39–41].

Further characterization classifies ligands according to their biological responses on the structure and biophysical properties, also known as efficacy, as depicted in fig. 1.3. Many receptors exhibit basal or constitutive activity without a bound compound. Full agonists produce a maximal receptor stimulation. Partial agonists on the other hand do not elicit maximal receptor response even at saturating concentrations. Neutral antagonists have no effect on signaling activity, but stabilize the receptor in its basal conformation and prevent other ligands from binding to the receptor. Finally inverse agonists reduce the level of constitutive activity below that of a GPCR without ligand [42].

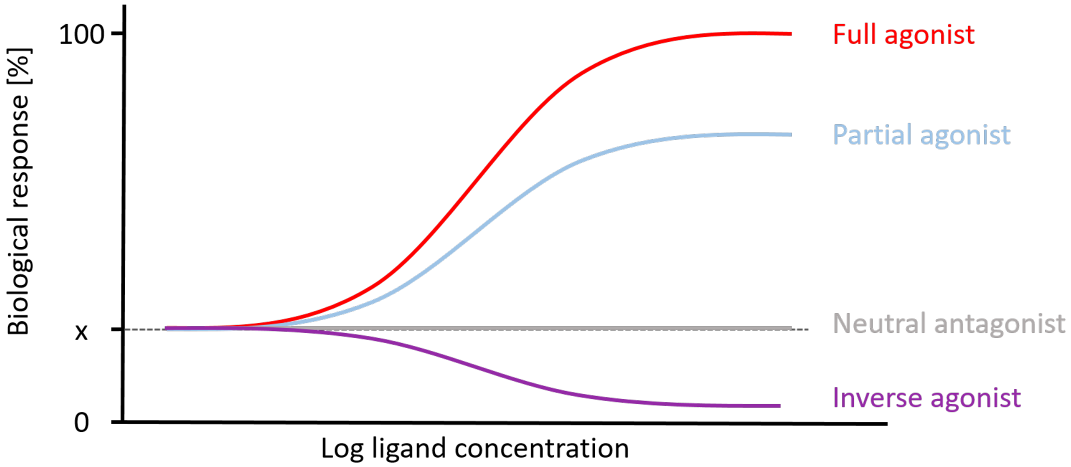

Figure 1.3: Many GPCRs exhibit an activity in their basal state, where no compound is bound at the extracellular side. They are constitutively active. Binding of a full agonist stimulates the biological response and increases the activity to maximal (full agonist) or submaximal (partial agonist) levels. Neutral antagonists stabilize the basal conformation of the receptor showing no effect. Inverse agonists decrease this activity and signaling and induce a transition to a more inactive receptor conformation.

1.1.2.2 GPCR desensitization and β-arrestin signaling

Essential cellular functions can be fine-tuned by many mechanisms that regulate receptor signaling. Therefore it is not surprising that signaling can occur with dampened signal, even in the presence of continuous stimulation. This phenomenom, referred to as ‘desensitization’, operates at the level of the receptor as well as downstream. Rapid dampening of receptor function is frequently controlled by receptor phosphorylation either mediated by second-messenger kinases (PKA and protein kinase C (PKC)), which directly uncouple receptors from their respective G protein, or by a distinct family of G protein-coupled receptor kinases (GRKs) via the GRK-β-arrestin system (fig. 1.4) mediating ‘homologous’ or agonist-specific desensitization. Thereby only the activated or agonist-occupied conformation of the receptors is phosphorylated by GRKs. GRK phosphorylation inhibits further interactions between the receptor and the G protein by promoting binding of an arrestin molecule to the receptor. There are seven members (GRK1-GRK7) of the family of serine/threonine kinases (GRKs) and four arrestin genes of which 2, the β-arrestin-1 (arrestin-2) and β-arrestin-2 (arrestin-3), are ubiquitously expressed (whereas the other 2 are exclusively expressed in the retina). β-arrestins recognize phosphorylated residues and bind to the cytosolic surfaces of receptors thereby firstly obstructing G protein heterotrimer reassembly at the receptor leading to a desensitzation together with GRKs. Secondly, β-arrestins may act as scaffolds or adaptors to bind other proteins such as clathrin and clathrin adapter proteins. The result is an invagination and eventually endocytosis of the membrane as clathrin is recruited and polymerized. In this way, β-arrestins desensitize and downregulate GPCRs as the clathrin-coated vesicles or endosomes, which contain the GPCR, either fuse to lysosomes for degradation of the receptor, recycle back to the PM or mediate additional signaling via re-engagement with G proteins.

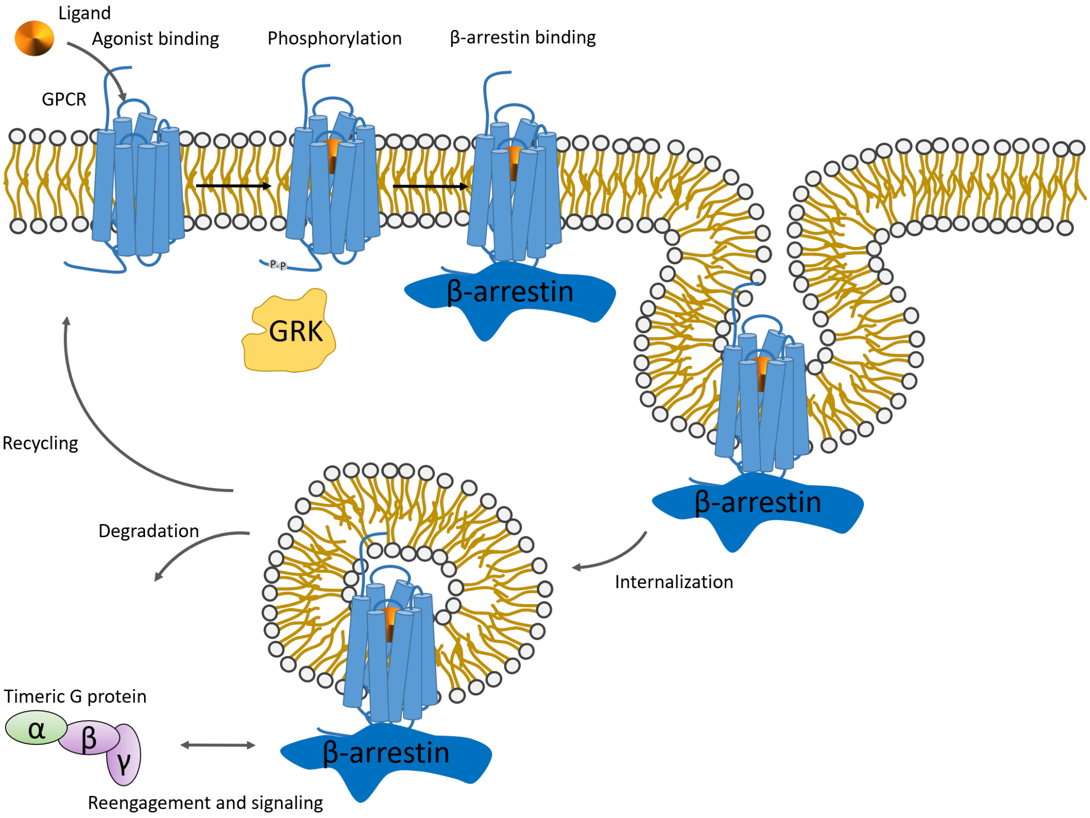

Figure 1.4: Schematic of β-arrestin signaling. Activated receptor gets phosphorylated by protein kinases or GRKs which promotes β-arrestin interaction with the receptor. After binding of β-arrestin to the phosphorylated receptor activated β-arrestins can interact with their C-terminal tail with components of the endocytic machinery including clathrin to promote the uptake of the receptor into clathrin-coated pits for internalization. The internalized receptor can then be sorted for various post-endocytic fates such as recycling or degradation in lysosomes or mediate additional signaling by re-engaging with G proteins [43].

In the heart the primary regulators of physiological β_1- and β_2-AR desensitization in response to catecholamines are GRK2 and GRK5. The expression and activity of these two GRKs is augmented during prolonged catecholamine exposure, which is the case in stressed and failing hearts. Underyling this sustained increase in the level of GRK expression is a pathological β-AR reduction and insensitivity leading eventually to a loss of inotropic, lusitropic, chronotropic and dromotropic reserve [2, 3, 43].

1.1.3 β-adrenergic receptors and their role in the heart

In the heart, cardiac physiology is regulated by numerous GPCRs on multiple cell types. Examples of such GPCRs are the adenosine, angiotensin II, muscarinic acetylcholine and the adrenergic receptors [2].

After the introduction of the concept of a receptor that binds drugs or transmitter substances onto the cell, thereby initiating or inhibiting biological effects or cellular functions, in the early 1900s, Ahlquist divided adrenergic receptors in 1948 into α and β according to their functional effects of vasoconstriction and vasodilatation. Later, it was shown that activation of β-ARs in the heart muscle mediated positive chronotropic and inotropic effects before in 1989 the existence of a third isoform of β-ARs was observed [43–45].

In cardiomyocytes ARs regulate functions such as contractile force, rate and growth [2].

In humans ARs, as a subfamily of GPCRs, are expressed in many cell types and can be categorized into three broad classes: the α_1-ARs, the α_2-ARs and the β-ARs. Each of these divides into three subtypes according to structural and functional differences. The α_1-ARs are highly expressed on vascular smooth muscle cells and cardiomyocytes and the α_2-ARs are primarily found in the central nervous system. The β-ARs consist of the β_1-, the β_2- and the β_3-AR and are targeted by the catecholamines adrenaline (epinephrine) and noradrenaline (norepinephrine) thereby regulating a wide variety of physiological processes including cardiac, pulmonary and metabolic function. They are ubiquitously expressed in humans, but predominantly found in the myocardium/cardiac tissue (predominantly β_1), vascular smooth muscle (β_2 expresses high levels in that tissue, especially in the airway) and adipose tissue (involving β_3 in lipolysis and thermogenesis). Additionally they are all expressed in cardiomyocytes. The predominant type, expressed in the cardiomyocytes with approximately 80%, is the β_1-AR. The remaining 20% are mostly β_2-ARs with a small extend of β_3-ARs (also depending on the species; some divide the ratio into 17% β_2-AR to 3% β_3-AR) [2, 10, 43–46].

1.1.3.1 β-adrenergic receptor signaling

β-AR signaling is initiated by binding of the catecholamines adrenaline or noradrenaline. The three receptor subtypes, the β_1-, the β_2- and the β_3-AR, exert functions based on the signaling pathway which they initiate. β_1-AR signaling, mediated via G_s (section 1.1.2), provokes cardiac responses, such as increasing contractility and cellular growth. The G_s pathway leads to the production of cAMP via the activation of adenylyl cyclayse. Consequently the cAMP dependent PKA phosphorylates substrates such as the L-type Ca^{2+} channels and the sacroplasmic reticulum calcium-release channels, thereby increasing the Ca^{2+} entry into the cell which promotes contraction. By the phosphorylation of myofilaments via PKA, such as troponin I, the sensitivity to calcium is reduced linking these respones to cardiac chronotropic and inotropic effects. Phosphorylation of phospholamban-tpye calcium channels accelerates the intake of Ca^{2+} into the sarcoplasmic reticulum and thereby accelerates cardiac relaxation. Increased chronotropy and dromotropy is achieved by activation of L-type Ca^{2+} channels in the sinoatrial and atrioventricular nodes. The β_2-AR, having a higher affinity for adrenaline than for noradrenaline, couples to both G_s and G_i thereby exerting stimulatory and inhibitatory effects on cAMP, that influence cardiac contractile function. β_3-ARs are G_i coupled, but additional intracellular signaling includes the activation of nitric oxide synthases, activation of guanylate cyclase and formation of cyclic guanosine monophosphate (cGMP) [2, 5, 8, 44].

In adult cardiomyocytes there is evidence that spatial difference in signaling critically influences downstream effects. In fact, the concept of compartmentalization of cAMP and of receptor-mediated cAMP signals has been suggested for decades [47–53]. This effect of local differential responses was directly visualized in adult murine CMs by observation of fluorescent biosensors, namely the Epac2-camps, reading local fluorescence resonance energy transfer (FRET)-based cAMP concentrations which reacted to local stimulation of the receptors administered via a scanning probe delivery method [13]. These results demonstrated that β_1-AR-stimulated cAMP signals could be elicited over the entire cell surface including T-tubules while β_2-ARs elicited cAMP signals only when the stimulus was delivered directly to the TTs of cardiomyocytes. An additional evidence for distinct compartments of β-AR-triggered cAMP was provided by Yang et al. [54]. They observed that, upon β_2-AR stimulation, β_1-AR-stimulated cAMP compartments were reduced to nanometer sizes. A more recent study by Bock et al. [55] investigates how such precise control of these nanometer sized domains is regulated and suggests a model in which these nanodomains can vary in size in order to govern the activation of downstream effectors.

So far, the mechanisms leading to the specific targeting of β_2-AR signaling to TTs remain unclear. In principle, the downstream compartmentalization of the second messenger could be the result of compartmentalization of, or spatial modulation at, any of the upstream signaling steps. Such processes could include cAMP-degrading enzymes such as phosphodiesterases [56], effectors producing cAMP (i.e. adenylyl cyclases), receptor to G-protein coupling [57] and receptor localization itself [58]. While β-AR activation is mediated by G proteins (mainly G_s), activated β-ARs are desensitized by regulatory kinases such as GRKs upon preceding phosphorylation [43]. Signaling is then terminated via interaction with β-arrestins. Further details about this interaction is found in section 1.1.2.2 [43].

β-AR signaling pathways are depicted as an overview in fig. 1.5. In balanced signaling interacts the receptor with G proteins, GRKs and arrestins. Biased signaling favors signaling either via G proteins (G protein biased signaling) or via the GRK/arrestin pathway (arrestin biased signaling). Figure 1.5 illustrates how it is possible to influence these receptors with cardiovascular drugs (section 1.1.3.3) by blocking or enhancing specific pathways in order to treat cardiovascular diseases (section 1.1.3.2).

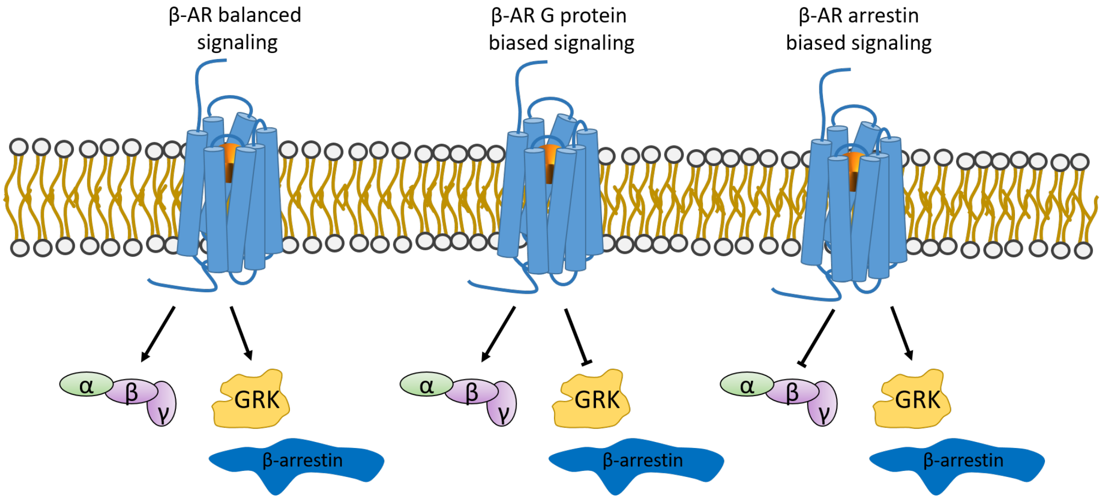

Figure 1.5: Schematic of β-AR signaling. Depicted is an overview of the singalling pathways of β-ARs. Balanced signaling allows the receptors to signal via the interaction with a G protein and GRKs as well as arrestins. G protein biased signaling can be provoked either by enhancing G protein mediated signaling relative to GRK and arrestin interaction or reduction of such by intact G protein signaling. On the contrary in arrestin biased signaling G protein signaling is reduced relative to the GRK/arrestin pathway [43].

1.1.3.2 β-adrenergic receptors in heart failure

Heart failure (HF) is accompanied with heart complications such as partial coronary artery occlusion leading to heart muscle ischemia, blood and oxygen deprivation, angina pectoris, acute myocardial infarction and ultimately sudden cardiac death. In a less severe state and initially blood clots, coronary artery constriction or atherosclerosis can lead to irreversible cardiomyocyte death further affecting cardiac function. To compensate the impaired cardiac function, the body activates an adaptive mechanism including the chronic sympathetic nervous system activation thereby also elevating the circulating catecholamine levels. While this adaptation is at first beneficial for contractile function, prolonged activation of the sympathetic system is deleterious. Thus in HF, numerous alterations of the cardiac β-AR system are observed leading to cardiac remodeling, cardiac myocyte apoptosis [9] and fibrosis, consequently resulting in fatal heart failure and arrhythmias [1]. Specifically prolonged stimulation of β-ARs has been described via second-messenger response of cAMP to alter β-AR localization in CMs. In this context it has been observed that signaling of β_2-ARs redistributed from TTs to the PM of CMs marking the loss of compartmentation and localized effects of cAMP upon receptor stimulation [2, 13]. Additional increased β_2-AR-coupling to inhibitory G_i proteins in HF reduces the contractile response [11, 12]. Further alterations are described by a β_1-AR subtype specific reduction and its mRNA level by up to $\sim$50%, depending on the severity of the disease. β_2-AR levels on the other hand are reported to remain unchanged. This β_1-AR subtype specific downregulation is accompanied by a desensitization of the β-ARs mostly via GRKs. Also increased G_i signaling in heart failure shifts signaling away from G_s-coupled receptor systems further reducing responsiveness and resulting in a loss of inotropic, lusitropic, chronotropic and dromotropic reserve [2, 10].

1.1.3.3 β-adrenergic receptor antagonists

Antagonists to the β-ARs possess the ability to block these receptors, thereby reducing sympathetic nervous system activity. That's why since around 1960 intensive research was conducted to find and to make use of these 'so-called' β-blockers as an essential class of cardiovascular drugs to reduce morbidity and mortality in patients with cardiovascular diseases aiming to decrease the number of deaths, strokes and heart attacks associated with hypertension. The specificity of β-blockers relates directly to the affinity the drug has for the β-AR subtypes at usual therapeutic levels. Over the years multiple β-blockers have been developed with distinct pharmacological and hemodynamic properties [44].

While some medications exert G protein biased signaling (an example would be the β_2-agonism providing bronchodilation in airway smooth muscle), arrestin biased signaling at the β_1-AR provides additional clinical utility compared to balanced antagonists (see fig. 1.5) for cardiopathies. In order to counteract the compensatory dysregulation of the sympathetic nervous system, which increases the catecholamines in circulation in compensated, stable congestive heart failure, blockage of G protein signaling, through cardiac β_1-AR reduces heart rate, ultimately improving the ejection fraction. This therapeutic strategy can be achieved by further desensitizing β_1-ARs at the cell membrane through β-arrestin biased signaling (agonists) [43].

Blockers can be divided into three distinct generations according to pharmacological properties. The first generation of β-blockers were non-selective with the consequence that they block both β_1- and β_2-ARs. They lower blood pressure through decreasing contractile strength and its rate. The result is a reduced cardiac output reducing the suffering from hypertension, angina and post-myocardial infarction. A prominent example is propranolol which should not be administered in case patients suffer from diabetes or specific lung pathologies, such as asthma or chronic obstructive pulmonary disease, because of its antagonistic effects on β_2-ARs.

With the second generation of β-blockers higher cardioselectivity was achieved marked by antagonists with higher affinity for the β_1-receptor (compared to the β_2-AR). They possess similar beneficial effects as the first generation with less risk of adverse effects associated with β_2-AR antagonism. Examples are atenolol and metoprolol.

The third generation of β-blockers, with examples like nebivolol and carvedilol, exhibit beneficial effects in patients with cardiovascular diseases such as to reduce peripheral vascular resistance, thereby lowering cardiac work, and decreasing the oxygen demands by the heart muscle. Additional effects are of angiogenic, anti-hypertrophic, antioxidant, antifibrotic and anti-apoptotic nature, resulting in lower blood pressure, reduction of cardiac remodeling and a decrease in endothelial and cardiac dysfunction [44].

Other prominent examples of β-AR antagonists, mostly used for research, are CGP 20712, which showed one of the highest selectivities for β_1-ARs over the other two subtypes [33], and ICI 118,551, which is among the most selective compounds for the β_2-AR [33]. Of the non-selective β-blockers carazolol antagonizes β-ARs with one of the highest affinities being about 10-20 times higher than those of propranolol [35, 36].

1.2 Fluorescence imaging

In biology, fluorescence microscopy has become one of the most versatile imaging modalities to investigate cells, tissues and cellular processes with molecular specificity noninvasively. Since the first description of fluorescence in 1852 by the British scientist Sir George G. Stokes the technique has become an essential tool to identify sub-microscopic cellular components and to visualize molecular interactions [59, 60]. By specific labeling with small fluorescent molecules or fluorescent proteins, endogenous proteins in living cells can be visualized up to single molecule accuracy.

The process of fluorescence can be schematically understood acoording to fig. 1.6 which illustrates a Jablonski diagram with a two singlet states and one triplet state fluorescence system. The ground state is named S_0 and the first excited state S_1. Normally the system is in the lowest vibrational energy level S_0 of the ground state. When a photon ($h\upsilon_a$) is absorbed it elevates the molecule to one of the vibrational energy levels of the first excited state S_1 which rapidly decays to the lowest vibrational energy level of the first excited state. The molecule can then undergo a non-radiative decay or a radiative process by emitting a Stokes-shifted photon ($h\upsilon_{fl}$), owing the energy difference to the relaxation of vibrational relaxation upon return to the ground state S_0. The molecule can also transition into a forbidden/triplet state T_1 which then will be followed by a reverse intersystem crossing either being radiative (phosphorescence) or non-radiative. The fluorescence blinks as the system crosses between the singlet (on) and triplet states (off) [61, 62].

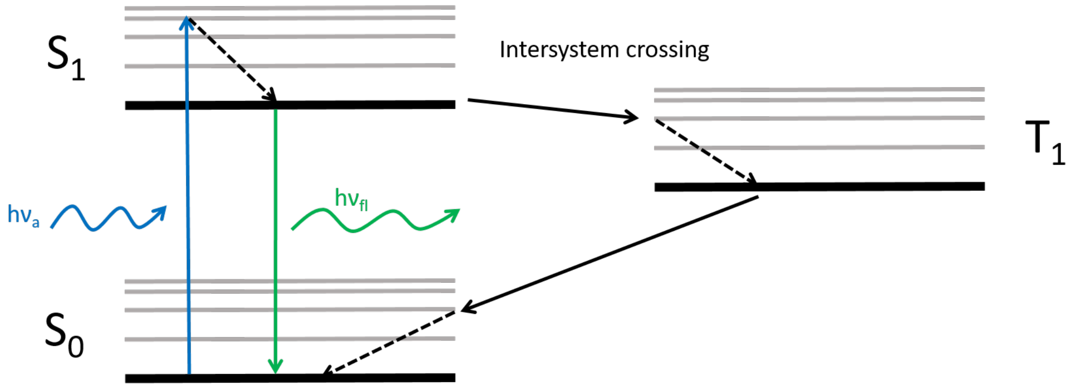

Figure 1.6: Jablonski diagram of two singlet states and one triplet state depicting the excitation and emission states as well as the intersystem crossing into the triplet state.

Nowadays, some of the most widely used systems in cell biology are widefield imaging techniques or laser scanning confocal fluorescence microscopy [63, 64], a technique which reduces out-of-focus fluorescence through defined optical sections inside specimens [65].

Example applications include the investigation of cAMP signaling [55], cAMP response in CMs [13] or dimerization studies [66, 67] with techniques such as confocal imaging, FRET, a FCS approach and total internal reflection fluorescence (TIRF) imaging.

Despite the enormous progress in the field and of high-resolution microscopy over the last two decades, development of effective cAMP biosensors [68] and better understanding of GPCR signaling mechanisms [69], reports of direct observation of receptor or G protein partitioning at single cell level are scarce [58]. While visualization of endogenous receptors labeled with fluorescent ligands on the basolateral membrane of primary cells has been successfully achieved by TIRF microscopy [70], limitations of penetration depth have prevented the acquisition of images at adult CMs and their intracellular network of T-tubular membranes. Visualization of endogenous proteins involved in the GPCRs signaling cascade at intracellular structures, including receptors, remains challenging and has been hampered by the lack of effective microscopic visualization tools. In particular, in imaging of primary cells at endogenous, low expression levels of the order of a few receptors per micrometer squared of cell membrane [71] the intensity contrast by conventional techniques (widefield and confocal) is very limited. On the other hand a confocal-based FCS approach, which has been described to be sensitive to very low concentrations, offers the possibility to circumvent this limitation.

1.2.1 Fluorescence correlation spectroscopy

FCS offers the possibility to measure dynamics in portions of the CM membranes which are illuminated by the microscope excitation volume or point spread function (PSF) and thereby to draw conclusions about the presence of the labeled receptors. Variants of classical FCS, such as linescan FCS [72] or spatio-temporal image correlation spectroscopy (STICS) [73, 74], allow for inference of the dynamic fingerprint (i.e. diffusion times or coefficient) of fluorescent molecules entering and exiting the microscope PSF. As these techniques are sensitive to very low concentrations [15, 74], it is well suited to allow measurements at concentrations below saturation labeling and to capture concentrations of receptors at endogenous expression levels. Additional details about FCS and STICS are found in sections 3.7.1 and 3.7.2.

1.2.2 Imaging in adult cardiomyocytes

In mammalian hearts cardiomyocytes account for ≈30% of the cell number and 70% of the cell mass [75]. The human heart, in particular, contains various cell types. Amongst these about 30% of atrial cells and about 50% of ventricular cells are cardiomyocytes [76]. Adult cardiomyocytes possess transverse tubules, which are orderly tubular invaginations of the suface membrane with an average spacing of 1.8-2 μm and an average diameter of 169 ± 15 nm [77, 78], crossing the entire volume of the cell. The widely distributed and highly organized T-tubule system is essential for cardiac cell function, such as electric excitation, initiation and synchronous triggering of sacoplasmic reticulum Ca^{2+} release coordinating contraction. Many studies focus on structural imaging of adult cardiomyocytes such as the investigation of TTs [79] and their influence on the function and signaling [13, 65, 80].

In order to investigate receptors and processes in adult cardiomyocytes via fluorescence imaging a nontrivial requirement is the specific labeling of the target of interest with a fluorophore. While insertion and labeling with fluorescent fusions and tags to specific sites of interest is successfully performed in a lot of cell systems, primary cell systems such as cardiomyocytes, and in particular adult cardiomyocytes, are poor candidates for transfection. Our own tests to transfect adult cardiomyocytes, including electroporation, were futile. Although neonatal and embryonic cardiomyocytes have been described to be successfully transfected, much greater success has been achieved with viral transduction in adult cardiomyocytes [81, 82]. Multiple viruses have been described to successfully transduce adult cardiomyocytes in-vitro. Some of the most commonly used viruses are the adenovirus, retrovirus, lentivirus and adeno-associated viruses (AAV) [81, 83–86]. Although transduction of adult cardiomyocytes with the adenoviruses was also successfully performed, in our hands, viral free probes could not be attained for imaging outside of an S2 laboratory.

The generation of genetic modified mice has proven its efficiency for the investigation of cardiac issues on multiple occasions, in particular on the overexpression of β-ARs in transgenic mice [6, 7]. Figure 1.7 shows an example of a Lifeact fused to EGFP transgenic CM staining filamentous actin [87].

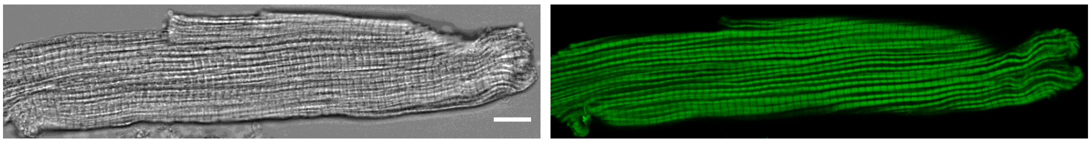

Figure 1.7: Brightfield (left) and confocal (right) image of an adult transgenic CM with Lifeact fused to enhanced green fluorescent protein (EGFP) staining filamentous actin. Scale bar of 10 μm applies to all images. Mice were a gift from Prof. Dr. Holger Gerhardt.

Alternative methods to elucidate the question of targeting and compartmentalization of endogenous receptors in adult cardiomyocytes include antibodies and labeling via fluorescent ligands. Antibodies against β-ARs mostly have insufficient specificity and sensitivity [88]. Requirements for receptor ligands are essentially that they label with highly specific binding and low background signal.

1.2.3 Autofluorescence

One influential factor affecting fluorescence imaging of biological tissue and cells is autofluorescence. This is a problem, especially in the visible range as autofluorescence interferes with fluorescent molecules of interest leading to a low signal to noise ratio by increasing background signal. Imaging at low concentration such as endogenous β-ARs in adult cardiomyocytes can in particular suffer from the influence of autofluorescence. Oxidized mitochondrial flavins and flavoproteins are reported as the main source of cell autofluorescence in the visible range of light. The influence of autofluorescence typically decreases with increasing wavelength. Cardiomyocytes are affected most in a spectral range of 450-560 nm. This makes fluorescent biosensors and markers in the spectral green range difficult to use as they can be hardly distinguished from background signal due to autofluorescence, especially when imaging the protein of interest at low concentrations. Much more favorable is the use of fluorescent tags in the red, far-red or even the infrared range, for latter e.g. by application of multiphoton microscopy. Other less favorable strategies to overcome the problem of autofluorescence could be to decrease the oxidization state of mitochondria, thereby often altering physiological function, and spectral unmixing, which requires reference spectra [14]. An example of autofluorescence in adult cardiomyocytes is depicted in fig. 1.8.

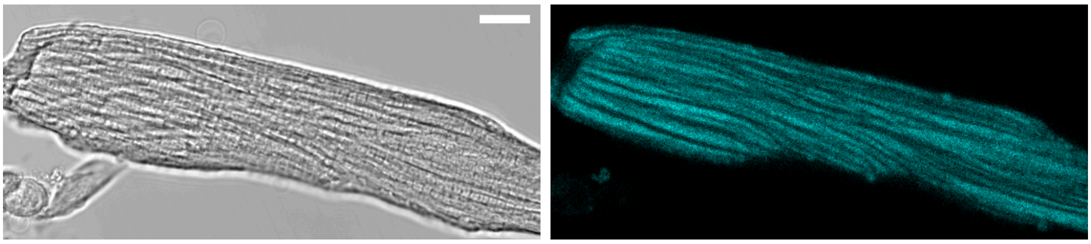

Figure 1.8: Brightfield (left) and confocal (right) image of an adult fixed cardiomyocyte excited at 405 nm and with collected emission between 440-490 nm. Scale bar of 10 μm applies to all images.

1.2.4 Fluorescent ligands

In an experiment with light microscopy one always needs to consider the tradeoffs of image resolution, imaging speed, and the amount of signal collected from a fluorescent sample, always keeping parameters such as photobleaching or phototoxicity in mind which can lead to destruction of the fluorophore or unwanted biological consequences such as cell death [64].

Specific labeling of the target of interest with a fluorophore or a fluorescent marker is a requirement for fluorescent microscopy and spectroscopy. Fluorescent ligands for GPCRs are generated by conjugation of usually known agonists or antagonists for the receptor of interest to a small organic fluorophore, typically seperated by a small molecule linker to allow the pharmacophore to access the binding site. Among the wide variety of fluorophores main classes of fluorophores which have been typically used for the generation of fluorescent ligands are BODIPY, the Alexa series and the rhodamine derivatives. The conjugated newly generated entity must be considered to posses other characteristics compared to its parent compound and must therefore be fully characterized [89].

Fluorescent ligands offer a wide spectrum of applications such as replacement of radioligands in binding assays, to study receptor dimerization or internalization, in kinetic experiments or to study receptor organization at endogenous expression levels [89].

On the other hand, these ligands need to possess qualities such as high specificity to the target with low background signal, which has rarely been achieved [90]. Additionally they should be blockable or displaceable by an unlabeled ligand.

To date only a few fluorescent ligands for the β-ARs have been developed [91–95], including commercial analogs such as from Cisbio and Abcam. An ideal ligand combines properties such as high photostability with high affinity and low non-specific binding. Given the high intrinsic autofluorescence of adult CMs, an asset would be a fluorophore emitting in the red or far-red spectrum.

In order to visualize the presence and localization of endogenous β_1- and β_2-ARs in adult murine CMs a ligand with the above mentioned requirements needs to be synthesized.

1.2.5 Autofocus control

In addition to the previous described imaging modalities for many acquisitions of microscopic data (even on short time scales) it is imperative to have some method of focus control. Microscopic imaging at high spatial and temporal resolution over time scales of minutes up to hours pose high demands on rapid and precise stabilization of the microscope focus. Since the focus in routine time lapse imaging, single molecule imaging, superresolution imaging and FCS measurements is prone to drifts as a consequence of mechanical and thermal fluctuations, a large number of strategies to oppose these inevitable fluctuations by automatic focal plane detection and stabilization systems has been developed [96].

In principle, such autofocus systems can be divided into two categories. One is software based, focusing on algorithms to analyze and compare in-focus and out-of-focus images [97–99], and the other applies optical approaches to measure the actual objective to sample distance [100–102]. The second approach usually makes use of a near-infrared laser or a light emitting diode which emits photons that are reflected by the sample interface. Such interfaces are typically glass coverslips. The reflected light is then collected in an optical detection system which is position or pattern sensitive to any displacement between the interface and the optical train and allows therefore the quantification of the focal displacement. The near-infrared beam can impinge hereby on the glass coverslip at normal incidence. Preferentially, if the NA of the objective is sufficient, the angle of incident light can be adjusted to allow a larger portion of the light to be reflected. In order to achieve position sensitivity, the relative position of the optical train to the sample has to be adjusted typically by mechanical means. Most of the current setups thereby make use of rather expensive and relatively slow piezoelectric stages or objective actuators. So far, in order to maintain focus, this relative mechanical movement between the objective and the sample cannot be avoided. One method to achieve an effective focal distance modulation and to avoid the mechanical objective to sample displacement is to make use of an electrically tunable lens (ETL) coupled to the microscope objective.

ETLs are fluid lenses consisting of two membranes which enclose a transparent liquid. An electromagnetic actuator is used in order to change the shape of the lens surfaces allowing to modulate the focal distance of the ETL continuously through an applied current [103]. When mounted close to the back focal plane of a microscope objective, application of currents up to 100 mA to the tunable lens allow rapid (below 0.1 s [104]) axial scans of the optical systems of hundreds of micrometers.

In microscopes ETLs have been demonstrated to be an effective focal distance modulator when coupled to objectives [105]. Therefore they have been applied in microscopic imaging to achieve fast changes of axial position. Examples of such usage is represented by tunable lens application in rapid change of plane in multi-photon microscopy [106], volumetric imaging by an acoustic optofluidic lens [107], optical axial scanning in epithelial tissue [108] or rapid 3D particle tracking [109]. Alternative applications involve ETLs acting as autofocus devices [110] to slowly correct for sample drifts arising from mechanical and thermal fluctuations. One shortcoming of most of the systems applying tunable lenses is that the focal position of the optical system is inferred by the value of the tunable lens input forcing the system to operate in an open-loop configuration. A true closed loop feedback system could be considered by not only inculing thermal drifts in the focal correction of tunable lenses [105], but additionally also taking potential

mechanical drifts of the optical train relative to the sample into account.
Here, in order to acquire focus stable data an ETL will be combined together with a totally internally reflected infrared (IR) laser and a quadrant photodiode (QPD) to build a true closed-loop feedback autofocus system, capable for high sensitivity readjustments of displacements of the objective to sample distance or focal loss.

2 Motivation and objectives of this study

β-adrenergic receptors play an essential role in the heart affecting almost any function from inotropic over lusitropic and chronotropic to dromotropic processes. In heart failure they have a major influence on altered signaling and cardiac function based on the reorganization of signaling. For decades now these receptors have been the target of a plethora of drugs to affect their function in hope of addressing pathological changes in cardiac processes to increase live quality and prevent deaths.

One aspect to drug development in general is to make drugs more specific in terms of cell and receptor targeting, eliminating all side effects in an optimal case. One key determinant is to fully understand how functioning and signaling of such targets of ligands, the receptors, is achieved. Thus an interesting question in cardiac function is the role of possible differential localization of β_1- and β_2-ARs in adult CMs. This differential localization has been suggested based on localized signaling of the second messenger cAMP, demonstrating an exclusive signaling cascade of the β_2-ARs initiated at the TTs in adult CMs, in contrast to the β_1-ARs which elicit their stimulated signal from the entire cell surface including TTs.

Despite major advances in the field of fluorescence microscopy including superresolution techniques, imaging endogenous receptors in such a complicated environment as adult CMs, which are hardly accessible by standard labeling techniques, has remained challenging.

This study is performed to solve the question of the differential localization of the β-ARs hoping that this is one of the first steps that lead to a better understanding of the subtype specific function of the receptors which can ultimately lead to the development of more specific drugs to alleviate suffering from cardiopathies.

The ultimate goals of this study are:

- the direct visualization of β_1- and β_2-ARs in adult CMs including the determination of their localization
- the characterization of the dynamic behavior of the β_1- and β_2-ARs in adult CMs at their location
- the development of techniques and microscopic equipment which allow to achieve the previous goals

3 Materials and methods

3.1 General methods

Methods are only mentioned if different from general methods in the laboratory or if of particular interest in this thesis. It is worth to mention that in general the best results with living adult CMs are obtained when experiments are performed on the day of isolation from the heart. Therefore all experiments with adult CMs are performed on the day of isolation.

3.1.1 Preparation of custom made imaging chamber

Melting of two stripes of parafilm (Bernis Company) between a glass slide and a microscope coverslip (24 mm # 1 VWR) yield a chamber with a volume of approximately 50 μl.

3.2 Fluorescent ligand

Methods describing the synthesis of the ligand JE1319 or the radioligand binding performed for the characterization of the ligand are described in [58].

3.3 Animal models and procedures

Name	Genotype	Background
β_1-AR-TG4	TG/wt	FVB/N
β_2-AR-TG32	TG/wt	FVB/N
wt	wt/wt	FVB/N
β_1/β_2-AR-k.o.	-/-	mixed

Table 3.1: Mouse models

All animal experiments were performed according to the German Animal Welfare Act. The guidelines of the NIH and the 2010/63/EU Directive of the European Parliament on the protection of animals used for scientific purposes were followed. For the animal experiments an approval of the Landesamt für Gesundheit und Soziales (Berlin) was obtained under the approval number G 0165/19. All animals had free access to food and water and were kept in individually ventilated cages.

A 12-:12-h light/dark regime (light from 6:30 AM to 6:30 PM), a constant 22°C ± 2°C temperature, and 55 ± 10% humidity was maintained for the animals in the facility.

The transgenic β_1-AR-TG4 and β_2-AR-TG32 mouse lines had been generated in house and express human β_1- or β_2-ARs, respectively, under the control of a murine α-myosin heavy-chain promoter [7]. β_1/β_2-AR knock-out (β_1/β_2-AR-k.o.) mice were originally generated and provided by the Kobilka laboratory, and obtained from The Jackson Laboratory (stock no. 003810) in this study and are homozygous null for the adrb1 and adrb2 genes [111]. Endogenous β-AR expression levels were studied on wild-type (wt) littermates that were generated during heterozygous breeding of the β_2-AR-TG32 mouse strain.

3.4 Cardiomyocyte isolation

The following buffers were generated as described by the Alliance for Cellular Signaling (AfCS) protocols (kindly obtained from the AG Gotthardt) and prepared freshly for each experimental day: the perfusion buffer (AfCS Solution Protocol PS00000451), myocyte (MC) digestion buffer (AfCS Solution Protocol PS00000447), MC stopping buffers (MC stop 1, AfCS Solution Protocol PS00000449 and MC stop 2, AfCS Solution Protocol PS00000450), MC plating medium (AfCS Solution Protocol PS00000448) and MC culture medium (AfCS Solution Protocol PS00000446). The following modifications were made to the buffer formulations: For the MC digestion buffer Liberase DH (Roche) was used instead of Liberase blendzyme 1 (Roche). As a basis for the MC culture and MC plating medium a phenol red-free minimum essential medium (MEM) with Earle's salts (Gibco) instead of Hank's salts was used. For the MC culture medium standard bovine serum albumin (BSA) (Sigma Aldrich) was used instead of myocyte BSA. Both the MC plating and the MC stop 1 and MC stop 2 buffer were produced using fetal bovine serum (FBS) (Sigma-Aldrich) instead of bovine calf serum (BCS).

For the isolation of hearts two forceps with straight and two with curved ends as well as surgical scissors with straight and curved blunt ends are needed. Optionally spring scissors with small cutting edges for fine cuts are useful. A Langendorff perfusion apparatus was used as depicted in fig. 3.1. Apart from connectors and tubes of different sizes is the apparatus constructed of technical components as the peristaltic pump (Model: CTP100 - 80RPM, Fisherbrand) and the thermostatic circulator bath (Grant Instruments TC120-P5). The glass elements were manufactured by a glassblower.

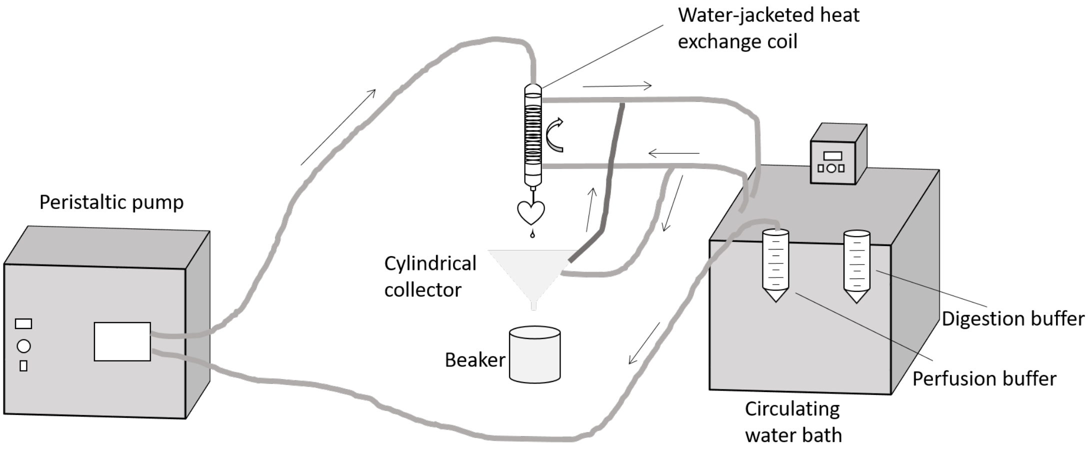

Figure 3.1: Illustration of Langendorff perfusion apparatus. Perfusion or digestion buffer are pumped via the peristaltic pump through the water-jacketed heat exchange coil for passage through the heart. The cylindrical collector and beaker collect the buffer. The circulating water bath keeps buffers in Falcons and in the coil at 37°C.

Procedure of isolation: Hearts of male and female mice at the age of 8 to 12 weeks were used for the isolation of murine adult ventricular cardiac myocytes. By usage of a Langendorff perfusion apparatus, as in fig. 3.1 and described in [112], CMs were isolated via enzymatic collagen digestion and retrograde perfusion through the aorta. I.e. after cervical dislocation hearts were quickly removed from mice and mounted onto a cannula of a custom-built perfusion system followed by an initial perfusion with perfusion buffer for 4 min at 3 ml/min. The perfusion was continued for 8 min using the MC digestion buffer which corresponds approximately to 5 mg liberase dispase high DH (Roche) enzyme per mouse in order to destruct the extracellular matrix of the heart. Hearts were removed from the perfusion system as soon as they became limp. Then with scalpels the ventricles were cut into small pieces and digestion was halted by taking up the heart tissue pieces in serum with MC stop 1 buffer. In order to dissociate the cells further serological plastic pipettes with large openings were used to gently pipet the cell suspension several times. After sedimentation and removal of supernatant the cells were resuspended in stop 2 buffer. To remove tissue leftovers cells were passed through a nylon mesh cell strainer (100-μm pore size; Falcon). Afterwards cells were stepwise introduced to physiological Ca^{2+} concentrations ($\sim$1 mM) and resuspended in MC plating medium before seeding them onto with Matrigel coated μ-slides (which were prepared freshly for each experiment).

Cell yield: CMs isolated via this method were typically 75-80% rod-shaped, which corresponds to an average cell number of 200000-300000. The two factors influencing cell quality and amount most are: the time it takes after cervical dislocation until perfusion of the heart starts and secondly the perfusion/digestion itself. Typically the quality of the cells decreases as the time between cervical dislocation and perfusion increases. Caution must be taken to eliminate blood clots in the heart during perfusion/digestion. Heart shape and texture need to be checked constantly during digestion as the cell amount and quality decreases if the digestion is either not enough or if the heart is over-digested.

3.5 Cell culture

HEK293AD (Biocat; AD-100-GVO-CB) and A431 (ATCC; CRL-1555) cells were cultured in Dulbecco's modified Eagle's medium (DMEM) (PAN-Biotech) at 37°C and 5% CO_2 and supplemented with 10% FBS, 2 mM L-glutamin and 1% penicillin/streptomycin. For passaging, human embryonic kidney (HEK)293AD cells were detached using 0.05% trypsin-(ethylenedinitrilo)tetraacetic acid (EDTA) (Gibco) and 0.25% trypsin-EDTA for A431 cells in phosphate buffered saline (PBS). Cells were seeded in glass bottom 8-well μ-slides (Ibidi). HEK293AD cells only were transfected with Effectene (Qiagen) according to the manufacturer's instructions.

3.6 Cell preparation for confocal Imaging

Cells were plated on glass-bottom eight-well μ-slide (Ibidi) and coated in a dilution of 1:30 or 1:50 growth factor reduced Matrigel (Corning) and serum free MC plating medium (150 μl/well). Frozen Matrigel stock aliquots were slowly thawed on ice at 4°C overnight. After isolation adult cardiomyocytes were given time to settle and attach on μ-slides for at least 2 h at 37°C and 5% CO_2. For imaging MC plating medium was changed to imaging buffer with a pH of 7.4 (20 mM 4-(2-hydroxyethyl)-1-piperazineethanesulfonic acid (Hepes), 137 mM NaCl, 5 mM KCl, 1 mM $MgCl_2$, 1 mM $CaCl_2$, 0.5% BSA).

For cell preparation for imaging of H9c2 and human induced pluripotent stem cells (hiPSCs) cells see ref. [58]. HEK293AD cells were imaged 2 days after transfection with Effectene (Qiagen) according to the manufacturer's instructions. Prior to imaging, transfected HEK293AD and isolated CM cells were preincubated for 40 min to 1 h with either 100 nM CGP 20712 (to image β_2-ARs) or 50 nM ICI 118,551 (to image β_1-ARs) diluted in the appropriate imaging buffer to block the other receptor type. Then, the ligand JE1319 was diluted in imaging buffer (with the antagonists CGP 20712 or ICI 118,551 in their respective concentrations) and directly added to the cells in a concentration of either 5 or 50 nM as indicated in the experiments. Incubation time was 40 min to 1 h.

Untransfected HEK293AD and A431 cells did not undergo any pre-incubation with the antagonist to block receptor labeling.

Then cells were washed three times (except CMs, which were washed only once) using imaging buffer. During imaging cells were kept at physiological conditions (37°C, 5% CO_2, 85% humidity) using a sample incubator (Stage Top Chamber, OKOlab) mounted on the stage of the Leica SP8 confocal laser scanning microscope. During imaging the cell buffer contained the respective β-AR antagonist (if applicable) as well as 50 μM para-aminoblebbistatin (Optopharma) to inhibit spontaneous CM contractions (only isolated adult CMs).

3.7 Microscopy and spectroscopy analysis

In general if not specified otherwise images of cells were acquired on a confocal laser scanning microscope, Leica SP8, with a white light laser (WLL) and a HC PLAP CS2 40x1.3 NA oil immersion objective (Leica). Excitation of the ligand JE1319 was performed at 633 nm (going up to 10% laser power, which corresponds to 6 μW). Other excitation lines are standard lines for the underlying fluorescent species.

In this thesis two spectroscopy methods are applied and compared to extract the behavior of the diffusing species. The first one is FCS and the other technique is STICS. Both techniques can be implemented using raw data consisting of kymographs or linescans [72] for the investigation of the diffusion behavior at the location under investigation over time of the underlying species of interest.

Such kymographs are acquired with a laser scanning microscope (Leica SP8), equipped with a resonant scanner moldule (12 kHz), in order to recover the fluorescent species and parts of it are displayed in figs. 3.3b, 3.3c and 3.4. The number of lines was between $3{\cdot}10^5$ and $6{\cdot}10^5$ and the pixel size was 50 nm. During acquisition the infrared laser based autofocus of the microscope (Leica, Adaptive Focus Control) was enabled in order to stabilize the focal position [113] (see section 1.2.5). The ligand JE1319 was excited at 633 nm with a laser power of 0.5 or 3 μW at the sample corresponding to 1% or 5% on the Leica SP8 respectively. The laser power was determined with a PM100A power meter (Thorlabs) with a S120VC (Thorlabs) photodiode power sensor head. Placement of the lines in adult CMs was either at the outer plasma membrane (along the outer cell) or crossing the TTs. At these positions the confocal beam is repeatedly scanned at an acquisition speed of 1800 Hz with a line size of 256 pixels over the same portion of the sample to extract diffusion data from the raw linecans by calculating the autocorrelation function.

Emission was detected on hybrid detectors (HyD) in photon counting mode de-

tecting either in the typical ranges of the common fluorophores or at 650-750 nm (JE1319).
Extraction of fitting parameters is performed by keeping the beam waist ω_0 constant. Average waists are calculated from single cell experiments for each receptor and mouse type. Beam waists for the analysis of the linescans were determined in two ways. The preferred method in this thesis is the extraction from mean square displacement curves (at the plasma membrane) at a $\tau = 0$ (sections 3.7.2 and 3.7.2.1). Alternatively, waists are obtained by the observation of the profiles of fluorescent microspheres (Tetraspeck, Thermofisher Scientific) as in [113–117] extracting a lateral waist of ω_0(633 nm)=0.33 μm and an axial waist of ω_z(633 nm)=1.12 μm (only used for β_2-AR in wt CMs at the PM and TTs).
Most autocorrelation curves were normalized to their g(0). In cases no correlation was obtained, as for the β_2-AR at the PM of wt and knock-out (ko) CMs, normalization was performed by taking the averaged g(0) at the TTs of the β_2-AR wt CMs. In case of 5 nM JE1319 curves were normalized to the average g(0) of the β_1-AR at the PM. Color coded autocorrelation function plots were smoothed with a gaussian filter for display.
Absorption spectra are collected on the Evolution 350 UV-Vis-Spectrophotometer whereas the excitation and emission spectra are acquired at the Horiba Spectrofluorometer FluoroMax.

3.7.1 Linescan fluorescence correlation spectroscopy analysis

FCS compares statistical fluctuations of fluorescent particles in the effective detection volume to gain information on equilibrium processes in the sample under investigation [16, 58]. Linescan FCS improves the statistical accuracy and thus the accuracy of diffusion measurements due to the repeated scanning of multiple pixels within one line [72]. The recorded time-trace of the fluorescent intensity in the effective detection volume allows for the calculation of an autocorrelation function g(τ) and G(τ) according to eqs. (3.7.1) and (3.7.2), which reflect the time-scale of the fluorescence intensity fluctuations. g(τ) is defined as the average of the products between the fluctuation at time t from the mean intensity and the fluctuation at some time interval $t + \tau$ over all values of measurement time t normalized to the average intensity (eq. (3.7.1)). G(τ) is defined as the intensity correlation function which represents the correlation of the intensity at time t and the intensity at some time interval $t + \tau$ over all values of measurement time t (eq. (3.7.2)) [61, 118].

$$g(\tau) = \frac{\langle \delta I(t) \cdot \delta I(t+\tau) \rangle}{\langle I(t) \rangle^2} \tag{3.7.1}$$

$$G(\tau) = \frac{\langle I(t) \cdot I(t+\tau) \rangle}{\langle I(t) \rangle^2} \tag{3.7.2}$$

with

$$\delta I(t) = I(t) - \langle I(t) \rangle \tag{3.7.3}$$

where the pointed backets $\langle\rangle$ represent an average over all times t [16], τ the time lag and I the intensity. The relationships of G(τ) and g(τ) is described in eq. (3.7.4) [61, 118].

$$G(\tau) = 1 + g(\tau) \tag{3.7.4}$$

The autocorrelation function is then fit to theoretical models usually derived by approximating the effective detection volume of a 3-dimensional Gaussian profile. The Gaussian profile describes the probability W(r,z) or the intensity I(r,z) of detecting a photon which is emitted by a fluorophore located at the position (r,z) and can be described by the eqs. (3.7.5) and (3.7.6).

$$W(r,z) = e^{-2\frac{r^2}{\omega_0^2}} \cdot e^{-2\frac{z^2}{\omega_z^2}} \tag{3.7.5}$$

$$I(r,z) = I_0 \cdot e^{-2\frac{r^2}{\omega_0^2}} \cdot e^{-2\frac{z^2}{\omega_z^2}} \tag{3.7.6}$$

In which r represents the radial distance from the optical axis and z the axial coordinate starting at the focal plane with z=0. ω_0 and ω_z are the radial and axial beam radii describing the extend of the effective detection volume in the focal plane and along the optical axis where the excitation volume intensity decays to the value $I(r,z)/I_0 = e^{-2}$ [16, 119–122].

The 3-dimensional autocorrelation function can be determined analytically by eq. (3.7.7) [118, 120].

$$g_{3D}(\tau) = \frac{\gamma}{N} \frac{1}{1+\frac{\tau}{\tau_D}} \frac{1}{\sqrt{1+\left(\frac{\tau}{\tau_D}\right)\cdot\left(\frac{\omega_0}{\omega_z}\right)^2}} + g_\infty \tag{3.7.7}$$

Alternatively the formula can be expressed in terms of the diffusion coefficient D by substituting τ_D with eq. (3.7.8) [16] yielding the eq. (3.7.9).

$$\tau_D = \frac{\omega_0^2}{4D} \tag{3.7.8}$$

$$g_{3D}(\tau) = \frac{\gamma}{N} \frac{1}{1 + \frac{4D\tau}{\omega_0^2}} \frac{1}{\sqrt{1 + \frac{4D\tau}{\omega_z^2}}} + g_\infty \tag{3.7.9}$$

In which γ represents a shape factor due to uneven illumination across the focal volume and is 0.3535 for a 3-dimensional Gaussian under ideal conditions [123], N represents the number of particles, τ_D the diffusion time, D the diffusion constant and g_∞ the limiting value of g(τ) for $\tau \longrightarrow \infty$ [120].
Noteworthy the particle number N is connected to the concentration via eq. (3.7.10) and can be calculated from the correlation curve at $\tau = 0$ (eq. (3.7.11)) [16, 61, 115].

$$N = c \cdot N_A \cdot V_{eff} \tag{3.7.10}$$

$$g(0) = \frac{1}{N} \tag{3.7.11}$$

where c is the concentration of the fluorescent particles, N_A the Avogadro constant of $6.022 \cdot 10^{23} mol^{-1}$ and V_{eff} the effective volume which is connected to the confocal volume V_{conf} by eq. (3.7.12) [61, 115, 124].

$$V_{eff} = \pi^{\frac{3}{2}} \cdot \omega_0^2 \omega_z = 2^{\frac{3}{2}} \cdot V_{conf} \tag{3.7.12}$$

From here on expressions are chosen in terms of g(τ).

3.7.1.1 2-Dimensional diffusion

In this work diffusion is measured in cell membranes. Because of that, the correlation function can be adapted to the 2-dimensional formula fitting the 2-dimensional Gaussian distribution simplifying eqs. (3.7.7) and (3.7.9) to eqs. (3.7.13) and (3.7.14) [119, 120, 125–127].

$$g_{2D}(\tau) = \frac{\gamma}{N} \frac{1}{1 + \frac{\tau}{\tau_D}} + g_\infty \tag{3.7.13}$$

$$g_{2D}(\tau) = \frac{\gamma}{N} \frac{1}{1 + \frac{4D\tau}{\omega_0^2}} + g_\infty \tag{3.7.14}$$

3.7.1.2 1-Dimensional diffusion

Since part of this work is to investigate the diffusion on TTs of adult CMs, diffusion occurs in a tubule with a radius smaller than the beam waist. In that case diffusion appears to be adequately represented by 1-dimensional diffusion. The analytical formula representing 1-dimensional diffusion is found in eqs. (3.7.15) and (3.7.16) [61, 128].

$$g_{1D}(\tau) = \frac{\gamma}{N} \frac{1}{\sqrt{1 + \frac{\tau}{\tau_D}}} + g_{\infty} \tag{3.7.15}$$

$$g_{1D}(\tau) = \frac{\gamma}{N} \frac{1}{\sqrt{1 + \frac{4D\tau}{\omega_0^2}}} + g_{\infty} \tag{3.7.16}$$

3.7.1.3 Photophysical processes - blinking

FCS is able to measure different physical processes on different timescales. Figure 3.2 illustrates schematically different processes monitored by autocorrelation analysis [125]. Besides antibunching and rotational fluctuations of molecules, which do not play a role in this thesis because of their very fast kinetics, photophysical processes can occur on the timescales used in this work.

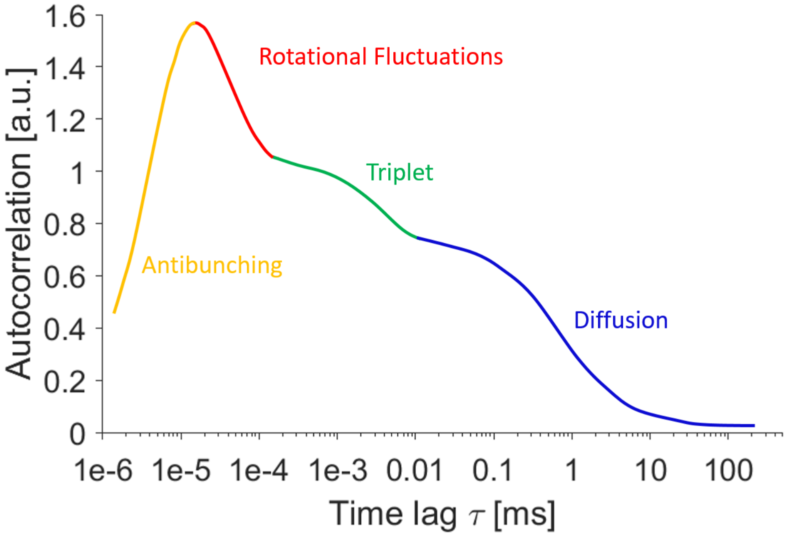

Figure 3.2: Processes in FCS and their time scales (in accordance with [125]).

Photophysical processes such as blinking of the dye occur when fluorophores transition in and out of so-called forbidden/triplet states as depicted in fig. 1.6. These processes are accounted for in eqs. (3.7.17) to (3.7.19) [16, 129, 130].

$$g_{3D}(\tau) = \frac{\gamma}{N} \frac{1}{1 + \frac{4D\tau}{\omega_0^2}} \frac{1}{\sqrt{1 + \frac{4D\tau}{\omega_z^2}}} \left(\frac{1 - T + T \cdot e^{-\frac{\tau}{\tau_T}}}{1 - T} \right) + g_\infty \tag{3.7.17}$$

$$g_{2D}(\tau) = \frac{\gamma}{N} \frac{1}{1 + \frac{4D\tau}{\omega_0^2}} \left(\frac{1 - T + T \cdot e^{-\frac{\tau}{\tau_T}}}{1 - T} \right) + g_\infty \tag{3.7.18}$$

$$g_{1D}(\tau) = \frac{\gamma}{N} \frac{1}{\sqrt{1 + \frac{4D\tau}{\omega_0^2}}} \left(\frac{1 - T + T \cdot e^{-\frac{\tau}{\tau_T}}}{1 - T} \right) + g_\infty \tag{3.7.19}$$

Where τ_T represents the lifetime of the photophysical process. Intersystem crossing alters the quantum efficiency of the system dividing the molecules into two fractions. T represents the fraction of the molecules underlying this process or being non-fluorescent whereas the fraction $(1 - T) + Te^{-\frac{\tau}{\tau_T}}$ remains fluorescent. As the fractions become a multiplier to the correlation function they are also reflected in the number of particles N by (1-T)N [61] (eqs. (3.7.17) to (3.7.19)).

3.7.1.4 Potential sources of artifacts affecting FCS

There are factors which can influence FCS measurements and which can be accounted for in different models. One important factor is photobleaching which can lead to a depletion of fluorophores over time. There are different approaches to address the effect. Most of them involve to model photobleaching by an exponential decay function, ranging from mono- to multi-exponential decay functions [72, 131]. Other methods involve correcting the trace by movemean or boxcar detrending such as [132] or develop their own algorithms [72].

3.7.1.5 Implementation of the analysis

The analysis method in this thesis calculates the temporal autocorrelation in each pixel of the linescan. It is custom implemented in MATLAB (code in appendix C.1). Figure 3.3 illustrates the analysis steps at the two compartments of an overexpressing β_1-AR-TG4 adult cardiomyocyte pre-incubated with 50 nM ICI 118,551 and incubated with 5 nM JE1319. After acquiring an image of the cell (fig. 3.3a) a region of interest (ROI) with 50 nm pixel size is chosen in which lines are scanned repeatedly. Figure 3.3a illustrates a blue line at the PM and a green line at the TTs. When scanning either of these lines repeatedly images like fig. 3.3b at the PM and fig. 3.3c at the TTs are recorded displaying time on the vertical and space/pixel on the horizontal axis. For representation purposes multiple lines in one scan are averaged together to show a maximum of 500 time points (which is not done in the analysis). As indicated by the boxes in figs. 3.3b and 3.3c the first 2^{17} lines are cut off, where photobleaching is most prominent, to reduce the influence of slow-timescale photobleaching fluctuations from the remaining (inside of the boxes) kymographs. When scans are performed at the TTs either spatial filtering around the T-tubular region, at which further analysis is performed (overexpression fig. 3.3c and simulated data), or the entire spatial line was analyzed like scans at the PM (at the TTs of wt and ko cells).

The remaining kymographs are further corrected for bleaching by a moving average [132] and high pass filtered by dividing the total time into smaller sections of about 2^{16} lines or 36 s (temporal filtering). Afterwards the autocorrelations are calculated by pixel and section to display an autocorrelation map as in fig. 3.3d at the outer PM and in fig. 3.3e at the TTs representing the autocorrelations from one pixel in one of the temporal sections in one column. In dependence of the length of the scan different amounts of temporal sections were created. Figure 3.3e illustrates the autocorrelations from the corresponding TTs marked by the colored boxes. Figures 3.3d and 3.3e are used to detect and remove artifacts by selection and removal of the affected correlations. The remaining correlations from all temporal sections are then averaged to yield an averaged and normalized autocorrelation function as in fig. 3.3f at the PM or fig. 3.3g at the TTs. Both curves encode the ‘classical’ autocorrelation curve (bottom) into a color coded bar (top) reflecting the correlation profile in transitions of colors ranging from high correlation (red), i.e. the receptors are still in the PSF at this time-scale, to low correlation (blue), i.e. the receptors have diffused out of the PSF by this time.

The autocorrelation functions are then fit to equation in section 3.7.1 to extract parameters such as the diffusion constant of diffusion in solution (3D), in membranes (2D) or in tubules (1D). For the CMs, photophysical processes are accounted for in the fitting functions (formulas in section 3.7.1.3).

Solutions in this thesis are water-glycerol mixtures which are prepared by equal weight of water and glycerol (Merck Chemicals GmbH).

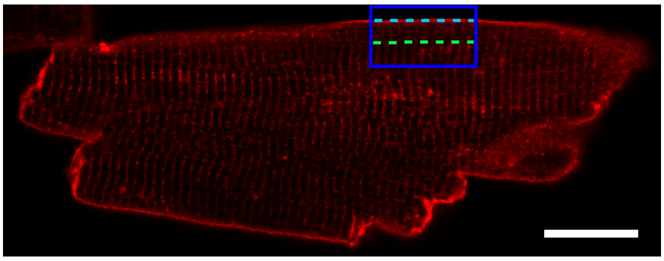

(a) β_1-AR-TG4 CM

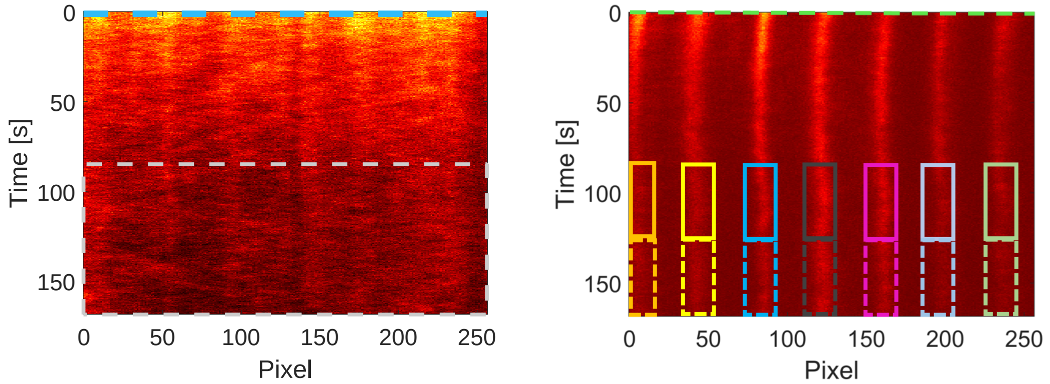

(b) Intensity map at outer PM (c) Intensity map at TTs

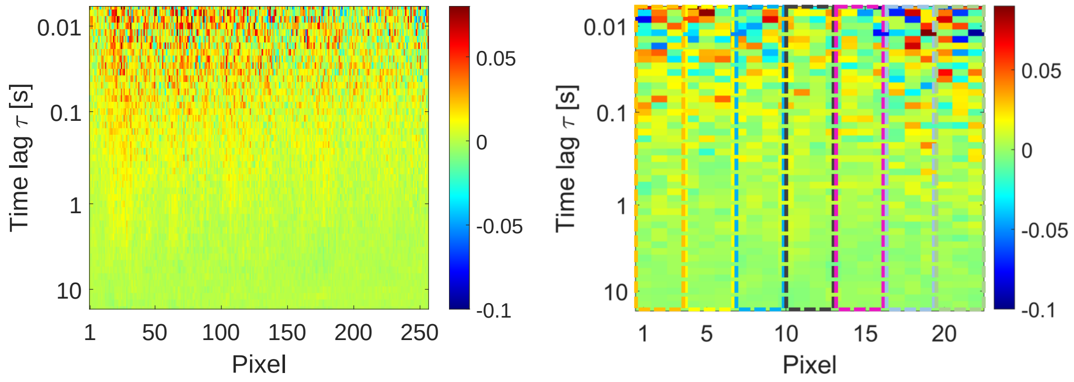

(d) Autocorrelation map at outer PM (e) Autocorrelation map at TTs

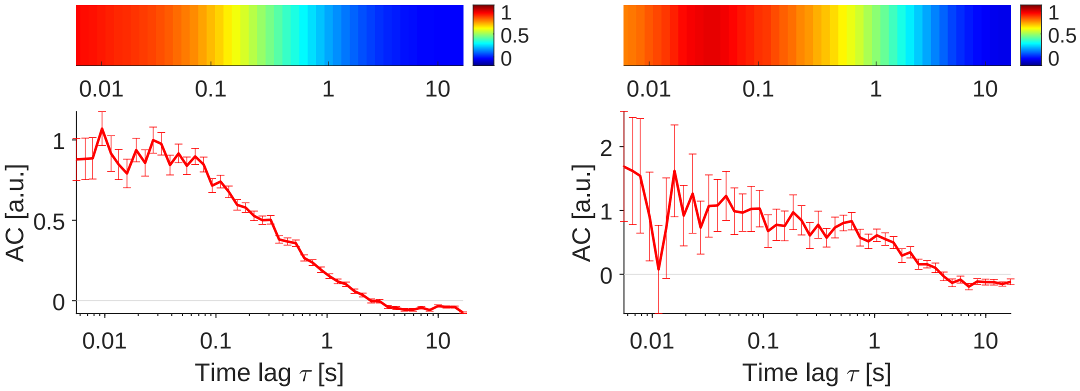

(f) Autocorrelation curve at outer PM (g) Autocorrelation curve at TTs

Figure 3.3: Schematic of the FCS analysis. (a) β_1-AR-TG4 CM stained with 5 nM JE1319 in the presence of 50 nM ICI 118,551. Box indicates a ROI with 2 lines. Blue line indicates scans at the outer PM and green line at the TTs. Lines are scanned either 303,104 or 507,904 times with a frequency of 1,800 Hz. Scale bar is 20 μm. Resulting kymographs at the outer PM (b) and TTs (c) show intensities of each pixel over time. For illustration purposes multiple time points are equally averaged together to display 500 time points in a red-hot color scale. Colored lines as indicated in a. Boxes indicate analyzed pixel and time ranges. Maps of autocorrelation at PM (d) and TTs (e). (f) and (g) are the corresponding averaged autocorrelation curves from the selected portions in (d) or (e) into one row each. Chart below represents the averaged and normalized autocorrelation curves. Grey lines mark an additional axis at 0. Error bars indicate standard error of the mean (SEM). Color scale on the side in (d)-(g) represent the amplitude of the autocorrelation curves. (a), (b), (d) and (f) adapted from Bathe-Peters et al. [58] & licensed under CC BY-NC-ND 4.0.

3.7.2 Spatio-temporal image correlation spectroscopy

In STICS linescan kymmographs are collected to perform a global spatial and temporal analysis on all pixels and times to yield the spatio-temporal correlation function. One striking advantage is that such spatio-temporal image correlations remove any influence of photobleaching [72]. Spatio-temporal correlation curves $g(\xi, \tau)$ are calculated according to eq. (3.7.20) [72, 74].

$$g(\xi, \tau) = \frac{\langle \delta I(x, t_i) \cdot \delta I(x + \xi, t_i + \tau) \rangle}{\langle I(x, t_i) \rangle^2} \tag{3.7.20}$$

with

$$\delta I(x, t_i) = I(x, t_i) - \langle I(x, t_i) \rangle \tag{3.7.21}$$

where $\langle\rangle$ denotes the average over all positions x and scans i, $t_i = iT$ the time as an integer multiple of the scanning period T, ξ the spatial lag variable, τ the time lag and I the intensity [72, 73].

Under the assumptions that the diffusion of the molecules in the membrane is not influenced by the scanning laser beam and that the spatial pixel size is much smaller than the waist ω_0 of the Gaussian detection area $\Omega(x, y) = e^{-2\frac{(x^2+y^2)}{\omega_0^2}}$ the spatio-temporal correlation function for pure diffusion in a 1-dimensional linescan can be calculated by eq. (3.7.22) [72, 73].

$$g_{STICS}(\xi,\tau) = \frac{\gamma}{N\pi}\frac{1}{\omega_0^2 + 4D\left(\tau + \frac{\xi}{v}\right)} e^{-\frac{\xi^2}{\omega_0^2 + 4D\left(\tau + \frac{\xi}{v}\right)}} \tag{3.7.22}$$

where γ represents a shape factor due to uneven illumination across the focal volume [123], N the average number of particles in the observation volume, ω_0 the lateral beam radius of the effective detection volume in the focal plane, D the diffusion coefficient and ξ/v accounts for the scanning speed inside a period T (where intensities are acquired at times $t_i + \xi/v$) [72]. The velocity v can be obtained from the line repetition rate and the amount of pixels in one line. For a line repetition rate of 1800 Hz and 256 pixels in one line the pixel dwell time would be $\tau_{pixel} = 2.17\ \mu s$ leading to a v of 0.46 $\frac{pixel}{\mu s}$ or 23 $\frac{nm}{\mu s}$. Since ξ/v becomes negligible small compared to τ, already from the 2nd or 3rd time lag, it is ignored, and the formula simplifies to eq. (3.7.23) for free diffusing particles [55, 73, 133, 134].

$$g_{STICS}(\xi,\tau) = \frac{\gamma}{N\pi}\frac{1}{\omega_0^2 + 4D\tau} e^{-\frac{\xi^2}{\omega_0^2 + 4D\tau}} \tag{3.7.23}$$

$$g_{STICS}(\xi,\tau) = g_t(\tau) \cdot e^{-\frac{\xi^2}{\sigma_r^2(\tau)}} \tag{3.7.24}$$

where

$$g_t(\tau) = \frac{\gamma}{N\pi}\frac{1}{\sigma_r^2(\tau)} \tag{3.7.25}$$

$$\sigma_r^2(\tau) = 4D\tau + \omega_0^2 \tag{3.7.26}$$

Equation (3.7.25) represents the temporal correlation function for free-diffusing particles and $\sigma_r^2(\tau)$ (eq. (3.7.26)) the mean square displacement (MSD) being linear in time [73]. Equation (3.7.26) contains the spatial extension in lateral direction ω_0 of the effective volume (if the particle size is negligible) and can be obtained at $\tau = 0$ [73, 133].

3.7.2.1 Implementation of STICS analysis

A second method to extract the behavior of the diffusing species from the raw lincescans is to calculate STICS functions performing a global spatial and temporal analysis on all pixels and times of the linescan kymograph (fig. 3.4b) obtained from scanning a confocal beam repeatedly at high speed over a ROI of a sample (fig. 3.4a), thereby having the advantage of removing any influence of photobleaching from the kinetic behavior (broadening of the STICS function) [72]. STICS functions are two-dimensional plots of time over space and display the process of diffusion in a shape of a 'plume' which broadens in space as a function of time (fig. 3.4c). Drifts and slow fluctuations of the kymographs are corrected using a random number addition detrending within a moving window of approximately 250 $\cdot 10^3$ lines at 12 kHz and 32 $\cdot 10^3$ lines at 1.8 kHz (about 20 s) similar to [55, 113]. The spatio-temporal correlation curve is calculated by eqs. (3.7.20) and (3.7.23) [72]. Here, the autocorrelation or STICS function was calculated by performing the inverse fast Fourier transform (FFT) of the product of the fast Fourier transform and its complex conjugate [55]. The custom algorithm was written in IGOR Pro (WaveMetrics) by Dr. Paolo Annibale. Broadening of the Gaussians measured from horizontal cross sections of the STICS function at different time lags allows for the extraction of the mean square displacement. The waist of the PSF can be extracted at $\tau = 0$ at these plots.

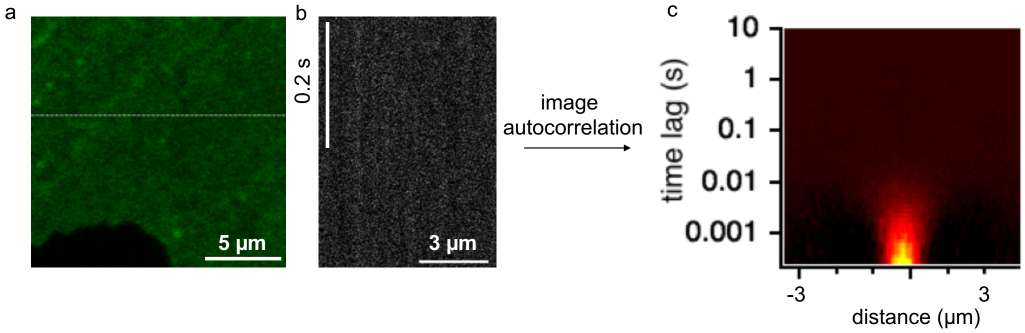

Figure 3.4: Illustration of generation of STICS-functions from linescans. (a) Representative confocal image of a H9c2 cell expressing β_2-AR c-terminally fused to EGFP. (b) Section of kymograph (time over space) built up from repeated scans of the line in panel a. (c) Resulting spatio-temporal correlation function displaying the time-lag on the vertical and the spatial distance/lag on the horizontal axis. Reprinted from Bathe-Peters et al. [113] & licensed under CC BY 4.0. STICS analysis performed by Dr. Paolo Annibale.

3.7.3 Combined widefield-confocal microscope

The combined widefield-confocal microscope in fig. 4.41 equips each level of the double deck body of an Olympus IX73 microscope independently with a dichroic mirror. The beam of the excitation source, either a 488 or 561 diode laser (Coherent), is common until a flip-mirror, enabling the switch between widefield and confocal imaging, splitting the beam into a confocal beam path entering the microscope body though the upper deck and a widefield path entering through the lower deck of the microscope. The collimated excitation light designated for widefiled imaging is diverted by a beam expander (10x), reflected 90 degrees by a mirror onto another mirror guiding the beam through a relay/ TIRF lens (f=250 mm) focusing on the back focal plane of the Olympus 1.45 NA 60X objective. Total internal reflection fluorescence is achieved by translating the beam and the lens perpendicular to the optical axis via positioning of the micrometer translation stage containing a mirror and the relay lens. An EM-CCD camera (iXon, Andor) mounted on the left port of the microscope collects the fluorescence. When imaged in confocal mode the laser excitation beam is reflected at 90 degrees by a dichroic mirror onto a pair of galvanometer scanners (Cambridge Technology 6215H). A scan lens (Olympus U TL-1-2) and a relay lens (Thorlabs CLS-SL) allow the by 5x expanded and collimated beam to enter through the microscope. The beam is further reflected at 90 degrees by a mirror mounted on a rotating turret. The fluorescence takes the same path as the excitation until a dichroic mirror separates the two. Another dichroic mirror separates the fluorescence by wavelength before it is focused by a f=75 mm achromatic lens onto a 20 μm pinhole which is placed in front of HyDs (Picoquant). The signal from the HyD is read by a custom made software (LaBView, National Instruments, appendix C.2) via a data acquisition board (DAQ3001, IO Tech) after being discriminated by a Phillips Scientific 6915 Constant Fraction Discriminator.

Both paths can use an autofocusing system based on a tunable lens to hold the foucs of the sample (section 4.3 & Bathe-Peters et al. [135]).

3.7.4 Materials for the autofocus

The ETL (EL-16-40-TC) from the Optotune AG in Switzerland has VIS coated cover glasses in the range of 420-950 nm, a clear aperature of 40 mm and a focal power ranging from -2 to +3 dioptre. More technical information are available on the manufacturer website [103]. Further optical components, mirrors and the single pigtailed laser diode with a wavelength of 776.7 nm, a fiber type of 780HP and the OEM Laser Driver Evaluation KIT EK2000 as well as C-Mount adapters were all acquired from Thorlabs, USA. The quadrant photodiode (QPD) MTQD5.8PV1-5 with a peak sensitivity at 940 nm is from Marktech Electronics. The rest of the electrical detection circuitry including the transimpedance, difference and sum amplifiers was custom assembled. The analog signals from the circuit were acquired via the NI DAQ 6363 Card from National Instruments. The custom made combined TIRF-confocal setup (sections 3.7.3 and 4.2), based on a frame of an Olympus IX73 microscope, allows for the acquisition of images of samples mounted on an MS2000 motorized stage from ASI (USA) including a

motorized actuator to achieve axial movement of the microscope turret with a step resolution of 50 nm. The lower deck of the microscope body encompasses the optical feedback setup illustrated in fig. 4.43. For the collection of images a Photometrics Cascade II 512 EMCCD camera was used. The analysis of the camera images of cells and beads was performed with ImageJ. Defocus of beads was determined by fitting a Gaussian function to a line profile placed through the center of the bead to extract the standard deviation.
Excitation of the sample was achieved by using a 488 nm laser diode cube (Coherent). A 250 mm lens (Thorlabs) focuses the excitation beam in the back focal plane of the 60x 1.49 numerical aperture (NA) TIRF objective (Olympus). By translation of the lens the focused excitation spot translates at the same time in the back focal plane of the objective away from the optical axis. Consequently as the beam exits the objective it tilts until the critical angle at the sample interface is reached and the beam is brought into TIRF. The feedback algorithm operates and is programmed in LabView (National Instruments).
Mitotracker Green from Thermo Fisher Scientific (USA) was used to stain mitochondria in live cell imaging.
Total internal reflection (TIR) occurs at two separating media with different refractive indices when an electromagnetic wave, such as a laser beam, hits this surface at an angle (critical angle) allowing the beam to be entirely reflected by the surface [136, 137]. Apart from a thin region in the proximity of the separation surface no light is transmitted (fig. 3.5).

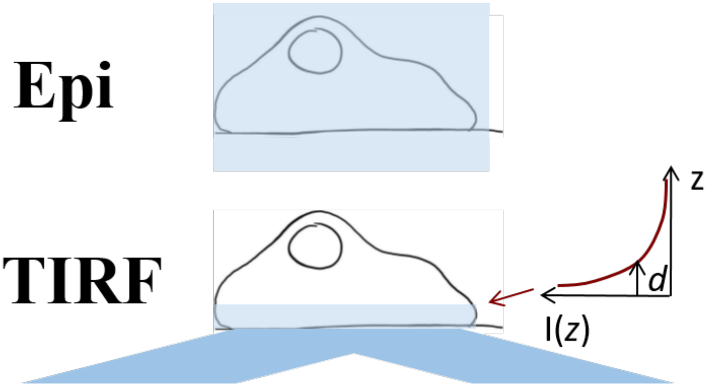

Figure 3.5: Transmitted light in epifluorescence (upper) and TIRF (lower). In TIRF the penetration depth of the light decays exponentially as indicated by the graph.

For an interface between glass and water the critical angle is 61.4 degree. The maximum angle of a ray exiting from an objective is related to the NA by eq. (3.7.27), where n_1 represent the refractive index of the medium between the cover glass and the front lens of the objective. Therefore an NA of 1.49 allows a ray to exit the objective at an angle of 78.9 degrees and is consequently above the critical angle even for a slightly diverging laser beam.

$$NA = n_1 \cdot sin(\theta) \tag{3.7.27}$$

The evanescent wave or penetration depth d of the transmitted beam can be obtained from the exponentially decaying evanescent field intensity I(z) in eq. (3.7.28) [138].

$$I(z) = I_0 \cdot e^{-\frac{z}{d}} \tag{3.7.28}$$

where z is the distance from the interface and I(0) the intensity at the interface. In particular, the penetration depth d is dependent on the wavelength λ, the incidence angle θ with respect to the normal to the interface and the refractive indices n_1 (medium of incident light with higher refractive index) and n_2 (medium with lower refractive index after the interface) according to eq. (3.7.29) [135, 138].

$$d = \frac{\lambda}{4\pi} \cdot \left(n_1^2 \cdot sin^2(\theta) - n_2^2\right)^{(-\frac{1}{2})} \tag{3.7.29}$$

With eq. (3.7.29) the penetration depth d of the IR beam with a wavelength of $\lambda = 785$ nm is calculated and of the order of 100 nm, a negligible penetration depth of the probe beam within the sample. The circular annulus of the back focal plane where a focused beam yields TIR is of the order of 0.3 mm for a 1.49 NA objective thus allowing for a comfortable tolerance in order to achieve TIR. Changes in the position of the reflected beam are registered as voltage outputs on the QPD. Particularly by labeling the quadrants of the photodiode in top(1), top(2), bottom(1) and bottom(2) the position sensitivity of the beam is achieved by combination of the voltage of each individual quadrant (proportional to the incident photon flux) according to eq. (3.7.30).

$$QPD(V) = \frac{(V_{top}(1) + V_{top}(2)) - (V_{bottom}(1) + V_{bottom}(2))}{V_{top}(1) + V_{top}(2) + V_{bottom}(1) + V_{bottom}(2)} \tag{3.7.30}$$

The denominator represents a normalization to the total incident light. The custom built electric circuit converts the signal into a voltage which gets converted by the software feedback algorithm into a current signal and fed into the ETL to account for changes in the position. This feedback algorithm was programmed in

LabView (National Instruments) making use of a proportional-integral-derivative (PID) controller out of the standard library of the software.

3.8 Analysis of saturation curves

Analysis of saturation curves was performed the same way throughout the thesis. The following formulas ([139]) were used:

$$specific = measured - nonspecific \tag{3.8.1}$$

$$nonspecific = NS \cdot background \tag{3.8.2}$$

$$specific = \frac{B_{max} \cdot c}{K_d + c} \tag{3.8.3}$$

With NS being the slope of the nonspecific binding, background being the background at no ligand added, B_{max} being the maximum specific binding, c the concentration of the ligand and K_d the dissociation constant.

Nonspecific binding was determined with pre-incubation of 1 μM (saturation curves in CMs) or 100 μM propranolol (saturation curves in HEK293AD cells) prior to incubation with the ligand JE1319. After acquisition of curves, curves were fit in GraphPad Prism 8 and the linear nonspecific line was subtracted from the measured curve to yield a specific binding curve (eq. (3.8.3)).

4 Results

4.1 Localization and dynamics of the β_1- and β_2-adrenergic receptor in cardiomyocytes

4.1.1 Selection of fluorescent ligand

In order to determine the localization and dynamics of the β_1- and β_2-ARs in adult cardiomyocytes (CMs) directly, fluorescently labeled ligands are used which bind to the receptors. Multiple ligands were tested among which are a commercially available version from Cisbio [140] (emitting at 520 nm), fluorescent ligands from the Hill lab in Nottingham conjugated to either the fluorophore Bodipy 630/650 or Bodipy FL and the high affinity fluorescent ligand from the Gmeiner lab termed JE1319.

Fluorescent ligands emitting in a green spectrum were quickly discarded because of the interference with the signal from the high amount of autofluorescence cardiomyocytes exhibit (strongest in a spectral range of 450-560 nm, see section 1.2.3). The interfering signal together with the low amount of receptors in endogenous expression levels of adult CMs excluded the Cisbio ligand and the green versions of Hill's ligands from further experiments. Additionally, the fluorescent ligands conjugated to Bodipy exhibited strong unspecific stain rendering them as unsuitable for localization studies. An example of such ligand conjugated to BODIPY 630/650 with a high amount of non-specific binding in β_1/β_2-AR knock-out cardiomyocytes is represented in fig. 4.1. Despite the knock-out of β-ARs the cell shows a significant amount of membrane and unspecific stain.

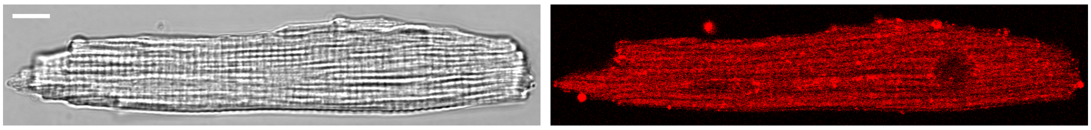

Figure 4.1: Brightfield (left) and confocal (right) image of an adult β_1/β_2-AR-k.o. CM after labeling with 50 nM of a BODIPY 630/650-conjugated antagonist. Scale bar of 10 μm applies to all images.
The ligand was kindly provided by Prof. Dr. Stephen Hill.

For the reasons mentioned above a high affinity fluorescent ligand with a negligible amount of unspecific binding and a low amount of interference of the autofluorescence of CMs is required in order to visualize the presence and localization of endogenous β_1- and β_2-ARs in adult murine cardiomyocytes. Such a fluorescent ligand, termed JE1319, was specifically developed for this purpose by Prof. Dr. Gmeiner and his group on the basis of the non-selective high-affinity (subnanomolar) antagonist carazolol [35, 36, 141, 142] conjugated to the photostable Alexa 647 fluorophore via an external linker. It effectively labels both receptors with negligible unspecific stain as will be shown in the following section 4.1.2.

4.1.2 Fluorescent ligand JE1319

At first, the high affinity, non-subtype selective antagonist for β_1- and β_2-ARs, named JE1319, was characterized. To this end competition binding experiments were performed. The chemical structure (fig. 4.2a) of the ligand and the competition curves with the radioligand [^{3}H]CGP12177 in membranes of (fig. 4.2b) and in transiently transfected HEK293T cells (fig. 4.2c) are displayed in fig. 4.2.

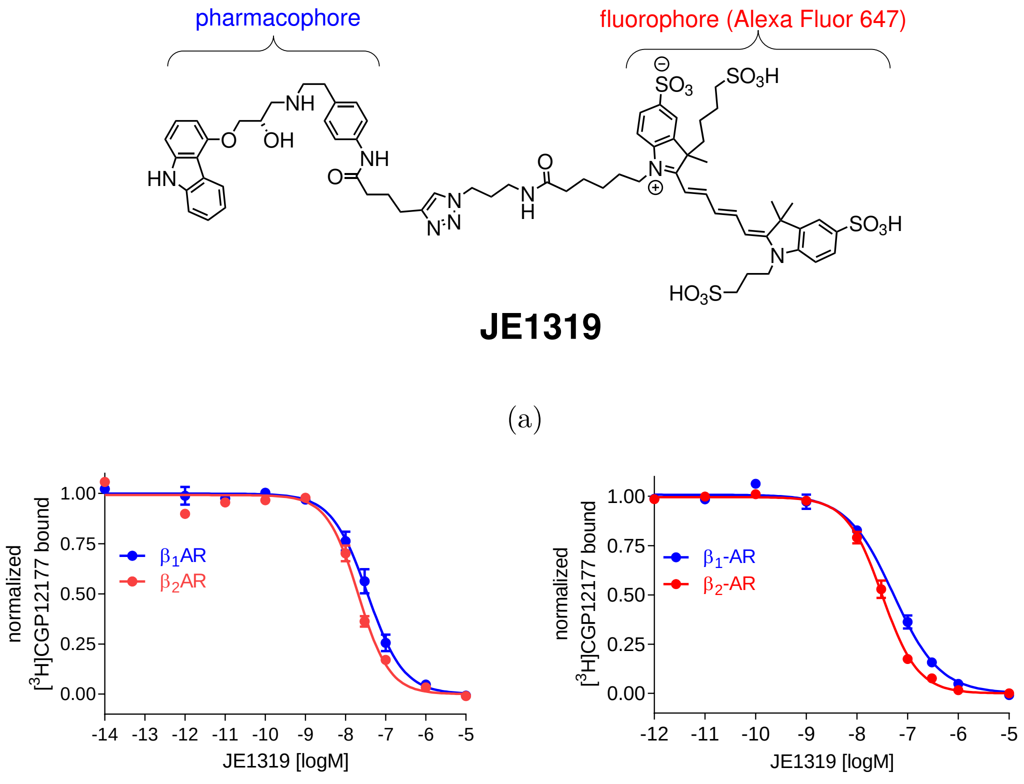

(a)

(b)

(c)

Figure 4.2: Chemical structure of the ligand JE1319 (a) and normalized radioligand competition curves for the β_1-AR (blue) and β_2-AR (red) performed on membranes (b) and cells (c) of transiently transfected HEK293T cells yielding inhibitory constant (K_i) values of 9.8 (β_1-AR, n=6) and 4.6 nM (β_2-AR, n=7) in membranes (b) and 42 (β_1-AR, n=2) and 22 nM (β_2-AR, n=8) in cells (c) respectively. Curves are normalized to their respective maximum values. Error represents SEM. (a), (c) adapted from Bathe-Peters et al. [58] & licensed under CC BY-NC-ND 4.0. Ligand synthesis and radioligand competition curves were performed by AGs Gmeiner and Hübner at the University of Erlangen.

From the curves the half maximal inhibitory concentration (IC_{50}) values are converted to the K_i values in table 4.1 via the Cheng-Prusoff equation [34]. More details about the synthesis and characterization by radioligand binding are found in [58].

Experiment	human β_1 $[^3H]$CGP12177	human β_2 $[^3H]$CGP12177
$[^3H]$CGP12177 competition in membranes	9.8 ± 2.1 nM (6)	4.6 ± 0.6 nM (7)
$[^3H]$CGP12177 competition in HEK293T cells	42 ± 8 nM (2)	22 ± 3 nM (8)

Table 4.1: Affinities of the fluorescent ligand JE1319 for the β_1- and β_2-AR determind by radioligand competition assays on membranes of transiently transfected HEK293T cells and transiently transfected HEK293T cells according to Bathe-Peters et al. [58]. Number of experiments is indicated in parenthesis and error represents SEM.

4.1.2.1 Spectra of JE1319

The absorption (Evolution 350 UV-Vis-Spectrophotometer), excitation and emission (Horiba Spectrofluorometer FluoroMax) spectra were recorded, matching those of Alexa 647. The spectra are displayed in fig. 4.3.

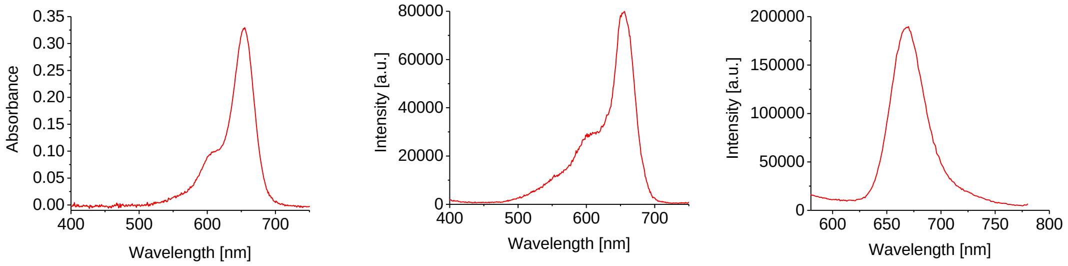

(a) Absorption (b) Excitation (c) Emission

Figure 4.3: Determined spectra of the ligand JE1319. (a) Absorption, (b) excitation and (c) emission spectrum. Reprinted from Bathe-Peters et al. [58] & licensed under CC BY-NC-ND 4.0.

4.1.2.2 Staining of β-adrenergic receptors with JE1319

Then the ability of the ligand JE1319 to bind to β-ARs was investigated. In order to achieve that at first endogenous β_2-ARs of A431 cells [143–146] were stained by incubation with 5 nM JE1319 for 30 min (fig. 4.4). The cells display clear labeling of the endogenous β_2-ARs at the cell surface (fig. 4.4a). Figure 4.4b on the other hand shows that the ligand can be displaced from the receptors by ICI 118,551.

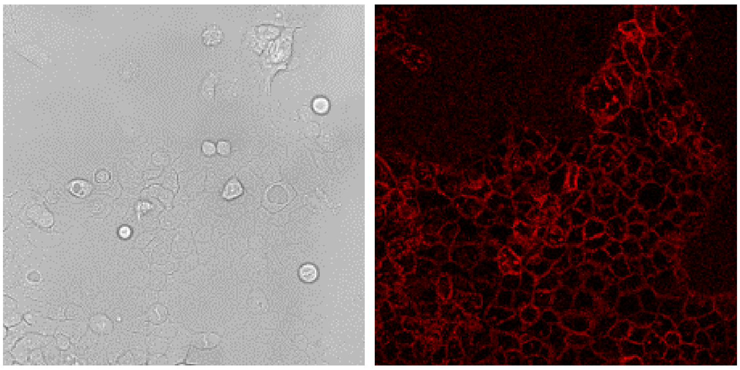

(a) A431 - β_2-AR stained

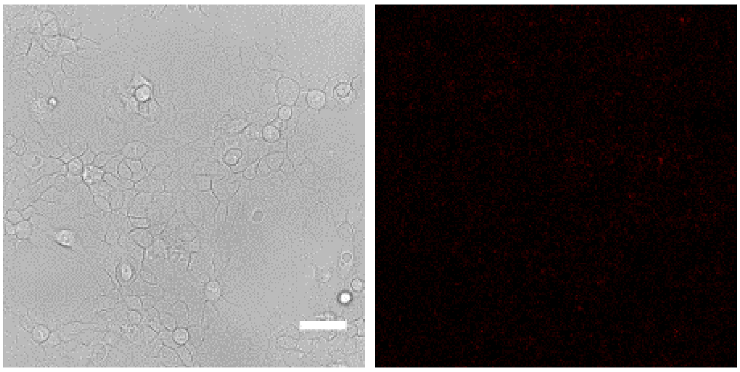

(b) A431 - β_2-AR - JE1319 displaced

Figure 4.4: Images of A431 cells, left brightfield and right fluorescent images. (a) A431 cells with 5nM JE1319 labeled endogenous β_2-ARs. (b) JE1319 was displaced with 50 nM ICI 118,551. Scale bar applies to all images and is 50 μm. Reprinted from Bathe-Peters et al. [58] & licensed under CC BY-NC-ND 4.0.

Similar observations were made with HEK293AD cells transiently transfected with CFP-labeled β_1-ARs. Incubation with 5 nM JE1319 for 30 min revealed a well-visible stain of the β_1-ARs at the cell surface (fig. 4.5a) whereas on the other hand no stain was observed when pre-incubating/blocking the receptors with the β_1-AR selective antagonist CGP 20712 (fig. 4.5b).

Further untransfected HEK cells display very low non-specific binding of the ligand when incubated with 5 nM JE1319 as indicated in fig. 4.6.

This indicates the control for subtype selective labeling of β-ARs with the ligand JE1319 by exhibition of very low non-specific binding.

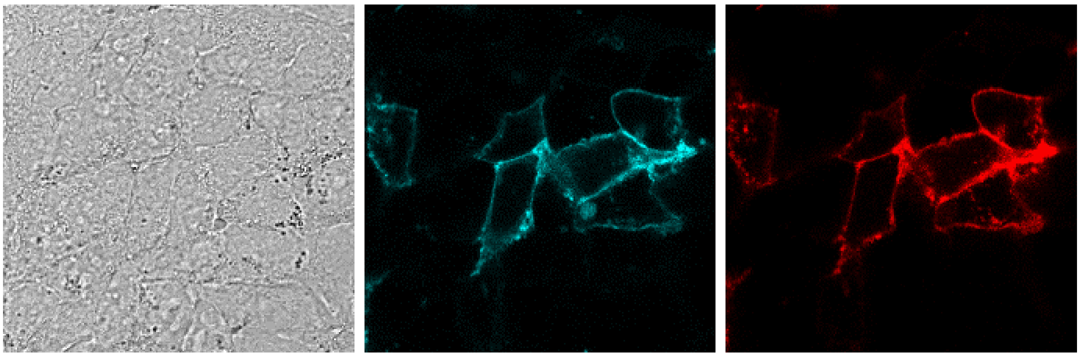

(a) HEK293AD - β_1-AR-CFP stained

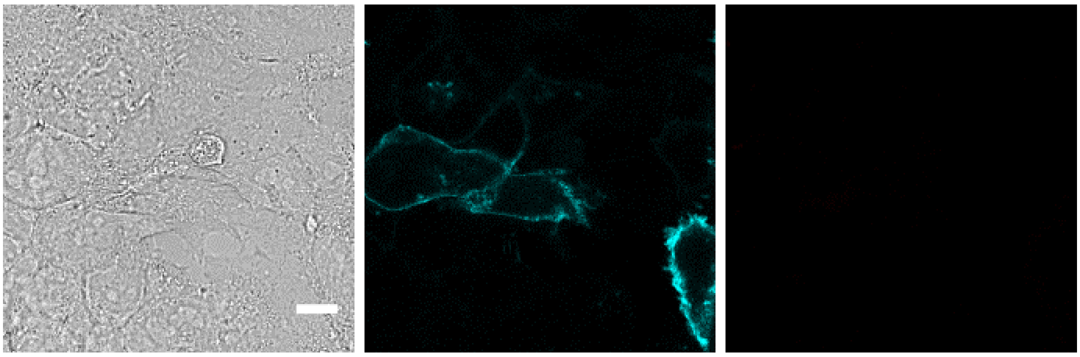

(b) HEK293AD - β_1-AR-CFP blocked

Figure 4.5: Images of HEK293AD cells transiently transfected with β_1-AR-CFP, left brightfield, center CFP-channel and right JE1319-channel. (a) HEK293AD cells with 5 nM JE1319 labeled β_1-ARs. (b) JE1319 was blocked from binding with 100 nM CGP 20712. Scale bar applies to all images and is 10 μm. Reprinted from Bathe-Peters et al. [58] & licensed under CC BY-NC-ND 4.0.

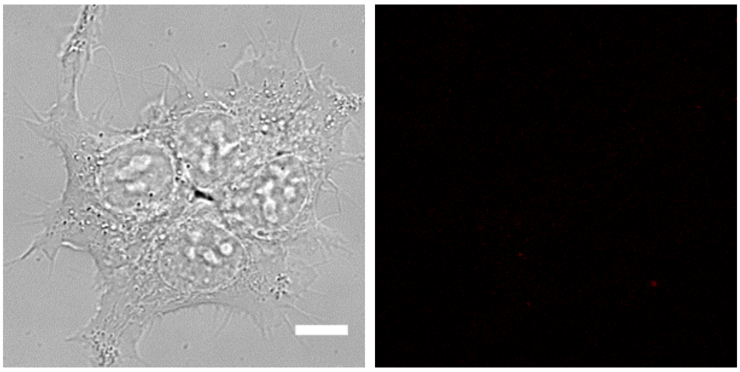

Figure 4.6: Images of untransfected HEK293AD cells, left brightfield and right JE1319-channel. HEK293AD cells incubated with 5 nM JE1319. Scale bar applies to all images and is 10 μm. Reprinted from Bathe-Peters et al. [58] & licensed under CC BY-NC-ND 4.0.

4.1.2.3 Association and dissociation of JE1319

The association and dissociation times in transfected HEK cells and ventricular cardiomyocytes from mice with a cardiac transgene were measured. These transgenic mice express the respective β-AR subtype under the control of the cardiomyocyte-specific α-myosin heavy chain promoter leading to two mouse lines, β_1-AR-TG4 and β_2-AR-TG32, which overexpress the respective β-AR at comparable levels ($\approx$ 2.5 pmol/mg membrane protein at 3 months of age) [7, 147, 148].

Figure 4.7 illustrates how the association and dissociation curves in adult cardiomyocytes and transfected HEK293AD cells were determined. An indication of exemplary ROIs of measurements is shown in fig. 4.7a and fig. 4.7b respectively. Figure 4.7a demonstrates the specific stain on a β_1-AR-TG4 CM at the compartments of the PM and the TTs with low background signal. The color-code of the ROIs matches the colors of the association curves in fig. 4.7c indicative of the region of measurement. Association and dissociation curves are acquired in β_2-AR-TG32 CMs. The association behavior displayed is asymptotic reaching a plateau in both compartments at around 45 min (fig. 4.7c). Dissociation of the ligand exhibited a half-life of 30-45 min (fig. 4.7e).

The same layout is used on the right panels for the HEK293AD cells. Figure 4.7b shows an example image of HEK293AD cells and selected ROIs of whole cells and background selections. HEK293AD cells were transfected with either β_1-AR-CFP or mTurquoise2-β_2-AR and labeled with 5 nM JE1319. Association curves and background signals are displayed in fig. 4.7d and dissociation curves in fig. 4.7f. Association of β_2-ARs in HEK cells appears to be in agreement with the data in CMs whereas the β_1-ARs seem to require additional time to reach a plateau (fig. 4.7d). Dissociation of the ligand from the receptors in HEK cells appears to be a bit faster than in adult CMs by dissociating from the receptors with a half-life of 20-30 min (fig. 4.7f). Reminiscent signal in the dissociation curves is most likely due to unbound ligand since no washout was performed at the end of the time series.

Time courses in HEK293AD cells are indicative of different affinities with similar dissociation and different association curves. Association appears on a faster time scale for the β_2-AR than for the β_1-AR. Indeed competition curves acquired on membranes and transiently transfected HEK293T cells (fig. 4.2 and table 4.1) as well as saturation experiments in adult CMs (section 4.1.2.5) indicate that the ligand is more affine to the β_2-AR.

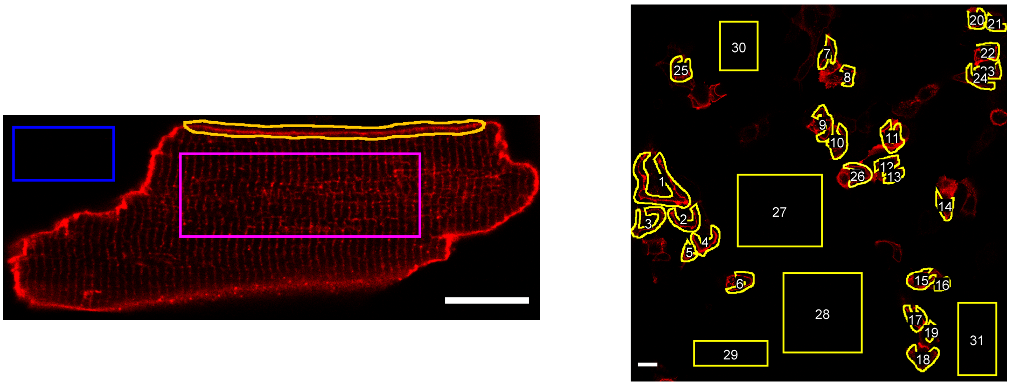

(a) ROI-selection CMs (b) ROI-selection HEK293AD

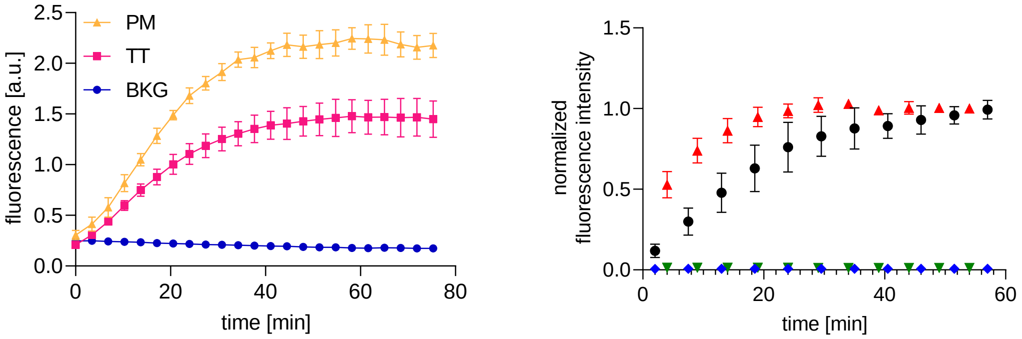

(c) Association CMs (d) Association in HEK293AD

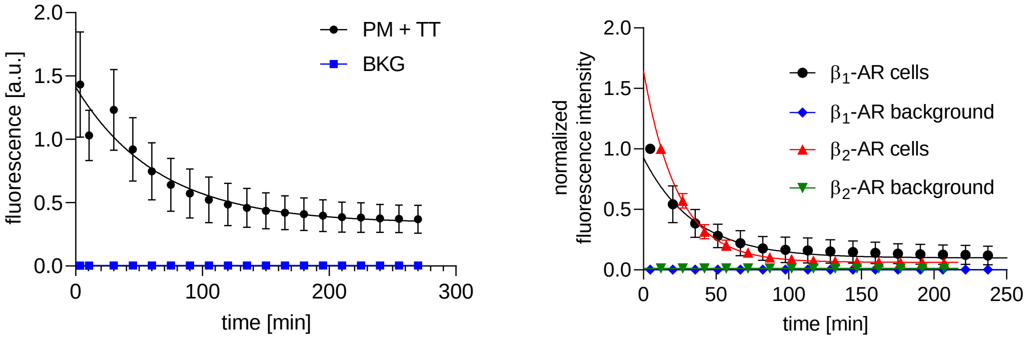

(e) Dissociation in CMs (f) Dissociation in HEK293AD

Figure 4.7: Determination of time courses in CMs and HEK293AD cells. (a) Image of a β_1-AR-TG4 CM staining β_1-ARs with 5 nM JE1319. (c) Association curves of three example ROIs at the outer PM (orange), TTs (pink) and in the background as indicated in (a). (e) Dissociation curve averaging the signal of the PM and TTs. (b) HEK293AD cells transfected with β_1-AR-CFP labeling β_1-ARs with 5 nM JE1319. Example ROIs are indicated at time frame 1 of the dissociation curve (ROIs 1-26 cell membranes, 27-31 background). (d, f) Association and dissociation curves of HEK293AD cells transiently transfected with β_1-AR-CFP or mTurquoise2-β_2-AR and labeled with 5 nM JE1319 (same legend). For reasons of comparison normalized to last (association) or first (dissociation) value. Dissociation half-lifes range from 20-45 min. Error represents SD. Scale bars are 20 μm. (a), (e) Reprinted and (c) adapted from Bathe-Peters et al. [58] & licensed under CC BY-NC-ND 4.0.

4.1.2.4 Saturation curves in transfected HEK293AD cells

Next, saturation curves were acquired in order to determine the affinity and the working concentrations. At first fluorescence saturation curves were acquired in the plate reader on transiently transfected HEK293AD cells (fig. 4.8) yielding the affinity values of the ligand JE1319 in table 4.2 for β_1- (62 ± 7 nM) and β_2-ARs (54 ± 9 nM); values are already corrected for unspecific binding by experiments with 100 μM propranolol pre-treated HEK293AD cells. Although the difference of the affinity values of the ligand for the β_1- and the β_2-AR, obtained at the plate reader, is smaller than expected from association and dissociation experiments and from previous competition experiments, it still indicates a higher affinity of JE1319 for the β_2-AR. By adding two additional concentration values between 10 and 100 nM the curves could possibly show a clearer difference in affinity. Overall these values are in good agreement with the previously determined affinities in transiently transfected whole HEK293T cells in competition experiments (table 4.1). By comparing those experiments in whole cells to competition experiments in HEK293T cell membranes a loss by 4-fold in whole cells of the affinity values is observed (table 4.1) suggesting a slightly facilitated or easier accessible binding to receptors in isolated membranes.

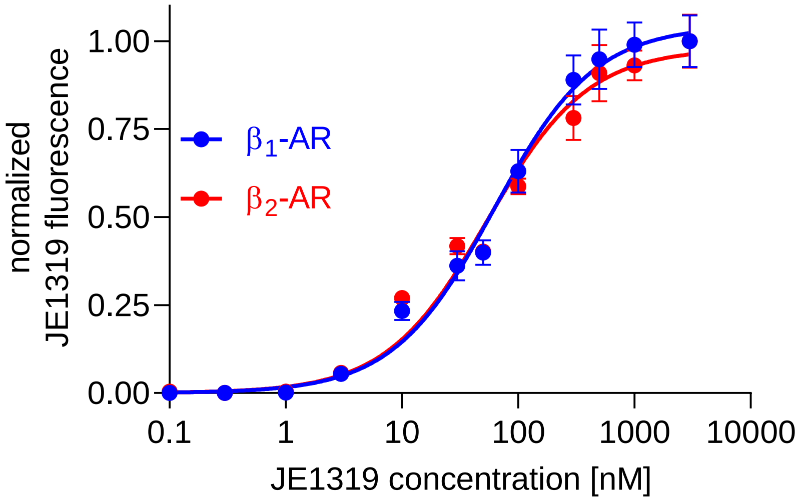

Figure 4.8: Saturation curves for JE1319 binding to intact transiently transfected (either β_1-AR-CFP or mTurquoise2-β_2-AR, n=2 transfections or 8 individual experiments) HEK293AD cells acquired on a plate reader with fluorescence as readout and normalized to their respective maximum values. Obtained dissociation constant (K_d)-values are found in table 4.2. Error is SEM. Adapted from Bathe-Peters et al. [58] & licensed under CC BY-NC-ND 4.0. Plate reader experiment performed by Philipp Gmach & analyzed by Marc Bathe-Peters.

4.1.2.5 Saturation curves in adult transgenic cardiomyocytes

So far saturation binding and affinities were determined in HEK cells. To exclude cell specific effects, saturation curves and affinities were also acquired in adult CMs at the confocal microscope to determine suitable working concentrations for the investigation of β-ARs in adult CMs. For better quantification curves were recorded in adult CMs of the β_1-AR-TG4- and β_2-AR-TG32-mouse lines. Additionally to adding the ligand JE1319 in different concentrations the cells were pre-incubated with either 50 nM ICI 118,551 (β_1-AR) or 100 nM CGP 20712 (β_2-AR) to block the other subtype. Saturation curves are found in fig. 4.9 (top) together with an image binding series indication the quantifiable staining of the β_1-AR and β_2-AR (bottom). Curves were corrected for unspecific binding (linear behavior) by pre-treatment with 1 μM of propranolol and fit to a one site specific binding curve (eq. (3.8.3). The extracted affinities are found in table 4.2 in the center row.

However, one has to keep in mind that the antagonists used for pre-incubation also bind with lower affinity to the other receptor and can therefore partially block binding to the targeted receptor. Accounting for the influence of the antagonists and by applying the Cheng-Prusoff equation [34, 149] affinities in table 4.2 bottom row of 56 ± 8 nM (β_1-AR) and 20 ± 9 nM (β_2-AR) are obtained. Values are of the order of the previously extracted values of the plate reader experiments in HEK cells. However, the curves reflect more distinct affinities between the receptor subtypes comparable to those of the competition binding experiments in fig. 4.2 and table 4.1.

Experiment	β_1-AR	β_2-AR
JE1319 in HEK293AD cells	62 ± 7 nM	54 ± 9 nM
JE1319 in CMs	113 ± 16 nM	21 ± 9 nM
JE1319 in CMs (antagonists)	56 ± 8 nM	20 ± 9 nM

Table 4.2: Dissociation constants of the fluorescent ligand JE1319 for the β_1- and β_2-AR determind by fluorescence assays on transiently transfected HEK293AD (either β_1-AR-CFP or mTurquoise2-β_2-AR, n=2 transfections or 8 individual experiments) acquired on a plate reader (fig. 4.8) or CMs at the confocal microscope (SP8, fig. 4.9, 1 experiment with cell numbers ranging from 17-41 for each concentration). Third row takes the presence of competing ligands into account. Error represents SEM.

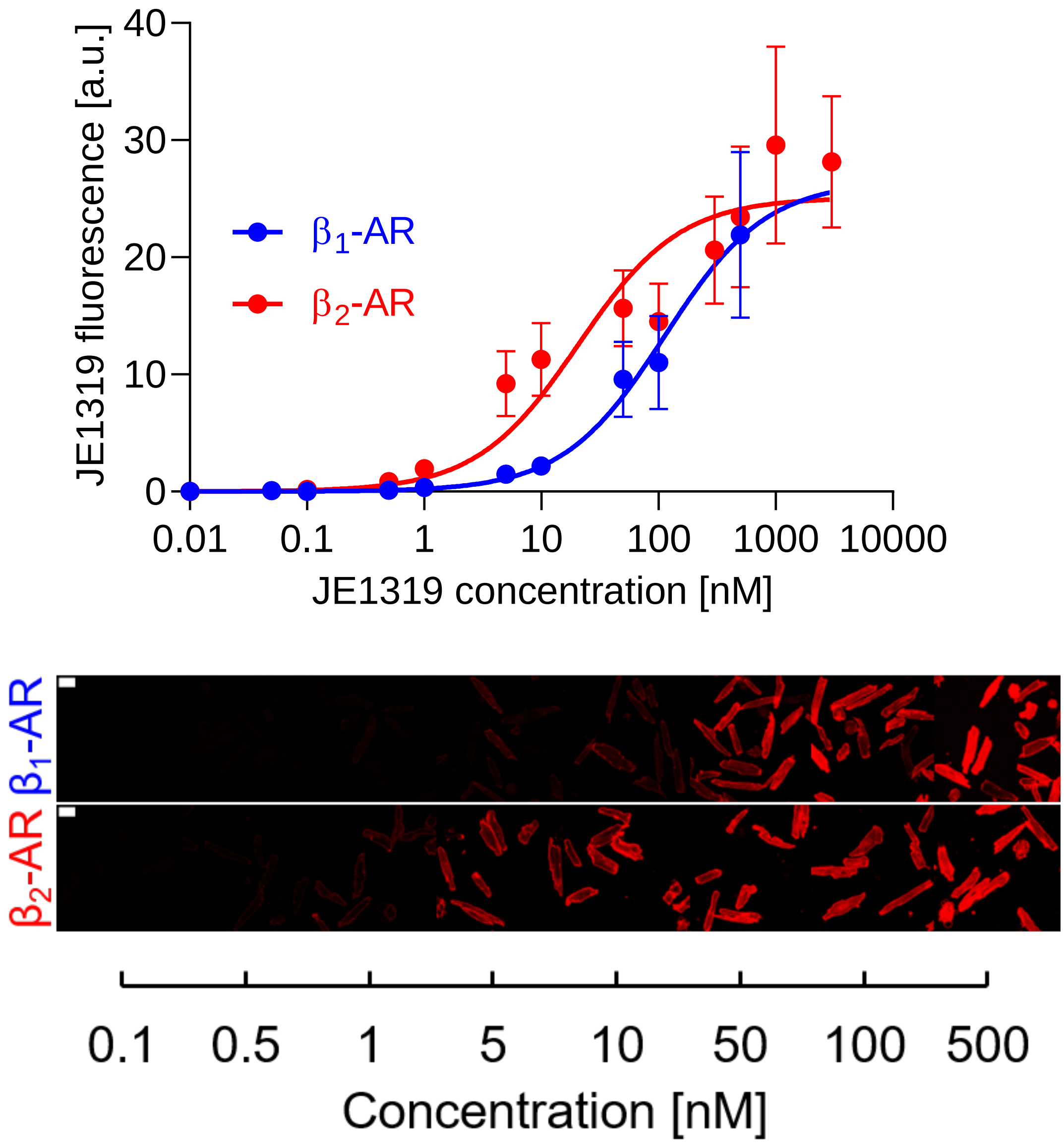

Figure 4.9: Saturation curves in CMs of β_1-AR-TG4- and β_2-AR-TG32-mouse lines pre-incubated with either 50 nM ICI 118,551 (β_1-AR) or 100 nM CGP 20712 (β_2-AR) respectively (top) and corresponding concentration series (bottom) determined with indicated concentrations of the ligand JE1319 on adult cardiomyocytes isolated from the corresponding transgenic mouse lines. Error bars are standard deviation (SD). Scale bar applies to all images and is 50 μm. Extracted affinities are indicated in table 4.2.

4.1.2.6 Comparison of overexpression levels of cardiomyocytes of transgenic mice

One interesting question is whether the two compartments, the PM and the TTs, can be treated as equal referring to the relative expression and abundance of the β-ARs. To answer this question several overexpression cells of the β_1-AR-TG4-

and β_2-AR-TG32-mice were labeled with JE1319 and additionally with a lipophilic membrane dye (CellMask Green). Such a membrane stain labels the membrane uniformly and its signal gives a reference of the amount of membrane being illuminated in the confocal volume. By normalizing the signal from the labeled receptors to the signal from the cell membrane the amount of labeled receptors per unit membrane area is calculated. The relative amount of receptors r between the compartments can then be calculated according to eq. (4.1.1).

$$r = \frac{JE1319_{TT}/cell\ mask_{TT}}{JE1319_{PM}/cell\ mask_{PM}} \tag{4.1.1}$$

For this purpose a semi-automatic selection (ImageJ) of the PM and the TTs was performed to select the outer PM (blue) and the TTs (yellow) separately as depicted in fig. 4.10. Indicated are the two compartments of both receptors and both stains.

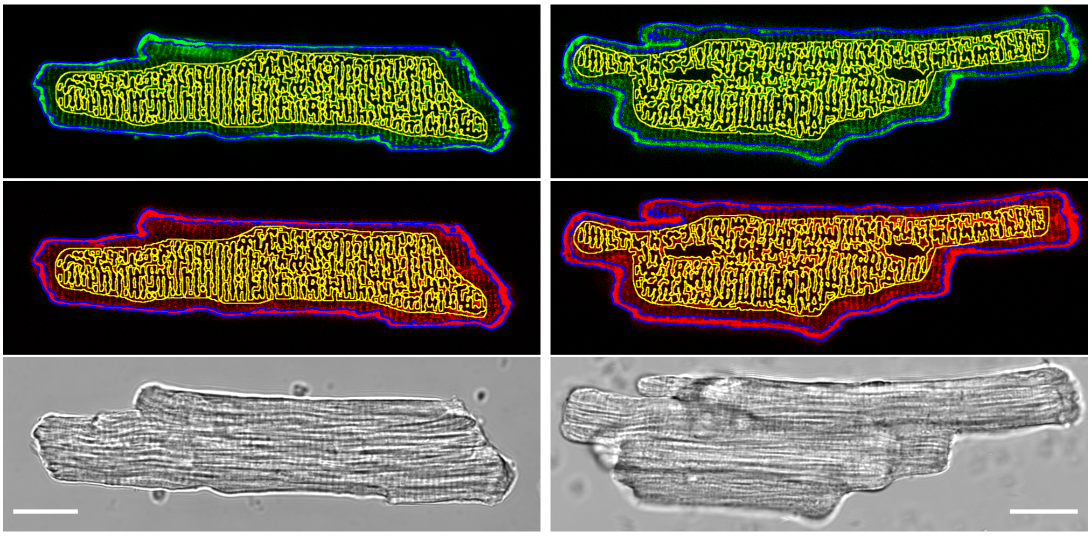

(a) β_1-AR

(b) β_2-AR

Figure 4.10: Comparison of relative abundance of labeled β_1-ARs and β_2-ARs of TTs (yellow selection) to PM (blue selection). Images show example selections of TTs and PM after labeling the surface area with cell mask and the receptors with JE1319 in transgenic CMs. First a normalization of the signal of the same ROIs of the same compartment to the cell mask channel is performed followed by an additional normalization of normalized TTs to normalized PM. Contrast is not the same among images. Scale bar applies to all images and is 20 μm.

The resulting ratios in table 4.3 indicate that both receptors are found in equal amounts in both compartments of overexpression cardiomyocytes.

Cell type	Ratio: TTs/PM	N
β_1-AR-TG4	1 ± 0.1	7
β_2-AR-TG32	0.9 ± 0.1	8

Table 4.3: Relative abundance of labeled β-ARs in TTs/PM of transgenic adult CMs. Normalized to surface area. N represents the number of cells. Errors are SEM.

4.1.3 Diffusion measurements

To measure the dynamics of β-ARs a variant of the general FCS approach, namely linescan FCS, is performed. It allows the acquisition of many single point FCS measurements in parallel [72] at the sample. This approach is well suited as the plasma membrane of adult CMs possesses such a linear morphology with just minor oscillations over the length of a few μm.

Prior to measuring diffusion via linescan FCS and STICS in adult CMs the procedures of measurements and analysis were set up in experiments in solution (fig. 4.11) and on H9c2 cells (fig. 4.12). Procedures of performing linescans and the analysis are described in section 3.7. Of note, only the central portion ($32 < x < 96$) of the linescan is calculated [113].

Figure 4.11 shows the result as STICS functions (figs. 4.11b to 4.11d) and the extracted autocorrelation curves (fig. 4.11a) of three samples containing the dye Alexa 647 measured in water-glycerol mixtures of varying ratios. To this end water-glycerol mixtures were prepared by weight adding the appropriate volume of water and fluorescent compound followed by extensive vortexing and imaging in custom made imaging chambers (section 3.1.1). From the STICS functions (figs. 4.11b to 4.11d) the autocorrelation functions (fig. 4.11a) are extracted at vertical profiles at position x = 0 as indicated by the dashed lines.

As the molecules can diffuse freely in all three dimensions the autocorrelation function is fit to the standard 3D model (eq. (3.7.9)) in order to recover the diffusion coefficient of the fluorescent species by keeping the beam waists constant. Beam waists were extracted beforehand by observation of the profiles of fluorescent microspheres yielding waists of: $\omega_0^{633nm} = 0.33\ \mu m$, $\omega_z^{633nm} = 1.12\ \mu m$, $\omega_0^{488nm} = 0.28\ \mu m$ and $\omega_z^{488nm} = 0.9\ \mu m$ [113–117].

The diffusion constants of Alexa 647 in three water-glycerol mixtures with different ratios are found in table 4.4. Reported are measured diffusion coefficients together with values which were calculated out of tabulated viscosity values of water-glycerol mixtures from [150]. In short, tabulated dynamic viscosity η values are calculated via the Stokes-Einstein relation (eq. (4.1.2)) [151, 152] where D is the diffusion coefficient, k_B the Botzmann constant ($1.3807 \cdot 10^{-23}\ J \cdot K^{-1}$) and r the hydrodynamic radius ($r_{Alexa647} = 7.52 \pm 0.23$ Å).

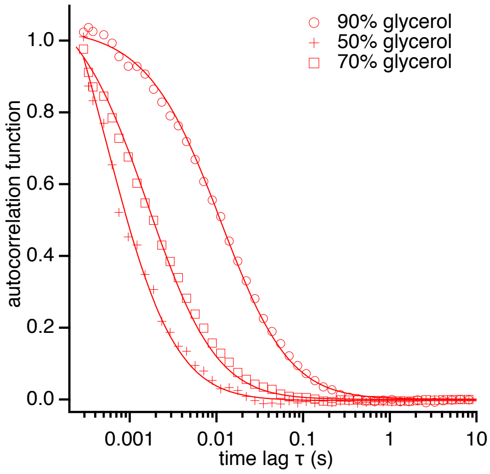

(a) Autocorrelation functions

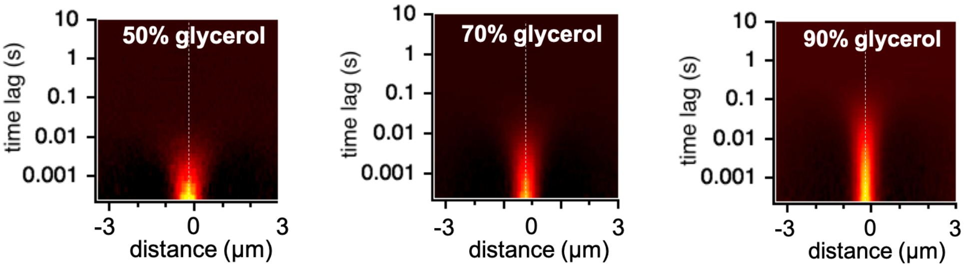

(b) 50% glycerol (c) 70% glycerol (d) 90% glycerol

Figure 4.11: Free diffusion of Alexa Fluor 647 in water-glycerol mixtures with increasing concentrations of glycerol. (a) Autocorrelation functions and representative STICS functions of (b) 50% glycerol, (c) 70% glycerol and (d) 90% glycerol. Dashed lines in (b)-(d) indicate the vertical profiles at distance 0 from where the autocorrelation functions were recovered. Reprinted from Bathe-Peters et al. [113] & licensed under CC BY 4.0. STICS analysis performed by Dr. Paolo Annibale.

Glyerol [% wt.]	20 °C	25 °C	Measured
	D Theory $[{}^{\mu m^2}/_{s}]$	D Theory $[{}^{\mu m^2}/_{s}]$	D (RT) $[{}^{\mu m^2}/_{s}]$
0	287 ± 9	330 ± 10	-
50	48 ± 1	57 ± 2	53 ± 3
70	12.8 ± 0.4	16.05 ± 0.5	17 ± 1
90	1.31 ± 0.04	1.85 ± 0.06	2.45 ± 0.05

Table 4.4: Diffusion coefficients of water-glycerol mixtures of the samples in fig. 4.11. Acc. to Bathe-Peters et al. [113] & licensed under CC BY 4.0.

$$D(T) = \frac{k_B T}{6\pi\eta(t) r} \tag{4.1.2}$$

$$\eta(T) = \eta_0 \cdot e^{\frac{E_A}{R \cdot T}} \tag{4.1.3}$$

If D is known at temperature T together with the tabulated viscosity values then D, at any temperature, can be calculated simply by relating Stokes-Einstein equations. Tabulated viscosity values can either be interpolated or fit to eq. (4.1.3) [153–155] with T being the temperature, η_0 a material specific constant, E_A the activation energy and R the universal gas constant (8.314 $^J/_{K \cdot mol}$).

Figure 4.12 on the other hand illustrates the acquisition and analysis of linescans in H9c2 cells. Visible in fig. 4.12a is a part of the cell with indication of the line which is scanned at the plasma membrane of a living H9c2 cell expressing the β_2-AR which is c-terminally fused to EGFP. Measurements of the embryonic rat heart tissue cells was performed at 37 °C and 5% CO_2. Figure 4.12b gives the resulting STICS function analyzed as described in section 3.7.2 . Figure 4.12c shows the recovered autocorrelation function from the vertical profile at spatial distance 0 with its fit (solid line) to the 2D diffusion eq. (3.7.14).

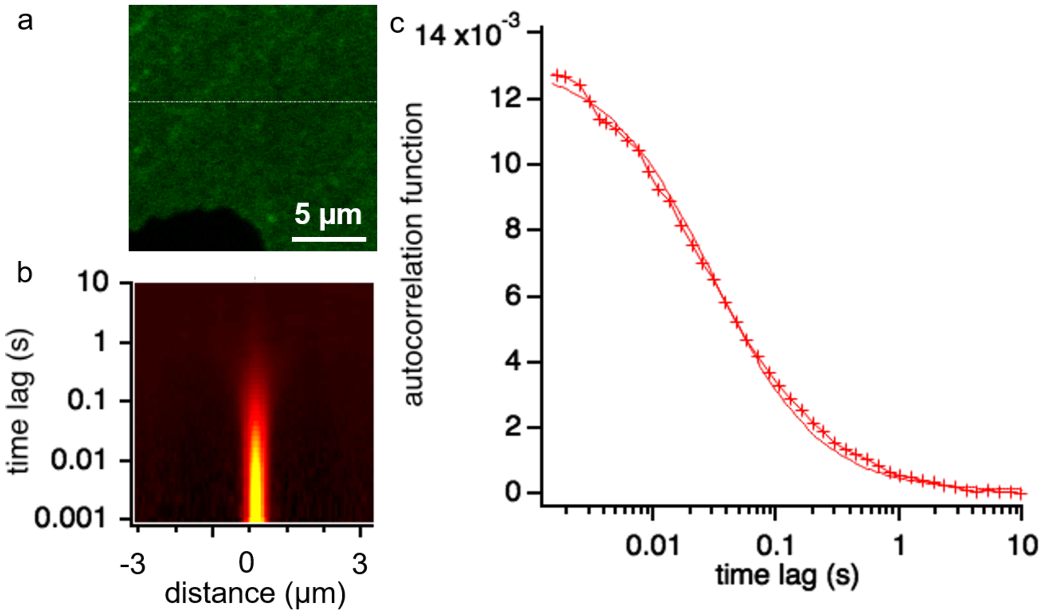

Figure 4.12: Diffusion of c-terminally fused EGFP β_2-ARs in H9c2 cells. (a) Confocal image of a part of the H9c2 cell. (b) STICS function calculated at the linescan along the line displayed in a. (c) Autocorrelation function extracted from the vertical profile at spatial distance 0 of panel b. Reprinted from Bathe-Peters et al. [113] & licensed under CC BY 4.0. STICS analysis performed by Dr. Paolo Annibale.

4.1.4 Simulated diffusion in tubules

By having demonstrated the feasibility of this approach in solution and on flat membranes in section 4.1.3, the next step is to investigate if this approach is still valid in more complicated geometries such as cylindrical tubules, mimicking the T-tubules in adult CMs. Therefore diffusion was simulated on tubules of the size of the real TTs. To this end kymographs of 1000 lines with 200 pixels each, similar to the ones recorded on the Leica SP8, are simulated with parameters of the tubular diameter of 175 nm (average diameter of 169 ± 15 nm [77]), the diffusion constant D of 0.1 $\mu m^2/s$, lateral beam waist of ω_0=0.33 μm and axial beam waist of ω_z=1.12 μm, scanning frequency of 1800 Hz=1/0.556 ms, pixels size of 50 nm and a particle density of 0.45 particles/μm^2. The resulting simulated kymographs, when linescans are performed across cylinders of comparable size to TTs, are displayed in fig. 4.14a. To also investigate the influence of the diffusive directions three different cases, as the diffusion at the surface of the tubules could appear either in axial (along the long axis of the tubule) direction, radially around the tubule or as a combination of both as depicted in fig. 4.13, are simulated.

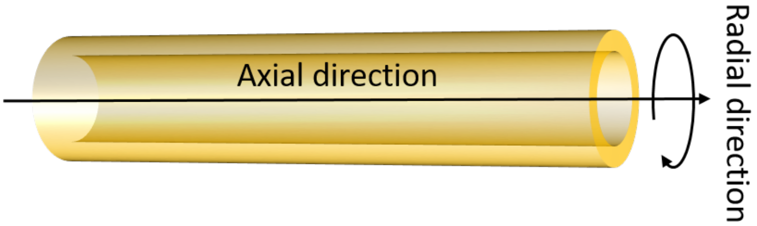

Figure 4.13: Illustration of the directions (axial vs. radial) of particles diffusing at tubules.

The analysis was performed as described in section 3.7.1 using the 1D diffusion eq. (3.7.16) yielding the autocorrelation curves in figs. 4.14b to 4.14d where fig. 4.14b displays the profile plots corresponding to freely diffusing particles on the surface of TTs recovering a diffusion coefficient of D = 0.107 ± 0.003 $\mu m^2/s$. This is in agreement with input parameters of the simulations. Therefore diffusion in tubules is fit to the 1D diffusion equation in this work.

The autocorrelations in fig. 4.14c and fig. 4.14d correspond to diffusion only in axial or radial direction respectively. Interestingly, the dynamics of the receptors on the TTs are governed by two timescales, most prominently caused by the geometry of the system. A slow diffusion timescale associated to only axial motion yielding a diffusion coefficient of D = 0.088 ± 0.003 $\mu m^2/s$ and an apparently faster timescale stemming from the periodic circular movement around the circumference of the tubule. Therefore it can be concluded that diffusion at TTs appears to happen freely, not excluding a certain direction of movement of the particles.

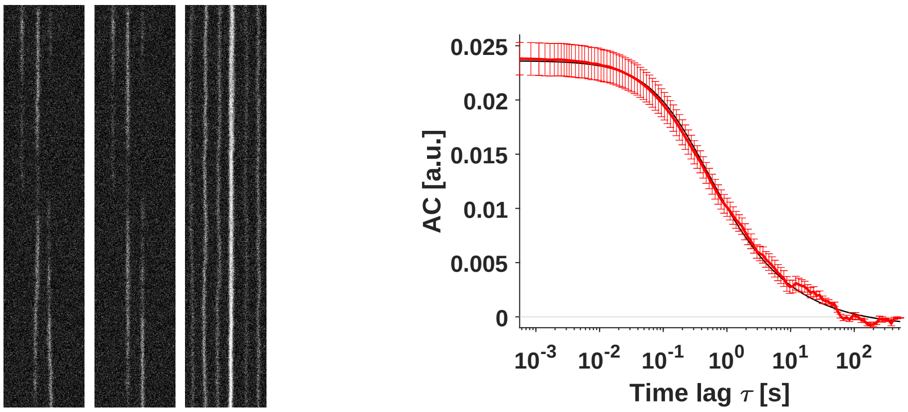

(a) Free - axial - radial

(b) Free diff.

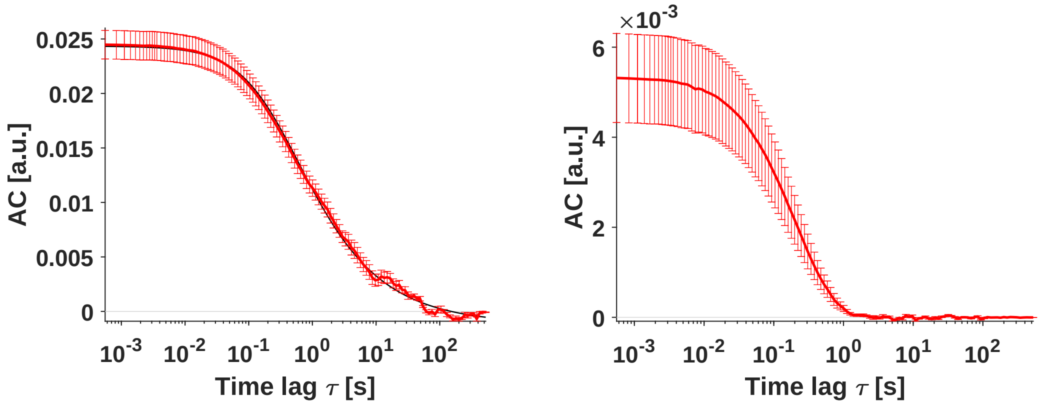

(c) Axial diff.

(d) Radial diff.

Figure 4.14: (a) From left to right: Simulated kymographs (200 pixel, 1000 time points displayed and 1800 Hz scan rate) of combined axial and radial/circumferential (left), only axial (center) and only radial (right) diffusion. (b)-(d) Autocorrelation curves (ACs) of (b) combined axial and radial diffusion, (c) only axial and (d) only radial diffusion with indicated SEM and 1 dimensional fits (black curves, eq. (3.7.16)). Radial/circumferential diffusion (d) has no simple fitting form, but timescale of de-correlation in this geometry is estimated by $\tau_D = \frac{d^2}{D} \sim 0.3s$ in line with what is observed. Simulation parameters are: d_{TT}=175 nm, ω_0=0.33 μm and D=0.1 $\frac{\mu m^2}{s}$. Grey line indicates 0. Reprinted from Bathe-Peters et al. [58] & licensed under CC BY-NC-ND 4.0. Simulations performed by Dr. Horst-Holger Boltz & analyzed by Marc Bathe-Peters.

4.1.5 β-adrenergic receptors in cardiomyocytes of transgenic animals

After confirmation that the ligand JE1319 specifically stains β_1- and β_2-ARs in live cells and acquisition of tools to analyze and extract diffusion data reliably subsequently the new obtained knowledge is used to characterize the localization and dynamics of both β-ARs in adult ventricular CMs. In analogy to [13] it is concentrated on two compartments, namely the outer plasma membrane and the

T-tubular membranes. At first these compartments are investigated in transgenic mice overexpressing either the β_1- or the β_2-AR (at comparable levels of $\approx$ 2.5 pmol/mg membrane protein at 3 months of age [7, 147, 148]). Given the overexpression of the receptors 5 nM JE1319 yielded an adequate signal to noise ratio found both in direct imaging, at the outer PM and the TTs (see fig. 4.15 and fig. 4.18), as well as in fluctuation spectroscopy measurements.

4.1.5.1 β_1-AR-TG4 cardiomyocytes

Figure 4.15 reports a brightfield and a confocal images clearly staining the β_1-ARs of both compartments, the outer PM and the TTs, of a transgenic mouse line overexpressing the β_1-AR (β_1-AR-TG4) CM with 5 nM JE1319 pre-incubated with 50 nM ICI 118,551 to block endogenous β_2-ARs.

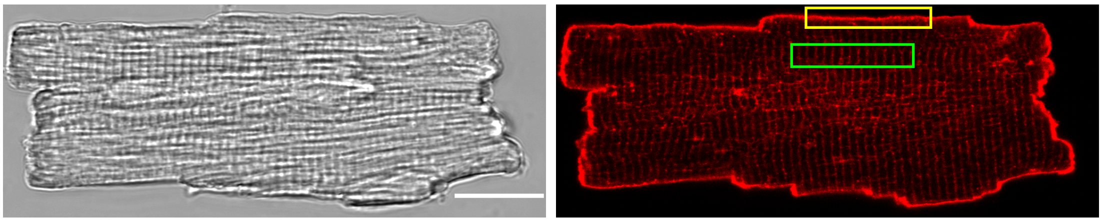

Figure 4.15: Brightfield (top) and confocal (bottom) image of a representative adult β_1-AR-TG4 CM after labeling with 5 nM JE1319 in the presence of 50 nM ICI 118,551. Boxes indicate ROIs of possible line scan areas (yellow at PM and green at TTs). Scale bar applies to all images and is 20 μm. Reprinted from Bathe-Peters et al. [58] & licensed under CC BY-NC-ND 4.0.

Linescans in the yellow regions of fig. 4.15 were performed at the confocal microscope to measure the dynamics of the β_1-ARs. STICS functions were then derived from the kymographs as described in section 3.7.2 and visualized as in the representative fig. 4.16a. The 'plume-like' pattern illustrate the characteristic diffusion process and describe the probability of molecular diffusion as a function of space and time. To quantify the beam waist and how rapid a molecule diffuses the molecular mean square displacement (MSD) can be analyzed from fig. 4.16a as described in section 3.7.2. The average MSD of 5 different adult CMs from β_1-AR-TG4 mice in fig. 4.16b is linear which indicates largely free diffusion of β_1-ARs. The PSF waist and a diffusion constant of 0.081 $^{\mu m^2}/_{s}$, which can be converted into the diffusion time via eq. (3.7.8) yielding 0.29 s, are extracted. These values are also found in summary tables 4.5 to 4.7.

This analysis of the linescans is global over the entire scanned line and therefore particularly advantageous for a continuous stretch as the lateral PM, but less for the periodic, interrupted pattern of the TTs. Therefore a second method was

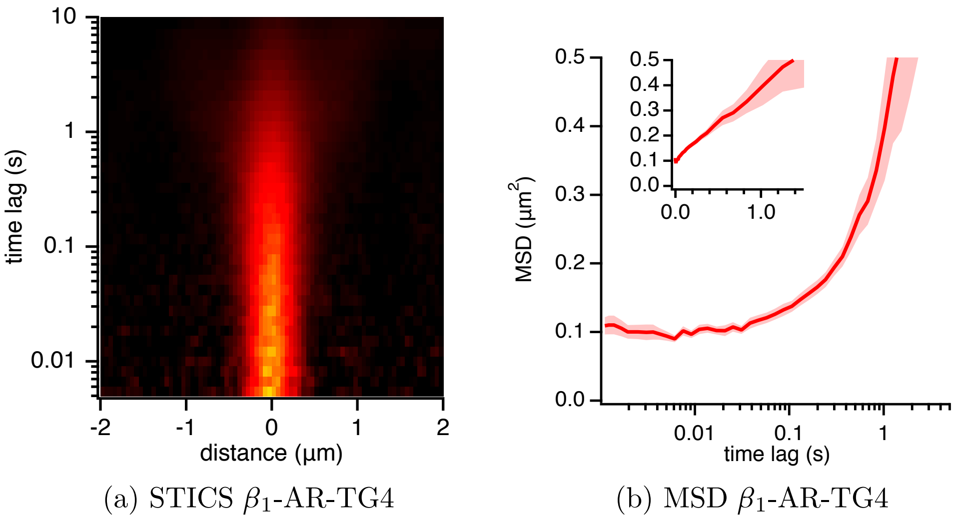

(a) STICS β_1-AR-TG4 (b) MSD β_1-AR-TG4

Figure 4.16: (a) Representative STICS function showing 5 nM JE1319 labeled β_1-AR diffusion at the PM in β_1-AR-TG4 CMs (yellow box fig. 4.15) after pre-treatment with 50 nM ICI 118,551. (b) Average MSD curve from n=5 β_1-AR-TG4 CMs (2 mice) with shadings representing SEM. Inset: MSD on linear scale. Reprinted from Bathe-Peters et al. [58] & licensed under CC BY-NC-ND 4.0. STICS and MSD analysis performed by Dr. Paolo Annibale.

implemented in this thesis which allows additionally the visual comparison of the differences between distinct experiments. This analysis of the linescans displays the characteristic diffusion time calculated on a pixel-by-pixel basis by plotting color-coded single normalized average fluorescence autocorrelation curves of individual cells. As described in section 3.7.1, each individual color-coded autocorrelation reflects the characteristic correlation time τ_D ranging from high correlation (red) to low correlation (blue). This approach is convenient since it allows to manually pick only those pixels corresponding to the TTs. Single cell autocorrelations are then combined in one plot (fig. 4.17). Both compartments show consistent dynamic behavior of the β_1-AR across different cells. By fitting the curves to a 2D diffusion model (eq. 3.7.18) at the outer PM and a 1D diffusion model (eq. 3.7.19) at the TTs which also account for photophysical processes (section 3.7.1.3) a characteristic average correlation constant of 0.06 $^{\mu m^2}/_{s}$ is extracted at the outer PM of the CMs which is then converted via eq. (3.7.8) into the correlation time τ_D of 0.36 s being in good agreement with the STICS analysis. By imaging those TTs that have their major axis in the imaging plane it is immediately visualized from fig. 4.17 that the dynamic behavior of the receptors in the 2 μm spaced TTs is analogous to the one measured at the PM obtaining a diffusion constant of 0.08 $^{\mu m^2}/_{s}$. Diffusion coefficients and times are indicated in tables 4.5 to 4.7. Figure A.1 represents the normalized residual plots to the fits of the averaged and normalized autocorrelation curves in fig. 4.17.

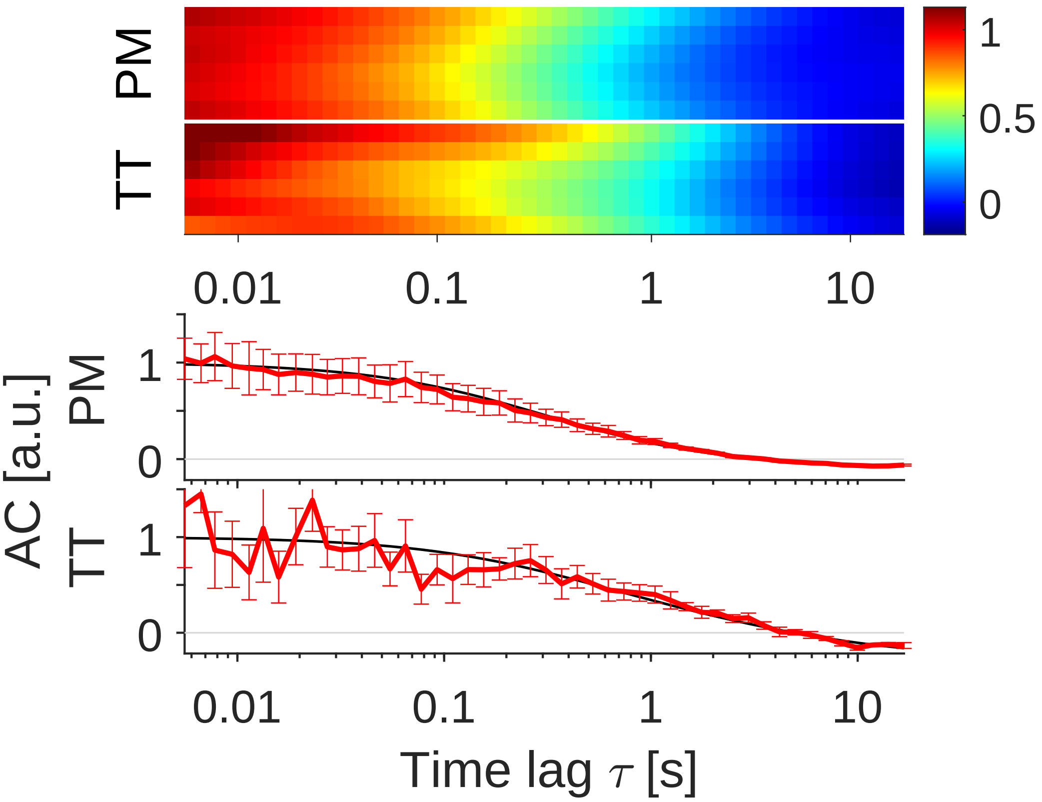

Figure 4.17: Diffusion of β_1-ARs in transgenic/overexpression CMs at the outer PM (yellow box fig. 4.15) and TTs (green box fig. 4.15). Each row represents the normalized AC of 1 cell; at TTs 1 row represents 6-7 averaged tubules. In total n=6 scans of 2 mice each of each compartment. Charts below represent the corresponding ACs with error bars indicating SEM and fit according to eq. (3.7.18) (PM) and eq. (3.7.19) (TTs); grey lines indicate 0. Color scale represents the amplitude of the ACs. Adapted from Bathe-Peters et al. [58] & licensed under CC BY-NC-ND 4.0.

4.1.5.2 β_2-AR-TG32 cardiomyocytes

The same approach of analysis was performed for the transgenic mouse line overexpressing the β_2-AR (β_2-AR-TG32) CMs showing in fig. 4.18 both receptors stained in both compartments, the outer PM and the TTs, with 5 nM JE1319 and pre-incubated with 100 nM CGP 20712 to block endogenous β_1-ARs.

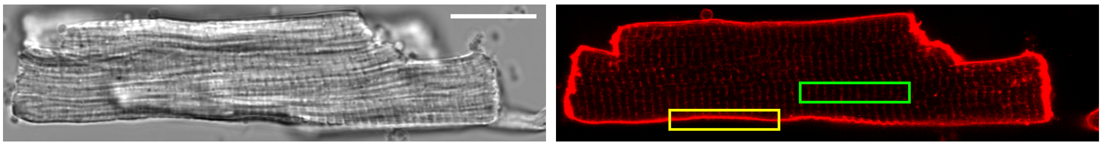

Figure 4.18: Brightfield (top) and confocal (bottom) image of a representative adult β_2-AR-TG32 CM after labeling with 5 nM JE1319 in the presence of 100 nM CGP 20712. Boxes indicate ROIs of possible line scan areas (yellow at PM and green at TTs). Scale bar applies to all images and is 20 μm. Reprinted from Bathe-Peters et al. [58] & licensed under CC BY-NC-ND 4.0.

As for the β_1-AR-TG4 a representative STICS function of the β_2-AR-TG32 is extracted in fig. 4.19a. From the STICS functions of 5 cells the average MSD is calculated showing its curve on a semi-log and linear scale fig. 4.19b. The extracted diffsion constant is D = 0.14 $^{\mu m^2}/_{s}$.

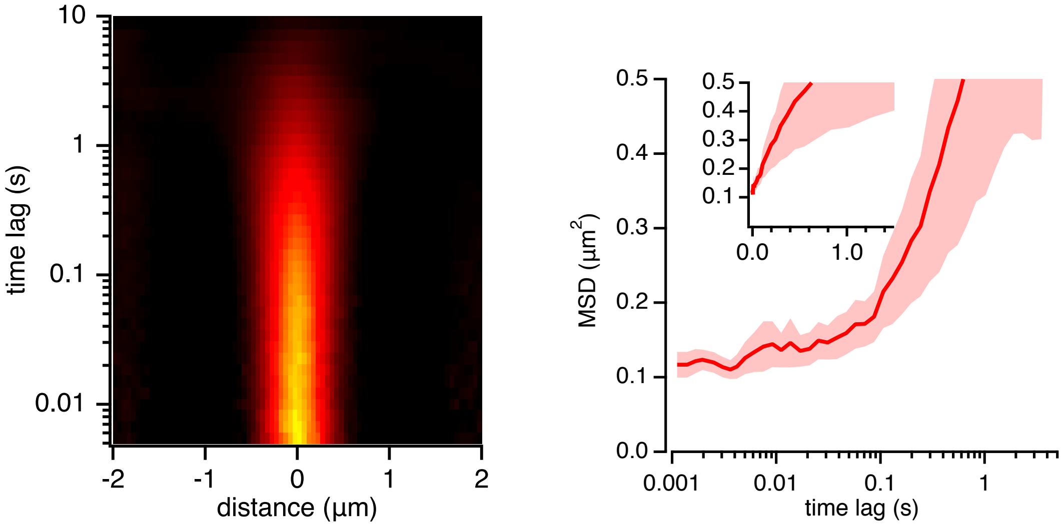

(a) STICS β_2-AR-TG32

(b) MSD β_2-AR-TG32

Figure 4.19: (a) Representative STICS function showing 5 nM JE1319 labeled β_2-AR diffusion at the PM in β_2-AR-TG32 CMs (yellow box fig. 4.18) after pre-treatment with 100 nM CGP 20712. (b) Average MSD curve from n=5 β_2-AR-TG32 CMs (2 mice) with shadings representing SEM. Inset: MSD on linear scale. Reprinted from Bathe-Peters et al. [58] & licensed under CC BY-NC-ND 4.0. STICS and MSD analysis performed by Dr. Paolo Annibale.

Also at the β_2-AR-TG32 the pixel-by-pixel analysis was performed to compare the dynamic behavior of the two compartments not only among themselves, but also to the β_1-AR-TG4. As it is immediately visualized from fig. 4.20, the dynamic behavior of both compartments is very similar, not only among the β_2-AR-TG32 compartments, but also in comparison to the β_1-AR-TG4, as also indicated by the diffusion values in tables 4.5 to 4.7 of D = 0.06 $^{\mu m^2}/_{s}$ at the outer PM and D = 0.05 $^{\mu m^2}/_{s}$ at the TTs when fit to the appropriate 2D and 1D diffusion model with photophysical processes (section 3.7.1.3). Diffusion constants and converted diffusion times are indicated in tables 4.5 to 4.7. The corresponding normalized residual plots are depicted in fig. A.1.

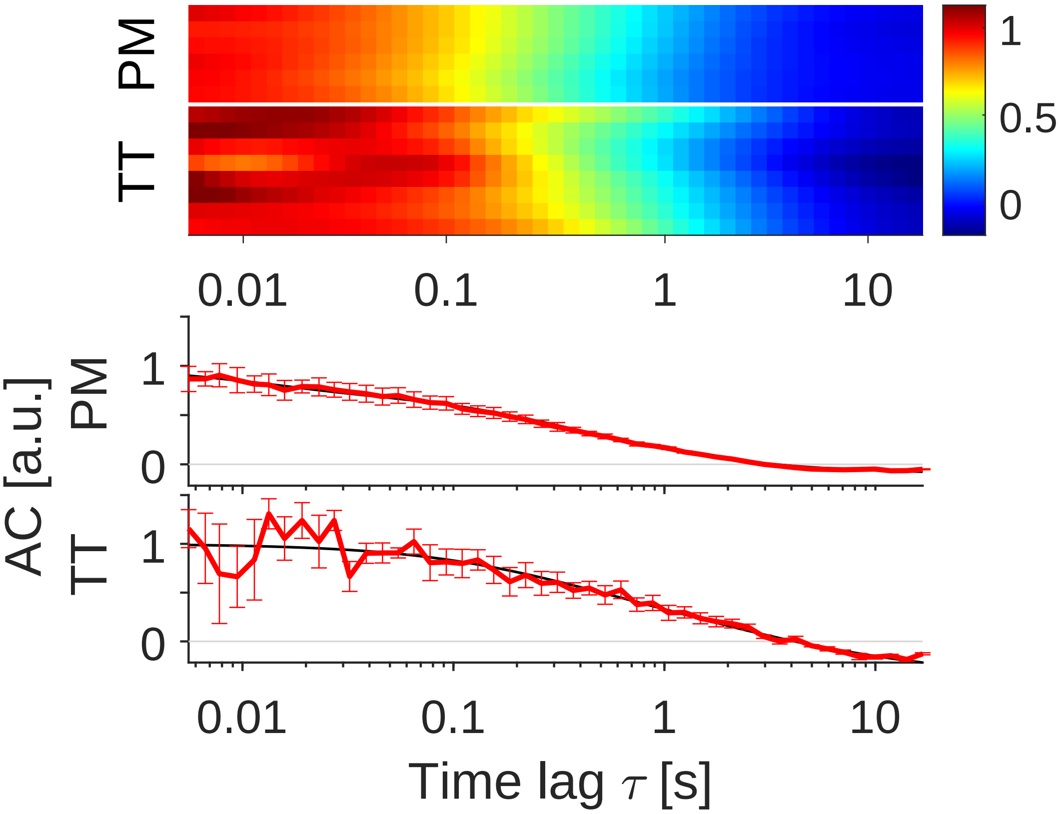

Figure 4.20: Diffusion of β_2-ARs in transgenic/overexpression CMs at the outer PM (yellow box fig. 4.18) and TTs (green box fig. 4.18). Each row represents the normalized AC of 1 cell; at TTs 1 row represents 6-7 averaged tubules. In total n=6 scans (PM) and n=8 scans (TTs) of 2 mice each. Charts below represent the corresponding ACs with error bars indicating SEM and their according to eq. (3.7.18) (PM) and eq. (3.7.19) (TTs); grey lines indicate 0. Color scale represents the amplitude of the autocorrelation curves. Adapted from Bathe-Peters et al. [58] & licensed under CC BY-NC-ND 4.0.

4.1.6 β_1/β_2-adrenergic receptor knock-out cardiomyocytes

To validate the results found in section 4.1.5 with β-AR overexpressing adult CMs and to get an idea of what to expect from an at least 50-60 fold lower expression in wt CMs of endogenous receptors adult β_1/β_2-AR knock-out (β_1/β_2-AR-k.o.) CMs are investigated. *β_1/β_2-AR-k.o.* mice are homozygous null for the adrb1 and adrb2 genes [111]. Representative images labeled with increasing concentrations of JE1319 are found in figs. 4.21 and 4.24. All images are lacking visible stain of the receptors neither at 5 nM JE1319 (fig. 4.21) nor at 50 nM JE1319 (fig. 4.24a) nor at 500 nM JE1319 (fig. 4.24b) stained receptors were observed, even with contrast settings lowered to 0.

Since transgenic CMs are labeled with 5 nM JE1319 it is also started to look for diffusion of receptors labeled with 5 nM JE1319 in β_1/β_2-AR-k.o. CMs (fig. 4.21).

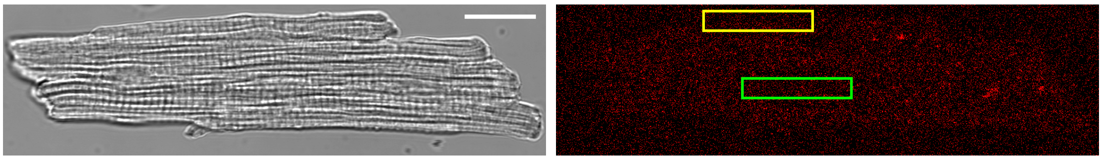

Figure 4.21: Brightfield (top) and confocal (bottom) image of a representative adult β_1/β_2-AR-k.o. CM after labeling with 5 nM JE1319 (contrast of red channel set to 0). Boxes indicate ROIs of possible line scan areas (yellow at PM and green at TTs). Scale bar applies to all images and is 20 μm. Reprinted from Bathe-Peters et al. [58] & licensed under CC BY-NC-ND 4.0.

Figure 4.22 shows STICS functions representative for not only 5 nM JE1319, but also for higher concentrations of the ligand at the PM and TTs. The absence of the 'plume-like' pattern is common across the concentrations of 5, 50 and 500 nM of the ligand and indicates that neither at the outer PM nor at the TTs diffusion of β-ARs is observed.

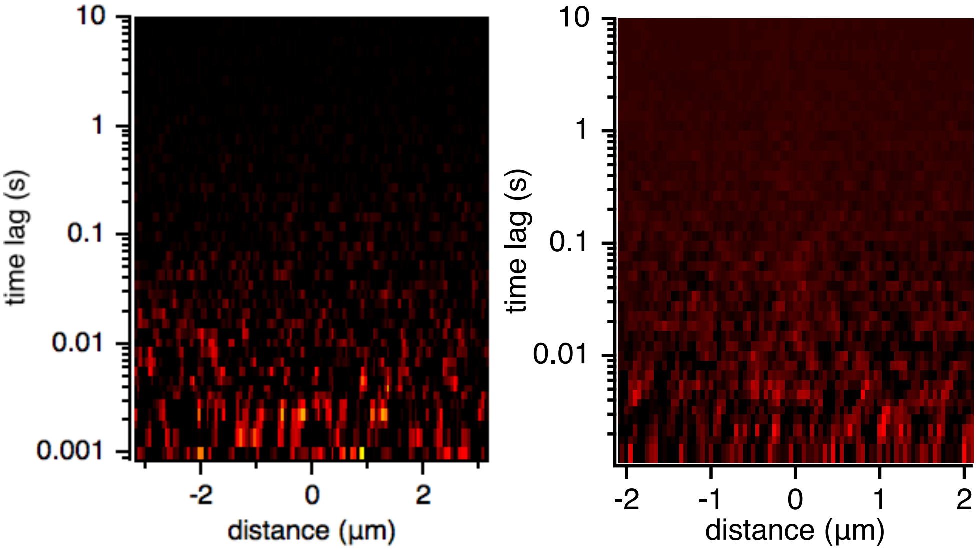

(a) STICS β_1/β_2-AR-k.o. PM

(b) STICS β_1/β_2-AR-k.o. TT

Figure 4.22: Representative STICS function of with 5 nM JE1319 incubated β_1/β_2-AR-k.o. CMs at the PM (a) and TTs (b; yellow and green box fig. 4.21). Reprinted from Bathe-Peters et al. [58] & licensed under CC BY-NC-ND 4.0. STICS analysis performed by Dr. Paolo Annibale.

By analysis via the pixel-by-pixel analysis to extract the autocorrelations fig. 4.23 clearly shows no diffusion fingerprint as indicated by the flat (bottom) and blue colored (top) autocorrelation curves.

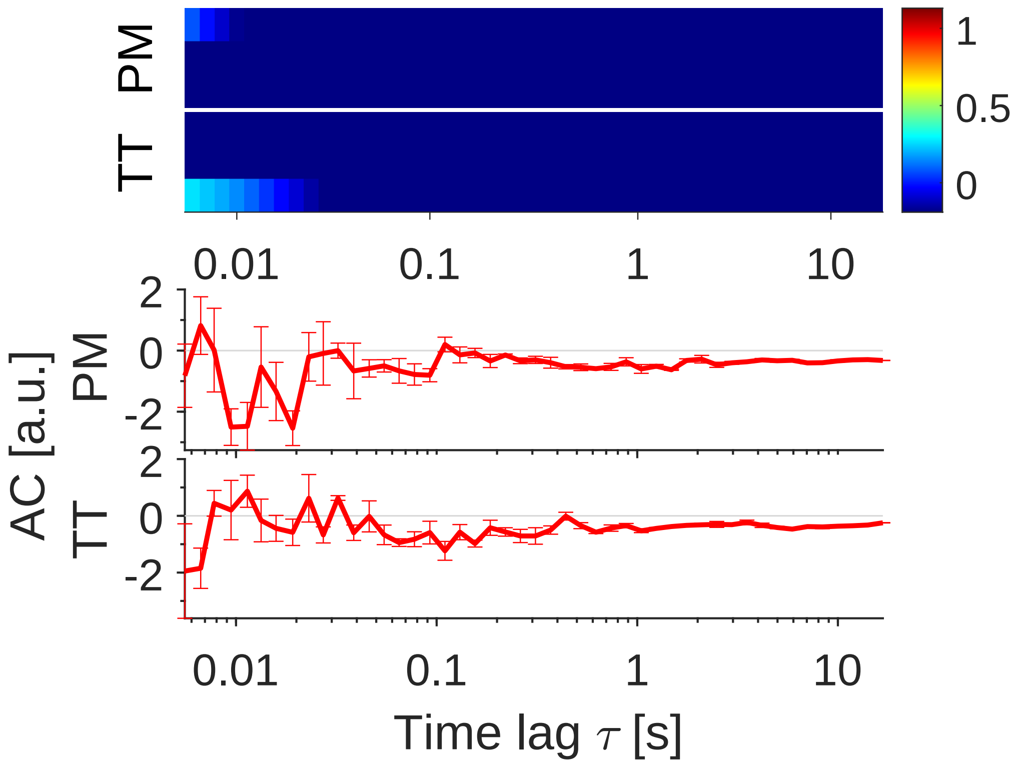

Figure 4.23: Normalized autocorrelation curves of β_1/β_2-AR-k.o. cells incubated with 5 nM JE1319. Autocorrelation curves at the outer PM (yellow box fig. 4.21) and TTs (green box fig. 4.21) are displayed together in one plot separated by a white line. Each row represents the normalized AC of 1 cell; at TTs 1 row represents 6-7 averaged tubules; in total n=3 scans of 1 mouse of each compartment. Charts below represent the corresponding ACs with error bars indicating SEM; grey lines indicate 0. It was normalized to the average g(0) from the TTs of the β_2-AR of wt CMs. Color scale represents the amplitude of the autocorrelation curves. Adapted from Bathe-Peters et al. [58] & licensed under CC BY-NC-ND 4.0.

4.1.6.1 β_1/β_2-AR-knock-out with 50 and 500 nM JE1319

The absence of labeled receptors was confirmed by increasing the concentration of the ligand JE1319 to 50 nM. Figure 4.24a depicts a representative CM showing no detectable stain of β-ARs.

Confirmation of no diffusion is obtained by calculation of the autocorrelation curves in the two compartments of the CMs (fig. 4.25a).

The concentration of the ligand JE1319 was then increased further to 500 nM (a concentration sufficient to almost occupy all receptors, fig. 4.9). Autocorrelation curves fluctuate around 0, but still do not show any detectable diffusion as depicted in figs. 4.24b and 4.25b.

These results state no detectable diffusion of β-ARs neither at the outer PM nor at the TTs in β_1/β_2-AR-k.o. cardiomyocytes at any concentration.

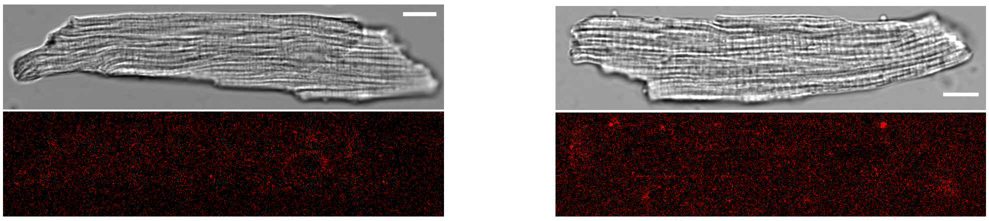

(a) 50 nM JE1319 (b) 500 nM JE1319

Figure 4.24: Brightfield (top) and confocal (bottom) image of a representative adult β_1/β_2-AR-k.o. CM after labeling with 50 (a) and 500 (b) nM JE1319 (contrast of red channel set to 0). Similar boxes are considered for scanning areas as in fig. 4.21. Scale bar is 10 μm.

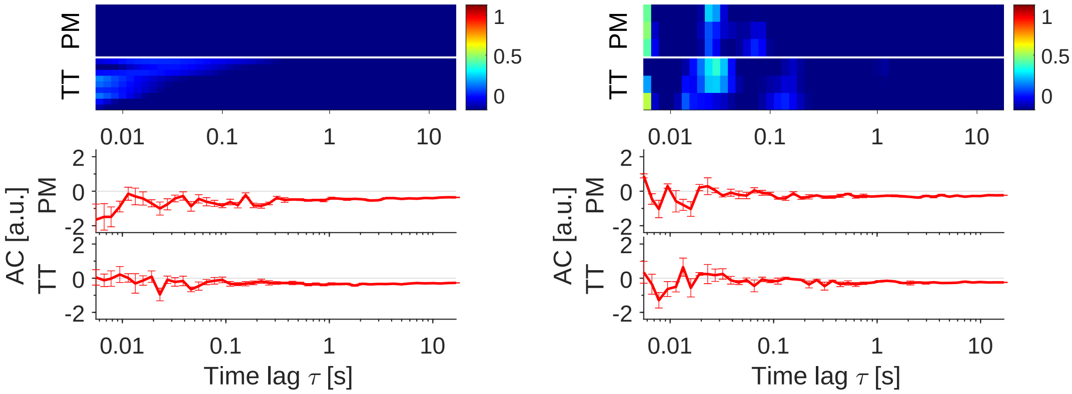

(a) 50 nM JE1319 (b) 500 nM JE1319

Figure 4.25: Normalized autocorrelation curves of β_1/β_2-AR-k.o. cells incubated with 50 (a) and 500 (b) nM JE1319. Autocorrelation curves (ACs) at the outer PM and TTs are displayed together in one plot separated by a white line. Each row represents the normalized AC of 1 cell; at TTs 1 row represents 6-7 averaged tubules; in total n=9 scans of 2 mice (a) and n=3 scans of 1 mouse (b) of each compartment. Charts below represent the corresponding ACs with error bars indicating SEM; grey lines indicate 0. It was normalized to the average g(0) from the TTs of the β_2-AR of wt CMs. Color scales represent the amplitude of the autocorrelation curves.

4.1.7 β_1/β_2-adrenergic receptors in adult wildtpye cardiomyocytes

Having demonstrated the results of the spectroscopy approaches in overexpression systems and in β_1/β_2-AR knock-out cardiomyocytes, the main question of this investigation, namely whether a differential localization of the β_1- and β_2-ARs exists between the outer PM and the TTs in wild-type cardiomyocytes, is addressed.

4.1.7.1 β_1/β_2-AR in wild-type cardiomyocytes labeled with 5 nM JE1319

To start the investigation in wild-type cardiomyocytes the same concentration of 5 nM JE1319 was used as for the experiments in overexpressing cells. The β_1- and β_2-ARs were again selectively labeled by either pre-incubating with the selective antagonists ICI 118,551 or CGP 20712.

Representative images of the selective stain of the β_1- and β_2-ARs do not appear much different from the β_1/β_2-AR-k.o. cells as shown in fig. 4.26.

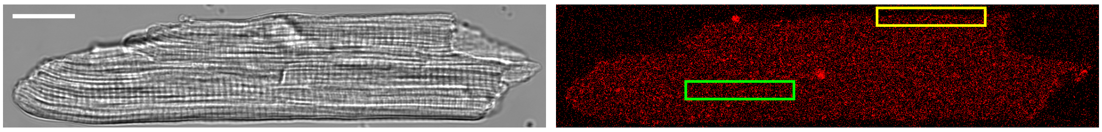

(a) β_1-AR

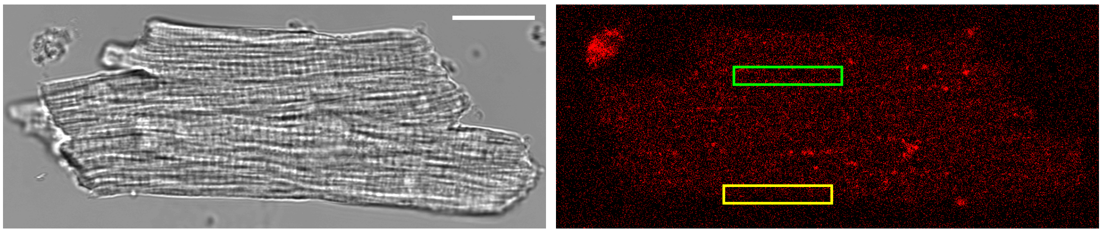

(b) β_2-AR

Figure 4.26: Brightfield (left) and confocal (right) images of representative adult wt CMs after labeling with 5 nM JE1319 (contrast of red channel set to 0). (a) Adult wt CM with labeled β_1-AR by pre-treatment with 50 nM ICI 118,551. (b) Adult wt CM with labeled β_2-AR by pre-treatment with 100 nM CGP 20712. Boxes indicate ROIs of possible line scan areas (yellow at PM and green at TTs). Scale bar is 20 μm. Reprinted from Bathe-Peters et al. [58] & licensed under CC BY-NC-ND 4.0.

In order to investigate the localization and dynamics of the β_1- and β_2-ARs in adult wild-type CMs spectroscopic measurements are performed like the ones in the transgenic cells. Similar to what was observed in overexpressing CMs in section 4.1.5, the β_1-AR displayed a diffusion profile, when performing the STICS analysis on wild-type cardiomyocytes at the outer PM. Figure 4.27 shows a representative STICS function and the extracted and averaged MSD curve of 6 wild-type CMs.

Notably different behavior is observed when performing the STICS analysis on labeled β_2-ARs at the outer PM in wild-type cardiomyocytes. Figure 4.28 displays a representative STICS function in the left panel, which looks very much like the STICS functions extracted from the β_1/β_2-AR-k.o. CMs (fig. 4.22) indicating no detectable diffusion of the β_2-ARs. Out of the same reason no MSD plot in fig. 4.28 can be extracted from the STICS function.

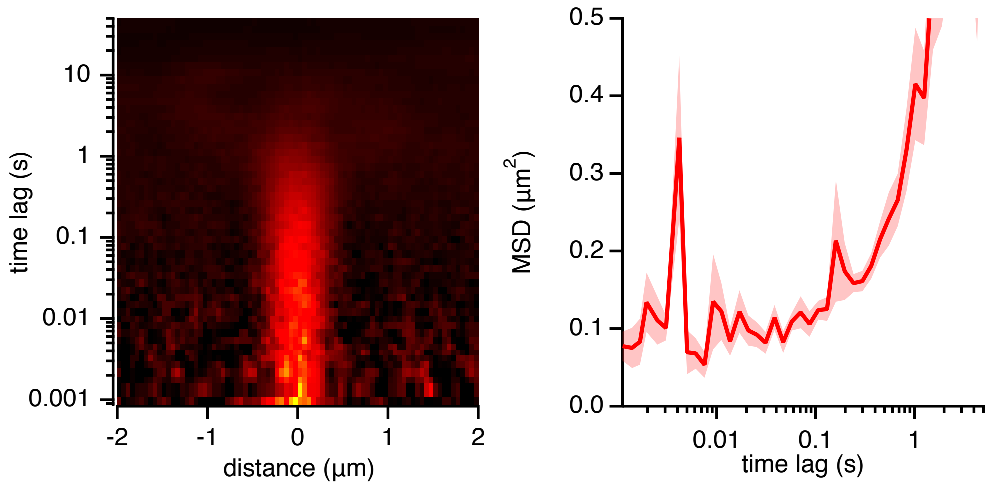

Figure 4.27: (Left) Representative STICS function showing 5 nM JE1319 labeled β_1-ARs diffusion at the PM in wt CMs (yellow box fig. 4.26a) after pre-treatment with 50 nM ICI 118,551. (Right) Average MSD curve from n=6 wt CMs (2 mice) with shadings representing SEM. Reprinted from Bathe-Peters et al. [58] & licensed under CC BY-NC-ND 4.0. STICS and MSD analysis performed by Dr. Paolo Annibale.

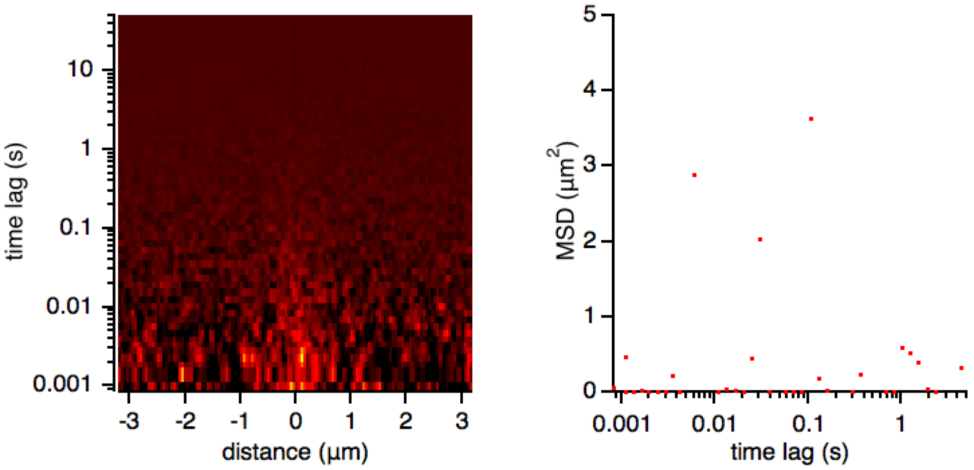

Figure 4.28: (Left) Representative STICS function with 5 nM JE1319 and pre-treatment with 100 nM CGP 20712 showing no diffusion of β_2-ARs at the PM in wt CMs (yellow box fig. 4.26b). (Right) Average MSD curve from n=6 wt CMs (1 mouse). Reprinted from Bathe-Peters et al. [58] & licensed under CC BY-NC-ND 4.0. STICS and MSD analysis performed by Dr. Paolo Annibale.

This behavior becomes more evident when displaying STICS functions of multiple cells of scans (indicated by the representative yellow boxes in fig. 4.26) at the outer PM of wt CMs in one figure as in fig. 4.29.

When performing the pixel-by-pixel analysis of the linescans the same results are obtained displaying a diffusive fingerprint of the β_1-AR at the outer PM, but not of the β_2-AR (fig. 4.30). At the same time autocorrelations of the linescans

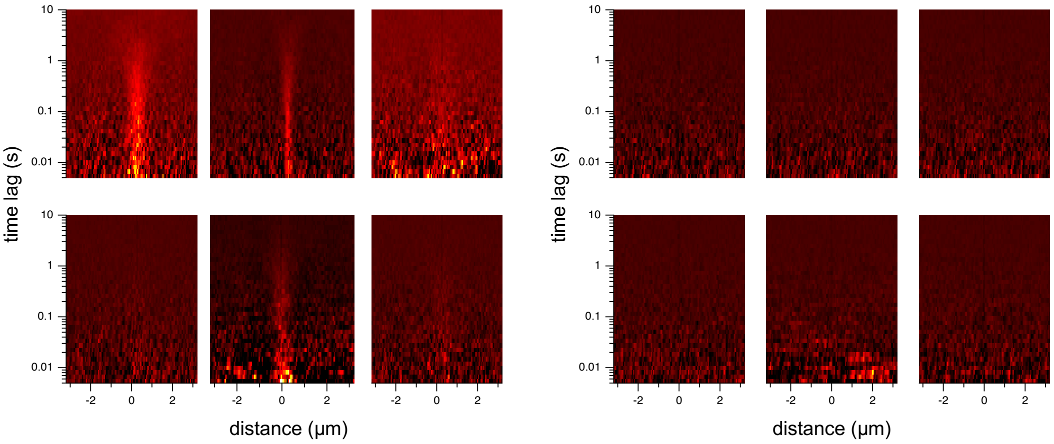

(a) β_1-AR wt

(b) β_2-AR wt

Figure 4.29: Representative STICS functions with 5 nM JE1319 for β_1-ARs and pre-treatment with 50 nM ICI 118,551 (a) and for β_2-ARs pre-treated with 100 nM CGP 20712 (b) at the PM in wild-type cardiomyocytes. Each panel represents the STICS function of 1 cell. Reprinted from Bathe-Peters et al. [58] & licensed under CC BY-NC-ND 4.0. STICS analysis performed by Dr. Paolo Annibale.

(fig. 4.26 green boxes) at the TTs show no detectable diffusion. The corresponding normalized residual plots are depicted in fig. A.1.

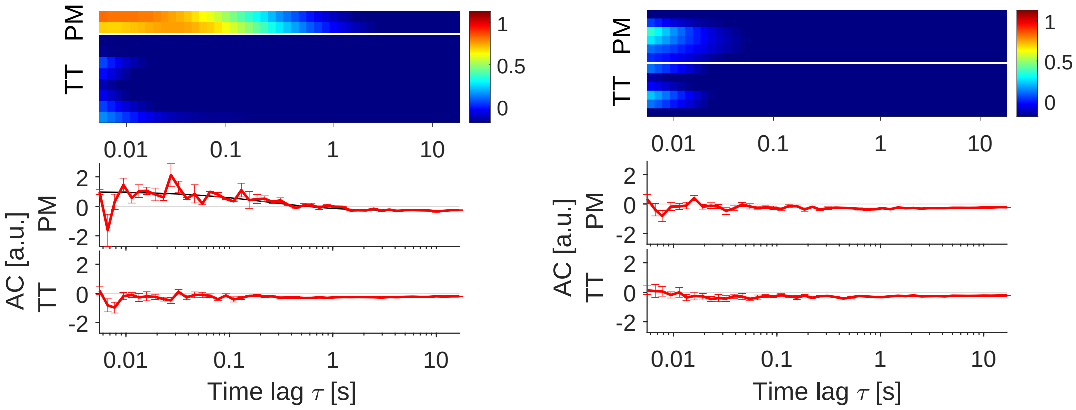

(a) β_1-AR

(b) β_2-AR

Figure 4.30: Normalized autocorrelation curves (ACs) of wild-type cells incubated with 5 nM JE1319 of β_1-ARs (a) and β_2-ARs (b). Autocorrelation curves at the outer PM (yellow box fig. 4.26) and TTs (green box fig. 4.26) are displayed together in one plot separated by a white line. Each row represents the normalized AC of 1 cell; at TTs 1 row represents 6-7 averaged tubules; in total n=2 scans at the PM and n=8 at the TTs of 2 mice for β_1-ARs and n=6 scans at both compartments of 1 mouse for β_2-ARs. Charts below represent the corresponding ACs with error bars indicating SEM and fit according to eq. (3.7.18) (PM β_1-AR); grey lines indicate 0. Color scales represent the amplitude of the autocorrelation curves.

4.1.7.2 β_1/β_2-AR in wild-type cardiomyocytes labeled with 50 nM JE1319

Considering the results from section 4.1.7.1 and the lower endogenous expression level of the β-ARs, experiments with an increased concentration of 50 nM JE1319 (around K_d) and a 5-fold increased laser power at the TTs were performed. Images of the labeled receptors in wild-type CMs are shown in fig. 4.31a with labeled β_1-ARs and in fig. 4.31b with labeled β_2-ARs showing again no visible stain and therefore no difference to previously reported images of labeling with lower concentration of the ligand (fig. 4.26) or in β_1/β_2-AR-k.o. cells (figs. 4.21 and 4.24).

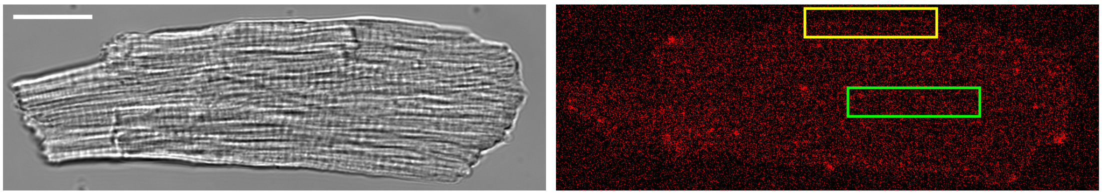

(a) β_1-AR

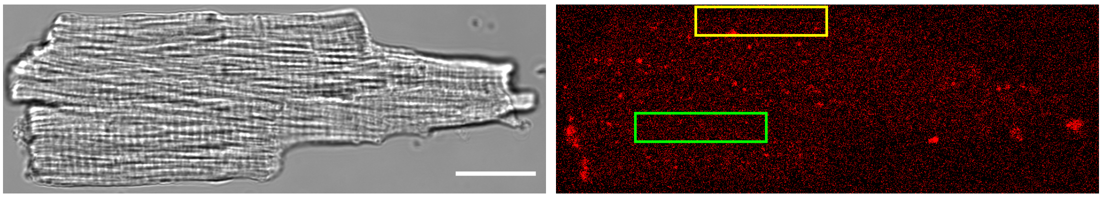

(b) β_2-AR

Figure 4.31: Images of β_1- (a) and β_2-ARs (b) in wild-type cardiomyocytes at the outer PM and TTs labeled with 50 nM JE1319. Brightfield (left) and confocal (right) image of a representative adult wt CM after pre-treatment with 50 nM ICI 118,551 (a) or 100 nM CGP 20712 (b) and labeling with 50 nM JE1319 (contrast of red channel set to 0). Boxes indicate ROIs of possible line scan areas (yellow at PM and green at TTs). Scale bars are 20 μm. Reprinted from Bathe-Peters et al. [58] & licensed under CC BY-NC-ND 4.0.

The same is observed by direct inspection of confocal images of parts of different CMs, imaged at the PM at low speed. Figures 4.32 and 4.33 display negligible signal. These images, organized in an image mosaic for each receptor, show hardly detectable differences between the two receptor subtypes.

On the other hand when performing and analyzing linescans at the outer PM (yellow box fig. 4.31a) ‘plume-like’ patterns in the STICS functions for the β_1-AR are recovered, indicative of diffusion (representative STICS function in fig. 4.34). These functions allow the extraction of an average MSD curve yielding a diffusion coefficient of 0.07 $\mu m^2/s$ as indicated in table 4.6.

However, no such diffusion profiles are observed at the outer PM when measuring the β_2-AR as indicated in fig. 4.35. The representative STICS function and the

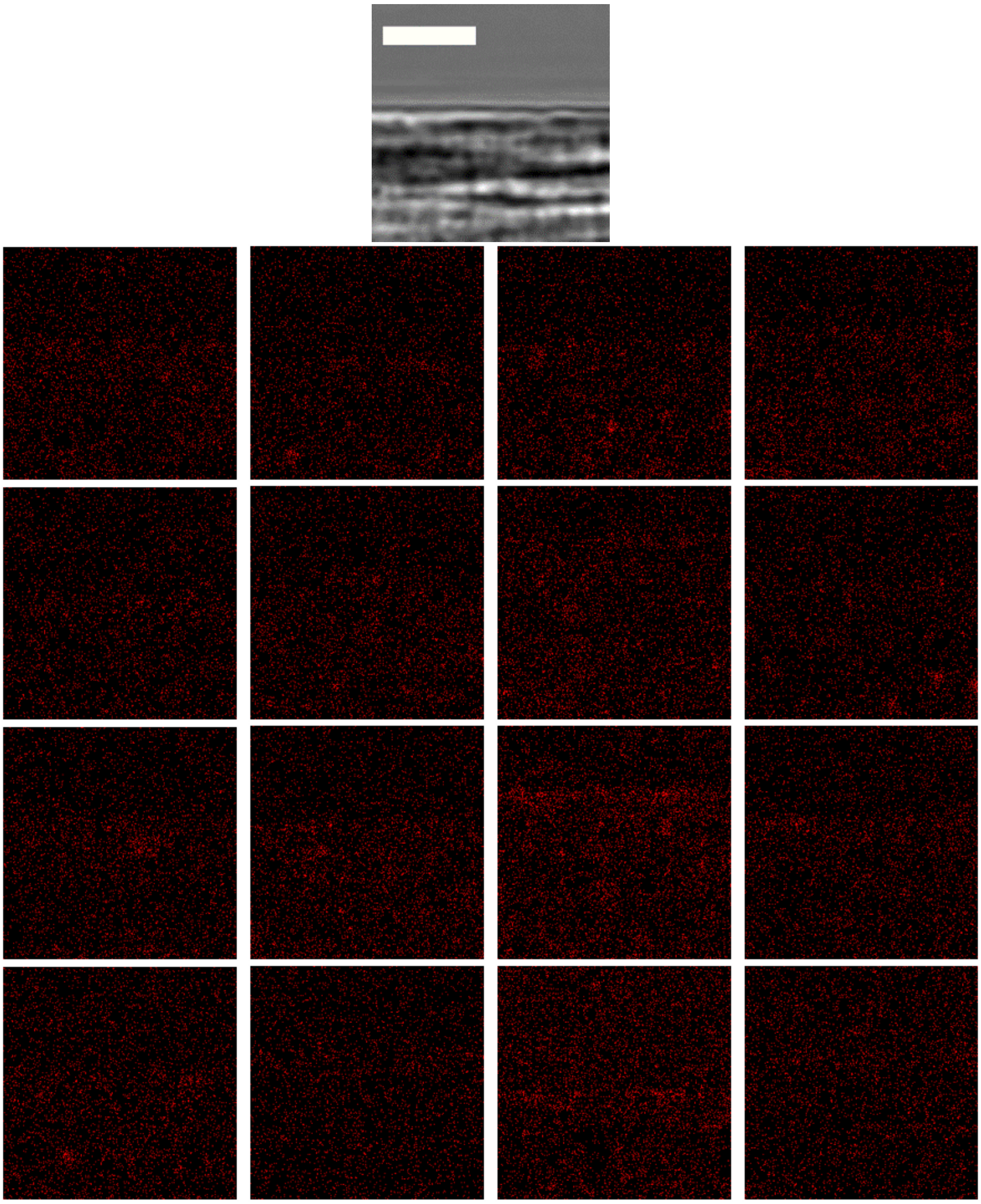

Figure 4.32: Representative fluorescence intensity mosaics of the outer PM of wild-type cardiomyocytes pre-incubated with 50 nM ICI 118,551 and labeled with 50 nM JE1319 staining the β_1-ARs. Each tile represents one cell and was imaged at slow speed (10 Hz) at the confocal microscope. Brightfield image on top highlights the outer plasma membrane and corresponds to the area shown. Scale bar is 5 μm. Contrast is set to 0, excitation wavelength: 633 nm and detection range: 650-750 nm. Reprinted from Bathe-Peters et al. [58] & licensed under CC BY-NC-ND 4.0.

MSD curve are similar to the data observed for the β_1/β_2-AR-k.o. cells and wt CMs when labeling with lower concentration of the ligand (fig. 4.22).

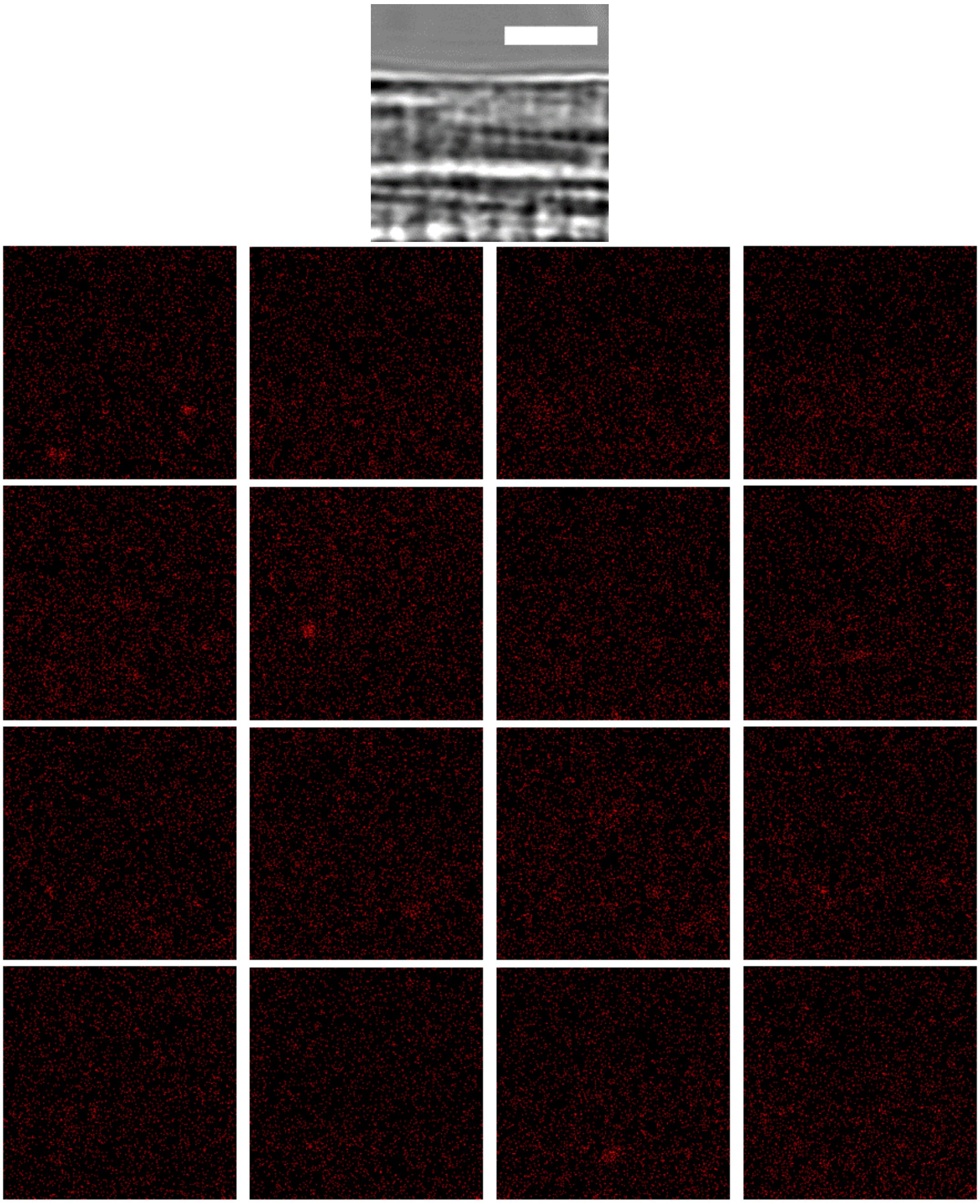

Figure 4.33: Representative fluorescence intensity mosaics of the outer PM of wild-type cardiomyocytes pre-incubated with 100 nM CGP 20712 and labeled with 50 nM JE1319 staining the β_2-ARs. Each tile represents one cell and was imaged at slow speed (10 Hz) at the confocal microscope. Brightfield image on top highlights the outer plasma membrane and corresponds to the area shown. Scale bar is 5 μm. Contrast is set to 0, excitation wavelength: 633 nm and detection range: 650-750 nm. Reprinted from Bathe-Peters et al. [58] & licensed under CC BY-NC-ND 4.0.

These results were confirmed by performing the pixel-by-pixels extraction of the autocorrelation curves in fig. 4.36 of the β_1-AR at the outer PM yielding a diffusion

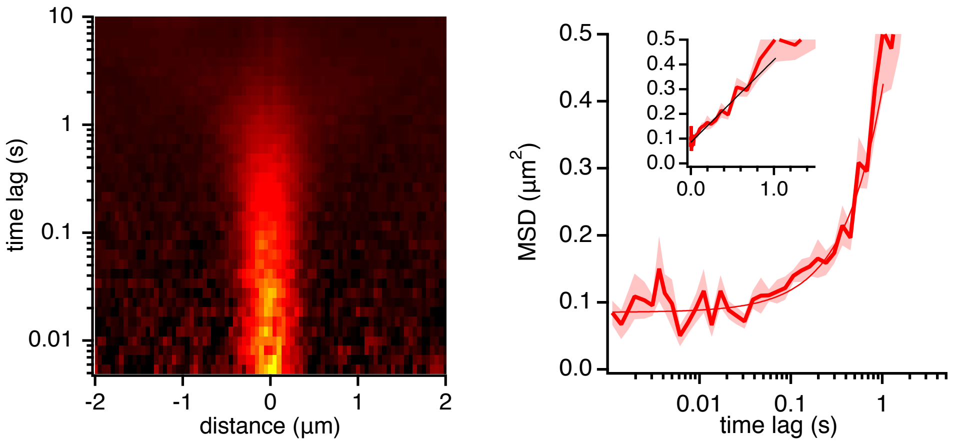

(a) STICS β_1-AR (b) MSD β_1-AR

Figure 4.34: (a) Representative STICS function showing 50 nM JE1319 labeled β_1-AR diffusion at the PM in wt CMs (yellow box fig. 4.31a) after pre-treatment with 50 nM ICI 118,551. (b) Average MSD curve from n=17 wt CMs (7 mice) with shadings representing SEM. Inset: MSD on linear scale. Reprinted from Bathe-Peters et al. [58] & licensed under CC BY-NC-ND 4.0. STICS and MSD analysis performed by Dr. Paolo Annibale.

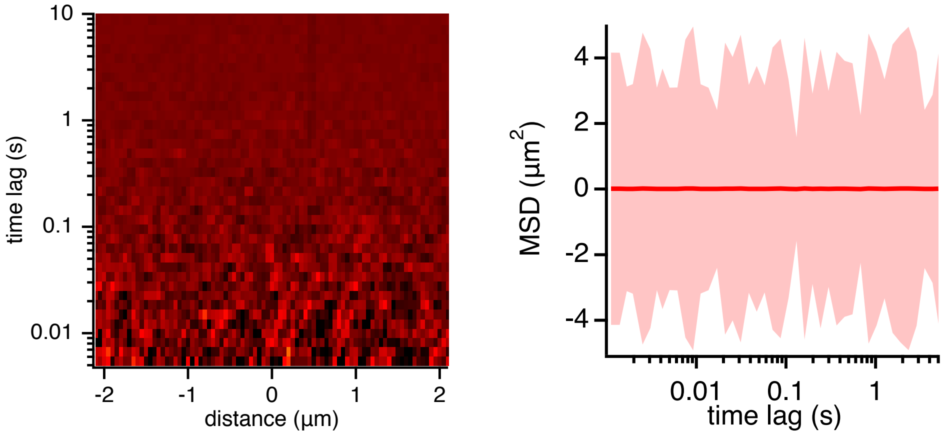

(a) STICS β_2-AR (b) MSD β_2-AR

Figure 4.35: (a) Representative STICS function with 50 nM JE1319 after pre-treatment with 100 nM CGP 20712 showing no diffusion of β_2-ARs at the PM in wt CMs (yellow box fig. 4.31b). (b) Average MSD curve from n=23 wt CMs (5 mice) with shadings representing SEM. Inset: MSD on linear scale. Reprinted from Bathe-Peters et al. [58] & licensed under CC BY-NC-ND 4.0. STICS and MSD analysis performed by Dr. Paolo Annibale.

coefficient in agreement with the one from the STICS analysis of D = 0.05 $^{\mu m^2}/_s$ as indicated in table 4.6 and in fig. 4.37 of the β_2-AR where no diffusion was detected.

Subsequently the single cell average correlation profiles at the TTs were calculated in fig. 4.36 highlighting the detection of β_1-ARs and extraction of correlation profiles for both the PM and the TTs. Together with fig. 4.34 these data unambiguously point to the presence of diffusing β_1-ARs at the PM and the TTs in wt CMs. The autocorrelation curves of the upper chart of fig. 4.36 indicate a characteristic diffusion time of the order of 0.4 s. The diffusion time recovered at the TTs is comparable, albeit on a faster timescale as indicated by tables 4.6 and 4.7.

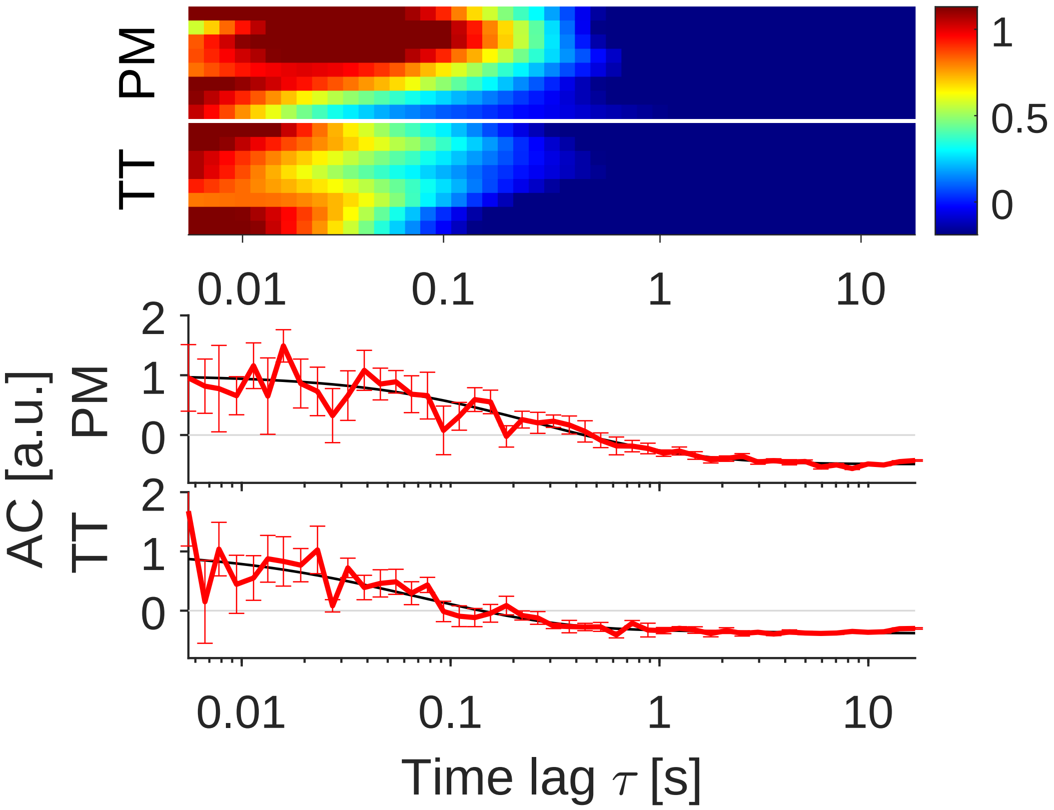

Figure 4.36: Diffusion of with 50 nM JE1319 labeled β_1-ARs in wild-type cardiomyocytes at the outer PM and TTs. Normalized autocorrelation curves (ACs) of β_1-ARs incubated with 50 nM JE1319 after pretreatment with 50 nM ICI 118,551. Autocorrelation curves at the outer PM (n=8 cells, yellow box fig. 4.31a) and TTs (n=8 cells, green box fig. 4.31a) of 6 mice are displayed together in one plot separated by a white line. Each row represents the normalized AC of 1 cell; at TTs 1 row represents 6-7 averaged tubules. Charts below represent the corresponding autocorrelation curves with error bars indicating SEM and fit according to eq. (3.7.18) (PM) and eq. (3.7.19) (TTs); grey lines indicate 0. Color scale represents the amplitude of the autocorrelation curves. Adapted from Bathe-Peters et al. [58] & licensed under CC BY-NC-ND 4.0.

Once again the β_2-AR did not display any diffusion fingerprint on the outer PM neither in the STICS functions nor in the MSD curves (fig. 4.35) nor in the single cell correlation functions (fig. 4.37) comparable to what was observed in the β_1/β_2-AR-k.o. cells. However, this is different in the TTs, where the β_2-AR is present with a diffusional fingerprint comparable to that of the β_1-AR at the TTs (tables 4.6 and 4.7 and fig. 4.37).

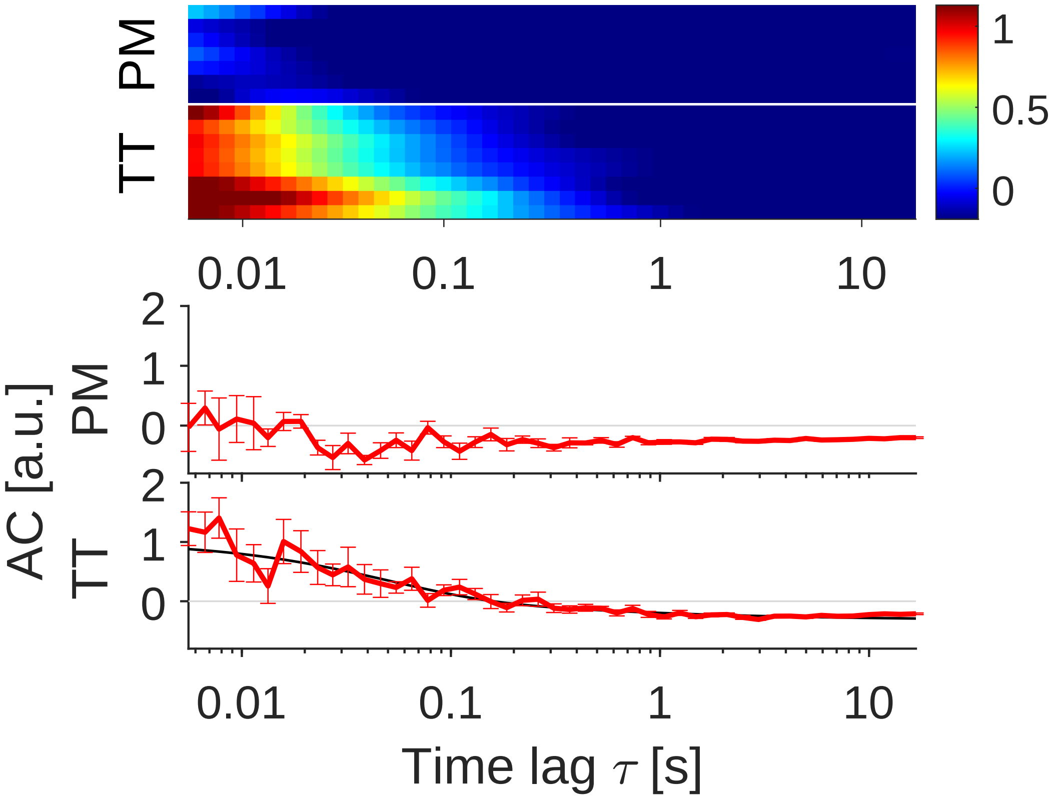

Figure 4.37: Diffusion of with 50 nM JE1319 labeled β_2-ARs in wild-type cardiomyocytes at the outer PM and TTs. Normalized autocorrelation curves of β_2-ARs incubated with 50 nM JE1319 after pre-treatment with 100 nM CGP 20712. Autocorrelation curves at the outer PM (n=7 cells, yellow box fig. 4.31b) and TTs (n=8 cells, green box fig. 4.31b) of 6 mice are displayed together in one plot separated by a white line. Each row represents the normalized AC of 1 cell; at TTs 1 row represents 6-7 averaged tubules. Charts below represent the corresponding autocorrelation curves with error bars indicating SEM and fit according to eq. (3.7.19) (TTs); grey lines indicate 0. Color scale represents the amplitude of the autocorrelation curves. Adapted from Bathe-Peters et al. [58] & licensed under CC BY-NC-ND 4.0.

These results are comparable to what was observed with 5 nM JE1319 at a lower signal to noise ratio at the outer PM. Increasing the signal to noise ratio made measurements at the T-tubular membrane possible.

As for 5 nM JE1319 (fig. 4.29) STICS function mosaics for 50 nM JE1319 in fig. 4.38 give a good overview of the ratio where the diffusion profiles were visible. They reflect the ratio of the amount of scans with diffusion and without as for the β_1-AR at the outer PM where diffusion was found in 19 out of 30 cells. Furthermore fig. 4.38 shows STICS functions of the T-tubular network of wild-type cardiomyocytes (figs. 4.38c and 4.38d).

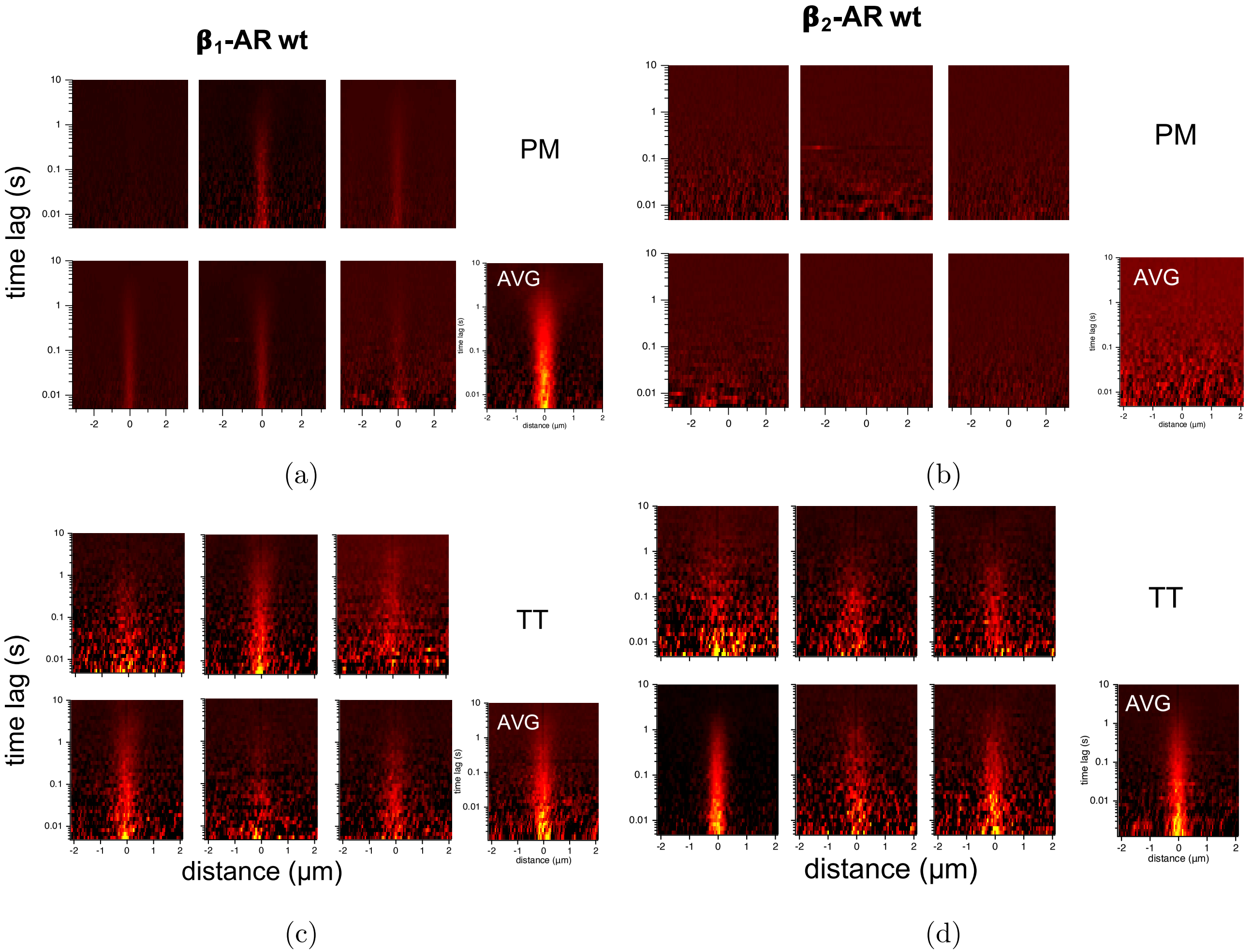

(a) (b) (c) (d)

Figure 4.38: Representative STICS functions of with 50 nM JE1319 labeled β_1- (a, c) and β_2-AR (b, d) in wild-type cardiomyocytes at the outer PM (a, b) and TTs (c, d). Each panel represents the STICS function of 1 cell except the average STICS function which is displayed on the sides. Labeling with JE1319 followed pre-treatment with either 50 nM ICI 118,551 (a, c) or 100 nM CGP 20712 (b, d). Reprinted from Bathe-Peters et al. [58] & licensed under CC BY-NC-ND 4.0. STICS analysis performed by Dr. Paolo Annibale.

To exclude that the results at the TTs are influenced by the increase in laser power, the pixel-by-pixel analysis was applied for scans at the PM with the same increase in laser power of 5-fold. The autocorrelation curves at the PM for the β_1- and β_2-ARs are displayed in fig. 4.39.

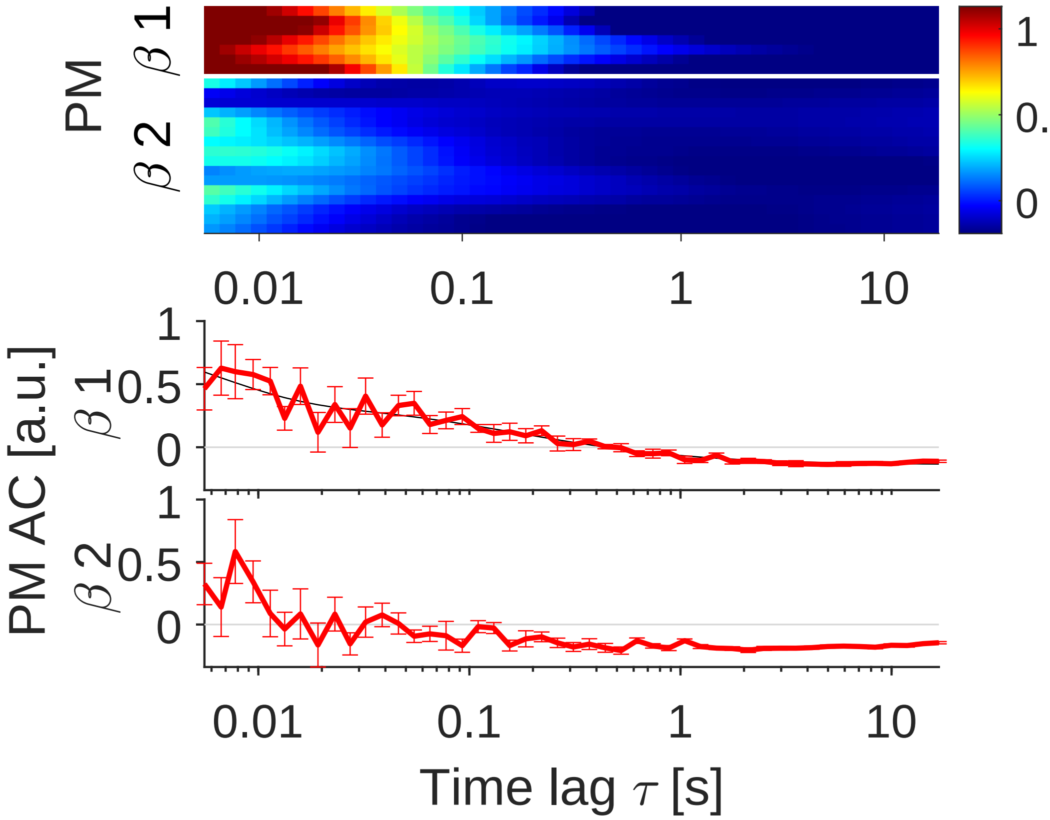

Figure 4.39: Diffusion of β_1- and β_2-ARs in wild-type cardiomyocytes at the outer PM labeled with 50 nM JE1319. Autocorrelation curves (ACs) are extracted at 5-fold increased laser power as for the TTs before. CMs are pre-incubated with either 50 nM ICI 118,551 to stain only the β_1-ARs or 100 nM CGP 20712 to label exclusively the β_2-ARs. Autocorrelation curves at the outer PM of β_1-ARs (n=7 cells, yellow box fig. 4.31a) and of β_2-ARs (n=16 cells, yellow box fig. 4.31b) of 3 and 4 mice respectively are displayed together in one plot separated by a white line. Each row represents the normalized autocorrelation curve of 1 cell. In case of the β_2-AR it is normalized to the average g(0) from the TTs. Charts below represent the corresponding ACs with error bars indicating SEM and fit according to eq. (3.7.18) (PM β_1-AR); grey lines indicate 0. Color scale represents the amplitude of the autocorrelation curves.

It is immediately visible from the top panel in fig. 4.39 that the β_1-AR diffuses at the PM. The calculated average diffusion constant, which is more affected by bleaching (as a consequence of the higher laser power), is of the order of D = 0.18 ± 0.03 μm^2/s ($\tau = 0.15 \pm 0.03$ s). The plot of the β_2-ARs confirms no detectable diffusing receptors at the PM although an influence of a 40-50 times faster component is visible in some scans at the increased laser power. This component could possibly stem from the fact that in some scans the signal of some receptors from the TTs is picked up, since at this higher laser power the amount of excitation light hitting the TTs is now increased. When moving away from the membrane to a region outside of the cell (here a wild-type cardiomyocyte with labeled β_2-ARs) no signal is picked up and no correlation profile can be extracted from the scan (fig. 4.40), ruling out the presence of ligand in solution causing this faster component. This possible influence of the TTs on the scan at the PM however has not been the case at lower laser power. This is one of the main reasons for choosing to acquire the scans at the PM with lower laser power.

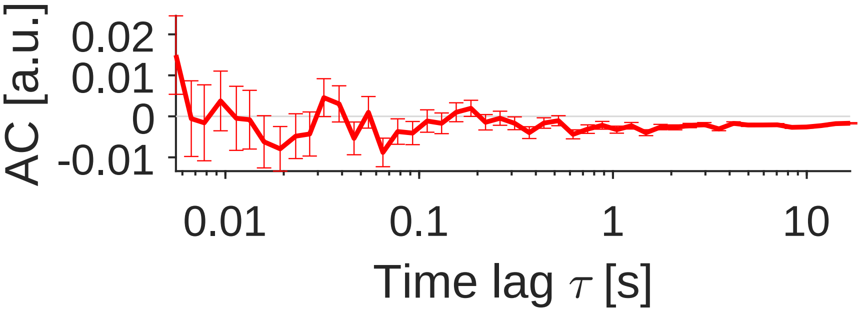

Figure 4.40: Diffusion evaluation of a scan which was acquired outside of a wild-type cardiomyocyte after labeling the β_2-ARs with 50 nM JE1319. Indicated is no diffusion when acquiring the scan outside of the cell. No diffusion profile is visible. Acquisition settings were the same as for the scans to investigate β_2-ARs in wt CMs at the PM. Laser power is also increased by 5-fold as for the scans at the TTs. A pre-incubation with 100 nM CGP 20712 was performed. Error bars indicate SEM; grey line indicates 0.

Correlation times are in agreement between the different analysis methods and are summarized in tables 4.6 and 4.7 and fig. 4.37. These data unambiguously indicate, other than in β-AR overexpressing CMs, a differential localization of the β_2-AR at the outer PM and the T-tubular network in wt CMs. The corresponding normalized residual plots are depicted in fig. A.1.

4.1.8 Summary of diffusion values of β_1/β_2-adrenergic receptors in adult cardiomyocytes

The beam waists which are used for the analysis are summarized in table 4.5. The beam waists were determined according to section 3.7. These waists were used to extract and calculate the reported diffusion values in table 4.6 from the above measurements.

receptor	Waist STICS PM (μm)
β_1-AR-TG	0.30 ± 0.01 (6)
β_2-AR-TG	0.34 ± 0.02 (6)
β_1-AR-wt	0.29 ± 0.01 (6)
β_2-AR-wt	0.33* ± 0.01

Table 4.5: Lateral beam waists extracted from the STICS analysis. Numbers of scans at different cells are indicated in parenthesis. Error represents SEM. * Beam waist is from the diameter of fluorescent microspheres.

Via eq. (3.7.8) diffusion constants D in table 4.6 can be converted into diffusion times τ_D in table 4.7 and vice versa. For both analysis methods (STICS and FCS) reported values are extracted from individual curves of one cell. Mean and standard error of the mean are then calculated from single values of multiple cells and are in very good agreement across methods as summarized in tables 4.6 and 4.7.

receptor	D FCS PM $\left(\frac{\mu m^2}{s}\right)$	D FCS TT $\left(\frac{\mu m^2}{s}\right)$	D STICS PM $\left(\frac{\mu m^2}{s}\right)$	D STICS TT $\left(\frac{\mu m^2}{s}\right)$
β_1-AR-TG	0.06 ± 0.01 (6)	0.08 ± 0.05 (6)	0.081 ± 0.007 (5)	-
β_2-AR-TG	0.062 ± 0.003 (6)	0.05 ± 0.01 (8)	0.14 ± 0.07 (5)	-
β_1-AR-wt	0.05 ± 0.02 (8)	0.2 ± 0.1 (7)*	0.07 ± 0.01 (17)	0.16 ± 0.03 (8)
β_2-AR-wt	-	0.3 ± 0.1 (7)*	-	0.23 ± 0.02 (8)

Table 4.6: Diffusion constants. Numbers of scans at different cells are indicated in parenthesis. Error represents SEM. *One scan was identified as an outlier by the Chauvenent's criterion and excluded from the mean.

receptor	τ_D FCS PM (s)	τ_D FCS TT (s)	τ_D STICS PM (s)	τ_D STICS TT (s)
β_1-AR-TG	0.36 ± 0.07 (6)	0.3 ± 0.2 (6)	0.29 ± 0.03 (5)	-
β_2-AR-TG	0.47 ± 0.02 (6)	0.6 ± 0.2 (8)	0.7 ± 0.4 (5)	-
β_1-AR-wt	0.4 ± 0.2 (8)	0.13 ± 0.08 (7)*	0.41 ± 0.06 (17)	0.13 ± 0.02 (8)
β_2-AR-wt	-	0.09 ± 0.03 (7)*	-	0.12 ± 0.01 (8)

Table 4.7: Diffusion time (τ_D) values. Numbers of scans at different cells are indicated in parenthesis. Error represents SEM. *One scan was identified as an outlier by the Chauvenent's criterion and excluded from the mean.

4.2 Combined widefield and confocal microscope

While section 4.1 shed light on the localization and dynamics of β-ARs in adult cardiomyocytes, this section is intended to give one perspective on techniques which would allow a closer investigation of processes and dynamics on special geometries such as T-tubules. As one of such techniques, a combined widefield and confocal system together with preliminary results of this setup are introduced. In this section, it is demonstrated how such a system can combine the advantage of FCS, to acquire temporal resolved data, with spatial awareness, obtained via TIRF microscopy.

In the light of the faster dynamics found at the TTs in the previous section in wild-type cardiomyocytes the combined widefield-confocal microscope holds promise to investigate via a confocal part spatially confined diffusion of prototypical GPCRs, such as the β-AR, on the surface of small tubular invaginations [13, 58, 156], by allowing to investigate the location of acquisition at the same time via the widefield part of the system.

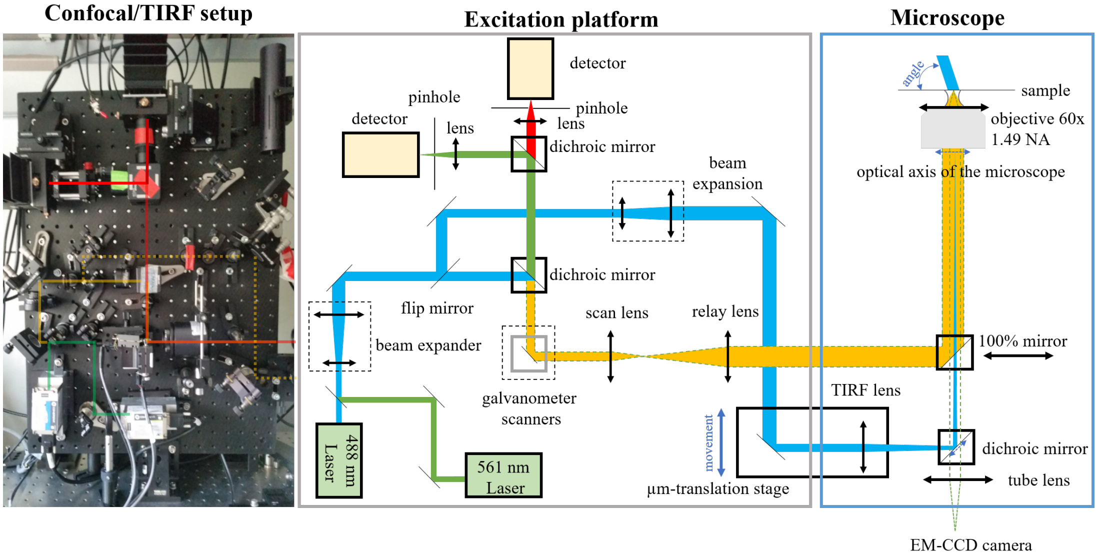

Figure 4.41: Schematic (right) of the widefield-confocal fluorescence excitation platform and microsope (here as TIRF-confocal setup). (left) Picture of microscope platform with indicated beam path. Adapted from Bathe-Peters et al. [156].

The combined platform was built as described in section 3.7.3 and according to fig. 4.41, which encompasses an image of the platform with the indicated beam path as well as a schematic drawing. A more detailed description including the components can be found in section 3.7.3. To demonstrate the capability of the combined system, TIRF images of HEK293TSA cells transfected with the neuropeptide Y receptor type 2 (Y_2R) C-terminally labeled with mCherry were acquired in fig. 4.42 (left). The confocal part was used to acquire FCS data from which the autocorrelation curve for the labeled receptor at the PM was acquired (fig. 4.42, right). The middle panel of fig. 4.42 shows the potential of the system: by inspection of the TIRF image the location of the acquired FCS trace becomes immediately visible as a bleached spot (region of FCS acquisition), indicated by the yellow cross, allowing not only for the extraction of highly resolved temporal data, but also to locate the acquired temporal data within the cell.

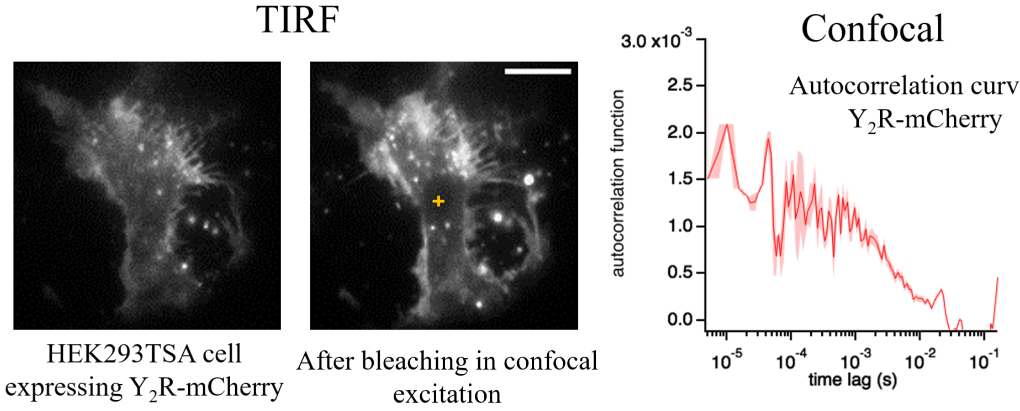

HEK293TSA cell expressing Y_2R-mCherry

After bleaching in confocal excitation

Figure 4.42: Acquisition of images and autocorrelation curves on the combined TIRF-confocal setup in HEK293TSA cells transfected with Y_2R-mCherry (left). (middle) Same cell with a bleached spot where the autocorrelation curve (right) at the membrane was acquired with the confocal part of the setup (marked by a cross). Scale bar is 10 μm.

The usage of the galvanometer scanners allows to extend the measurements to apply scanning FCS, thereby holding the potential of scanning in exact shapes.

4.3 Autofocus based on an electrically tunable lens and a totally internally reflected IR laser

One of the critical challenges in optical microscopy, particularly on such a custom built setup as in section 4.2, is the maintenance of the focal position of the optical system over time. The focus is prone to drifts as a consequence of mechanical and thermal fluctuations as well as thermal instability of the microscope body.

We therefore developed an adaptive focus control system based on an electrically tunable lens (ETL) combined with a totally internally reflected IR laser. The novel application combines, for the first time, a true closed-loop autofocus system with a tunable lens. By using a totally internally reflected IR laser and its reflection on a quadrant photodiode (QPD), displacement in the objective to sample distance is indicated with high sensitivity. Correction of the focal position is achieved via a displacement dependent moving set-point. This way, a cost effective all-optical autofocus solution is setup in which the ETL, coupled to the microscope objective, readjusts the focal position rapidly.

Materials are described in section 3.7.4. The optical setup, within a standard inverted fluorescence microscope, is represented in fig. 4.43(a) and as part of the combined system in fig. 4.41.

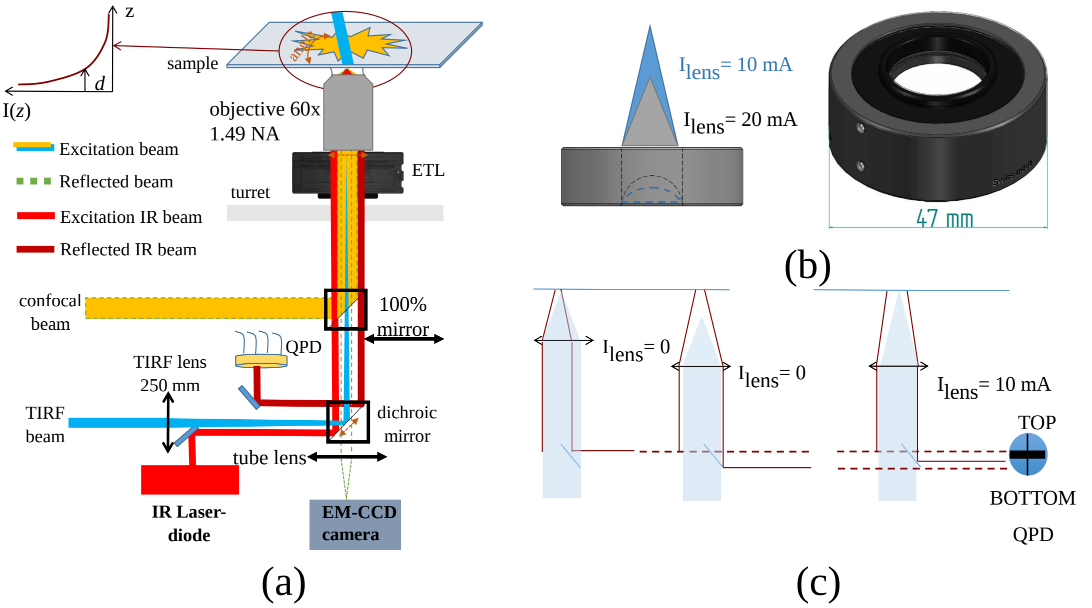

Figure 4.43: (a) Experimental setup embedded into the combined widefield-confocal setup. Working principle of the autofocus: an IR laser diode emits its beam (red) into the microscope which then gets reflected by mirrors passing through an ETL and the objective to get totally internally reflected (dark red). The reflected beam is then guided by mirrors onto a QPD. The conventional laser excitation of the inverted microscope, here dependent on the application either confocal (yellow) or TIRF (blue) microscopy, is reflected onto the sample and the fluorescence (green dashed), in case of confocal microscopy, is taking a similar path as the incident light (fig. 4.41) or is being transmitted onto the detector (TIRF). (b) Left: ETL with different curvatures and focal points dependent on the current. Right: ETL with its physical dimensions. (c) Illustration of the application of different currents on the reflected IR beam and the focal position. Hereby is the combination of the objective-ETL illustrated as a thin lens. The reflected IR laser beam (dark red lines) hits the QPD after exiting the lens in distinct positions dependent on the relative physical objective to sample distance (left and middle illustration) and the current applied to the ETL (right illustration). The focal position also changes upon the application of a current (here shaded blue illustrates a collimated excitaiton beam). Adapted with permission from Bathe-Peters et al. [135] © Optica Publishing Group.

The autofocus system couples the ETL to the microscope objective. As depicted in fig. 4.43a the IR (red) laser beam, coming from its source, is reflected by a 0.5 inch mirror, enters through the side of the lower deck of the Olympus IX73 microscope (confocal part through the upper deck), and passes the 1 inch aperture of the filter cube to hit the dichroic mirror (Chroma ET 488/561) which is aligned to the optical axis of the microscope. Reflected by the dichroic it enters the combined ETL and microscope objective block on the back focal plane in such a position that the IR laser is totally internally reflected at the coverslip-sample interface. The reflected IR beam (dark red) hits the other side of the aperture of the dichroic filter cube and is steered onto the QPD. The entire setup including the optics of the IR beam path are installed in such way to affect minimally the excitation path and to not affect the emission pathway at all.

The dimensions of the ETL together with two different focal positions, corresponding to distinct currents, are depicted in fig. 4.43(b). The working principle of the tunable lens is indicated in fig. 4.43(c). Two distinct effects can influence the position of the reflected beam. First, the reflected beam is influenced by the objective to sample distance, second, it is sensitive to the deformation of the tunable lens due to the application of a current. Either method changes the position of the reflected beam on the QPD and therefore the voltage output of the electric circuit attached to it. A QPD set-point indicates when the sample is in focus for a given current applied to the ETL.

The block diagram in fig. 4.44 illustrates the simplified work flow of the autofocus. It starts with the IR laser beam hitting the QPD in a position which corresponds to the sample being in focus. The QPD delivers two voltage signals to the DAQ card which reads out the position specific signal. This signal enters a feedback loop in which the proportional-integral-derivative (PID) controller continuously calculates the error signal as the difference between a desired set-point value (which is moved by the system with the axial displacement) and the measured position value. In case of deviations it applies corrective values based on proportional, integral and derivative values and converts the differential signal, in dependence of the position voltage, into an input current to the tunable lens which therefore becomes autotunable. With this it changes the curvature of the lens until the reflected IR beam reaches the desired position on the photodiode. The conversion and the recognition of the desired positions of the reflected beam are part of the calibration process explained in section 4.3.1 and fig. 4.45. The input of the current is achieved via a serial port of the lens. A manual adjustment of the lens curvature via an input current is possible by selecting the ‘Manual Adjustment’ in the mode section of the program as indicated in the frontpanel in fig. C.3. The code in LabView is visible as a block diagram in fig. C.4.

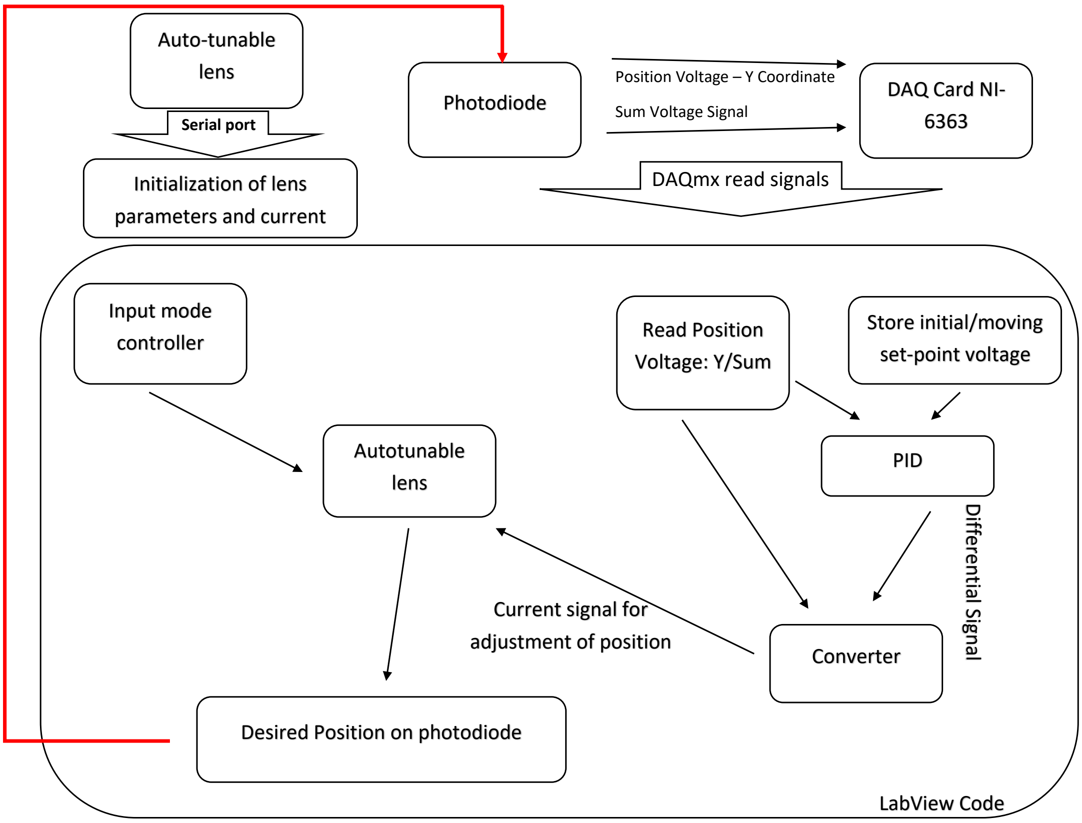

Figure 4.44: Block diagram of the autofocus depicting the most important components and their dependence to establish a stable focus.

4.3.1 Calibration of the autofocus

The QPD voltage changes as a consequence of two factors. First, the voltage is responsive to physical displacements of the objective to sample distance, and second to inputs of the ETL current. For this reason, calibration curves which convert both the physical axial position, as objective to sample distance, and the focal change of the ETL, as a change in current (physical deformation of the lens), into a QPD voltage, for the proper operation of the autofocus system to regulate the difference between a set-point value and the measured QPD voltage, are required. The calibration curves are based on measurements with 100 nm diameter fluorescent microspheres (Tetraspeck, Thermofisher Scientific). The effect of the two influential factors on the QPD voltage is illustrated in fig. 4.45a (QPD vs. displacement) and fig. 4.45(b) (QPD vs. current). Figure 4.45(a) illustrates how the QPD voltage changes with axial displacements at different lens current values. The inset illustrates which lens input current corresponds to which axial displacement. Figure 4.45(b) relates the QPD voltage to the ETL input current. Shown is a family of curves in dependence on the physical axial z-displacement with recorded steps of 50-100 nm.

The implementation requires specifically that the set-point prediction also accounts for the changes in QPD voltage as a consequence to a new current upon application to the lens as the focus and therefore the axial position drifts. Figure 4.45(c) illustrates the set-point dependence on the QPD voltage, the ETL input current and the axial position change. Within a specific current range (in this example 15-24 mA) the curve exhibits a quasi-linear dependence. This allows to adjust the set-point value for the QPD as a function of physical displacement of the objective to sample distance as well as ETL input current.

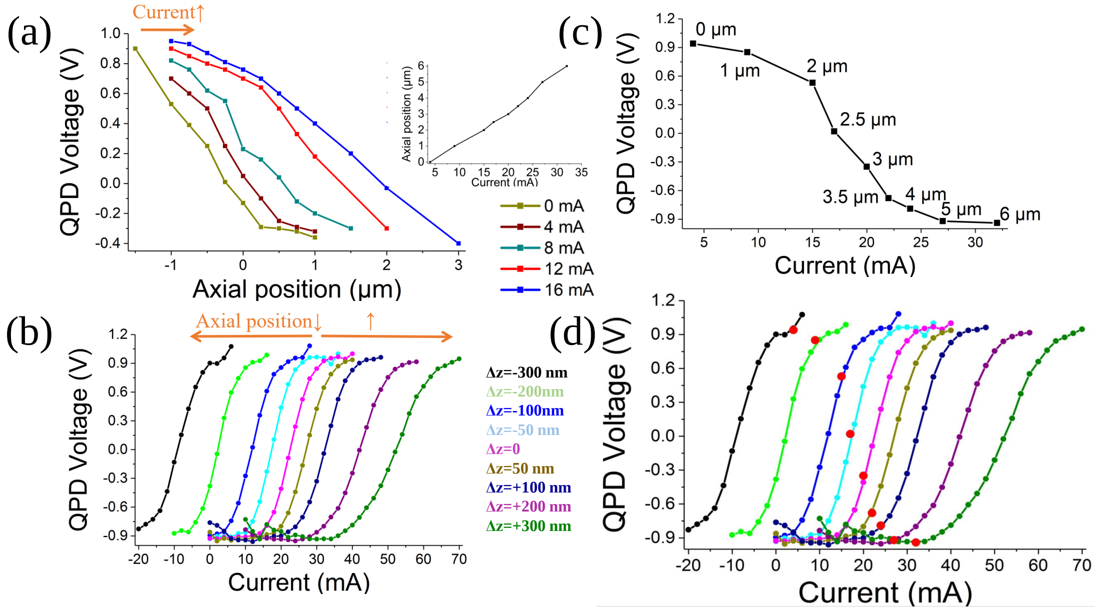

Figure 4.45: Calibration curves of the autofocus. (a) QPD voltage dependence by variation of axial positions at constant lens input currents (colored curves). Inset: Axial position in dependence of ETL current. (b) QPD voltage in dependence of the ETL current. Each curve represents the dependence for a constant axial position. The orange arrows indicate how the curves in the family shift to the right for increasing objective to sample separation and move to the left upon reduction of this separation. (c) Represents the in-focus positions at each axial position in the QPD voltage vs. ETL current plot. (d) Combines the in-focus positions (red dots) of (c), for which the autofocus corrects, with the QPD voltage vs. ETL current plot from (b). Reprinted with permission from Bathe-Peters et al. [135] © Optica Publishing Group.

Figure 4.45(d) combines the family of curves indicating the behavior of the QPD voltage in dependence on the lens input current for different axial positions with the set-point values as red markers. The results together indicate that QPD values for physical displacements of less than 750-1000 nm shift linearly and can bring the sample back into focus by applying an input current. This behavior opens up the possibility to set up a feedback loop with set-point ramping in which a set-point (which is a QPD target voltage associated to focus) changes linearly, within a certain range, as a function of the applied current.

Focal positions were determined by bringing individual beads into focus for different displacements and current values. PID parameters are set appropriately in the software to provoke a response of desire of the feedback loop. Hereby, the slope of the linear portion of the in-focus curve (V/mA) is used to determine the QPD set-point as a function of the applied current and depending on the axial position.

Two schematics of the calibration procedure are found in appendix B figs. B.1 and B.2.

4.3.2 Working principle of the autofocus

A flow chart describing the feedback stabilization process is presented in appendix B fig. B.3.

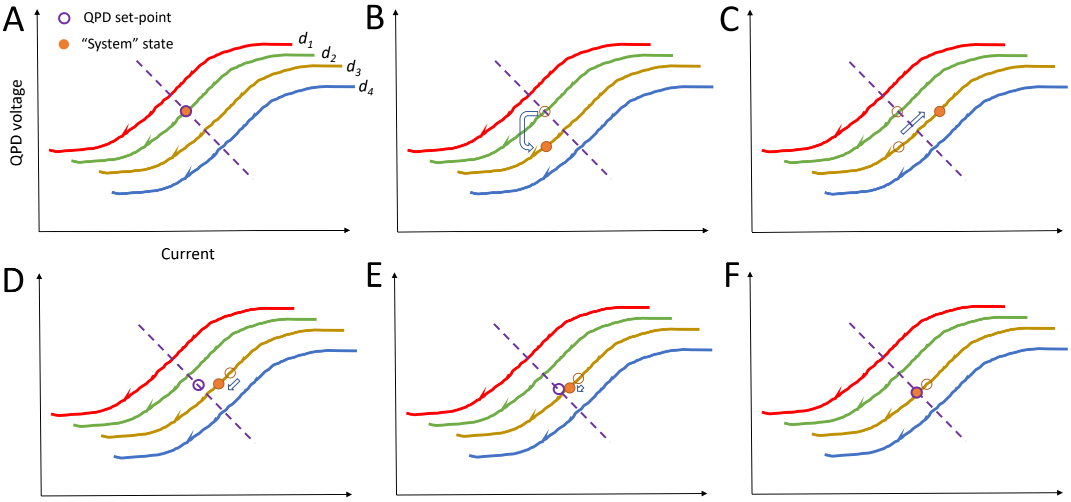

Figure 4.46: The working principle of the autofocus. Shown is a family of QPD voltage vs. current curves marked with their axial distances d_1 to d_4. Panels show how the state of the system (QPD voltage, current) changes in response to an axial displacement from the in-focus position d_2 (Panel A) to an out-of-focus position at d_3 (Panel B). (C) Illustrates how the current is varied in order to match the original set-point QPD voltage. Panel (D) shows the adaptive change of the set-point along the in-focus curve (dashed) while the system state moves along the curve d_3 to reach the new set-point. The process is iterated (E) until the sample reaches the new in-focus condition where the set-point and the system state overlap (F). Reprinted with permission from Bathe-Peters et al. [135] © Optica Publishing Group.

The principle of operation of the autofocus system and how the stabilization works in detail is described in fig. 4.46. The process starts with initialization of the autofocusing when the QPD set-point voltage and the current system state (meaning the QPD set-point voltage is the same as the measured QPD voltage and therefore no change in input current is applied) are in agreement at the in-focus point (fig. 4.46, panel A). Next, a physical displacement or a drift of the system state happened and the system lost its focus (panel B). At this point the QPD set-point voltage remained the same. By increasing the ETL current the system state shifts back to the voltage value of the set-point (panel C). But because a physical displacement of the objective to sample distance happened the sample at this point is still not in focus. The new in-focus point is represented by the intersection of the dashed purple line and the new system displacement curve (gold). Therefore the set-point moves along the in-focus curve (dashed purple line). At the same time the current reduces, as it tries to match the new QPD set-point. This process continues and is iterative as depicted in panels D and E. The process stops when the new QPD set-point and the new system state match at the in-focus position at the intersection of the dashed purple line and the golden curve (panel F). The speed of this process and the numbers of iterations as well as the overshoot of the system when trying to match the two points can be controlled with the PID input parameters. Additionally, by adjusting the moving average controlling the current applied to the ETL, a slow rate of ramping of the set-point relative to the current changes can be achieved.

4.3.3 The autofocus in experiments

After setting up the autofocus the first measurements to demonstrate the performance, after storage of the calibration information, were to measure immobilized fluorescent beads on the glass coverslip. To this end the first measurement in fig. 4.47(a) shows traces of the applied current to the lens (left axis) which allows the QPD voltage to follow the QPD set-point voltage (right axis) with enabled feedback. Figure 4.47(b) shows a time series of 25 min of one fluorescent bead with enabled autofocus. At the top, images of the bead are shown. In the images it is visible that the bead remains in focus over the entire time. The lower part of the fig. 4.47(b) shows time traces of the QPD voltage and the ETL current and how the current is adjusted by the feedback as a result of the focal drift over time. The QPD trace on the other hand is affected again by a combination of the focal drift and the current adjustments. While the autofocus is able to maintain focus when enabled in panel (b), panel (c) shows a fluorescent bead imaged over a time series of 30 min with disabled feedback. The constant input current to the lens is a clear indicator of the disabled feedback, while the QPD voltage drifts as a result of the mechanical defocus alone. The images of the bead in fig. 4.47(c) show also a clear loss of focus over the imaged 30 min. This is illustrated in figs. 4.47(d) and 4.47(e) which show the line profiles across the beads (as indicated by the line through the beads) on top of the images in figs. 4.47(b) and 4.47(c) with enabled and disabled feedback respectively. Hereby is the focus quantitatively estimated by the standard deviation of a fitted Gaussian curve (as the best approximation to the microscope PSF). Compared were the width at time 0 and after 25 min in case of enabled feedback and after 30 min in case of disabled feedback. The deviations at the end of the time series were 30% of the starting width of the bead in case of a disabled feedback and 3% in case of an enabled feedback, thus confirming the ability of the autofocus to maintain focus.

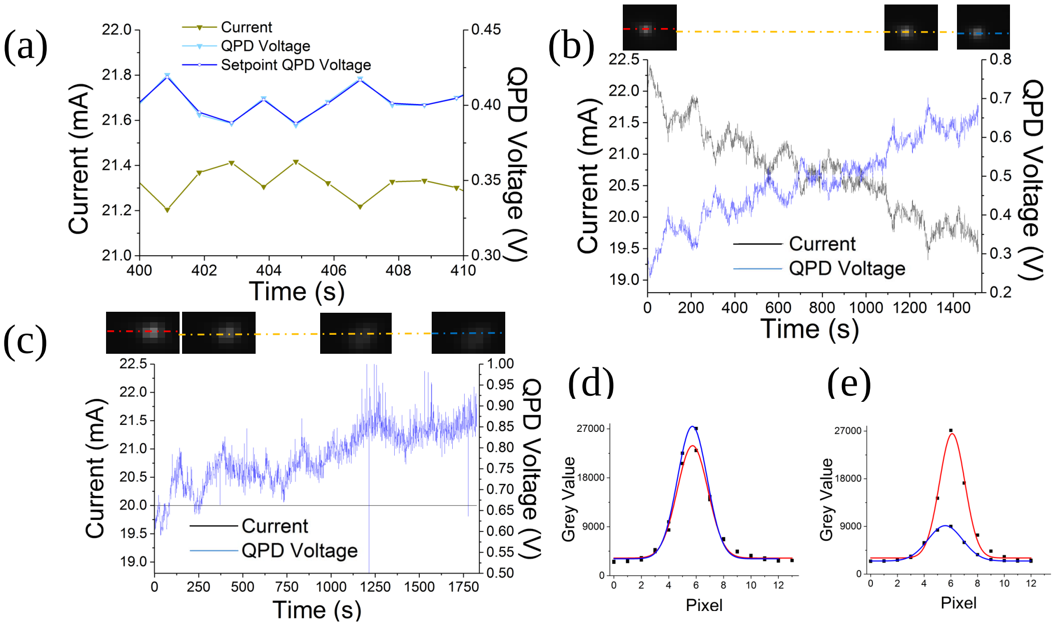

Figure 4.47: The autofocus working in standard procedure. (a) Magnified time course of the lens input current and QPD voltage following the QPD set-point voltage. (b) Time traces of the QPD voltage and the lens input current with enabled autofocus when keeping a fluorescent bead in focus (top). Color code of line corresponds to profiles in d. (c) Same as in b without autofocus by holding the lens input current constant. As a consequence the QPD voltage changes as a result of the focal drift which is also observed at the loss of focus over time in the images of the beads (top). Lines indicate bead profile in e with the same color code. (d) Measured bead profiles in b and (e) in c, taken at the beginning and end of the imaging series. Reprinted with permission from Bathe-Peters et al. [135] © Optica Publishing Group.

Probably due to a minor mechanical misalignment between the ETL and the microscope objective the autofocus system displayed a small degree of intrinsic astigmatism. This astigmatism of the bead images over time is used to quantify the defocus additionally since astigmatism is a well known indicator of axial displacement [157]. Therefore quantification of astigmatism was done by the cross-correlation coefficient of a two-dimensional Gaussian fit. The calibration of cross-correlation vs. defocus displayed a linear behavior within a ± 1 μm excursion from the focal position. The coefficient was -0.34 cross-correlation/μm. According to this calibration, bead samples with enabled autofocus displayed axial fluctuations below 10 nm, as opposed to defocus values in excess of 50 nm with disabled autofocus for an observation time of 25-30 min.

Next the ability of the system to regain focus in response to a sudden perturbation was tested. This characterization of the performance of the all-optical autofocus was achieved by changing manually the distance between the objective and sample rapidly. In other words what was illustrated in fig. 4.46 is performed in fig. 4.48 in practice with different parameters and on different time scales. Therefore the images and figures in fig. 4.48(a)-(c) show the response of the autofocus system when imaging fluorescent beads depending on different PID constants upon a displacement of the objective of the order of 400-500 nm. In this regards fig. 4.48(a) illustrates the response to such a displacement by only using a proportional term of the PID and a moving average of the current to ramp towards the set-point. Although the response shows that the current and the QPD voltage converge towards a new in-focus point, as depicted by the images on top of panel (a), the process happens with a long time constant because of the averaging of the current. When this moving average of the set-point is significantly reduced and an integral term of the PID is applied in addition to the proportional term the response to the step is more rapid as shown in fig. 4.48(b), but starts to include characteristic oscillations upon convergence of the QPD voltage in the new in-focus value. However, the focus of the fluorescent bead is recovered as shown in the upper images of panel (b). Upon optimization of the PID parameters the system response improves in speed and stability as visible in fig. 4.48(c) as the focus recovers rapidly (< 1 s) without sizable oscillations in response to a 500 nm jump as also visible in the fluorescent beads on top. In this case the full spectrum of PID parameters is applied by setting the proportional constant to 0.25, the integral constant to 0.2 and the differential constant to 0.01. As the images on top of the panels show the performance of the system on images of fluorescent beads before, during and after the rapid displacement (jump) a certain degree of astigmatism of the lens during the jump is visible in fig. 4.48(b).

After having determined the optimal parameters of the autofocus system for maintaining the focus, the performance was tested on HEKAD cells labeled with a mitochondrial dye. Figure 4.49 shows images of the labeled cell at the beginning and end of a time series of 30 min with enabled autofocus in the left and middle image of panel (a) respectively. An image acquired at the end of further 30 min with disabled autofocus is presented in the rightmost image of panel (a). Figure 4.49 panel (b) shows the time traces of the ETL current and the QPD

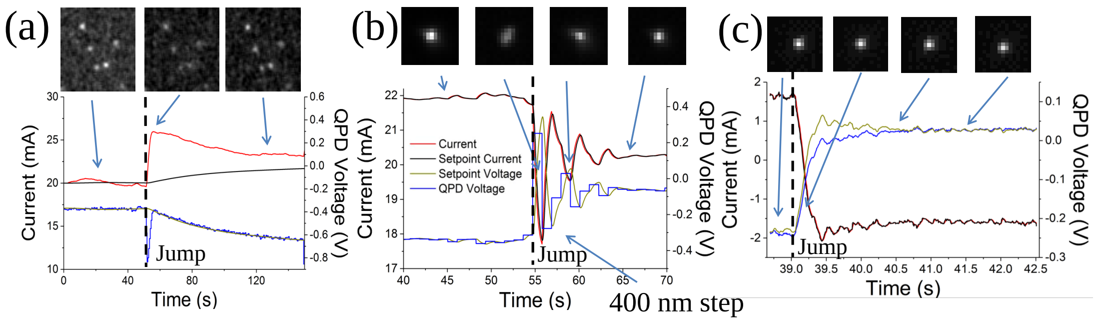

Figure 4.48: The autofocus working in extreme situations such as sudden jumps and steps and with different PID-paramters. (a)-(c) Show time traces of QPD voltages and lens input currents as well as images of fluorescent beads (top) with rapid axial displacements of about 400-500 nm from the focus point and the recovery of the autofocus to the new focus points. (a) A low proportional value and moving average of the current allow for a slow recovery after the displacement. (b) By just keeping the proportional term, adding an integral term and removing the moving average of the current graphs recover faster after the displacement. (c) Fastest recovery of focus after displacement by using optimized PID-paramters (here: proportional constant of 0.25, integral constant 0.2 and differential constant 0.01). Reprinted with permission from Bathe-Peters et al. [135] © Optica Publishing Group.

voltage while holding the focus during the 30 min time period with enabled autofocus, thus confirming the viability of the current setup for live-cell imaging in applications. As a more quantitative assessment of the degree of sample defocus an edge detection of a region of interest (yellow box) was performed encoding the amplitude of the gradient image as directly proportional to the steepness of the edges.

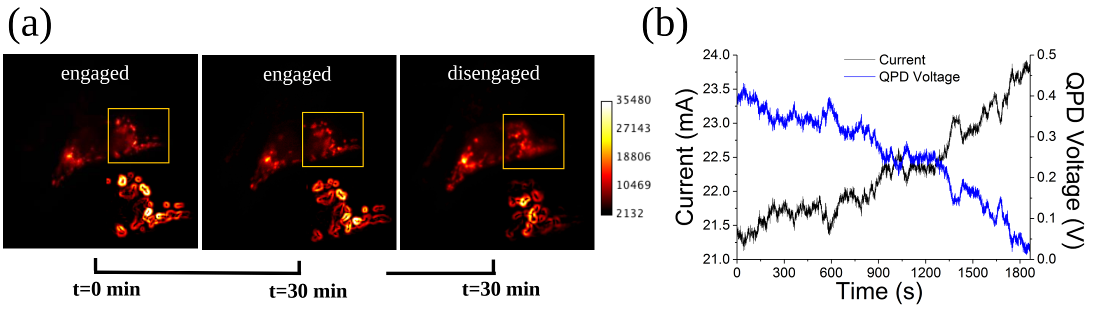

Figure 4.49: The autofocus holds focus in cells. (a) HEK293AD cell with labeled mitochondria imaged for over 30 min with enabled autofocus (left and middle) and for another 30 min with disabled autofocus (right). The insets show edge detection in a sub-region of the cell emphasizing the defocussing with disabled and focussing with enabled autofocus. (b) Time traces of the QPD voltage and the lens input current as the cell is held in focus. Reprinted with permission from Bathe-Peters et al. [135] © Optica Publishing Group.

5 Discussion

The elucidation of the localization and dynamics of the β_1- and β_2-AR in adult cardiomyocytes can be divided into two parts and the respective results are discussed in the following sections.

5.1 β_1 and β_2-adrenergic receptors localization and dynamics in adult cardiomyocytes

This thesis has addressed the question of the localization and dynamics of endogenous β_1- and β_2-ARs in adult cardiomyocytes. The key question of how these two receptors achieve signaling specificity when triggering the same biochemical pathways, such as coupling to stimulatory G$_s$ proteins, mediating increases in cAMP, and stimulation of cardiac contractility, had been around for decades. Moreover, the question of receptor localization had been re-stimulated by the discovery of the spatially compartmentalized activity of these receptors based on the observation of localized β_2-AR-induced cAMP response at the TTs of cardiomyocytes [13]. To date the visualization of endogenously expressed β-ARs in wild-type cardiomyocytes had not been achieved. So far investigations of the distribution of β-ARs in adult cardiomyocytes involved methods of modification of the endogenous system, i.e. viral transduction with receptor genes coding for an antibody tag [158]. Here, a fluorescent ligand specifically synthesized with high affinity for both the β_1- and β_2-AR and negligible non-specific binding has been applied to target endogenous receptors in living cells. Furthermore, a confocal-based FCS method has been adapted to extract spatial-temporal correlations from repeated line scans. Together this allowed the determination of the locations and dynamics of the labeled receptors, even at the very low endogenous expression levels.

Three major biological observations can be drawn from these results. The first is that when imaging in wild-type cardiomyocytes, at endogenous expression levels, the localization of the two receptors is different. The β_1-ARs can be localized and display a dynamic fingerprint in both compartments, the PM and the TTs. A different localization of the endogenous β_2-ARs is detected which localized confined to the T-tubular network exclusively.

The second key observation is that, different from endogenous expression, in overexpression systems the β_1-ARs and β_2-ARs are homogeneously distributed across the outer PM and the T-tubular system of adult CMs. Both receptors are expressed at almost identical amounts (section 4.1.2.6) in the two compartments, namely the PM and the TTs, in the respective overexpression. Additionally, the diffusion rates of the two receptors are comparable in both compartments and agree with the expected diffusion rates commonly found for seven-transmembrane receptors in literature of ~0.1 $\mu m^2/s$ [15].

The third key observation is the observation of a heterogeneous expression of the endogenous β_1-AR in adult cardiomyocytes. While the β_1-AR displays to a certain degree cell to cell variability in the expression (with only ~60% of the imaged cells showing a dynamic fingerprint for the receptor at the outer PM), none of the cells with selectively labeled β_2-ARs displayed any trace of diffusion for the receptor on the outer PM.

The first key finding has been modeled in image 5.1 illustrating the localization and the diffusion times of β_1- and β_2-ARs in wild-type cardiomyocytes.

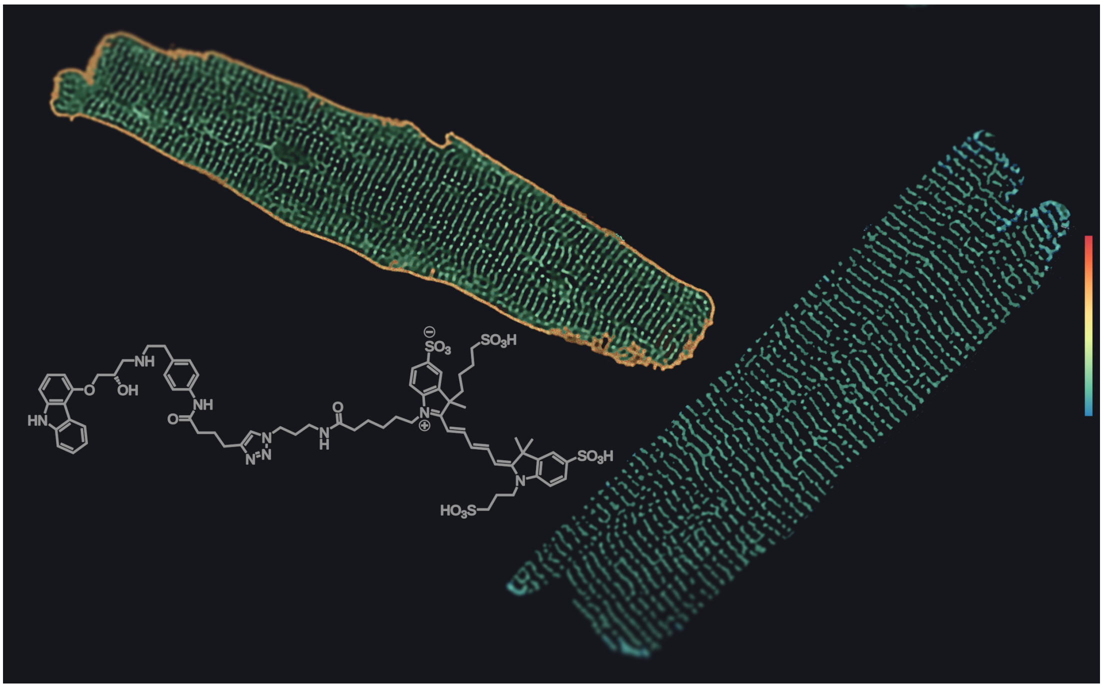

Figure 5.1: Illustrative model of diffusion times of the β_1- and β_2-ARs in ventricular cardiomyocytes of wild-type mice constructed from confocal images. Left cell illustrates the diffusion times of the β_1-ARs at the surface of the plasma membrane (orange) and in the T-tubules (green). Right cell marks the β_2-ARs (green) only at the T-tubules and not at the plasma membrane (therefore not visible in image). The color bar represents diffusion times ranging from short (blue) to long (red) times. The schematic of the novel fluorescent ligand used for this investigation is shown in grey. Image: Dr. Horst-Holger Boltz & Marc Bathe-Peters

The most interesting questions arising from the observation of the differential localization of the two receptors involves the topic of the molecular mechanisms leading to the different segregation of the β_2-AR from the β_1-AR. One explanation for this behavior could be based on the specific C-terminal interactions of the β_2-AR with cytoskeletal scaffolds [159], which were described and shown to localize GPCRs along cytoskeletal stress fibers and the cortical actin network [160–163]. Responsible for these interactions are proteins involved in the regulation of endocytic sorting and membrane localization such as the N-ethylmaleimide-sensitive factor (NSF) and the Na^+/H^+ exchange regulatory factor (NHERF), more specific NHERF1. Both effectors interact with the C-terminus of the β_2-AR. More closely NHERF1 has been shown to anchor β_2-ARs C-terminally via the PDZ motif to the cytoskeleton, thereby confining receptor mobility and receptor coupling to G_i [161, 164, 165]. Studies involving modifications of the PDZ binding domain or the NSF or a knock-out of either the PDZ motif or NHERF1 leading to altered or disrupted interaction with the cytoskeletal scaffolds are promising candidates to investigate the cause of this differential localization. Further, a domain swap of the PDZ domains of the β_1- and β_2-AR could give a valuable insight into the responsible mechanisms behind their distribution. Another reason, which does not exclude the first, might be associated with the dynamic partitioning of the receptors in the region of higher curvature, as recent observations state the dynamic sorting of GPCRs in response to varying membrane curvature. In fact membrane curvature alone has been observed to be sufficient for GPCR sorting. In particular, upon ligand binding and therefore changes in the conformation of the receptor the β_2-AR has been shown to prefer membranes with higher curvature in comparison to the β_1-AR which preferentially resides in 'flatter' regions [166]. This observation could have striking relevance in adult cardiac myocytes as they posses a regular network of T-tubules. This network of tubules spans across the entire cell and represents, with an average tubule diameter of 169 nm, curved regions which could drive β-AR partitioning. On the other hand this could theoretically allow the hypothesis of a mechanism that permits the partitioning of the β_2-AR into these compartments only upon binding of a ligand either by curvature sorting alone or/and where it finds cytoskeletal interaction partners, where it then starts to signal once the compartments are reached. In such a model would the ligand also act as a driving force for the localization itself. Studies which monitor the binding process and initial movement of the β-ARs in adult cardiomyocytes could deliver a more detailed insight on the mechanisms of sorting. At the same time could the creation of a mouse line with endogenously tagged receptors with a bright and photostable fluorophore give another hint to the location, binding and possibly sorting processes of the receptors (also without a bound ligand).

The acquired data cannot exclude that in a minority of cells the β_1-AR may also be predominantly localized to the TTs. In order to make a clear statement about this a follow-up study with larger statistics will be necessary.

The observation that receptor compartmentalization is lost in overexpression favors the hypothesis that intracellular protein scaffolds modulate receptor localization. In this case the localization of these scaffolds responsible for interacting with the β_2-AR appear to be mainly at the T-tubular membranes of the CMs. As the expression level increases above a certain threshold these interaction points become saturated and receptors re-localize. Alternatively, such re-localization of the β_2-AR could result from species dependent differences of the receptor itself. Since the coding sequences in overexpression are of the human β_1- and β_2-AR, interaction with the cytoskeletal scaffold could be disrupted as it had been documented that the key residue (leucine 410) in the human β_2-AR, responsible for NSF binding, is not conserved in the mouse β_2-AR [164]. This could hint to the fact that NSF, and maybe other scaffolding proteins, are not required for localization of the β_2-AR in murine CMs or at all. Investigation of this interaction via mutated or knocked-out interaction sites could elucidate the involvement of NSF and possibly species dependent differences in the localization mechanisms of β-ARs in the heart.

Additionally, the more rapid apparent correlation time observed from the experimental dataset of the wild-type cardiomyocytes at the T-tubular membranes agrees with the observation made in simulated T-tubular membranes where receptors can predominantly diffuse radially. This could mean that the receptor confinement may arise due to a suppression of axial diffusion in the TTs which is not the case in overexpression when the interaction points with the scaffold become over-saturated or not accessible. Further investigation needs to be performed to fully address this question. One starting point could be the investigation of the diffusion of the β-ARs directly at the T-tubular membrane. The introduced combined widefield-confocal microscope holds the potential of scanning the surface of TTs in specific patterns. In this respect, circular scans around the TTs could be the starting point for the investigation of the localized and potentially directed diffusion. At the same time the mechanisms that keep the β_2-ARs at the TTs should be addressed. In this regards, not only diffusion, but possibly interactions of the receptors with cytoskeletal interaction partners, such as NHERF1 or the PDZ motif, under conditions of intact and disrupted structures (knock-out or mutation) in combination with techniques with high temporal resolution such as linescan-FCS are a promising starting point for this investigation.

It is noteworthy that the 5-fold increase in laser power made it possible to detected the receptors at the TTs, but confirmed the same results of differential distribution of the β_1-AR and the β_2-AR at the PM of wt CMs as with lower laser power.

A further interesting observation has been made in the experiments with cells of a rat cardiomyoblast cell line (H9c2) and hiPSC cells differentiated to CMs which do not possess T-tubular membranes. The β_2-ARs are present and were observed to diffuse at the cell surface of the PM of both cell types (Bathe-Peters et al. [58]). This would suggest that the diffusing receptors could target specifically the TTs in adult CMs as they progressively form. Stem cell derived cardiomyocytes offer many opportunities to further investigate the re-localization process of the β_2-ARs as the T-tubular system gradually forms. With maturation protocols that are able to induce TTs the process of the development of the compartmentalization could be studied at a more accessible modeling system.

Lastly, specific cardiomyocytes do not appear to express the β_1-AR at all, neither at the TTs nor at the PM. In this respect, such cell-to-cell variability of GPCRs has been described before, including in cardiac settings. In particular the β_1-AR has been described before in such context [160]. The muscarinic M_2 receptor expression has been reported to be heterogenous in isolated cardiomyocytes [70]. On a more general basis, five different ventricular CM populations with distinct transcricptomic profiles were recently identified [76]. Expression heterogeneity of GPCRs also has been observed in smooth muscle and endothelial cells depending on the anatomical localization of the cells [167]. Based on those observations the results obtained here are in general agreement.

5.2 Technical Setup

The combined setup of a confocal and widefield microscope was built in order to explore the possibility of combined measurements of FCS with single molecule imaging or particle tracking. The setup has shown its capability of acquiring TIRF images and confocal FCS measurements fig. 4.42. Nevertheless, in order to build a permanently stable working setup some improvements of the system have to be made. In this regard, the electronic equipment, including the photon detection card, and some preliminary mechanical parts need revision. Additionally, in order to obtain a suitable setup for measurements of more complicated structures, such as on the circumferential membrane of TTs of CMs, the galvanometer scanners will need to be set up to allow circular scanning around the center of the tabulations. Additionally, by enhancing this setup with an autofocus based on an ETL it becomes a valuable tool to perform precise measurements of cellular processes.

The autofocus system employs an ETL in order to rapidly alter the position of the focal plane by application of a reflected IR laser beam as a precise position sensor. Hereby, it not only fits most commercial microscopes, but is also fast and cost-effective compared to state-of-the-art autofocus devices based on piezoelectric actuators which move either the objective or the sample.

Total internal reflection of the IR beam is not a strictly necessary feature of the proposed autofocus device, but it is advantageous as it maximizes the signal to noise ratio in the estimate of the objective to sample distance. Thus it allows reflection of most of the energy of the IR monitoring beam onto the position sensor, the QPD in this case. The system with enabled feedback can compensate rapid changes of the focal position and demonstrated its capability of maintaining a sample in focus over a period of 25-30 min with a minimal focal loss compared to the case when no feedback is applied. As the manufacturer describes coma to be a possible geometry induced aberration in their lenses [103], tunable lenses are not aberration free. Thus they are expected to degrade the quality of the image produced by the microscope objective to a certain extent. In this regards Fuh et al. [168] have characterized aberrations produced by ETLs. The dominant form of aberration here was astigmatism, as observed in fig. 4.48(b), which has likely occurred due to a slight mechanical offset between the lens and the objective axis. Moreover the small degree of astigmatism was helpful in identifying the defocus of the beads more clearly. From the rapid improvement of ETL technology over the last few years, further improvements in aberration correction are likely expected to be soon available.

6 Conclusions and Perspectives

6.1 Conclusions

The thesis has addressed the question of the localization and dynamics of the β_1- and β_2-AR in adult cardiomyocytes. Further it describes the implementation of a combined widefield-confocal microscopy platform and the invention of an autofocus based on an electrically tunable lens and an infrared laser.

The present results provide for the first time a method to directly detect the localization of endogenous β-adrenergic receptors, and more in general, labeled GPCRs, in live adult CMs. The results include that in wild-type cardiomyocytes at the cell surface only the β_1-AR is present whereas the β_2-AR is absent. At the T-tubules both types of adrenergic receptors are present. Further, in overexpression this localization is disturbed and a redistribution of the β_2-AR takes place which removes the compartmentalization of the β_2-ARs. Therefore the β_2-ARs are also found at the surface plasma membrane of adult CMs. The two independently applied analysis methods deliver dynamics in agreement with each other and with values known from literature for these receptors. Herewith, the longstanding observation of compartmentalized cAMP signaling in the TTs of adult CMs is explained by the heterogeneous localization of the receptors themselves. This clearly demonstrates that receptor function is influenced by more than just biochemical signals elicited from receptors but also by their specific cellular localization. It also demonstrates that receptor amounts may vary between cells and that not all cells express receptors equally. The applied approach to study the localization and dynamics holds also the potential to be applied in other systems or settings to investigate low levels of receptor expression.

The described setup, combining a widefield and a confocal part in one microscopy body, showed its potential in acquiring images with both imaging modes in HEK cells. This approach holds promise to investigate spatially confined diffusion by obtaining widefield images of live cell samples before performing FCS in selected positions or within organelles of interest.

Further, a novel and cost effective autofocus system, based on an electrically tunable lens, has been set up which rapidly alters the position of the focal plane by lens curvature changes. It is capable of continuous focus adjustment without the need of objective to sample displacements and it fits most commercial microscopes.

By confirmation of the differential localization of the β_1-AR and β_2-AR a further step towards a better understanding of the processes involving the β-ARs and their role in the cardiac setting has been achieved. In the process, this thesis has led to the development of multiple tools capable of the investigation of endogenous receptor localization, dynamics and interactions. One of these tools is a high affinity fluorescent ligand specific for the β-ARs. Other techniques can easily be utilized to study dynamics, localization and protein interaction on a more general level in low expression. These techniques involve the implementation of sensitive spectroscopic analysis methods, the development of a combined widefield-confocal setup and the novel and innovative autofocus. A follow up on some of the studies and questions mentioned in section 6.2 could lead eventually to a greater and more complete understanding of the role of β-adrenergic receptors in the heart and their signaling specificity. The results obtained in this work represent one piece at the basis that lead to this understanding in hope that ultimately this can lead to a better and more precise application and development of medications to alleviate sufferings from cardiac diseases and to save lives.

6.2 Future Investigation

After having solved the question of location of β-ARs in adult CMs and having confirmed their differential localization, future studies on the role of β-ARs in cardiac function should concentrate on directing research into different paths. First, future investigation should concentrate on deciphering the processes and the driving forces that lead to the differential localization of the subtypes of β-ARs. As discussed one starting point could be the investigation of selective modifications or knockouts of PDZ binding scaffolds, such as the NHERF proteins, in particular NHERF1, C-terminal modification of the β_2-AR, such as elimination of the particular interaction motif, and domain swapping of the two β-AR subtypes. As either of these proposed alterations could lead to a non-compartmentalized distribution this could be interesting candidates to investigate their influence on location bias. Investigation of the PDZ domain swap of the two receptors, the β_1-AR and the β_2-AR, could be of particular interest since if that motif is a major actor in the localization process of the β_2-AR it could show a confined localization of the β_1-AR at the TTs if swapped. Further, the investigation of the C-terminal interaction of the β_2-AR with NSF should be investigated keeping species dependent differences in mind (see chapter 5). Additionally, a helpful tool in order to investigate the determinants of localization during every single step of cell maturation could be obtained by further differentiating hiPSCs towards adult CMs, which form a T-tubular network [169]. As they are an easier accessible system (compared to adult CMs) at each step during maturation they could be useful to address the underlying mechanisms responsible for localization of the receptors.

Next, as the TTs represent a membrane structures with higher curvature, the influence of biophysical factors, such as membrane curvature should be the focus of further investigation. As the β_2-AR was reported to prefer membranes of higher curvature particularly upon binding a ligand [166] future investigation should aim at the investigating and monitoring of binding process to elucidate if receptor sorting of the β_2-AR could occur as a result of the interaction with the ligand. A further starting point to investigate the importance of the interaction of the receptor with a ligand and with cytoskeletal scaffold in membrane sorting is the creation of a mouse line with labeled receptors in the unbound state as this would allow monitoring of the receptor distribution without an interacting ligand.

However, not only molecular interactions between the receptors and interacting proteins such as the G proteins and scaffold proteins, as prototypes of intracellular GPCR-interacting proteins to modulate downstream interactions, should be investigated, but also dynamical interaction between the interaction partners could allow to draw conclusions about important processes for cardiac function. Thus a combined microscope platform as the one introduced in this work with a widefield part, capable to deliver high spatial information via application of superresolving techniques such as photoactivated localization microscopy (PALM) and stochastic optical reconstruction microscopy (STORM), and a confocal part, allowing for measurements of very fast dynamics via FCS, could ultimately elucidate questions about β-AR diffusion and interactions on the surface of TTs in adult CMs. By usage of the galvanometer scanners of the confocal part to perform circular scans [170, 171] the combined widefield-confocal microscope could allow access to study diffusion on intracellular tubulations such as the T-tubules of adult CMs. This approach would allow the scanning beam to follow the surface of the tubule and therefore the determination of the possible diffusion path of receptors at all times to measure kinetics and interactions of the receptors with the cytoskeleton at the membrane of the tubular invaginations constantly.

In order to exclude species dependent differences all of these studies should be performed or at least validated in human cardiac myocytes, starting with the confirmation of the differential localization of the two β-ARs in human cardiomyocytes.

Lastly, the tools used in this work will be helpful for the investigation of the altered localization as well as mechanisms and interactions that lead to a loss of compartmentalization and redistribution of the β-ARs in cardiomyocytes in heart failure.

Appendix A Residual plots

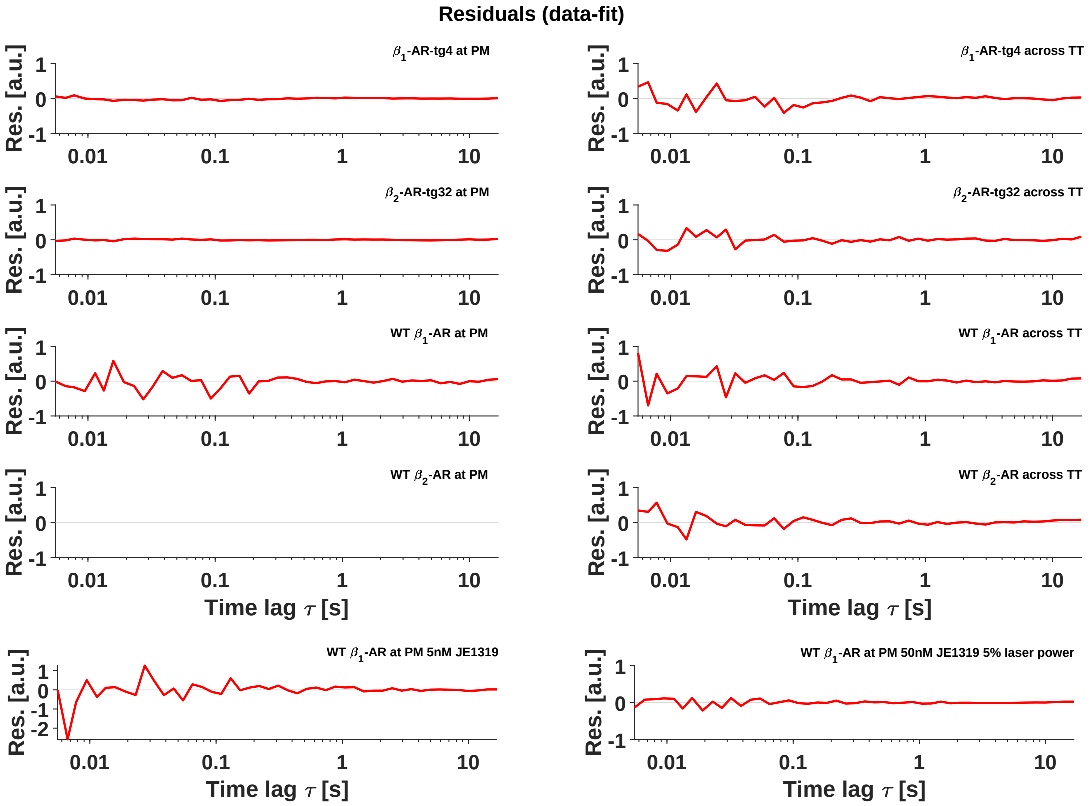

Figure A.1: Normalized residual plots of fitted autocorrelation functions. Residuals of cases for which no autocorrelation curve was extracted are similar to the plot of the wt β_2-AR at the PM and are not further displayed. Grey lines indicate 0.

Appendix B Autofocus-calibration

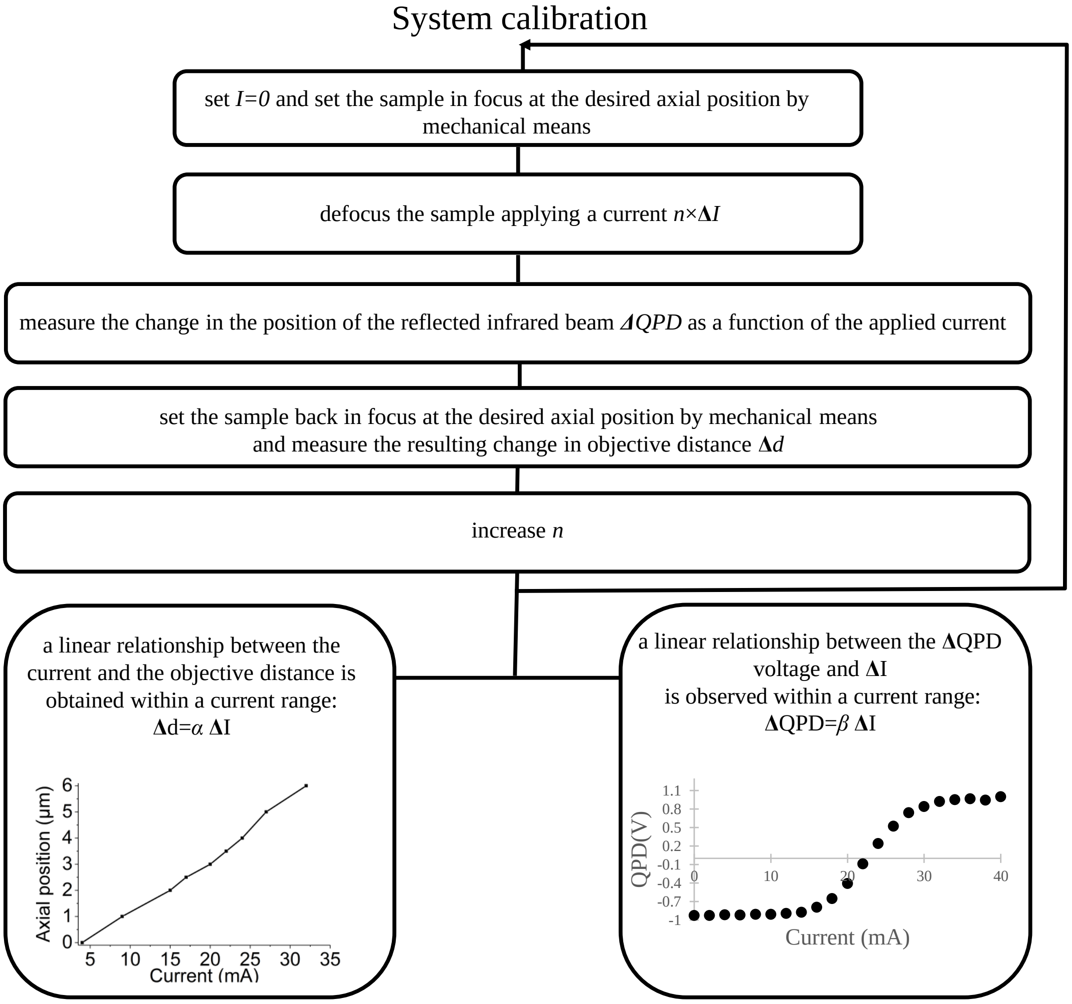

Figure B.1: Flow chart of the calibration of the autofocus. Establishment of the relation of the axial position to the current (fig. 4.45a inset) and the QPD voltage vs. current curves in dependence on the axial position (fig. 4.45b). Adapted from Annibale, Bathe-Peters et al. [172].

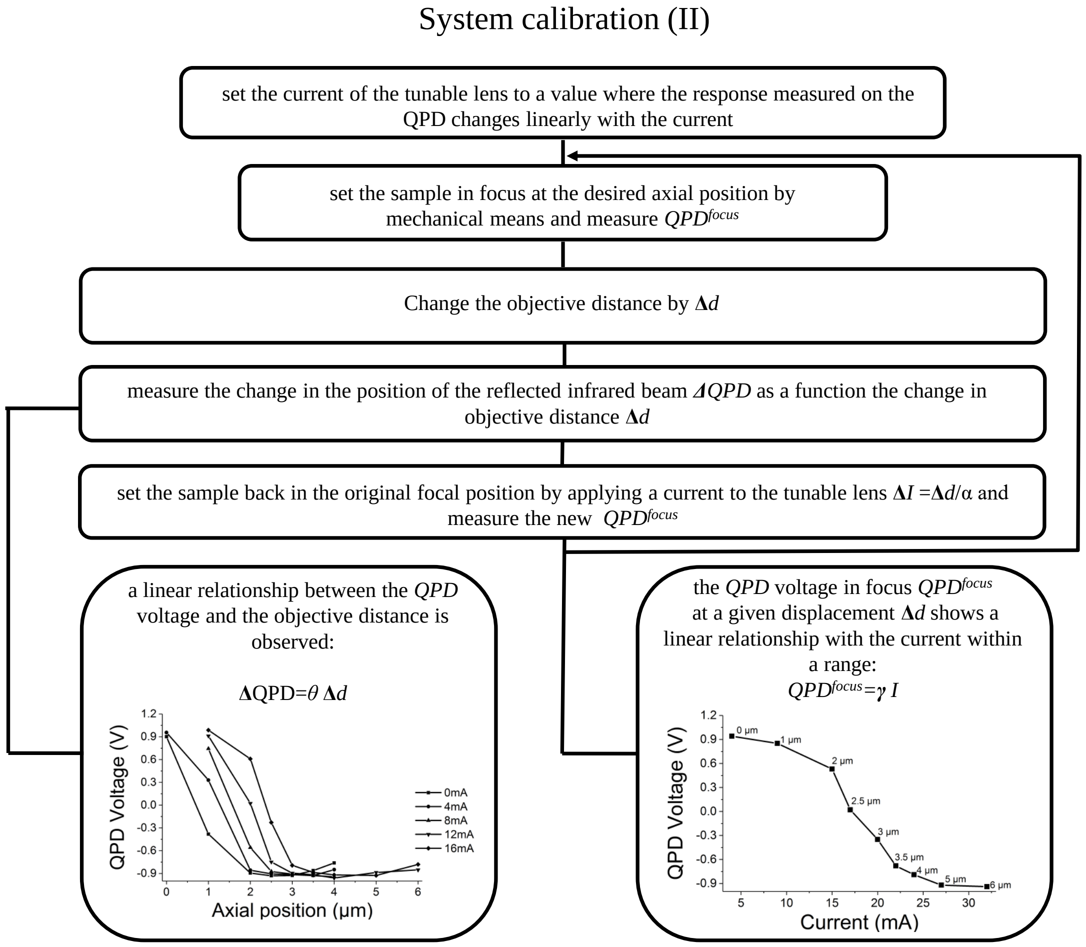

Figure B.2: Flow chart of the calibration of the autofocus II. Establishment of the relation of the axial position to the QPD voltage (fig. 4.45a) and the QPD voltage vs. current in-focus positions in dependence on the axial position (fig. 4.45c). Adapted from Annibale, Bathe-Peters et al. [172].

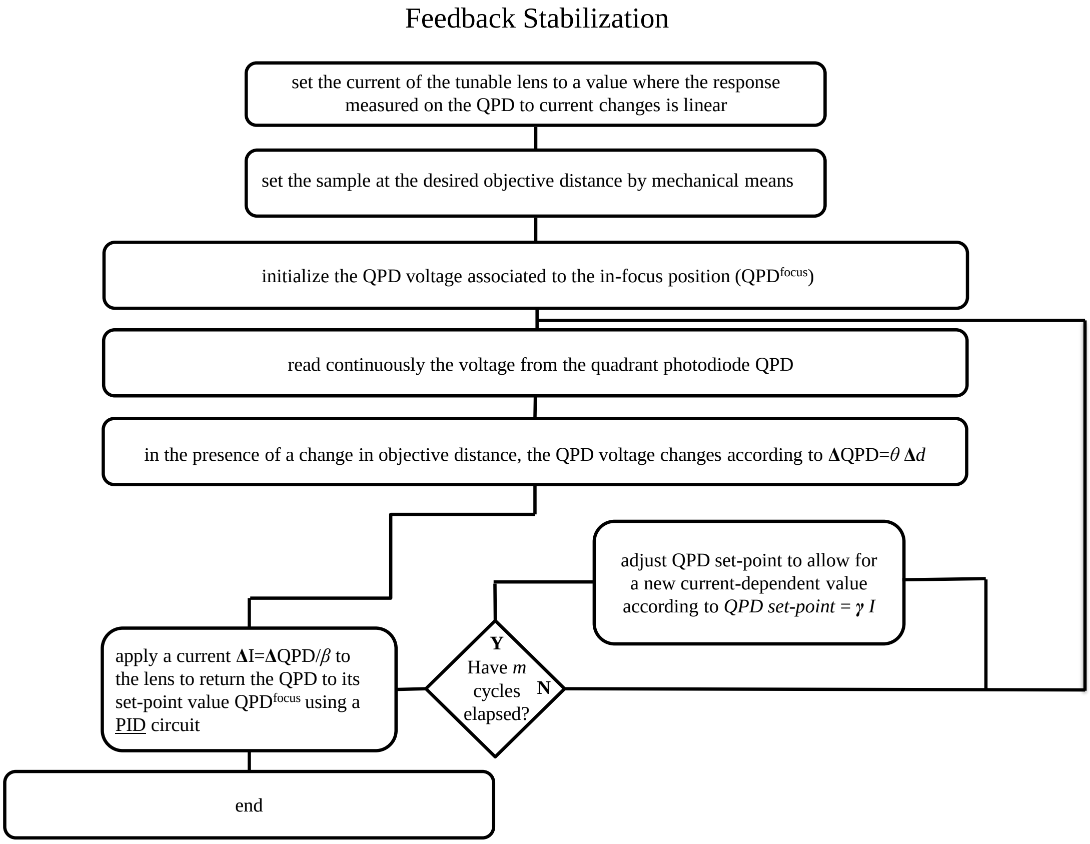

Figure B.3: Flow chart of the feedback stabilization. Adapted from Annibale, Bathe-Peters et al. [172].

Appendix C Codes

C.1 MATLAB code to analyze diffusion

The MATLAB code used for the pixel-by-pixel analysis of the linescan data is provided here and under: https://gitlab.com/marcbp/autocorrelation-analysis-from-linescans. The code consists of different blocks which allow a stop after each step of the analysis. The code for the analysis of the linescans is executed in the following order:

1. autocorrelation_bleaching_control.m
2. average_acrossTT.m
3. selection_fit_TT.m
4. save_ac_norm.m
5. normalization_ac.m

The code average_acrossTT.m is only used for analyses of multiple pieces of an image (e.g. TTs), otherwise it can be skipped in the order. The code blocks have the following function:

- autocorrelation_bleaching_control.m: main code to read the tiff images in and to calculate the autocorrelations. Options are single pixel analysis (0), multiple pixel analysis (not connected pixels; 1) and image or multiple pixel block analysis (2).
  It also allows under bleaching_treatment.m the following options how to deal with possible bleaching:
  0. no removal of time points and no filtering
  1. removal of time points (by graphical selection)
  2. removal of time points (by graphical selection) and moving average filtering
  3. removal of time points by precise input of lines to remove
  4. removal of time points by precise input of lines to remove and moving average filtering of the rest

   5. removal of time points by precise input of lines to remove and fit of over pixels averaged curve to a double exponential with succeeding subtraction of trace from data and addition of the mean intensity
   6. same as previous except fit of double exponential to time traces of individual pixels. Time trace is filtered pixel by pixel.
   7. removal of time points by precise input of lines to remove and fit of over pixels averaged curve to a double exponential with succeeding correction as in [72]

- average_acrossTT.m: only used to average and fit blocks of images together, such as TTs.
- selection_fit_TT.m: allows the removal of lines from further analysis as described in section 3.7.1. Uses ac_selectorp_axis.m for the selection of autocorrelations.
- save_ac_norm.m: saves the data (code not enclosed).
- normalization_ac.m: normalizes data.

Other relevant functions or blocks which are called by the main codes:

- assign_correct_labels.m: function used by selection_fit_TT.m and autocorrelation_bleaching_control.m to determine axis labels of autocorrelation maps.
- read_tif2.m: reads tif images and concatenates data of single image frames.
- create_Fit_x.m: where x stands for the fitting function. Formulas in section 3.7.1 are applied.
- autocorrflb.m: calculates the autocorrelation.
- logbinmatrix/logbinmatrix_remove_rep_full/logbinning.m: perform the log-binning of the data.
- line_evaluation.m: is optional in autocorrelation_bleaching_control.m and would calculated the autocorrelations of each block of pixels individually.

autocorrelation_bleaching_control.m

```
clear all
close all

%%
%string to image
string='Filepath\filename.tif';

%reads in tif images properly and combines tif stacks
Ir = read_tif2(string);
%%
%determines dimensions of image
sz = size(Ir)

%define parameters such as line scan frequency, temporal chunk length and
%binning of time steps
prompt = {'Enter temporal resolution:','Enter length of pieces to analyze:','
    Enter bin number:'};
dlgtitle = 'Input';
dims = [1 35];
definput = {'1800','65536','64'};
answer = inputdlg(prompt,dlgtitle,dims,definput)
parameters=str2double(answer)

temp_res=1/parameters(1);
length_chunks=parameters(2);
bins=parameters(3);

%for display purposes averages all time points into equal 500 points
for i=1:500
    counter=floor(sz(1)/500);
    imageviewer(i,:)=mean(Ir((i-1)*counter+1:i*counter,:),1);
end

%plot the image over the averaged parts
f22=figure('Name','Averaged image chunks')
%imagesc(imageviewer);
imagesc([0:1:sz(2)],[0:counter:sz(1)]*temp_res,imageviewer);
%colorbar
%set(gca, 'YScale', 'log')
title('Line Scan with averaged temporal values (500)')
ylabel('Time [s]')
xlabel('Pixel')
xticks([0:10:sz(2)])

%%
```

```
%let's one select the points in an image and returns the coordinates of the
%points in x and y as column and row vectors respectively
%2021-06-01 adds if clause in case there is only 1 pixel, impixel requires
%mroe than one pixel to work
if size(Ir,2)==1
    x=1;
else
[x,y,P] = impixel
end
%%
%plots the averaged intensity over time to see bleaching
f11=figure('Name','Mean intensity')
plot((1:1:sz(1)),mean(Ir,2))
ylabel('Average intensity [a.u.]')
xlabel('bins')

%plot the averaged intensity profile, here 1000 bins with 303,104/507,904
    lines
%each (also to get a better overview)
for i=1:1000
    counteri=floor(sz(1)/1000);
    imagevieweri(i,:)=mean(Ir((i-1)*counteri+1:i*counteri,:),1);
end

f1=figure('Name','Averaged line profile')
plot([0:1:size(imagevieweri,1)-1]*size(Ir,1)/1000,mean(imagevieweri,2));
title('Temorally averaged intensity profile (1000 bins)')
ylabel('Average intensity [a.u.]')
xlabel('bins/lines')


%remove the initial times points with bleaching
prompt = {'Options: 0 - no filtering, no cut off, 1- cut off, 2 - cut off and
    filtering, 3 - specify cut off value, 4 - specify cut off value and
    filtering'};
dlgtitle = 'Input';
dims = [1 35];
definput = {'0'};
answer = inputdlg(prompt,dlgtitle,dims,definput);
bleaching=str2double(answer);

%initialize to not remove any time points
tbleach=0;

%let's one choose how to treat bleaching
bleaching_treatment

```

```
%redetermines size (for the case of removal of time points)
sz2 = size(Ir);
%and calculate the amount of chunks new
amount_chunks=sz2(1)/length_chunks;
%devide the time into averaged pieces to better get an idea of the tubules
%over the entire time - replot adjusted
for i=1:500
    counter=floor(sz2(1)/500);
    imageviewer(i,:)=mean(Ir((i-1)*counter+1:i*counter,:),1);
end

%plot the image over the averaged parts
f2=figure('Name','Averaged image chunks')
imagesc([0:1:sz(2)],[tbleach:counter:sz(1)]*temp_res,imageviewer);
title('Line Scan with averaged temporal values (500)')
ylabel('Time [s]')
xlabel('Pixel')

%%
%selector whether it should analyze 1 line, option 0, more lines, option 1,
%or ranges, option 2
%mainly option 2 since it allows for a selection of multiple groups of lines together
prompt = {'Enter selector 0 to analyze 1 line, enter 1 to analyze more lines and enter 2 to analyze ranges'};
dlgtitle = 'Input';
dims = [1 35];
definput = {'0'};
answer = inputdlg(prompt,dlgtitle,dims,definput);
d=str2double(answer);

%%
% initialize the counter and cell to store the image pieces and start the
% if condition to analyze chunks (more than 1 line) in a region of the
% image
j=0;
%choose option 2 to select multiple concatenated columns and even more than
%1 of these blocks of lines (if condition to analyze chunks (more than 1 line) in a region of the
% image)
if d==2
% initialize the cell to store the image pieces
imgCell=cell(1, length(x)-1);

%selection of image pieces until lenth-1
for i=1:length(x)-1
   %cut the image into pieces as defined; uses 2 adjacent points to
```

```
   %calculate the piece of the image
Ic=imcrop(Ir,[x(i) 1 x(i+1)-x(i) sz(1)-1]);%[xmin ymin width height]
%store the image pieces into cells
imgCell{i}=Ic;
% optionally: display the image pieces
% figure(i+2)
% imshow(Ic)

%%
%select the pieces which are desired with odd numbers in the vector because
%even numbers are the not desired pieces since regions between odd and even
%numbers are desired; even and odd are just space between the desired
%regions; example: region between x= 1 and 2 is supposed to be analyzed,
%then with the next 2 points 3 and 4 another region is selected, but the
%image crop also crops from point 2-3 as region 2 (this is the undesired
%space). So this checks the beginnings of the chunks and only if the
%remainder is 1 by deviding by 2 the image piece is the desired selection
%This is selected here and stored into Iss
 if mod(i,2)==1
       j=j+1;
       Iss{j}=imgCell{i};
    end
end

%%
% optional: shows the image selections which are desired and cut out
% for i=1:length(Iss)
% figure(i+10)
% imshow(cell2mat(Iss(i)))
% end

%%
%select the piece and calculate the autocorrelation
for i=1:length(Iss)
    k=cell2mat(Iss(i));
%converts the image data from uint8 to double since with uint8 it doesn't
%go below 0 -> wrong results
    l=double(k);

%initialize values so they have the correct size
t=[];
g=[];
c=[];
tlogbin=[];
clogbin=[];
clogstd=[];
clogbin_help=[];
```

```
clogbin_std=[];
clogbinm=[];
clogbinstd=[];
Clogbin=[];
G=[];
Clogstd=[];
valuenan=[];

    for j=1:length(l(1,:))
   %do not initialize the values inside the loop. This overwrites the
        %previous values each time and for the mean value the sum is still
        %divided by the number of pixels, but all the pixels except the
        %last are 0, therefore the amplitude is smaller by the size of the
        %pixels
        %g=[];
        %c=[];
        %clogbin=[];
        %clogbin_help=[];
        %clogbinm=[];
        %clogstd=[];

        %optional code with fft or loop (use fft since faster)
        [t,c(j,:),g(:,:),valuenan{j}]=autocorrflb(l(:,j),amount_chunks,temp_res
            );
        %calculates the logbinned chunks depending on the binsize:bins
        %either logbinmatrix_remove_rep_full which removes replicates, if
            replicates at
        % the beginning of the vector are fine use instead logbinmatrix
        [tlogbin,clogbin(:,:),clogstd(:,:)]=logbinmatrix_remove_rep_full(t,g
            (:,:),bins);
        %calculates the dimensions of all chunks of logbinned autocorrelations

        G(:,:,j)=g;
        Clogbin(:,:,j)=clogbin;
        Clogstd(:,:,j)=clogstd;

[m, n]=size(clogbin(:,:));


% %plots the image as a colormap with each autocorrelation going from the top
% %to the bottom (over time) and each chunks along the x-axis
% figure('Name','Color-coded ACs')
% Selector=imagesc([1 n],[tlogbin(1) tlogbin(end)],clogbin(:,:));
% colorbar
% %set(gca, 'YScale', 'log')
% title('Color-coded ACs')
% ylabel('Time lag \tau [s]')
```

```
% xlabel('AC [a.u.]')
%
% %have the selection if there are any bad autocorrelation chunks
% prompt = {'Enter selector 0 to not remove any lines or 1 to remove lines'};
% dlgtitle = 'Input';
% dims = [1 35];
% definput = {'0'};
% answer = inputdlg(prompt,dlgtitle,dims,definput);
% d=str2double(answer);

%assign help clogbin because in a 3D matrix the dimensions have to be the
%same, therefore store the matrix in a seperate variable and calculate the
%mean before moving on
%clogbin_help holds all the autocorrelations of all the cuts of 1 line
clogbin_help=clogbin(:,:);
clogbin_std=clogstd(:,:);

%here only remove the colums from the logbinned vectors and ask if there
%are more to erase after a first selection; then cut the matrix and take
%only the good ones for further calculations
% while d==1
% [px,yp,Pp] = impixel;
% clogbin_help(:,px)=[];
% clogbin_std(:,px)=[];
% imagesc(clogbin_help)
% colorbar
% prompt = {'Enter selector 0 to not remove any lines or 1 to remove lines'};
% dlgtitle = 'Input';
% %dims = [1 35];
% definput = {'0'};
% answer = inputdlg(prompt,dlgtitle,dims,definput);
% d=str2double(answer);
% end

%now calculate the mean of all the logbinned autocorrelations
%here it is the same if first averaging and then logbinning or first
%logbinning of each chunk and then averaging over all af the chunks; not
%identical, but very similar
%clogbinm holds all the mean autocorrelations of all the lines in 1 chunk
%of image
clogbinm(:,j)=mean(clogbin_help,2);
%calculates the standard deviation of 1 line over all the segments
clogbinstd(:,j)=std(clogbin_help,1,2)/sqrt(size(clogbin_help,2));
    end

 %first averaging and logbinning
 cmean(i,:)=mean(c,1);
```

```
[tlogbin2,a(i,:),b(i,:)]=logbinning(t,cmean(i,:),bins);
% Plot fit with data.
f3=figure( 'Name', 'averaged and logged' );
h2=plot( tlogbin2, a(i,:), 'b--.' );
% hold on;
% errorbar(tlogbin, clogbin_meanchunk(:,i), clogbin_stdchunk(:,i),'b','
    LineStyle','none');
legend( h2, 'data', 'Location', 'NorthEast' );
set(gca, 'XScale', 'log')
% Label axes
xlabel 'Time lag \tau [s]'
ylabel 'AC [a.u.]'
grid on

    %clogbin_meanchunk holds the averaged autocorrelations of all lines
    %averaged together for each image chunk seperately
    clogbin_meanchunk(:,i)=mean(clogbinm,2);
    %this holds all the standard deviations averaged together from the
    %logbinning;
    %this holds the standard deviation of here the standard error of the
    %averaged chunks over each line in a chunk
    clogbin_stdchunk(:,i)=std(clogbinm,1,2)/sqrt(size(clogbinm,2));

    %clogbin_lines holds all the autocorrelations of each line in 1 chunk
    %on a seperate page; it has to be a cell array because a 3D matrix has
    %to have the same dimensions for the matrices inside the 3rd dimension
    clogbin_lines{i}=clogbinm;
    %holds the standard deviations of each line for a chunk on 1 page
    clogbin_lines_std{i}=clogbinstd;
    %saves in a cell array of each image chunk all the ACs in chunks of
    %each pixel
    ACs_raw{i}=G;
    ACs{i}=Clogbin;

%fit: here choose which parameters to keep constant and which ones to alter
%according to the selector input
%choose fitting model and output of values

[fitresult, gof] = createFit1D(tlogbin, clogbin_meanchunk(:,i),
    clogbin_stdchunk(:,i))
r(i,:)=coeffvalues(fitresult)

%ignore 0 standard deviation values just for plotting by including NaN
%values
index=find(clogbin_stdchunk(:,i)==0);
clogbin_stdchunk(index,i)=NaN;

```

```
% Plot fit with data.
f4=figure( 'Name', 'Fitted autocorrelation' );
h = plot( fitresult, tlogbin, clogbin_meanchunk(:,i), 'b--.' );
hold on;
errorbar(tlogbin, clogbin_meanchunk(:,i), clogbin_stdchunk(:,i),'b','LineStyle','none');
% hold on
% plot(tlogbin2, a(i,:), 'g--.')
legend( h, 'data', 'fit', 'Location', 'NorthEast' );
set(gca, 'XScale', 'log')
% Label axes
xlabel 'Time lag \tau [s]'
ylabel 'AC [a.u.]'
grid on
end

%produce the output labels in str and combine them in Cmean, display them
%afterwards
str=["gamma", "n", "D", "w_xy", "wz", "offset"];
Cmean={str;r};
celldisp(Cmean)

%select wheter to fit all the lines 1 by 1 and to get a 1 by 1 output or to
%get just the data of the averaged autocorrelation
%[C]=line_evaluation(clogbin_lines,tlogbin,clogbin_lines_std);


%the condition for d=0 only works for the selection of 1 line
elseif d==0
    l=double(Ir(:,x));
        %[t,c,g]=autocorr(l,length(l)/1024,5e-6);
        %[fitresult]=autocorrelator(l,temp_res,length_chunks,bins);

%plots the amplitudes
f1=figure('Name','Amplitude')
plot(temp_res*(1:1:length(l)),l)
%title('Raw amplitudes over counts')
xlabel('Time t [s]')
ylabel('Amplitudes [a.u.]')

%calculate the autocorrelation
[t,c,g, valuenan]=autocorrflb(l,amount_chunks,temp_res);

%calculates the logbinned chunks depending on the binsize:bins
[tlogbin,clogbin,clogstd]=logbinmatrix_remove_rep(t,g,bins);
%calculated the dimensions of all chunks of logbinned autocorrelations
[m, n]=size(clogbin);
```

```
%plot the AC before the selection of lines (2021-06-01)
faca=figure('Name','ACs cleaned')
plot( tlogbin, mean(clogbin,2), 'b--.' );
set(gca, 'XScale', 'log')
% Label axes
xlabel 'Time lag \tau [s]'
ylabel 'AC [a.u.]'
grid on
%moves the position on the screen
movegui(faca,'east');
%plots the image as a colormap with each autocorrelation going from the top
%to the bottom (over time) and each chunks along the x-axis; time vs.
%temporal chunk
f2=figure('Name','Color-coded ACs')
%assigns correct temporal axis labels
%need to calculate the ticks and labels in a function otherwise it messes
%up counter i
[ticks,tlabels]=assign_correct_labels(tlogbin, clogbin);
imagesc(clogbin(:,:));
yticks(ticks);
yticklabels(tlabels);
colorbar
title('Color-coded ACs')
ylabel('Time lag \tau [s]')
xlabel('AC chunks [a.u.]')

%moves the position on the screen
movegui(f2,'west');

%have the selection if there are any bad autocorrelation chunks
prompt = {'Enter selector 0 to not remove any lines or 1 to remove lines'};
dlgtitle = 'Input';
dims = [1 35];
definput = {'0'};
answer = inputdlg(prompt,dlgtitle,dims,definput);
d=str2double(answer);

%here only remove the colums from the logbinned vectors and ask if there
%are more to erase after a first selection; then cut the matrix and take
%only the good ones for further calculations
while d==1
    figure(f2);
    [xp,yp,Pp] = impixel;
    clogbin(:,xp)=[];
    clogstd(:,xp)=[];
    imagesc(clogbin)
    %use the counter from above
```

```
yticks(ticks);
yticklabels(tlabels);
colorbar
title('Color-coded ACs')
ylabel('Time lag \tau [s]')
xlabel('AC chunks [a.u.]')
%replot the AC with selected ACs (2021-06-01)
figure(faca);
clf
plot( tlogbin, mean(clogbin,2), 'b--.' );
set(gca, 'XScale', 'log')
% Label axes
xlabel 'Time lag \tau [s]'
ylabel 'AC [a.u.]'
grid on
prompt = {'Enter selector 0 to not remove any lines or 1 to remove lines'};
dlgtitle = 'Input';
%dims = [1 35];
definput = {'0'};
answer = inputdlg(prompt,dlgtitle,dims,definput);
d=str2double(answer);
end

%now calculate the mean of all the logbinned autocorrelations
%here it is the same if first averaging and then logbinning or first
%logbinning of each chunk and then averaging over all af the chunks; not
%identical, but very similar
clogbinm=mean(clogbin,2);
%clogbinstd=mean(clogstd,2);
clogbinstd=std(clogbin,1,2)/sqrt(size(clogbin,2));

%fit: here choose which parameters to keep constant and which ones to alter
%according to the selector input

[fitresult, gof] = createFit2D(tlogbin, clogbinm,clogbinstd )
r=coeffvalues(fitresult)

%ignore 0 standard deviation values just for the plotting by including NaN
%values
index=find(clogbinstd==0);
clogbinstd(index)=NaN;

% Plot fit with data.
f4=figure( 'Name', 'Fitted autocorrelation' );
h = plot( fitresult, tlogbin, clogbinm, 'b--.' );
hold on;
errorbar(tlogbin, clogbinm, clogbinstd,'b','LineStyle','none');
```

```
legend( h, 'data', 'fit', 'Location', 'NorthEast' );
set(gca, 'XScale', 'log')
% Label axes
xlabel 'Time lag \tau [s]'
ylabel 'AC [a.u.]'
grid on

% if d=1 then if takes only the selected lines and calculates and fits the
% autocorrelation for these lines
elseif d==1

    %store the selected lines in a vector l
    l=double(Ir(:,x));

 %initialize values so they have the correct size
g=[];
c=[];
clogbin=[];
clogbin_help=[];
clogbinm=[];
clogstd=[];
clogbinstd=[];

    %now calculate the autocorrelations and logbin them
    for i=1:1:length(x)
% g=[];
% c=[];
% clogbin=[];
% clogbin_help=[];
% clogbinm=[];
% clogstd=[];
% clogbinstd=[];

        [t,c(i,:),g(:,:), valuenan{i}]=autocorrflb(l(:,i),amount_chunks, temp_res);
        %calculates the logbinned chunks depending on the binsize:bins
        [tlogbin,clogbin(:,:),clogstd(:,:)]=logbinmatrix_remove_rep(t,g(:,:), bins);

        %save all the data
        G(:,:,i)=g;
        Clogbin(:,:,i)=clogbin;
        Clogstd(:,:,i)=clogstd;
%calculated the dimensions of all chunks of logbinned autocorrelations
[m, n]=size(clogbin(:,:));

%plot the AC before the selection of lines (2021-06-01)
```

```
faca=figure('Name','ACs cleaned')
plot( tlogbin, mean(clogbin,2), 'b--.' );
set(gca, 'XScale', 'log')
% Label axes
xlabel 'Time lag \tau [s]'
ylabel 'AC [a.u.]'
grid on
%moves the position on the screen
movegui(faca,'east');

%plots the image as a colormap with each autocorrelation going from the top
%to the bottom (over time) and each chunks along the x-axis
f2=figure('Name','Color-coded ACs')
%need to calculate the ticks and labels in a function otherwise it messes
%up counter i
[ticks,tlabels]=assign_correct_labels(tlogbin, clogbin);
imagesc(clogbin(:,:));
yticks(ticks);
yticklabels(tlabels);
colorbar
%set(gca, 'YScale', 'log')
title('Color-coded ACs')
ylabel('Time lag \tau [s]')
xlabel('AC chunks [a.u.]')

%moves the position on the screen
movegui(f2,'west');

%have the selection if there are any bad autocorrelation chunks
prompt = {'Enter selector 0 to not remove any lines or 1 to remove lines'};
dlgtitle = 'Input';
dims = [1 35];
definput = {'0'};
answer = inputdlg(prompt,dlgtitle,dims,definput);
d=str2double(answer);

%assign help clogbin because in a 3D matrix the dimensions have to be the
%same, therefore store the matrix in a seperate variable and calculate the
%mean before moving on
clogbin_help=clogbin(:,:);
clogbin_std=clogstd(:,:);

%here only remove the colums from the logbinned vectors and ask if there
%are more to erase after a first selection; then cut the matrix and take
%onyl the good ones for further calculations
while d==1
   figure(f2);
```

```
    [xr,yr,Pr] = impixel;
    clogbin_help(:,xr)=[];
    clogbin_std(:,xr)=[];
imagesc(clogbin_help)
%use the counter from above
yticks(ticks);
yticklabels(tlabels);
colorbar
title('Color-coded ACs')
ylabel('Time lag \tau [s]')
xlabel('AC chunks [a.u.]')
%replot the AC with selected ACs (2021-06-01)
figure(faca);
clf
plot( tlogbin, mean(clogbin_help,2), 'b--.' );
set(gca, 'XScale', 'log')
% Label axes
xlabel 'Time lag \tau [s]'
ylabel 'AC [a.u.]'
grid on
prompt = {'Enter selector 0 to not remove any lines or 1 to remove lines'};
dlgtitle = 'Input';
%dims = [1 35];
definput = {'0'};
answer = inputdlg(prompt,dlgtitle,dims,definput);
d=str2double(answer);
end

%now calculate the mean of all the logbinned autocorrelations
%here it is the same if first averaging and then logbinning or first
%logbinning of each chunk and then averaging over all af the chunks; not
%identical, but very similar
clogbinm(:,i)=mean(clogbin_help,2);

clogbinstd(:,i)=std(clogbin_help,1,2)/sqrt(size(clogbin_help,2));

%fit: here choose which parameters to keep constant and which ones to alter
%according to the selector input

[fitresult, gof] = createFit2D(tlogbin, clogbinm(:,i),clogbinstd(:,i) )
r(i,:)=coeffvalues(fitresult)

%ignore 0 standard deviation values just for the plotting by including NaN
%values
index=find(clogbinstd(:,i)==0);
clogbinstd(index,i)=NaN;

```

```
% Plot fit with data.
f4=figure( 'Name', 'Fitted autocorrelation' );
h = plot( fitresult, tlogbin, clogbinm(:,i),'b--.');
hold on;
errorbar(tlogbin, clogbinm(:,i), clogbinstd(:,i),'b','LineStyle','none');
legend( h, 'data', 'fit', 'Location', 'NorthEast' );
set(gca, 'XScale', 'log')
% Label axes
xlabel 'Time lag \tau [s]'
ylabel 'AC [a.u.]'
grid on
    end

%produce the string and get the output, display the fitted data in a matrix
str=["gamma", "n", "D", "w_xy", "wz", "offset"];
C={str;r};
celldisp(C)
end
```

bleaching_treatment.m

```
%option 1 removes only the bleaching by cutting off the beginning up to
%tbleach
if bleaching==1

%removes the from the image selected amount of first lines
[tbleach,y1,button] = ginput;
%removes the beginning with the bleached values
Ir=Ir(tbleach:end,:);

%option 2 removes beginning up to tbleach and does movemean filtering
elseif bleaching==2

%removes the selected amount of lines and does a filtering with a movemean
    filter
[tbleach,y1,button] = ginput;
%removes the beginning with the bleached values
Ir=Ir(tbleach:end,:);
    %choose filter parameters
prompt = {'Lower','Upper'};
dlgtitle = 'Enter filter parameter';
dims = [1 35];
definput = {'16384','16384'};
answer = inputdlg(prompt,dlgtitle,dims,definput);
filterp=str2double(answer);
```

```
M = movmean(Ir,[filterp(1) filterp(2)],1); %if there are less points avaiable in the beginning or the end it takes the amount of points avaiable, see documentation
Irmean=mean(Ir);
Ir=Ir-M;
Ir=Ir+Irmean;

%option 3 removes the first specified value lines (here to leave 5*65536
%chunks for analysis)
elseif bleaching==3

%just cuts off the lines at the specified value
prompt = {'Initial cut off'};
dlgtitle = 'Enter filter parameter';
dims = [1 35];
definput = {'180225'};
answer = inputdlg(prompt,dlgtitle,dims,definput);
tbleach=str2double(answer);
%removes the beginning with the bleached values
Ir=Ir(tbleach:end,:);

%option 4: cuts off the values up to a specified value and then does a
%movemean filtering
elseif bleaching==4

%cuts off the lines at the specified value and does a movemean filtering
%afterwards
prompt = {'Initial cut off'};
dlgtitle = 'Enter filter parameter';
dims = [1 35];
definput = {'180225'};
answer = inputdlg(prompt,dlgtitle,dims,definput);
tbleach=str2double(answer);
%removes the beginning with the bleached values
Ir=Ir(tbleach:end,:);
    %choose filter parameters
prompt = {'Lower','Upper'};
dlgtitle = 'Enter filter parameter';
dims = [1 35];
definput = {'32768','32768'};
answer = inputdlg(prompt,dlgtitle,dims,definput);
filterp=str2double(answer);
M = movmean(Ir,[filterp(1) filterp(2)],1); %if there are less points available in the beginning or the end it takes the amount of points avaiable, see documentation
Irmean=mean(Ir);
Ir=Ir-M;
```

```
Ir=Ir+Irmean;

%option 5: cuts off the values up to a specified value and then fits the averaged curve to a double exponential for correction
elseif bleaching==5

%just cuts off the lines at the specified value
prompt = {'Initial cut off'};
dlgtitle = 'Enter filter parameter';
dims = [1 35];
definput = {'180225'};
answer = inputdlg(prompt,dlgtitle,dims,definput);
tbleach=str2double(answer);
%removes the beginning with the bleached values
Ir=Ir(tbleach:end,:);

%creation of temporal vectors
tt=[0:1:size(Ir,1)-1]'*temp_res;
tt2=[0:1:size(imageviewerі,1)-1]'*temp_res*size(Ir,1)/1000;

%recalculation of bins depending on the cut-off size
for i=1:1000
    countercutf=floor(size(Ir,1)/1000);
    imageviewercutf(i,:)=mean(Ir((i-1)*countercutf+1:i*countercutf,:),1);
end

    %averages the data in 1000 chunks over time and then over all pixels
    %fits the result to a double exponential function and then subtracts
    %this function from the original data and adds the mean over time to
    %each pixel trace

Irs=mean(imageviewercutf,2);
irsstd=std(imageviewercutf,1,2);
Irm=mean(Ir,2);
Irmean=mean(Ir,1);
%prepares the data over time averaged data (1000) for the fit and fits it to the double exponential below
[xData, yData] = prepareCurveData( tt2, Irs );

% Set up fittype and options.
ft = fittype( 'afast*exp(-kfast*t)+aslow*exp(-kslow*t)+offset', 'independent', 't', 'dependent', 'y','coefficients', {'afast','kfast','aslow','kslow','offset'} );
opts = fitoptions( 'Method', 'NonlinearLeastSquares' );
opts.Display = 'Off';
opts.StartPoint = [1 1 1 1 0];
%opts.StartPoint =[36 0.5 9 1];
```

```
opts.Lower = [-Inf -Inf -Inf -Inf -Inf];
opts.Upper = [Inf Inf Inf Inf Inf];
%opts.Weights=weight;

% Fit model to data.
[fitexp, gofexp] = fit( xData, yData, ft, opts );

%calculation of the time trace by subtracting the fit from the original
%data
Irb=Ir-fitexp(tt);
Irbs=Irs-fitexp(tt2);
%asign new Ir
Ir=Irb+Irmean;

%option 6: cuts off the values up to a specified value and corrects each pixel individually by a double exponential
elseif bleaching==6

    %just cuts off the lines at the specified value
prompt = {'Initial cut off'};
dlgtitle = 'Enter filter parameter';
dims = [1 35];
definput = {'180225'};
answer = inputdlg(prompt,dlgtitle,dims,definput);
tbleach=str2double(answer);
%removes the beginning with the bleached values
Ir=Ir(tbleach:end,:);

%creation of temporal vectors
tt=[0:1:size(Ir,1)-1]'*temp_res;
tt2=[0:1:size(imageviewer i,1)-1]'*temp_res*size(Ir,1)/1000;
Irmean=mean(Ir,1);

%recalculation of bins depending on the cut-off size
for i=1:1000
    countercutf=floor(size(Ir,1)/1000);
    imageviewercutf(i,:)=mean(Ir((i-1)*countercutf+1:i*countercutf,:),1);
end

    %averages the data in 1000 chunks over time and fits the result to a
    %double exponential function for each pixel individually and then
    %subtracts this function from the original data and adds the mean over
    %time to each pixel trace

    %correction of individual fits and subtraction
for i=1:1:size(imageviewercutf,2)
     [xDatas, yDatas] = prepareCurveData( tt2, imageviewercutf(:,i) );
```

```

% Set up fittype and options.
fts = fittype( 'afast*exp(-kfast*t)+aslow*exp(-kslow*t)+offset', 'independent',
     't', 'dependent', 'y','coefficients', {'afast','kfast','aslow','kslow','
    offset'} );
optss = fitoptions( 'Method', 'NonlinearLeastSquares' );
optss.Display = 'Off';
optss.StartPoint = [1 1 1 1 0];
%opts.StartPoint =[36 0.5 9 1];
%optss.Lower = [-Inf -Inf -Inf -Inf -Inf];
%optss.Upper = [Inf Inf Inf Inf Inf];
optss.Lower = [-5 -5 -5 -5 -5];
optss.Upper = [10 10 10 10 10];
%opts.Weights=weight;

% Fit model to data.
[fitexps, gofexps] = fit( xDatas, yDatas, fts, optss );

%save the fits
Irind(:,i)=fitexps(tt);
end
%calculate the difference and then add the mean of each curve
Irdif=Ir-Irind;
Irindmean=Irdif+Irmean;

%assign Ir
Ir=Irindmean;

%option 7: cuts off the values up to a specified value and then fits the
    averaged curve to a double exponential and uses a formula in Ries paper
    for correction
elseif bleaching==7

       %just cuts off the lines at the specified value
prompt = {'Initial cut off'};
dlgtitle = 'Enter filter parameter';
dims = [1 35];
definput = {'180225'};
answer = inputdlg(prompt,dlgtitle,dims,definput);
tbleach=str2double(answer);
%removes the beginning with the bleached values
Ir=Ir(tbleach:end,:);

%creation of temporal vectors
tt=[0:1:size(Ir,1)-1]'*temp_res;
tt2=[0:1:size(imageviewer i,1)-1]'*temp_res*size(Ir,1)/1000;

```

```
%recalculation of bins depending on the cut-off size
for i=1:1000
    countercutf=floor(size(Ir,1)/1000);
    imageviewercutf(i,:)=mean(Ir((i-1)*countercutf+1:i*countercutf,:),1);
end

   %fit of double exponential to indvidual lines
for i=1:1:size(imageviewercutf,2)
     [xData, yData] = prepareCurveData( tt2, imageviewercutf(:,i) );

% Set up fittype and options.
fts = fittype( ’a1*exp(-k1*t)+a2*exp(-k2*t)+a0’, ’independent’, ’t’, ’dependent’, ’y’,’coefficients’, {’a1’,’k1’,’a2’,’k2’,’a0’} );
optss = fitoptions( ’Method’, ’NonlinearLeastSquares’ );
optss.Display = ’Off’;
optss.StartPoint = [1 1 1 1 0];
%opts.StartPoint =[36 0.5 9 1];
% optss.Lower = [-Inf -Inf -Inf -Inf -Inf];
% optss.Upper = [Inf Inf Inf Inf Inf];
optss.Lower = [-1 -1 -1 -1 -10];
optss.Upper = [10 10 10 10 10];
%opts.Weights=weight;

% Fit model to data.
[fitexps, gofexps] = fit( xData, yData, fts, optss );

%save the fits
Irind(:,i)=fitexps(tt);
end

 %correction from the Ries paper
intenscorr=Ir./sqrt(Irind./Irind(1,:))+Irind(1,:).*(1-sqrt(Irind./Irind(1,:)));

Ir=intenscorr;

end

%recalculation of bins depending on the cut-off size
for i=1:1000
    counter2=floor(size(Ir,1)/1000);
    imageviewer2(i,:)=mean(Ir((i-1)*counter2+1:i*counter2,:),1);
end

f12=figure(’Name’,’Averaged line profile’)
%imagesc(imageviewer);
plot([0:1:size(imageviewer2)-1]*size(Ir,1)/1000,mean(imageviewer2,2));
```

```
%colorbar
%set(gca, 'YScale', 'log')
title('Temorally averaged intensity profile (1000 bins)')
ylabel('Average intensity [a.u.]')
xlabel('bins/lines')
```

average_acrossTT.m

```
before_selection=mean(clogbin_meanchunk,2);
before_selection_std=std(clogbin_meanchunk,1,2)/sqrt(size(clogbin_meanchunk,2)
    );

%plot correlation curve
f3=figure( 'Name', 'averaged and logged' );
h3=plot( tlogbin, before_selection, 'b--.' );
hold on;
errorbar(tlogbin, before_selection, before_selection_std,'b','LineStyle','none
    ');
legend( h3, 'data', 'Location', 'NorthEast' );
set(gca, 'XScale', 'log')
% Label axes
xlabel 'Time lag \tau [s]'
ylabel 'AC [a.u.]'
grid on

%plot with fit
[fitresultaverage, gofaverage] = createFit2D(tlogbin, before_selection,
    before_selection_std)
raverage=coeffvalues(fitresultaverage)

% ignore 0 standard deviation values just for plotting by including NaN
% values
% index=find(clogbin_stdchunk(:,i)==0);
% clogbin_stdchunk(index,i)=NaN;

% Plot fit with data.
f4=figure( 'Name', 'Fitted autocorrelation' );
h4 = plot( fitresultaverage, tlogbin, before_selection, 'b--.' );
hold on;
errorbar(tlogbin, before_selection, before_selection_std,'b','LineStyle','none
    ');
legend( h4, 'data', 'fit', 'Location', 'NorthEast' );
set(gca, 'XScale', 'log')
% Label axes
xlabel 'Time lag \tau [s]'
ylabel 'AC [a.u.]'
grid on
```

selection_fit_TT.m

```
%in case there are more than 1 image chunk
if size(ACs,2)>1
    %in this part all the lines from each image chunk (tubule) get
    %concatenated. This way there is a multidimensional array as if all the
        chunks were just 1 image. It's the same as with 1 image chunk. This is
        the final form in which the matrix is also
    %given to ac_selectorp when there is only 1 image chunk. Then it can be
    %resumed where left off.
chelp=cell2mat(ACs(1));
chelp2=[];
for i=2:size(ACs,2)
    c2=cell2mat(ACs(i));
    chelp=cat(3,chelp,c2);
end
else
chelp=Clogbin;
end

%do the line autocorrelation selection
    [Clogbinm,CStd,Clog_orig,Clog_final] = ac_selectorp_axis(tlogbin, chelp);

%plot the correlation curve
fav=figure( 'Name', 'averaged and logged' );
hav=plot( tlogbin, Clogbinm, 'b--.' );
hold on;
errorbar(tlogbin, Clogbinm, CStd,'b','LineStyle','none');
legend( hav, 'data', 'Location', 'NorthEast' );
set(gca, 'XScale', 'log')
% Label axes
xlabel 'Time lag \tau [s]'
ylabel 'AC [a.u.]'
grid on

%plot with fit
[fitresultav, gofav] = createFit1D(tlogbin, Clogbinm,CStd)
rav=coeffvalues(fitresultav)

% ignore 0 standard deviation values, just for plotting by including NaN
% values
% index=find(clogbin_stdchunk(:,i)==0);
% clogbin_stdchunk(index,i)=NaN;

% Plot fit with data.
ffit=figure( 'Name', 'Fitted autocorrelation' );
hfit = plot( fitresultav, tlogbin, Clogbinm, 'b--.' );
```

```
hold on;
errorbar(tlogbin, Clogbinm, CStd,'b','LineStyle','none');
legend( hfit, 'data', 'fit', 'Location', 'NorthEast' );
set(gca, 'XScale', 'log')
% Label axes
xlabel 'Time lag \tau [s]'
ylabel 'AC [a.u.]'
grid on
```

ac_selectorp_axis.m

```
function [Clogbinm,CStd,Clog_orig,Clog_final] = ac_selectorp_axis(tlogbin,
    Clogbin)
Clog_final=[];
for i=1:1:size(Clogbin,2)
    Clog_orig(:,:,i)=Clogbin(:,i,:);
    Clog_help=[];
    Clog_help (:,:)=Clog_orig(:,:,i);

    %plot the AC before the selection of lines
faca=figure('Name','ACs adjusted')
plot( tlogbin, mean(Clog_help,2), 'b--.' );
set(gca, 'XScale', 'log')
% Label axes
xlabel 'Time lag \tau [s]'
ylabel 'AC [a.u.]'
grid on
%moves the position on the screen
movegui(faca,'east');
%plots the image as a colormap with each autocorrelation going from the top
%to the bottom (over time) and each chunks along the x-axis
fima=figure('Name','Color-coded ACs')
%assigns correct temporal axis labels
%need to calculate the ticks and labels in a function otherwise it messes
%up counter i
[ticks,tlabels]=assign_correct_labels(tlogbin, Clog_help);
imagesc(Clog_help);
yticks(ticks);
yticklabels(tlabels);
colorbar
%set(gca, 'YScale', 'log')
title('Color-coded ACs')
ylabel('Time lag \tau [s]')
xlabel('AC [a.u.]')
%impixelinfo
%moves the position on the screen
movegui(fima,'west');
```

```
%have the selection if there are any bad autocorrelation chunks
prompt = {'Enter selector 0 to not remove any lines or 1 to remove lines'};
dlgtitle = 'Input';
dims = [1 35];
definput = {'0'};
answer = inputdlg(prompt,dlgtitle,dims,definput);
d=str2double(answer);

%here only remove the colums from the logbinned vectors and ask if there
%are more to erase after a first selection; then cut the matrix and take
%only the good ones for further calculations
while d==1
   figure(fima);
   [px,yp,Pp] = impixel;
    Clog_help(:,px)=[];
%corrects the time axis of the imagesc
imagesc(Clog_help)
yticks(ticks);
yticklabels(tlabels);
colorbar
title('Color-coded ACs')
ylabel('Time lag \tau [s]')
xlabel('AC [a.u.]')
%impixelinfo
%replot the AC
figure(faca);
clf
plot( tlogbin, mean(Clog_help,2), 'b--.' );
set(gca, 'XScale', 'log')
% Label axes
xlabel 'Time lag \tau [s]'
ylabel 'AC [a.u.]'
grid on
prompt = {'Enter selector 0 to not remove any lines or 1 to remove lines'};
dlgtitle = 'Input';
%dims = [1 35];
definput = {'0'};
answer = inputdlg(prompt,dlgtitle,dims,definput);
d=str2double(answer);
end
%calculation of the mean over the pixels for each chunk
Clog_final=[Clog_final Clog_help];
end
%calculation of the mean over the last 2 dimensions
Clogbinm=mean(Clog_final,2);
CStd=std(Clog_final,1,2)/sqrt(size(Clog_final,2)); %here 0 means that the division is done with n-1 instead of n
```

```
end
```

normalization_ac.m

```
%determine the amplitude at 0 at the fit and normalize the entire data to
%it

%calculation of normalization values
clognorm=Clogbinm/fitresultav(0);

%normalization of error (through error propagation)
stdnorm=CStd/fitresultav(0);

% Plot fit with data.
fnorm=figure( 'Name', 'normalized autocorrelation' );
plot( tlogbin, clognorm, 'b--.' );
hold on;
plot( tlogbin,fitresultav(tlogbin)/fitresultav(0) );
errorbar(tlogbin, clognorm, stdnorm,'b','LineStyle','none');
legend( 'data', 'fit', 'Location', 'NorthEast' );
set(gca, 'XScale', 'log')
% Label axes
xlabel 'Time lag \tau [s]'
ylabel 'AC [a.u.]'
grid on
```

assign_correct_labels.m

```
function [jac,tr]=assign_correct_labels(tlogbin, clogbin)


%calculate the decimal vector of the time scale for imagesc
tr=10.^(ceil(log10(min(tlogbin))):1:floor(log10(max(tlogbin))));
if floor(max(tlogbin)/10^floor(log10(max(tlogbin))))>floor(log10(max(tlogbin))
    )
    %in case there is one more after the last decade insert it additionally
tr=[tr, max(tr)*floor(max(tlogbin)/10^floor(log10(max(tlogbin))))];
end

%get the indices of the value closest to the decades
for j=1:length(tr)
[kac(j),jac(j)]=min(abs(tlogbin-tr(j)));
end


%calculate the image and assign the ticks and the labels (where this is
%just a rounded value to make it look nicer (especially the last value was
%rounded from 28.18 to 30)
```

```
%imagesc(clogbin_help);
%yticks(jac);
%yticklabels(10.^round(log10(t(j))))
%yticklabels(tr);

end
```

read_tif2.m

```
%this function reads tif images and combines multi-page images to 1
function concimaged = read_tif2(imagestring)
%read the entire multi-image stack of tif
FileTif=imagestring;
InfoImage=imfinfo(FileTif);
mImage=InfoImage(1).Width;
nImage=InfoImage(1).Height;
NumberImages=length(InfoImage);
FinalImage=zeros(nImage,mImage,NumberImages,'uint16');

TifLink = Tiff(FileTif, 'r');
for i=1:NumberImages
   TifLink.setDirectory(i);
   FinalImage(:,:,i)=TifLink.read();
end
TifLink.close();

%combine the multi-images to 1 image
[m n k]=size(FinalImage);
if k==1
concimage=FinalImage(:,:,1);
else
    concimage=FinalImage(:,:,1);
for i=2:k
    concimage=[concimage;FinalImage(:,:,i)];
end
end

%convert to double
concimaged=double(concimage);
end
```

createFit2D.m

```
function [fitresult, gof] = createFit2D(t, c,std)

%presettings
prompt = {'Enter gamma:','Enter n:','Enter D:','Enter w_{xy}:','Enter offset',
    'Enter selector:'};
```

```
dlgtitle = 'Input';
dims = [1 35];
definput = {'0.35','50','0.15','0.33','0.001','2'};
answer = inputdlg(prompt,dlgtitle,dims,definput)
d=str2double(answer)

%assign input variables to readable variables
gamma=d(1);
n=d(2);
D=d(3);
wxy=d(4);
offset=d(5);
fix=d(6);

%create weights out of standard deviation by weighing the ones with a low
%standard deviation more than the other way around;replace the Inf values
%with 0 to give the first values low importance
weight=1./std;
index=find(weight==Inf);
weight(index)=0;

%choose which values to be fitted and which to keep constant
%0: everything free fit
%1: only gamma fixed
%2: gamma and wxy fixed
%3: gamma, wxy and offset fixed
%4: gamma and D fixed
%5: gamma, n and D fixed
if fix==0
    gammastart=0.35;
    gammalow=0;
    gammahigh=+Inf;
    nstart=50;
    nlow=0;
    nhigh=+Inf;
    Dstart=0.15;
    Dlow=0;
    Dhigh=+Inf;
    wxystart=0.25;
    wxylow=0;
    wxyhigh=+Inf;
    offsetstart=0.000001;
    offsetlow=-5;
    offsethigh=5;
elseif fix==1
        gammastart=gamma;
    gammalow=gamma;
```

```
gammahigh=gamma;
nstart=50;
nlow=0;
nhigh=+Inf;
Dstart=0.15;
Dlow=0;
Dhigh=+Inf;
wxystart=0.25;
wxylow=0;
wxyhigh=+Inf;
offsetstart=0;
offsetlow=-5;
offsethigh=5;
elseif fix==2
        gammastart=gamma;
gammalow=gamma;
gammahigh=gamma;
nstart=50;
nlow=0;
nhigh=+Inf;
Dstart=0.15;
Dlow=0;
Dhigh=+Inf;
wxystart=wxy;
wxylow=wxy;
wxyhigh=wxy;
offsetstart=0.0000001;
offsetlow=-5;
offsethigh=5;
elseif fix==3
        gammastart=gamma;
gammalow=gamma;
gammahigh=gamma;
nstart=50;
nlow=0;
nhigh=+Inf;
Dstart=0.15;
Dlow=0;
Dhigh=+Inf;
wxystart=wxy;
wxylow=wxy;
wxyhigh=wxy;
offsetstart=offset;
offsetlow=offset;
offsethigh=offset;
elseif fix==4
        gammastart=gamma;
```

```
    gammalow=gamma;
    gammahigh=gamma;
    nstart=50;
    nlow=0;
    nhigh=+Inf;
    Dstart=D;
    Dlow=D;
    Dhigh=D;
    wxystart=0.25;
    wxylow=0;
    wxyhigh=+Inf;
    offsetstart=0.0000001;
    offsetlow=-5;
    offsethigh=5;
    elseif fix==5
            gammastart=gamma;
    gammalow=gamma;
    gammahigh=gamma;
    nstart=n;
    nlow=n;
    nhigh=n;
    Dstart=D;
    Dlow=D;
    Dhigh=D;
    wxystart=0.25;
    wxylow=0;
    wxyhigh=+Inf;
    offsetstart=0.0000001;
    offsetlow=-5;
    offsethigh=5;
end

%% Fit:
%only prepares the vectors to be column vectors
%here transpose the vectors only
[xData, yData] = prepareCurveData( t, c );

% Set up fittype and options.
ft = fittype( '(gamma/n)*(1./(1+4*D*x/(wxy^2)))+offset', 'independent', 'x', 'dependent', 'y','coefficients', {'gamma','n','D','wxy','offset'} );
opts = fitoptions( 'Method', 'NonlinearLeastSquares' );
opts.Display = 'Off';
opts.StartPoint = [gammastart nstart Dstart wxystart offsetstart];
opts.Lower = [gammalow nlow Dlow wxylow offsetlow];
opts.Upper = [gammahigh nhigh Dhigh wxyhigh offsethigh];
opts.Weights=weight;

```

```
% Fit model to data.
[fitresult, gof] = fit( xData, yData, ft, opts );
end
```

createFit2D_blinking.m

```
function [fitresult, gof] = createFit2D_blinking(t, c,std)

%presettings
prompt = {'Enter gamma:','Enter n:','Enter D:','Enter w_{xy}:','Enter offset',
    'Enter selector:','Enter fraction of triplet state:','Enter triplet state
    constant:'};
dlgtitle = 'Input';
dims = [1 35];
definput = {'0.35','50','0.1','0.33','0.001','2','.2','0.1'};
answer = inputdlg(prompt,dlgtitle,dims,definput)
d=str2double(answer)

gamma=d(1);
n=d(2);
D=d(3);
wxy=d(4);
offset=d(5);
fix=d(6);
T=d(7);
tauT=d(8);

%create weights out of standard deviation by weighing the ones with a low
%standard deviation more than the other way around;replace the Inf values
%with 0 to give the first values low importance
weight=1./std;
index=find(weight==Inf);
weight(index)=0;

if fix==0
    gammastart=0.35;
    gammalow=0;
    gammahigh=+Inf;
    nstart=50;
    nlow=0;
    nhigh=+Inf;
    Dstart=0.15;
    Dlow=0;
    Dhigh=+Inf;
    wxystart=0.25;
    wxylow=0;
    wxyhigh=+Inf;
```

```
    offsetstart=0.000001;
    offsetlow=-5;
    offsethigh=5;
    Tstart=T;
    Tlow=0;
    Thigh=1;
    tauTstart=tauT;
    tauTlow=0;
    tauThigh=100;
elseif fix==1
       gammastart=gamma;
    gammalow=gamma;
    gammahigh=gamma;
    nstart=50;
    nlow=0;
    nhigh=+Inf;
    Dstart=0.15;
    Dlow=0;
    Dhigh=+Inf;
    wxystart=0.25;
    wxylow=0;
    wxyhigh=+Inf;
    offsetstart=0;
    offsetlow=-5;
    offsethigh=5;
    Tstart=T;
    Tlow=0;
    Thigh=1;
    tauTstart=tauT;
    tauTlow=0;
    tauThigh=100;
    elseif fix==2
            gammastart=gamma;
    gammalow=gamma;
    gammahigh=gamma;
    nstart=50;
    nlow=0;
    nhigh=+Inf;
    Dstart=0.15;
    Dlow=0;
    Dhigh=+Inf;
    wxystart=wxy;
    wxylow=wxy;
    wxyhigh=wxy;
    offsetstart=0.0000001;
    offsetlow=-5;
    offsethigh=5;
```

```
    Tstart=T;
    Tlow=0;
    Thigh=1;
    tauTstart=tauT;
    tauTlow=0;
    tauThigh=100;
    elseif fix==3
            gammastart=gamma;
    gammalow=gamma;
    gammahigh=gamma;
    nstart=50;
    nlow=0;
    nhigh=+Inf;
    Dstart=0.15;
    Dlow=0;
    Dhigh=+Inf;
    wxystart=wxy;
    wxylow=wxy;
    wxyhigh=wxy;
    offsetstart=offset;
    offsetlow=offset;
    offsethigh=offset;
    Tstart=T;
    Tlow=0;
    Thigh=1;
    tauTstart=tauT;
    tauTlow=0;
    tauThigh=100;
    elseif fix==4
            gammastart=gamma;
    gammalow=gamma;
    gammahigh=gamma;
    nstart=50;
    nlow=0;
    nhigh=+Inf;
    Dstart=D;
    Dlow=D;
    Dhigh=D;
    wxystart=0.25;
    wxylow=0;
    wxyhigh=+Inf;
    offsetstart=0.0000001;
    offsetlow=-5;
    offsethigh=5;
    Tstart=T;
    Tlow=0;
    Thigh=1;
```

```
tauTstart=tauT;
tauTlow=0;
tauThigh=100;
elseif fix==5
        gammastart=gamma;
gammalow=gamma;
gammahigh=gamma;
nstart=n;
nlow=n;
nhigh=n;
Dstart=D;
Dlow=D;
Dhigh=D;
wxystart=0.25;
wxylow=0;
wxyhigh=+Inf;
offsetstart=0.0000001;
offsetlow=-5;
offsethigh=5;
Tstart=T;
Tlow=0;
Thigh=1;
tauTstart=tauT;
tauTlow=0;
tauThigh=100;
  elseif fix==6
        gammastart=gamma;
gammalow=gamma;
gammahigh=gamma;
nstart=50;
nlow=0;
nhigh=+Inf;
Dstart=0.15;
Dlow=0;
Dhigh=+Inf;
wxystart=wxy;
wxylow=wxy;
wxyhigh=wxy;
offsetstart=0.0000001;
offsetlow=-5;
offsethigh=5;
Tstart=T;
Tlow=0;
Thigh=1;
tauTstart=tauT;
tauTlow=tauT;
tauThigh=tauT;
```

```
end

%% Fit:
%only prepares the vectors to be column vectors
%here transpose the vectors only
[xData, yData] = prepareCurveData( t, c );

% Set up fittype and options.
ft = fittype( '(gamma/n)*(1./(1+4*D*x/(wxy^2))).*((1-T+T*exp(-x/tauT))/(1-T))+
    offset', 'independent', 'x', 'dependent', 'y','coefficients', {'gamma','n',
    'D','wxy','offset','T','tauT'} );
opts = fitoptions( 'Method', 'NonlinearLeastSquares' );
opts.Display = 'Off';
opts.StartPoint = [gammastart nstart Dstart wxystart offsetstart Tstart
    tauTstart];
opts.Lower = [gammalow nlow Dlow wxylow offsetlow Tlow tauTlow];
opts.Upper = [gammahigh nhigh Dhigh wxyhigh offsethigh Thigh tauThigh];
opts.Weights=weight;

% Fit model to data.
[fitresult, gof] = fit( xData, yData, ft, opts );
end
```

createFit1D.m

```
function [fitresult, gof] = createFit1D(t, c,std)

%presettings
prompt = {'Enter gamma:','Enter n:','Enter D:','Enter w_{xy}:','Enter offset',
    'Enter selector:'};
dlgtitle = 'Input';
dims = [1 35];
definput = {'0.35','50','0.15','0.33','0.001','2'};
answer = inputdlg(prompt,dlgtitle,dims,definput)
d=str2double(answer)

gamma=d(1);
n=d(2);
D=d(3);
wxy=d(4);
offset=d(5);
fix=d(6);

%create weights out of standard deviation by weighing the ones with a low
%standard deviation more than the other way around;replace the Inf values
%with 0 to give the first values low importance
weight=1./std;
```

```
index=find(weight==Inf);
weight(index)=0;

if fix==0
    gammastart=0.35;
    gammalow=0;
    gammahigh=+Inf;
    nstart=50;
    nlow=0;
    nhigh=+Inf;
    Dstart=0.15;
    Dlow=0;
    Dhigh=+Inf;
    wxystart=0.25;
    wxylow=0;
    wxyhigh=+Inf;
    offsetstart=0.000001;
    offsetlow=-5;
    offsethigh=5;
elseif fix==1
        gammastart=gamma;
    gammalow=gamma;
    gammahigh=gamma;
    nstart=50;
    nlow=0;
    nhigh=+Inf;
    Dstart=0.15;
    Dlow=0;
    Dhigh=+Inf;
    wxystart=0.25;
    wxylow=0;
    wxyhigh=+Inf;
    offsetstart=0;
    offsetlow=-5;
    offsethigh=5;
    elseif fix==2
             gammastart=gamma;
    gammalow=gamma;
    gammahigh=gamma;
    nstart=50;
    nlow=0;
    nhigh=+Inf;
    Dstart=0.15;
    Dlow=0;
    Dhigh=+Inf;
    wxystart=wxy;
    wxylow=wxy;
```

```
    wxyhigh=wxy;
    offsetstart=0.0000001;
    offsetlow=-5;
    offsethigh=5;
    elseif fix==3
            gammastart=gamma;
    gammalow=gamma;
    gammahigh=gamma;
    nstart=50;
    nlow=0;
    nhigh=+Inf;
    Dstart=0.15;
    Dlow=0;
    Dhigh=+Inf;
    wxystart=wxy;
    wxylow=wxy;
    wxyhigh=wxy;
    offsetstart=offset;
    offsetlow=offset;
    offsethigh=offset;
    elseif fix==4
            gammastart=gamma;
    gammalow=gamma;
    gammahigh=gamma;
    nstart=50;
    nlow=0;
    nhigh=+Inf;
    Dstart=D;
    Dlow=D;
    Dhigh=D;
    wxystart=0.25;
    wxylow=0;
    wxyhigh=+Inf;
    offsetstart=0.0000001;
    offsetlow=-5;
    offsethigh=5;
    elseif fix==5
            gammastart=gamma;
    gammalow=gamma;
    gammahigh=gamma;
    nstart=n;
    nlow=n;
    nhigh=n;
    Dstart=D;
    Dlow=D;
    Dhigh=D;
    wxystart=0.25;
```

```
    wxylow=0;
    wxyhigh=+Inf;
    offsetstart=0.0000001;
    offsetlow=-5;
    offsethigh=5;
end

%% Fit
%only prepares the vectors to be column vectors
%here transpose the vectors only
[xData, yData] = prepareCurveData( t, c );

% Set up fittype and options.
ft = fittype( ’(gamma/n)*(1./sqrt(1+4*D*x/(wxy^2)))+offset’, ’independent’, ’x’, ’dependent’, ’y’,’coefficients’, {’gamma’,’n’,’D’,’wxy’,’offset’} );
opts = fitoptions( ’Method’, ’NonlinearLeastSquares’ );
opts.Display = ’Off’;
opts.StartPoint = [gammastart nstart Dstart wxystart offsetstart];
opts.Lower = [gammalow nlow Dlow wxylow offsetlow];
opts.Upper = [gammahigh nhigh Dhigh wxyhigh offsethigh];
opts.Weights=weight;

% Fit model to data.
[fitresult, gof] = fit( xData, yData, ft, opts );
end
```

createFit1D_blinking.m

```
function [fitresult, gof] = createFit1D_blinking(t, c,std)

%presettings
prompt = {’Enter gamma:’,’Enter n:’,’Enter D:’,’Enter w_{xy}:’,’Enter offset’,’Enter selector:’,’Enter fraction of triplet state:’,’Enter triplet state constant:’};
dlgtitle = ’Input’;
dims = [1 35];
definput = {’0.35’,’50’,’0.1’,’0.33’,’0.001’,’2’,’.2’,’0.1’};
answer = inputdlg(prompt,dlgtitle,dims,definput)
d=str2double(answer)

gamma=d(1);
n=d(2);
D=d(3);
wxy=d(4);
offset=d(5);
fix=d(6);
T=d(7);
```

```
tauT=d(8);

%create weights out of standard deviation by weighing the ones with a low
%standard deviation more than the other way around;replace the Inf values
%with 0 to give the first values low importance
weight=1./std;
index=find(weight==Inf);
weight(index)=0;

if fix==0
    gammastart=0.35;
    gammalow=0;
    gammahigh=+Inf;
    nstart=50;
    nlow=0;
    nhigh=+Inf;
    Dstart=0.15;
    Dlow=0;
    Dhigh=+Inf;
    wxystart=0.25;
    wxylow=0;
    wxyhigh=+Inf;
    offsetstart=0.000001;
    offsetlow=-5;
    offsethigh=5;
    Tstart=T;
    Tlow=0;
    Thigh=1;
    tauTstart=tauT;
    tauTlow=0;
    tauThigh=100;
elseif fix==1
        gammastart=gamma;
    gammalow=gamma;
    gammahigh=gamma;
    nstart=50;
    nlow=0;
    nhigh=+Inf;
    Dstart=0.15;
    Dlow=0;
    Dhigh=+Inf;
    wxystart=0.25;
    wxylow=0;
    wxyhigh=+Inf;
    offsetstart=0;
    offsetlow=-5;
    offsethigh=5;
```

```
Tstart=T;
Tlow=0;
Thigh=1;
tauTstart=tauT;
tauTlow=0;
tauThigh=100;
elseif fix==2
        gammastart=gamma;
gammalow=gamma;
gammahigh=gamma;
nstart=50;
nlow=0;
nhigh=+Inf;
Dstart=0.15;
Dlow=0;
Dhigh=+Inf;
wxystart=wxy;
wxylow=wxy;
wxyhigh=wxy;
offsetstart=0.0000001;
offsetlow=-5;
offsethigh=5;
Tstart=T;
Tlow=0;
Thigh=1;
tauTstart=tauT;
tauTlow=0;
tauThigh=100;
elseif fix==3
        gammastart=gamma;
gammalow=gamma;
gammahigh=gamma;
nstart=50;
nlow=0;
nhigh=+Inf;
Dstart=0.15;
Dlow=0;
Dhigh=+Inf;
wxystart=wxy;
wxylow=wxy;
wxyhigh=wxy;
offsetstart=offset;
offsetlow=offset;
offsethigh=offset;
Tstart=T;
Tlow=0;
Thigh=1;
```

```
    tauTstart=tauT;
    tauTlow=0;
    tauThigh=100;
    elseif fix==4
            gammastart=gamma;
    gammalow=gamma;
    gammahigh=gamma;
    nstart=50;
    nlow=0;
    nhigh=+Inf;
    Dstart=D;
    Dlow=D;
    Dhigh=D;
    wxystart=0.25;
    wxylow=0;
    wxyhigh=+Inf;
    offsetstart=0.0000001;
    offsetlow=-5;
    offsethigh=5;
    Tstart=T;
    Tlow=0;
    Thigh=1;
    tauTstart=tauT;
    tauTlow=0;
    tauThigh=100;
    elseif fix==5
            gammastart=gamma;
    gammalow=gamma;
    gammahigh=gamma;
    nstart=n;
    nlow=n;
    nhigh=n;
    Dstart=D;
    Dlow=D;
    Dhigh=D;
    wxystart=0.25;
    wxylow=0;
    wxyhigh=+Inf;
    offsetstart=0.0000001;
    offsetlow=-5;
    offsethigh=5;
    Tstart=T;
    Tlow=0;
    Thigh=1;
    tauTstart=tauT;
    tauTlow=0;
    tauThigh=100;
```

```
     elseif fix==6
            gammastart=gamma;
    gammalow=gamma;
    gammahigh=gamma;
    nstart=50;
    nlow=0;
    nhigh=+Inf;
    Dstart=0.15;
    Dlow=0;
    Dhigh=+Inf;
    wxystart=wxy;
    wxylow=wxy;
    wxyhigh=wxy;
    offsetstart=0.0000001;
    offsetlow=-5;
    offsethigh=5;
    Tstart=T;
    Tlow=0;
    Thigh=1;
    tauTstart=tauT;
    tauTlow=tauT;
    tauThigh=tauT;
end

%% Fit:
%only prepares the vectors to be column vectors
%here transpose the vectors only
[xData, yData] = prepareCurveData( t, c );

% Set up fittype and options.
ft = fittype( ’(gamma/n)*(1./sqrt(1+4*D*x/(wxy^2))).*((1-T+T*exp(-x/tauT))/(1-T))+offset’, ’independent’, ’x’, ’dependent’, ’y’,’coefficients’, {’gamma’,’n’,’D’,’wxy’,’offset’,’T’,’tauT’} );
opts = fitoptions( ’Method’, ’NonlinearLeastSquares’ );
opts.Display = ’Off’;
opts.StartPoint = [gammastart nstart Dstart wxystart offsetstart Tstart tauTstart];
opts.Lower = [gammalow nlow Dlow wxylow offsetlow Tlow tauTlow];
opts.Upper = [gammahigh nhigh Dhigh wxyhigh offsethigh Thigh tauThigh];
opts.Weights=weight;

% Fit model to data.
[fitresult, gof] = fit( xData, yData, ft, opts );
end
```

createFit_exponential.m

```
function [fitresult, gof] = createFit_exponential(t, c,std)

%presettings
prompt = {'Enter n:','Enter offset','Enter selector:','Enter fraction of
    triplet state:','Enter triplet state constant:'};
dlgtitle = 'Input';
dims = [1 35];
definput = {'50','0.001','2','.2','0.1'};
answer = inputdlg(prompt,dlgtitle,dims,definput)
d=str2double(answer)

n=d(1);
offset=d(2);
fix=d(3);
T=d(4);
tauT=d(5);

%create weights out of standard deviation by weighing the ones with a low
%standard deviation more than the other way around;replace the Inf values
%with 0 to give the first values low importance
weight=1./std;
index=find(weight==Inf);
weight(index)=0;

if fix==0
    nstart=50;
    nlow=0;
    nhigh=+Inf;
    offsetstart=0.000001;
    offsetlow=-5;
    offsethigh=5;
    Tstart=T;
    Tlow=0;
    Thigh=1;
    tauTstart=tauT;
    tauTlow=0;
    tauThigh=100;
elseif fix==1
    nstart=50;
    nlow=0;
    nhigh=+Inf;
    offsetstart=0;
    offsetlow=-5;
    offsethigh=5;
    Tstart=T;
```

```
    Tlow=0;
    Thigh=1;
    tauTstart=tauT;
    tauTlow=0;
    tauThigh=100;
    elseif fix==2
    nstart=50;
    nlow=0;
    nhigh=+Inf;
    offsetstart=0.0000001;
    offsetlow=-5;
    offsethigh=5;
    Tstart=T;
    Tlow=0;
    Thigh=1;
    tauTstart=tauT;
    tauTlow=0;
    tauThigh=100;
    elseif fix==3
    nstart=50;
    nlow=0;
    nhigh=+Inf;
    offsetstart=offset;
    offsetlow=offset;
    offsethigh=offset;
    Tstart=T;
    Tlow=0;
    Thigh=1;
    tauTstart=tauT;
    tauTlow=0;
    tauThigh=100;
    elseif fix==4
    nstart=50;
    nlow=0;
    nhigh=+Inf;
    offsetstart=0.0000001;
    offsetlow=-5;
    offsethigh=5;
    Tstart=T;
    Tlow=0;
    Thigh=1;
    tauTstart=tauT;
    tauTlow=0;
    tauThigh=100;
    elseif fix==5
    nstart=n;
    nlow=n;
```

```
    nhigh=n;
    offsetstart=0.0000001;
    offsetlow=-5;
    offsethigh=5;
    Tstart=T;
    Tlow=0;
    Thigh=1;
    tauTstart=tauT;
    tauTlow=0;
    tauThigh=100;
end

%% Fit:
%only prepares the vectors to be column vectors
%here transpose the vectors only
[xData, yData] = prepareCurveData( t, c );

% Set up fittype and options.
%fit of bleaching T=B
ft = fittype( '1/n*((1-T+T*exp(-x/tauT)))+offset', 'independent', 'x', '
    dependent', 'y','coefficients', {'n','offset','T','tauT'} );
%Triplet state term without diffusion fitting function
%ft = fittype( '1/n*((1-T+T*exp(-x/tauT))/(1-T))+offset', 'independent', 'x',
    'dependent', 'y','coefficients', {'n','offset','T','tauT'} );
opts = fitoptions( 'Method', 'NonlinearLeastSquares' );
opts.Display = 'Off';
opts.StartPoint = [nstart offsetstart Tstart tauTstart];
opts.Lower = [nlow offsetlow Tlow tauTlow];
opts.Upper = [nhigh offsethigh Thigh tauThigh];
opts.Weights=weight;

% Fit model to data.
[fitresult, gof] = fit( xData, yData, ft, opts );
end
```

autocorrflb.m

```
%autocorrfl floors d if it is not of the right size and ignores the data
%which are too much at the end; it also doesn't initialize g; autocorr does
%both of the things
function [t,c,g,m]=autocorrflb(data,filter,time)
%check if value is of type double and convert it if necessary
if isa(data,'double')==1
    data=data;
else
    data=double(data);
end
```

```

%%
%define the amount of pieces in which the column is cut = filtering
v=filter;
d=floor(length(data)/v);
%create/initialize a vector which is of the desired length with 2*d-1

%doesn't need the initialization
%g=zeros([v 2*d-1]); %pad at least with 2*length-1, bc that's what the
%convoluted signal needs to be linear
%g=zeros([v 4*d]); %only pad with 2*length-1 bc everything above is too
%high and everything below too short
if isempty(time)
ts=0.005;
else ts=time;
end

%%
%for each piece of the vector calculate the correlation via fft with
%zero-padding
for i=1:1:v
    %first part is to cut the vector into pieces v
    b(i,1:d)=data((i-1)*d+1:i*d);
end
    %calculate the mean of each piece
    me=mean(b,2);
    %calculate the fft of the vector and pad to the desired length for
    %linear fft
    %calculate the difference from the mean
    b2=b-me;
B=fft(b2,2*d-1,2);
%calcualate the power spectral density
G=B.*conj(B);%it doesn't matter if divided by the length (d) here or later
g=ifft(G,2*d-1,2); %since the vector g has a length of 2n-1 we have to
%devide by 2n-1 instead of n (definition of fft in matlab)
g=g./((2*d-1)*me.^2);


t=(0:1:d-1)*ts;
%eliminates NaN values
[m, ~]=find(isnan(g));
g(m,:)=[];
if filter==1
    c=g;
else
    c=mean(g,1);
end
```

```
c=c(1:d);
g=g(:,1:d);
end
```

logbinmatrix.m

```
function [tlogbin,clogbin,clogstd]=logbinmatrix(t,g,bins)

[m, ~]=size(g);

clogbin=zeros([bins m]);
clogstd=zeros([bins m]);

for i=1:1:m

   [tlogbin,a,b]=logbinning(t,g(i,:),bins);
   clogbin(:,i)=a;
   clogstd(:,i)=b;

end
end
```

logbinmatrix_remove_rep_full.m

```
function [tlogbin,clogbin,clogstd]=logbinmatrix_remove_rep_full(t,g,bins)

[m, ~]=size(g);

clogbin=zeros([bins m]);
clogstd=zeros([bins m]);

for i=1:1:m

   [tlogbin,a,b]=logbinning(t,g(i,:),bins);
   clogbin(:,i)=a;
   clogstd(:,i)=b;

end
%elimination of replicates at the beginning - here not just looks at first
%column, but at all and finds minimum amount of values to remove
%places column indices of where the condition is met in col
[~,col,~]=find(tlogbin==tlogbin(1,:) & clogbin==clogbin(1,:));
%stores in C the unique values of col in order and only once and in ic each
%value as it appears in the original matrix
[C,~,ic]=unique(col);
%accumarray uses an input here ic which defines the groups (and would put
%it into the ascending order, but here already done) and takes each value
%only once then it would use the values (where there is a 1 now) if
```

```
%multiple of the same index in ic and add them. Since there is a one it
%adds ones as many as belong to the same position/index in ic. This is how
%accumarray counts data
%then this is combined with unique
a_counts = accumarray(ic,1);

%removes the values below the minimum duplicate value
tlogbin(C<min(a_counts))=[];
clogbin(C<min(a_counts),:)=[];
clogstd(C<min(a_counts),:)=[];
end
```

logbinning.m

```
function [tavg,cavg,cstd]=logbinning(t,c,bins)
t=t(2:end);
c=c(2:end);
n=length(c);
index=zeros([bins 2]);
tavg=zeros([bins 1]);
cavg=zeros([bins 1]);
cstd=zeros([bins 1]);
for i=1:1:bins
   index(i,:)=[floor(exp((i-1)*log(n)/bins)), floor(exp((i)*log(n)/bins))];
   tavg(i)=mean(t(index(i,1):index(i,2)));
   cavg(i)=mean(c(index(i,1):index(i,2)));
   cstd(i)=std(c(index(i,1):index(i,2)),1);
end
end
```

line_evaluation.m

```
function [C]=line_evaluation(clogbin_lines,tlogbin,clogbin_lines_std)
prompt = {'Enter selector 0 to not fit all the lines per image chunk or 1 to
    fit all the lines of each image chunk'};
dlgtitle = 'Input';
dims = [1 35];
definput = {'0'};
answer = inputdlg(prompt,dlgtitle,dims,definput);
d2=str2double(answer);

if d2==0
    str=["It was chosen to not fit all the autocorrelation lines"];
    C={str};
celldisp(C)
elseif d2==1
    for i=1:1:length(clogbin_lines)
        k=clogbin_lines(i);
```

```
        l=cell2mat(k);
        m=clogbin_lines_std(i);
        n=cell2mat(m);
        sz=size(l);
        r=[];
        for j=1:1:sz(2)
%fit: here choose which parameters to keep constant and which ones to alter
%according to the selector input

[fitresult, gof] = createFit2D(tlogbin, l(:,j),n(:,j) );
r(j,:)=coeffvalues(fitresult);

%ignore 0 standard deviation values just for the plotting by including NaN
%values
index=find(n(:,j)==0);
n(index,j)=NaN;

% Plot fit with data.
figure( 'Name', 'Fitted autocorrelation' );
h = plot( fitresult, tlogbin, l(:,j) );
hold on;
errorbar(tlogbin, l(:,j), n(:,j),'b','LineStyle','none');
legend( h, 'data', 'fit', 'Location', 'NorthEast' );
set(gca, 'XScale', 'log')
% Label axes
xlabel 'Time lag \tau [s]'
ylabel 'AC [a.u.]'
grid on
        end
        r_help{i}=r;
    end
    str=["gamma", "n", "D", "w_xy", "wz", "offset"];
C={str;r_help};
celldisp(C)
end
end
```

C.2 Combined setup

This small LabView program allows for digital counting of the detected photons. As described in section 3.7.3 detected photons are read out through a DAQ3001 board via the program in figs. C.1 and C.2 after being discriminated by a discriminator. Figure C.1 shows counts per seconds with 2 acquisition rates. Figure C.2 shows two loops which record the data with an acquisition sampling every 500 ms and 4 ms.

Kanaleinstellungen

Zähler: Dev1/ctr0

Eingangsanschluss: /Dev1/PFI0

Aktive Flanke: Steigend

Erfasste Daten

Zählwert: 0

Timing-Einstellungen

Schleifendauer (ms): 1

Trigger-Einstellungen

Kein Trigger | Start (digital) | Pause (digital) | Zähler-Reset

Um einen Trigger oder Zähler-Reset zu konfigurieren und verwenden, muss die entsprechende Registerkarte ausgewählt sein. Nicht alle Geräte unterstützen die oben aufgeführten Optionen. Weitere Informationen erhalten Sie in der Dokumentation Ihres Geräts.

Stopp

Save data

Path to data file: Filepath\Filename.lvm

Counts/500ms: 0

Zeit ist verstrichen

subtractor: 0

subtractor 10ms: 0

Counts/ 4ms: 0

Figure C.1: Frontpanel of a digital counter to count detected photons.

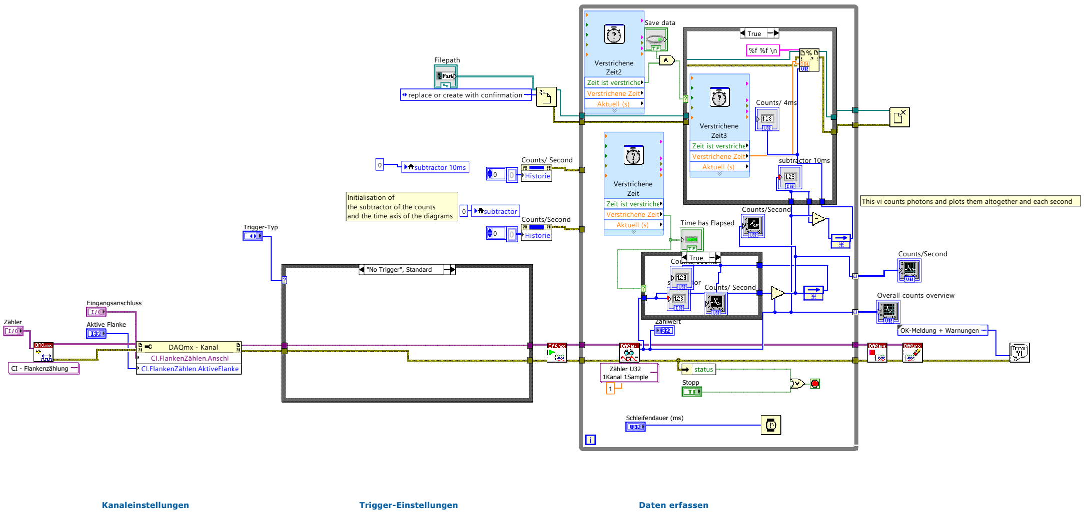

Initialisation of the subtractor of the counts and the time axis of the diagrams

This vi counts photons and plots them altogether and each second

Figure C.2: Code block diagram of a digital counter to count the detected photons. Two loops allow acquisition and recording of 2 time scales every 500 ms and every 4 ms.

C.3 LabView code - autofocus

Front panel (fig. C.3) and block diagram (fig. C.4) in LabView of the autofocus.

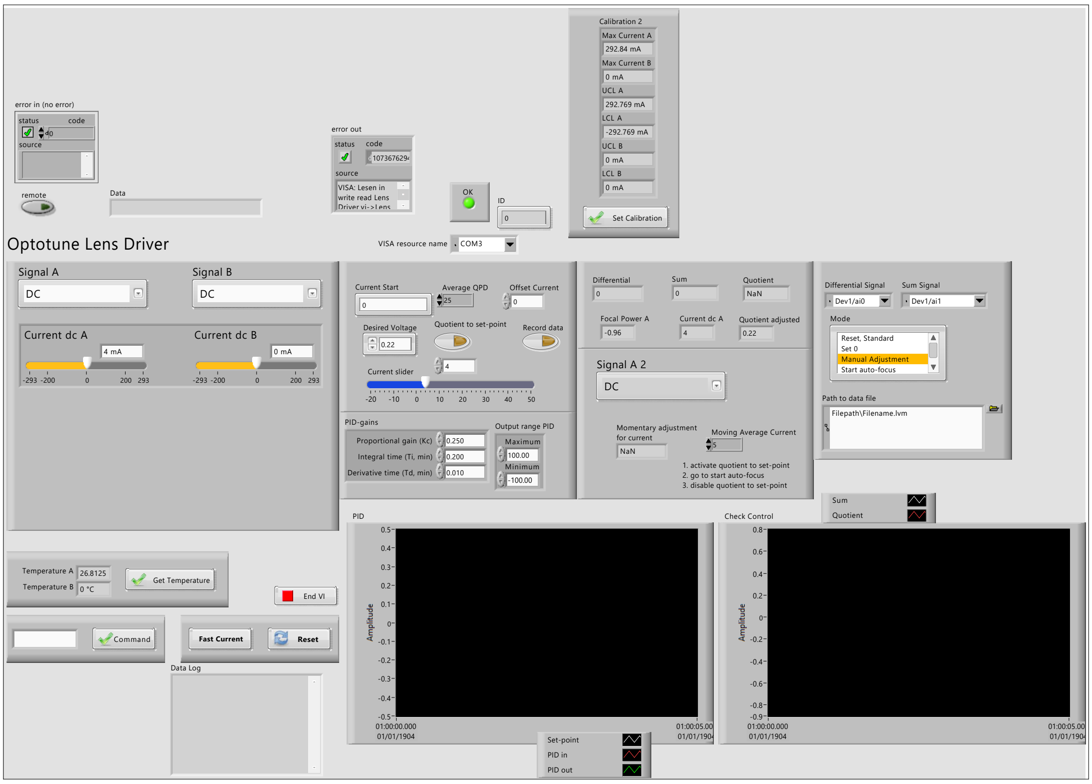

Calibration 2
Max Current A: 292.84 mA
Max Current B: 0 mA
UCL A: 292.769 mA
LCL A: -292.769 mA
UCL B: 0 mA
LCL B: 0 mA

error in (no error): status ☑, code 0
error out: status ☑, code 107367629
source: VISA: Lesen in write read Lens Driver vi->Lens
ID: 0
VISA resource name: COM3

Optotune Lens Driver

Signal A: DC
Signal B: DC
Current dc A: 4 mA
Current dc B: 0 mA

Current Start: 0
Average QPD: 25
Offset Current: 0
Desired Voltage: 0.22
Current slider: 4

PID-gains
Proportional gain (Kc): 0.250
Integral time (Ti, min): 0.200
Derivative time (Td, min): 0.010

Output range PID
Maximum: 100.00
Minimum: -100.00

Differential: 0
Sum: 0
Quotient: NaN
Focal Power A: -0.96
Current dc A: 4
Quotient adjusted: 0.22

Signal A 2: DC
Momentary adjustment for current: NaN
Moving Average Current: 5

1. activate quotient to set-point
2. go to start auto-focus
3. disable quotient to set-point

Differential Signal: Dev1/ai0
Sum Signal: Dev1/ai1
Mode: Reset, Standard / Set 0 / Manual Adjustment / Start auto-focus (Manual Adjustment selected)
Path to data file: Filepath\Filename.lvm

Temperature A: 26.8125
Temperature B: 0 °C

Figure C.3: Frontpanel of the autofocus control showing 4 main panels (below 'Optotune Lens Driver') for adjustments. From left to right: System current and start value, center left: start value of the current, regulator for the averaging of the moving average of the QPD voltage, offset current, desired voltage/set-point QPD voltage, a button to write the current QPD voltage to the set-point and another button to record the data. Input current can also be adjusted by manual input or a slider. PID-gains can be adjusted together with the output range of the PID-controller. The third panel reports on the differential and sum signal, the quotient of the two, the focal power, the input current, as well as the varying set-point QPD voltage (quotient adjusted). Also a moving average for the current is implemented. The right panel allows to choose the input device channels and the operating mode of the program. Further, the signals of the PID and the sum and quotient signals of the QPD can be read out graphically.

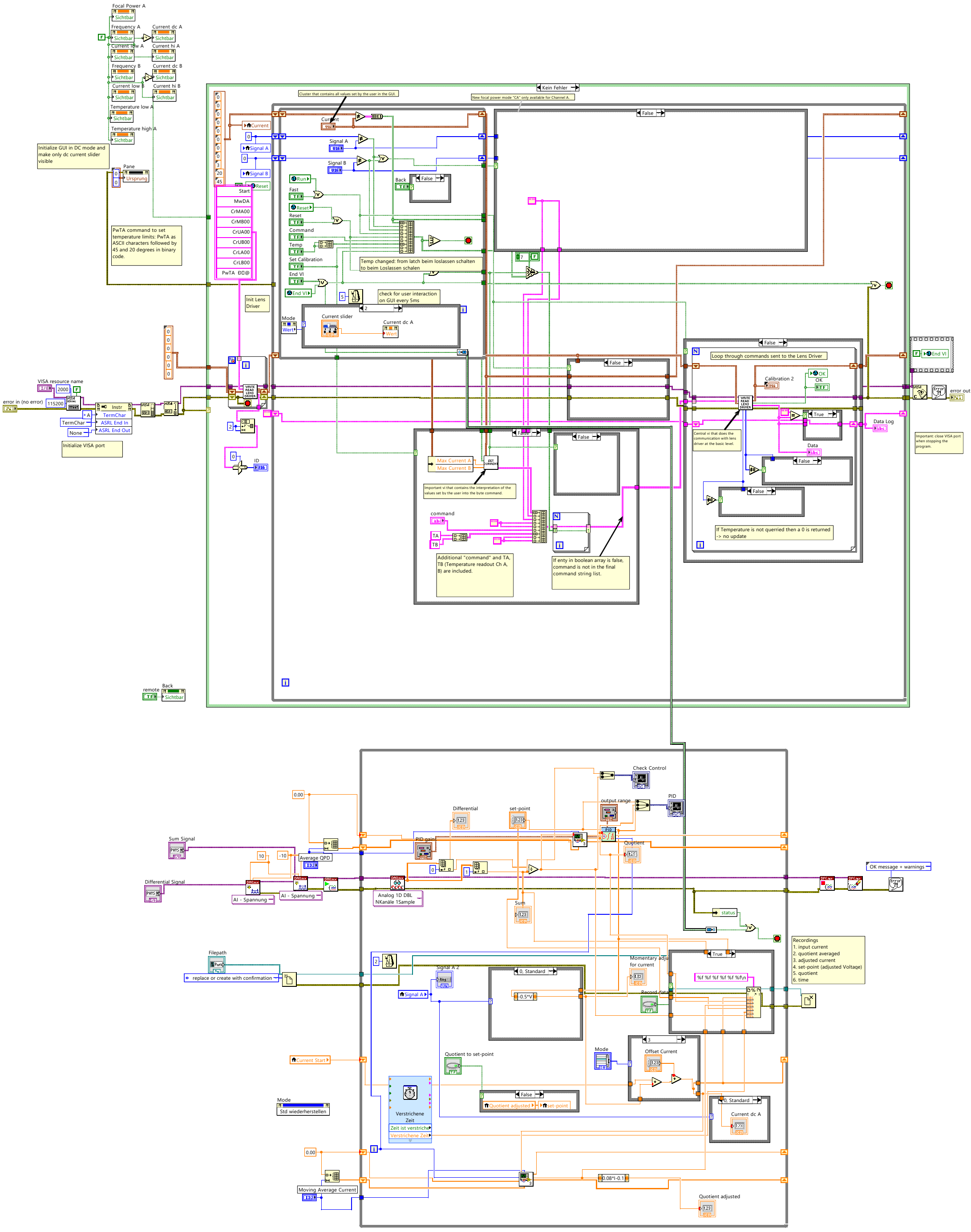

Figure C.4: Code block diagram of the autofocus divided into 2 main blocks. The upper block represents the native control block of the lens (from the manufacturer Optotune.AG) adjusted to work with the second lower block which encompasses the algorithms to operate the autofocus.

Bibliography

1. Colombe, A. S. & Pidoux, G. *Cardiac cAMP-PKA Signaling Compartmentalization in Myocardial Infarction.* Cells **10**(4), 922 (2021).
2. Pfleger, J., Gresham, K. & Koch, W. J. *G protein-coupled receptor kinases as therapeutic targets in the heart.* Nat. Rev. Cardiol. **16**(10), 612–622 (2019).
3. Pierce, K. L., Premont, R. T. & Lefkowitz, R. J. *Seven-transmembrane receptors.* Nat. Rev. Mol. Cell Biol. **3**(9), 639–650 (2002).
4. Simon, M. I., Strathmann, M. P. & Gautam, N. *Diversity of G proteins in signal transduction.* Science **252**(5007), 802–808 (1991).
5. Xiang, Y. & Kobilka, B. K. *Myocyte adrenoceptor signaling pathways.* Science **300**(5625), 1530–1532 (2003).
6. Milano, C. A. *et al. Enhanced myocardial function in transgenic mice overexpressing the $\beta 2$-adrenergic receptor.* Science **264**(5158), 582–586 (1994).
7. Engelhardt, S., Hein, L., Wiesmann, F. & Lohse, M. J. *Progressive hypertrophy and heart failure in $\beta 1$-adrenergic receptor transgenic mice.* Proc. Natl. Acad. Sci. U. S. A. **96**(12), 7059–7064 (1999).
8. Xiao, R. P. *Beta-adrenergic signaling in the heart: dual coupling of the beta2-adrenergic receptor to G(s) and G(i) proteins.* Sci. STKE **2001**(104), re15–re15 (2001).
9. Communal, C., Singh, K., Sawyer, D. B. & Colucci, W. S. *Opposing effects of $\beta 1$- and $\beta 2$-adrenergic receptors on cardiac myocyte apoptosis: Role of a pertussis toxin-sensitive G protein.* Circulation **100**(22), 2210–2212 (1999).
10. Lohse, M. J., Engelhardt, S. & Eschenhagen, T. *What Is the Role of β-Adrenergic Signaling in Heart Failure?* Circ. Res. **93**(10), 896–906 (2003).
11. Daaka, Y., Luttrell, L. M. & Lefkowitz, R. J. *Switching of the coupling of the $\beta 2$-adrenergic receptor to different g proteins by protein kinase A.* Nature **390**(6655), 88–91 (1997).
12. Xiao, R. P. *et al. Coupling of $\beta 2$-adrenoceptor to G(i) proteins and its physiological relevance in murine cardiac myocytes.* Circ. Res. **84**(1), 43–52 (1999).
13. Nikolaev, V. O. *et al. Beta2-adrenergic receptor redistribution in heart failure changes cAMP compartmentation.* Science **327**(5973), 1653–1657 (2010).

14. Chorvat, D. *et al. Spectral unmixing of flavin autofluorescence components in cardiac myocytes.* Biophys. J. **89**(6), L55–L57 (2005).
15. Scarselli, M. *et al. Revealing G-protein-coupled receptor oligomerization at the single-molecule level through a nanoscopic lens: methods, dynamics and biological function.* FEBS J. **283**(7), 1197–1217 (2016).
16. Radek, M. & Hof, M. *Practical Manual for Fluorescence Microscopy Techniques / PicoQuant.* Tech. rep. (PicoQuant, 2016), 105–128.
17. Yang, D. *et al. G protein-coupled receptors: structure- and function-based drug discovery.* Signal Transduct. Target. Ther. **6**(1), 1–27 (2021).
18. Hauser, A. S., Attwood, M. M., Rask-Andersen, M., Schiöth, H. B. & Gloriam, D. E. *Trends in GPCR drug discovery: New agents, targets and indications.* Nat. Rev. Drug Discov. **16**(12), 829–842 (2017).
19. Trzaskowski, B. *et al. Action of Molecular Switches in GPCRs - Theoretical and Experimental Studies.* Curr. Med. Chem. **19**(8), 1090–1109 (2012).
20. Stevens, R. C. *et al. The GPCR Network: A large-scale collaboration to determine human GPCR structure and function.* Nat. Rev. Drug Discov. **12**(1), 25–34 (2013).
21. Santos, R. *et al. A comprehensive map of molecular drug targets.* Nat. Rev. Drug Discov. **16**(1), 19–34 (2017).
22. Mombaerts, P. *Genes and ligands for odorant, vomeronasal and taste receptors.* Nat. Rev. Neurosci. **5**(4), 263–278 (2004).
23. Fredriksson, R., Lagerström, M. C., Lundin, L. G. & Schiöth, H. B. *The G-protein-coupled receptors in the human genome form five main families. Phylogenetic analysis, paralogon groups, and fingerprints.* Mol. Pharmacol. **63**(6), 1256–1272 (2003).
24. Southan, C. *et al. The IUPHAR/BPS Guide to PHARMACOLOGY in 2016: Towards curated quantitative interactions between 1300 protein targets and 6000 ligands.* Nucleic Acids Res. **44**(D1), D1054–D1068 (2015).
25. Atwood, B. K., Lopez, J., Wager-Miller, J., Mackie, K. & Straiker, A. *Expression of G protein-coupled receptors and related proteins in HEK293, AtT20, BV2, and N18 cell lines as revealed by microarray analysis.* BMC Genomics **12**(1), 1–14 (2011).
26. Schiöth, H. B. & Fredriksson, R. *The GRAFS classification system of G-protein coupled receptors in comparative perspective.* Gen. Comp. Endocrinol. **142**(1-2), 94–101 (2005).

27. Manglik, A. & Kruse, A. C. *Structural Basis for G Protein-Coupled Receptor Activation.* Biochemistry **56**(42), 5628–5634 (2017).
28. Downes, G. B. & Gautam, N. *The G protein subunit gene families.* Genomics **62**(3), 544–552 (1999).
29. Milligan, G. & Kostenis, E. *Heterotrimeric G-proteins: A short history.* Br. J. Pharmacol. **147**(SUPPL. 1), S46–S55 (2006).
30. Rasmussen, S. G. *et al. Crystal structure of the β 2 adrenergic receptor-Gs protein complex.* Nature **477**(7366), 549–557 (2011).
31. Maudsley, S., Martin, B. & Luttrell, L. M. *The origins of diversity and specificity in G protein-coupled receptor signaling.* J. Pharmacol. Exp. Ther. **314**(2), 485–494 (2005).
32. Vischer, H. F., Watts, A. O., Nijmeijer, S. & Leurs, R. *G protein-coupled receptors: Walking hand-in-hand, talking hand-in-hand?* Br. J. Pharmacol. **163**(2), 246–260 (2011).
33. Hoffmann, C., Leitz, M. R., Oberdorf-Maass, S., Lohse, M. J. & Klotz, K. N. *Comparative pharmacology of human β-adrenergic receptor subtypes - Characterization of stably transfected receptors in CHO cells.* Naunyn. Schmiedebergs. Arch. Pharmacol. **369**(2), 151–159 (2004).
34. Yung-Chi, C. & Prusoff, W. H. *Relationship between the inhibition constant (KI) and the concentration of inhibitor which causes 50 per cent inhibition (I50) of an enzymatic reaction.* Biochem. Pharmacol. **22**(23), 3099–3108 (1973).
35. Morris, T. H., Birnbaumer, L. & Kaumann, A. J. *High affinity of carazolol for β-adrenoceptors coupled to the adenylyl cyclase in ventricular myocardium of kitten and xenopus laevis.* Naunyn. Schmiedebergs. Arch. Pharmacol. **303**(3), 295–297 (1978).
36. Innis, R. B., Corrêa, F. M. & Snyder, S. H. *Carazolol, an extremely potent β-adrenergic blocker: Binding to β-receptors in brain membranes.* Life Sci. **24**(24), 2255–2264 (1979).
37. Hübner, H. *et al. Structure-guided development of heterodimer-selective GPCR ligands.* Nat. Commun. **7**(1), 12298 (2016).
38. Hulme, E. C. & Trevethick, M. A. *Ligand binding assays at equilibrium: validation and interpretation.* Br. J. Pharmacol. **161**(6), 1219–1237 (2010).
39. Wootten, D., Christopoulos, A. & Sexton, P. M. *Emerging paradigms in GPCR allostery: Implications for drug discovery.* Nat. Rev. Drug Discov. **12**(8), 630–644 (2013).

40. Foster, D. J. & Conn, P. J. *Allosteric Modulation of GPCRs: New Insights and Potential Utility for Treatment of Schizophrenia and Other CNS Disorders.* Neuron **94**(3), 431–446 (2017).

41. Kamal, M. & Jockers, R. *Bitopic ligands: all-in-one orthosteric and allosteric.* F1000 Biol. Rep. **1**(10), 77 (2009).

42. Rosenbaum, D. M., Rasmussen, S. G. & Kobilka, B. K. *The structure and function of G-protein-coupled receptors.* Nature **459**(7245), 356–363 (2009).

43. Ippolito, M. & Benovic, J. L. *Biased agonism at β-adrenergic receptors.* Cell. Signal. **80**, 109905 (2021).

44. Do Vale, G. T., Ceron, C. S., Gonzaga, N. A., Simplicio, J. A. & Padovan, J. C. *Three Generations of β-blockers: History, Class Differences and Clinical Applicability.* Curr. Hypertens. Rev. **15**(1), 22–31 (2019).

45. Wachter, S. B. & Gilbert, E. M. *Beta-adrenergic receptors, from their discovery and characterization through their manipulation to beneficial clinical application.* Cardiol. **122**(2), 104–112 (2012).

46. Strosberg, A. D. *Structure, function, and regulation of adrenergic receptors.* Protein Sci. **2**(8), 1198–1209 (1993).

47. Buxton, I. L. & Brunton, L. L. *Compartments of cyclic AMP and protein kinase in mammalian cardiomyocytes.* J. Biol. Chem. **258**(17), 10233–10239 (1983).

48. Brunton, L. L., Hayes, J. S. & Mayer, S. E. *Hormonally specific phosphorylation of cardiac troponin I and activation of glycogen phosphorylase.* Nature **280**(5717), 78–80 (1979).

49. Hayes, J., Brunton, L. & Mayer, S. *Selective activation of particulate cAMP-dependent protein kinase by isoproterenol and prostaglandin E1.* J. Biol. Chem. **255**(11), 5113–5119 (1980).

50. Guellich, A., Mehel, H. & Fischmeister, R. *Cyclic AMP synthesis and hydrolysis in the normal and failing heart.* Pflugers Arch. Eur. J. Physiol. **466**(6), 1163–1175 (2014).

51. Judina, A., Gorelik, J. & Wright, P. T. *Studying signal compartmentation in adult cardiomyocytes.* Biochem. Soc. Trans. **48**(1), 61–70 (2020).

52. Zaccolo, M., Zerio, A. & Lobo, M. J. *Subcellular Organization of the cAMP Signaling Pathway.* Pharmacol. Rev. Pharmacol Rev **73**, 278–309 (2021).

53. Nikolaev, V. O., Bünemann, M., Schmitteckert, E., Lohse, M. J. & Engelhardt, S. *Cyclic AMP imaging in adult cardiac myocytes reveals far-reaching beta1-adrenergic but locally confined beta2-adrenergic receptor-mediated signaling.* Circ Res **99**(10), 1084–1091 (2006).

54. Yang, H.-Q. *et al. β2-Adrenergic Stimulation Compartmentalizes β1 Signaling Into Nanoscale Local Domains by Targeting the C-Terminus of β1-Adrenoceptors.* Circ. Res. **124**(9), 1350–1359 (2019).

55. Bock, A. *et al. Optical Mapping of cAMP Signaling at the Nanometer Scale.* Cell **182**(6), 1519–1530.e17 (2020).

56. Stangherlin, A. & Zaccolo, M. *Phosphodiesterases and subcellular compartmentalized cAMP signaling in the cardiovascular system.* Am. J. Physiol. - Hear. Circ. Physiol. **302**(2), H379–H390 (2012).

57. Sungkaworn, T. *et al. Single-molecule imaging reveals receptor-G protein interactions at cell surface hot spots.* Nature **550**(7677), 543–547 (2017).

58. Bathe-Peters, M. *et al. Visualization of β-adrenergic receptor dynamics and differential localization in cardiomyocytes.* Proc. Natl. Acad. Sci. **118**(23), e2101119118 (2021).

59. Bates, M., Huang, B., Dempsey, G. T. & Zhuang, X. *Multicolor super-resolution imaging with photo-switchable fluorescent probes.* Science **317**(5845), 1749–1753 (2007).

60. Spring, K. R. & Davidson, M. W. *Introduction to Fluorescence Microscopy | Nikon's MicroscopyU.* https://www.microscopyu.com/techniques/fluorescence/introduction-to-fluorescence-microscopy (23/06/2021).

61. Sensor Technologies LLC. *FCSXpert Solutions - Fluorescence Correlation Spectroscopy Simplified!* http://www.fcsxpert.com/classroom/%20http://www.fcsxpert.com/classroom/theory/autocorrelation-function-list.html%20http://www.fcsxpert.com/classroom/theory/autocorrelation-fluorescence-intensity.html (20/10/2020).

62. Vogelsang, J. *Advancing Single-Molecule Fluorescence Spectroscopy and Super-Resolution Microscopy with Organic Fluorophores.* PhD thesis (Ludwig-Maximilians-University, Munich, 2009).

63. Singh, A. & Gopinathan, K. P. *Confocal microscopy: A powerful technique for biological research.* Curr. Sci. **74**(10), 841–851 (1998).

64. Combs, C. A. & Shroff, H. *Fluorescence microscopy: A concise guide to current imaging methods.* Curr. Protoc. Neurosci. **79**(1), 2.1.1–2.1.25 (2017).

65. Kohl, T., Westphal, V., Hell, S. W. & Lehnart, S. E. *Superresolution microscopy in heart - Cardiac nanoscopy.* J. Mol. Cell. Cardiol. **58**(1), 13–21 (2013).
66. Möller, J. *et al. Single-molecule analysis reveals agonist-specific dimer formation of μ-opioid receptors.* Nat. Chem. Biol. **16**(9), 946–954 (2020).
67. Işbilir, A. *et al. Advanced fluorescence microscopy reveals disruption of dynamic CXCR4 dimerization by subpocket-specific inverse agonists.* Proc. Natl. Acad. Sci. **117**(46), 29144–29154 (2020).
68. Nikolaev, V. O., Bünemann, M., Hein, L., Hannawacker, A. & Lohse, M. J. *Novel single chain cAMP sensors for receptor-induced signal propagation.* J. Biol. Chem. **279**(36), 37215–37218 (2004).
69. Plouffe, B., Thomsen, A. R. & Irannejad, R. *Emerging Role of Compartmentalized G Protein-Coupled Receptor Signaling in the Cardiovascular Field.* ACS Pharmacol. Transl. Sci. **3**(2), 221–236 (2020).
70. Nenasheva, T. A. *et al. Abundance, distribution, mobility and oligomeric state of M2 muscarinic acetylcholine receptors in live cardiac muscle.* J. Mol. Cell. Cardiol. **57**(1), 129–136 (2013).
71. Ostrom, R. S., Post, S. R. & Insel, P. A. *Stoichiometry and Compartmentation in G Protein-Coupled Receptor Signaling: Implications for Therapeutic Interventions Involving Gs.* J. Pharmacol. Exp. Ther. **294**(2), 407–412 (2000).
72. Ries, J., Chiantia, S. & Schwille, P. *Accurate Determination of Membrane Dynamics with Line-Scan FCS.* Biophys. J. **96**(5), 1999–2008 (2009).
73. Di Rienzo, C., Gratton, E., Beltram, F. & Cardarelli, F. *Fast spatiotemporal correlation spectroscopy to determine protein lateral diffusion laws in live cell membranes.* Proc. Natl. Acad. Sci. U. S. A. **110**(30), 12307–12312 (2013).
74. Hebert, B., Costantino, S. & Wiseman, P. W. *Spatiotemporal image correlation spectroscopy (STICS) theory, verification, and application to protein velocity mapping in living CHO cells.* Biophys J **88**(5), 3601–3614 (2005).
75. Wang, J., Gareri, C. & Rockman, H. A. *G-protein-coupled receptors in heart disease.* Circ. Res. **123**(6), 716–735 (2018).
76. Litviňuková, M. *et al. Cells of the adult human heart.* Nature **588**(7838), 466–472 (2020).

77. Kong, C. H. T., Rog-Zielinska, E. A., Orchard, C. H., Kohl, P. & Cannell, M. B. *Sub-microscopic analysis of t-tubule geometry in living cardiac ventricular myocytes using a shape-based analysis method.* J Mol Cell Cardiol **108**, 1–7 (2017).

78. Soeller, C. & Cannell, M. B. *Examination of the Transverse Tubular System in Living Cardiac Rat Myocytes by 2-Photon Microscopy and Digital Image–Processing Techniques.* Circ. Res. **84**(3), 266–275 (1999).

79. Wei, S. *et al. T-tubule remodeling during transition from hypertrophy to heart failure.* Circ. Res. **107**(4), 520–531 (2010).

80. Schobesberger, S. *et al. T-tubule remodelling disturbs localized* $\beta 2$*-adrenergic signalling in rat ventricular myocytes during the progression of heart failure.* Cardiovasc Res **113**(7), 770–782 (2017).

81. Louch, W. E., Sheehan, K. A. & Wolska, B. M. *Methods in cardiomyocyte isolation, culture, and gene transfer.* J. Mol. Cell. Cardiol. **51**(3), 288–298 (2011).

82. Hodne, K., Lipsett, D. B. & Louch, W. E. in *Card. Gene Ther. Methods Protoc.* (ed Ishikawa, K.) 169–182 (Springer New York, 2017).

83. Zhou, Y. Y. *et al. Culture and adenoviral infection of adult mouse cardiac myocytes: Methods for cellular genetic physiology.* Am. J. Physiol. - Hear. Circ. Physiol. **279**(1), H429–H436 (2000).

84. Bonci, D. *et al. 'Advanced' generation lentiviruses as efficient vectors for cardiomyocyte gene transduction in vitro and in vivo.* Gene Ther. **10**(8), 630–636 (2003).

85. Katz, M. G., Fargnoli, A. S., Weber, T., Hajjar, R. J. & Bridges, C. R. *Use of Adeno-Associated Virus Vector for Cardiac Gene Delivery in Large-Animal Surgical Models of Heart Failure.* Hum. Gene Ther. Clin. Dev. **28**(3), 157–164 (2017).

86. Zincarelli, C., Soltys, S., Rengo, G. & Rabinowitz, J. E. *Analysis of AAV serotypes 1-9 mediated gene expression and tropism in mice after systemic injection.* Mol. Ther. **16**(6), 1073–1080 (2008).

87. Riedl, J. *et al. Lifeact mice for studying F-actin dynamics.* Nat. Methods **7**(3), 168–169 (2010).

88. Hamdani, N. & Van Der Velden, J. *Lack of specificity of antibodies directed against human beta-adrenergic receptors.* Naunyn. Schmiedebergs. Arch. Pharmacol. **379**(4), 403–407 (2009).

89. Stoddart, L. A., Kilpatrick, L. E., Briddon, S. J. & Hill, S. J. *Probing the pharmacology of G protein-coupled receptors with fluorescent ligands.* Neuropharmacology **98**, 48–57 (2015).

90. Hern, J. A. *et al. Formation and dissociation of M1 muscarinic receptor dimers seen by total internal reflection fluorescence imaging of single molecules.* Proc. Natl. Acad. Sci. U. S. A. **107**(6), 2693–2698 (2010).

91. Mitronova, G. Y. *et al. High-Affinity Functional Fluorescent Ligands for Human β-Adrenoceptors.* Sci. Rep. **7**(1) (2017).

92. Baker, J. G., Hall, I. P. & Hill, S. J. *Pharmacology and direct visualisation of BODIPY-TMR-CGP: A long-acting fluorescent β 2-adrenoceptor agonist.* Br. J. Pharmacol. **139**(2), 232–242 (2003).

93. Daly, C. J. *et al. Fluorescent ligand binding reveals heterogeneous distribution of adrenoceptors and 'cannabinoid-like' receptors in small arteries.* Br. J. Pharmacol. **159**(4), 787–796 (2010).

94. Hegener, O. *et al. Dynamics of β2-adrenergic receptor-ligand complexes on living cells.* Biochemistry **43**(20), 6190–6199 (2004).

95. Baker, J. G. *et al. Synthesis and characterization of high-affinity 4,4-difluoro-4-bora-3a,4a- diaza-s-indacene-labeled fluorescent ligands for human β-adrenoceptors.* J. Med. Chem. **54**(19), 6874–6887 (2011).

96. Stephens, D. J. & Allan, V. J. *Light microscopy techniques for live cell imaging.* Science **300**(5616), 82–86 (2003).

97. Price, J. H. & Gough, D. A. *Comparison of phase-contrast and fluorescence digital autofocus for scanning microscopy.* Cytometry **16**(4), 283–297 (1994).

98. Li, S., Cui, X. & Huang, W. *High resolution autofocus for spatial temporal biomedical research.* Rev. Sci. Instrum. **84**(11), 114302 (2013).

99. Yazdanfar, S. *et al. Simple and robust image-based autofocusing for digital microscopy.* Opt. Express **16**(12), 8670 (2008).

100. Liron, Y., Paran, Y., Zatorsky, N. G., Geiger, B. & Kam, Z. *Laser autofocusing system for high-resolution cell biological imaging.* J. Microsc. **221**(2), 145–151 (2006).

101. Pertsinidis, A., Zhang, Y. & Chu, S. *Subnanometre single-molecule localization, registration and distance measurements.* Nature **466**(7306), 647–651 (2010).

102. Henze, K. *Leica DMI6000 B with Adaptive Focus Control Inverses Mikroskop Leica DMI6000 B.* https://www.leica-microsystems.com/de/produkte/lichtmikroskope/p/leica-dmi6000-with-adaptive-focus-control/downloads/ (01/06/2021).

103. Optotune. *Optotune Data Sheet.* http://www.optotune.com/products/focus-tunable-lenses (01/06/2021).

104. Annibale, P., Dvornikov, A. & Gratton, E. *Optical measurement of focal offset in tunable lenses.* Opt Express **24**(2), 1031–1036 (2016).

105. Blum, M., Büeler, M., Grätzel, C. & Aschwanden, M. *Compact optical design solutions using focus tunable lenses.* in *Opt. Des. Eng. IV* (ed Jean-Luc M. Tissot and Jeffrey M. Raynor and Laurent Mazuray and Rolf Wartmann and Andrew Wood) **8167** (SPIE, 2011), 274–282.

106. Grewe, B. F., Voigt, F. F., van 't Hoff, M. & Helmchen, F. *Fast two-layer two-photon imaging of neuronal cell populations using an electrically tunable lens.* Biomed. Opt. Express **2**(7), 2035 (2011).

107. Piazza, S., Bianchini, P., Sheppard, C., Diaspro, A. & Duocastella, M. *Enhanced volumetric imaging in 2-photon microscopy via acoustic lens beam shaping.* J. Biophotonics **11**(2), e201700050 (2018).

108. Jabbour, J. M. *et al. Optical axial scanning in confocal microscopy using an electrically tunable lens.* Biomed. Opt. Express **5**(2), 645 (2014).

109. Annibale, P., Dvornikov, A. & Gratton, E. *Electrically tunable lens speeds up 3D orbital tracking.* Biomed. Opt. Express **6**(6), 2181 (2015).

110. Wang, Z. *et al. Compact multi-band fluorescent microscope with an electrically tunable lens for autofocusing.* Biomed. Opt. Express **6**(11), 4353 (2015).

111. Rohrer, D. K., Chruscinski, A., Schauble, E. H., Bernstein, D. & Kobilka, B. K. *Cardiovascular and metabolic alterations in mice lacking both* β*1- and* β*2-adrenergic receptors.* J. Biol. Chem. **274**(24), 16701–16708 (1999).

112. O'Connell, T. & Ni, Y. *Isolation of Adult Mouse Cardiac Myocytes from One Heart, AfCS Procedure Protocol ID PP00000125.* Tech. rep. (Alliance for Cellular Signaling, 2002), 1–13.

113. Bathe-Peters, M., Gmach, P., Annibale, P. & Lohse, M. J. *Linescan microscopy data to extract diffusion coefficient of a fluorescent species using a commercial confocal microscope.* Data Br. **29**, 105063 (2020).

114. Cole, R. W., Jinadasa, T. & Brown, C. M. *Measuring and interpreting point spread functions to determine confocal microscope resolution and ensure quality control.* Nat. Protoc. **6**(12), 1929–1941 (2011).

115. Rüttinger, S. *et al. Comparison and accuracy of methods to determine the confocal volume for quantitative fluorescence correlation spectroscopy.* J. Microsc. **232**(2), 343–352 (2008).

116. Buschmann, V., Krämer, B., Koberling, F. & Macdonald, R. *Quantitative FCS: Determination of the Confocal Volume by FCS and Bead Scanning with the MicroTime 200.* Tech. rep. (PicoQuant GmbH, Physikalisch Technische Bundesanstalt, 2009).

117. Rüttinger, S. *Confocal Microscopy and Quantitative Single Molecule Techniques for Metrology in Molecular Medicine.* Doctoral Thesis (Technische Universität Berlin, 2007).

118. Haustein, E. & Schwille, P. *Fluorescence Correlation Spectroscopy: Novel Variations of an Established Technique.* Annu. Rev. Biophys. Biomol. Struct. **36**(1), 151–169 (2007).

119. Elson, E. L. & Magde, D. *Fluorescence correlation spectroscopy. I. Conceptual basis and theory.* Biopolymers **13**(1), 1–27 (1974).

120. Milon, S., Hovius, R., Vogel, H. & Wohland, T. *Factors influencing fluorescence correlation spectroscopy measurements on membranes: simulations and experiments.* Chem. Phys. **288**(2-3), 171–186 (2003).

121. Magde, D., Elson, E. & Webb, W. W. *Thermodynamic fluctuations in a reacting system measurement by fluorescence correlation spectroscopy.* Phys. Rev. Lett. **29**(11), 705–708 (1972).

122. Magde, D., Elson, E. L. & Webb, W. W. *Fluorescence correlation spectroscopy. II. An experimental realization.* Biopolymers **13**(1), 29–61 (1974).

123. Brown, C. M. *et al. Raster image correlation spectroscopy (RICS) for measuring fast protein dynamics and concentrations with a commercial laser scanning confocal microscope.* J. Microsc. **229**(1), 78–91 (2008).

124. Wolf, D. E. *What is the Confocal Volume?* www.fcsxpert.com%20http://www.fcsxpert.com/classroom/theory/what-is-confocal-volume.html (08/06/2020).

125. Schwille, P. & Haustein, E. *Fluorescence Correlation Spectroscopy - An Introduction to its Concepts and Applications.* Tech. rep. (2002).

126. Schwille, P., Korlach, J. & Webb, W. W. *Fluorescence correlation spectroscopy with single-molecule sensitivity on cell and model membranes.* Cytometry **36**(3), 176–182 (1999).

127. Elson, E. L. *Fluorescence correlation spectroscopy: past, present, future.* Biophys. J. **101**(12), 2855–2870 (2011).

128. Jiang, Y., Melnykov, A. & Elson, E. *FCS in closed systems and application for membrane nanotubes.* bioRxiv, 134742 (2017).

129. Kandula, H. N., Jee, A. Y. & Granick, S. *Robustness of FCS (Fluorescence Correlation Spectroscopy) with Quenchers Present.* J. Phys. Chem. A **123**(46), 10184–10189 (2019).

130. Dix, J. A., Hom, E. F. & Verkman, A. S. *Fluorescence correlation spectroscopy simulations of photophysical phenomena and molecular interactions: A molecular dynamics/monte carlo approach.* J. Phys. Chem. B **110**(4), 1896–1906 (2006).

131. Hodges, C., Kafle, R. P., Hoff, J. D. & Meiners, J. C. *Fluorescence Correlation Spectroscopy with Photobleaching Correction in Slowly Diffusing Systems.* J. Fluoresc. **28**(2), 505–511 (2018).

132. Nolan, R. *Algorithms for the Correction of Photobleaching.* PhD thesis (University of Oxford, Oxford, 2018).

133. Di Rienzo, C. & Annibale, P. *Visualizing the molecular mode of motion from a correlative analysis of localization microscopy datasets.* Opt. Lett. **41**(19), 4503 (2016).

134. Zhou, C. *et al. Motility and segregation of Hsp104-associated protein aggregates in budding yeast.* Cell **147**(5), 1186–1196 (2011).

135. Bathe-Peters, M., Annibale, P. & Lohse, M. J. *All-optical microscope autofocus based on an electrically tunable lens and a totally internally reflected IR laser.* Opt. Express **26**(3), 2359–2368 (2018).

136. Ross, S. T., Schwartz, S., Fellers, T. J. & Davidson, M. W. *Total Internal Reflection Fluorescence (TIRF) Microscopy.* https://www.microscopyu.com/techniques/fluorescence/total-internal-reflection-fluorescence-tirf-microscopy (03/06/2021).

137. Kawano, Y. & Enders, R. G. *Total Internal Reflection Fluorescence Microscopy.* https://www.olympus-lifescience.com/de/microscope-resource/primer/techniques/confocal/applications/tirfmintro/ (03/06/2021).

138. Axelrod, D., Long, J. C. & Davidson, M. W. *Evanescent Field Penetration Depth.* https://www.olympus-lifescience.com/en/microscope-resource/primer/java/tirf/penetration/ (03/06/2021).

139. GraphPad Software. *GraphPad Prism 9 Curve Fitting Guide - Equation: One site – Specific binding.* https://www.graphpad.com/guides/prism/latest/curve-fitting/reg%7B%5C_%7Done%7B%5C_%7Dsite%7B%5C_%7Dspecific.htm (10/05/2021).

140. PerkinElmer & Cisbio. *Receptor binding - By universe - Life sciences.* https://www.cisbio.eu/dd/by-universe/receptor-binding (29/01/2021).

141. Bartsch, W., Dietmann, K., Leinert, H. & Sponer, G. *Cardiac action of carazolol and methypranol in comparison with other beta-receptor blockers - PubMed.* Arzneimittelforschung **27**(5), 1022–1026 (1977).

142. Dubois, E. A. *et al. Synthesis and in vitro and in vivo characteristics of an iodinated analogue of the β-adrenoceptor antagonist carazolol.* J. Med. Chem. **39**(17), 3256–3262 (1996).

143. Giard, D. J. *et al. In vitro cultivation of human tumors: Establishment of cell lines derived from a series of solid tumors.* J. Natl. Cancer Inst. **51**(5), 1417–1423 (1973).

144. Delavier-Klutchko, C., Hoebeke, J. & Strosberg, A. D. *The human carcinoma cell line A431 possesses large numbers of functional β-adrenergic receptors.* FEBS Lett. **169**(2), 151–155 (1984).

145. Kashles, O. & Levttzki, A. *Characterization of the β2-adrenoceptor-dependent adenylate cyclase of A431 epidermoid carcinoma cells.* Biochem. Pharmacol. **36**(9), 1531–1538 (1987).

146. Pippig, S., Andexinger, S. & Lohse, M. J. *Sequestration and recycling of beta 2-adrenergic receptors permit receptor resensitization. | Molecular Pharmacology.* Mol. Pharmacol. **47**(4), 666–676 (1995).

147. Engelhardt, S. *Transgene Mausmodelle zur Charakterisierung der Funktion kardialer beta-adrenerger Rezeptoren.* Doctoral Thesis (Universität Würzburg, 2001).

148. Willecke, F. *Erzeugung und phänotypische Charakterisierung von transgenen Mäusen, die β1- und β2-adrenerge Rezeptoren überexprimieren.* Doctoral Thesis (Universität Würzburg, 2006).

149. Van Der Velden, W. J., Heitman, L. H. & Rosenkilde, M. M. *Perspective: Implications of Ligand-Receptor Binding Kinetics for Therapeutic Targeting of G Protein-Coupled Receptors.* ACS Pharmacol. Transl. Sci. **3**(2), 179–189 (2020).
150. Segur, J. B. & Oderstar, H. E. *Viscosity of Glycerol and Its Aqueous Solutions.* Ind. Eng. Chem. **43**(9), 2117–2120 (1951).
151. Kapusta, P. *Absolute Diffusion Coefficients: Compilation of Reference Data for FCS Calibration.* Tech. rep. (PicoQuant, 2010).
152. Loman, A. *Molecular Sizing using Fluorescence Correlation Spectroscopy.* PhD thesis (Georg-August-Universität Göttingen, 2010).
153. Raman, C. V. *A theory of the viscosity of liquids.* Nature **111**(2790), 532–533 (1923).
154. Fasina, O. & Colley, Z. *Viscosity and Specific Heat of Vegetable Oils as a Function of Temperature: 35°C to 180°C.* Int. J. Food Prop. **11**(4), 738–746 (2008).
155. Goh, S. E. G. *The Hidden Property of Arrhenius-type Relationship: Viscosity as a Function of Temperature.* J. Phys. Sci. **21**(1), 29–39 (2010).
156. Bathe-Peters, M., Gmach, P., Annibale, P. & Lohse, M. J. *All-in-one confocal and widefield fluorescence microscope to investigate membrane receptor dynamics.* in *Imaging Appl. Opt. 2019 (COSI, IS, MATH, pcAOP) (2019), OSA Tech. Dig.* (Optical Society of America, 2019), paper JW2A.4.
157. Xu, J., Tehrani, K. F. & Kner, P. *Multicolor 3D super-resolution imaging by quantum dot stochastic optical reconstruction microscopy.* ACS Nano **9**(3), 2917–2925 (2015).
158. Nooh, M. M., Mancarella, S. & Bahouth, S. W. *Novel Paradigms Governing β1-Adrenergic Receptor Trafficking in Primary Adult Rat Cardiac Myocytes.* Mol. Pharmacol. **94**(2), 862–875 (2018).
159. Hall, R. A. *β-adrenergic receptors and their interacting proteins.* Semin. Cell Dev. Biol. **15**(3), 281–288 (2004).
160. Calebiro, D. *et al. Single-molecule analysis of fluorescently labeled G-protein-coupled receptors reveals complexes with distinct dynamics and organization.* Proc. Natl. Acad. Sci. U. S. A. **110**(2), 743–748 (2013).
161. Wheeler, D., Sneddon, W. B., Wang, B., Friedman, P. A. & Romero, G. *NHERF-1 and the Cytoskeleton Regulate the Traffic and Membrane Dynamics of G Protein-coupled Receptors *.* J. Biol. Chem. **282**(34), 25076–25087 (2007).

162. Wheeler, D. *et al. Regulation of parathyroid hormone type 1 receptor dynamics, traffic, and signaling by the Na+/H+ exchanger regulatory factor-1 in rat osteosarcoma ROS 17/2.8 cells.* Mol. Endocrinol. **22**(5), 1163–1170 (2008).

163. Scarselli, M., Annibale, P. & Radenovic, A. *Cell Type-specific β2-Adrenergic Receptor Clusters Identified Using Photoactivated Localization Microscopy Are Not Lipid Raft Related, but Depend on Actin Cytoskeleton Integrity *.* J. Biol. Chem. **287**(20), 16768–16780 (2012).

164. Xiang, Y. & Kobilka, B. *The PDZ-binding motif of the β2-adrenoceptor is essential for physiologic signaling and trafficking in cardiac myocytes.* Proc. Natl. Acad. Sci. **100**(19), 10776–10781 (2003).

165. Cao, T. T., Deacon, H. W., Reczek, D., Bretscher, A. & von Zastrow, M. *A kinase-regulated PDZ-domain interaction controls endocytic sorting of the β2-adrenergic receptor.* Nature **401**(6750), 286–290 (1999).

166. Rosholm, K. R. *et al. Membrane curvature regulates ligand-specific membrane sorting of GPCRs in living cells.* Nat. Chem. Biol. **13**(7), 724–729 (2017).

167. Kaur, H. *et al. Single-cell profiling reveals heterogeneity and functional patterning of GPCR expression in the vascular system.* Nat. Commun. **8**(1), 1–15 (2017).

168. Fuh, Y. K., Chen, J. K. & Chen, P. W. *Characterization of electrically tunable liquid lens and adaptive optics for aberration correction.* Optik (Stuttg). **126**(24), 5456–5459 (2015).

169. Ronaldson-Bouchard, K. *et al. Advanced maturation of human cardiac tissue grown from pluripotent stem cells.* Nature **556**(7700), 239–243 (2018).

170. Petrášek, Z., Derenko, S. & Schwille, P. *Circular scanning fluorescence correlation spectroscopy on membranes.* Opt. Express **19**(25), 25006 (2011).

171. Ruan, Q., Cheng, M. A., Levi, M., Gratton, E. & Mantulin, W. W. *Spatial-temporal studies of membrane dynamics: Scanning fluorescence correlation spectroscopy (SFCS).* Biophys. J. **87**(2), 1260–1267 (2004).

172. Annibale, P., Bathe-Peters, M. & Lohse, M. J. *Autofocus-control of a microscope including an electrically tunable lens. Priorities 2017. Patent WO2019081333A1 (2019); EP3474060A1 (2019); EP3701310A1 (2020); CN111247471A (2020); US2020301124A1 (2020)*

Publications

During my thesis the following publications and patent were published:

2018	Bathe-Peters, M., Annibale, P. & Lohse, M. J. *All-optical microscope autofocus based on an electrically tunable lens and a totally internally reflected IR laser.* Opt. Express **26**(3), 2359–2368 (Feb. 2018). DOI: 10.1364/OE.26.002359
2019	Bathe-Peters, M., Gmach, P., Annibale, P. & Lohse, M. J. *All-in-one confocal and widefield fluorescence microscope to investigate membrane receptor dynamics.* in *Imaging Appl. Opt. 2019 (COSI, IS, MATH, pcAOP) (2019), OSA Tech. Dig.* (Optical Society of America, June 2019), paper JW2A.4. DOI: 10.1364/COSI.2019.JW2A.4
2020	Bathe-Peters, M., Gmach, P., Annibale, P. & Lohse, M. J. *Linescan microscopy data to extract diffusion coefficient of a fluorescent species using a commercial confocal microscope.* Data Br. **29**, 105063 (Apr. 2020). DOI: 10.1016/j.dib.2019.105063
2021	Bathe-Peters, M., Gmach, P., Boltz, H.-H., Einsiedel, J., Gotthardt, M., Hübner, H., Gmeiner, P., Lohse, M. J. & Annibale, P. *Visualization of β-adrenergic receptor dynamics and differential localization in cardiomyocytes.* Proc. Natl. Acad. Sci. **118**(23), e2101119118 (June 2021). DOI: 10.1073/pnas.2101119118

International Patent

2017	Annibale, P., Bathe-Peters, M. & Lohse, M. J. *Autofocus-control of a microscope including an electrically tunable lens. Priorities 2017. Patent WO2019081333A1 (2019); EP3474060A1 (2019); EP3701310A1 (2020); CN111247471A (2020); US2020301124A1 (2020)*

Acknowledgements

I would like to thank Prof. Dr. Martin J. Lohse for the opportunity to conduct research under his supervision and to perform my doctoral studies with his support. I thank him for all the input, valuable advices and supervision with his expertise in the field which have lead to progress of the project.

Further, I would especially like to express my gratitude to Dr. Paolo Annibale for his supervision, support and scientific input from the very beginning of my doctoral studies. His support and excellent guidance of technologies and knowledge in the scientific field were extremely valuable.

I want to thank my other committee members Prof. Dr. Markus Sauer, Prof. Dr. Christoph Maack and Prof. Dr. Katrin Heinze for their valuable input and for the help to critically reassess the results in our meetings.

I would like to thank Prof. Dr. Peter Gmeiner, Prof. Dr. Harald Hübner and Dr. Jürgen Einsiedel for developing, characterizing and providing us with such a valuable fluorescent ligand.

A special thanks goes to Prof. Michael Gotthardt and his group for teaching us how to isolate cardiomyocytes from mice. In particular Dr. Michael Radke provided much help in learning the procedure and to set up our own perfusion system.

Further, I want to thank Prof. Dr. Holger Gerhardt for allowing us to set up our perfusion system and to let us do the mouse work in his laboratory.

I would like to thank Mr. Roland Wartha for his help in building mechanic parts and the electric circuit for the autofocus system.

Many thanks to all the members of the AG Lohse, especially to the technicians Marlies Grieben, Ruth Pareja, Nicole Grunert and Bärbel Pohl. A big thank you to Philipp Gmach for the discussions and the collaboration on a large part of the project.

Am Ende möchte ich mich bei meiner Familie für die Unterstützung während der gesamten Zeit bedanken.